Abstract

Title of Dissertation: TILTROTOR NOISE REDUCTION THROUGH FLIGHT TRAJECTORY MANAGEMENT AND AIRCRAFT CONFIGURATION CONTROL

Marc Gervais, Doctor of Philosophy, 2004

Dissertation directed by: Professor Fredric H. Schmitz
Department of Aerospace Engineering

A tiltrotor can hover, takeoff and land vertically as well as cruise at high speeds and fly long distances. Because of these unique capabilities, tiltrotors are envisioned as an aircraft that could provide a solution to the issue of airport gridlock by operating on stub runways, helipads, or from smaller regional airports. However, during an approach-to-land a tiltrotor is susceptible to radiating strong impulsive noise, in particular, Blade-Vortex Interaction noise (BVI), a phenomenon highly dependent on the vehicle's performance-state.

A mathematical model was developed to predict the quasi-static performance characteristics of a tiltrotor during a converting approach in the longitudinal plane.

Additionally, a neural network was designed to model the acoustic results from a flight test of the XV-15 tiltrotor as a function of the aircraft's performance parameters. The performance model was linked to the neural network to yield a combined performance/ acoustic model that is capable of predicting tiltrotor noise emitted during a decelerating approach.

The model was then used to study noise trends associated with different combinations of airspeed, nacelle tilt, and flight path angle. It showed that BVI noise is the dominant noise source during a descent and that its strength increases with steeper descent angles. Strong BVI noise was observed at very steep flight path angles, suggesting that the tiltrotor's high downwash prevents the wake from being pushed above the rotor, even at such steep descent angles.

The model was used to study the effects of various aircraft configuration and flight trajectory parameters on the rotor inflow, which adequately captured the measured BVI noise trends. Flight path management effectively constrained the rotor inflow during a converting approach and thus limited the strength of BVI noise. The maximum deceleration was also constrained by controlling the nacelle tilt-rate during conversion. By applying these constraints, low BVI noise approaches that take into account the first-order effects of deceleration on the acoustics were systematically designed and compared to a baseline approach profile. The low-noise approaches yielded substantial noise reduction benefits on a hemisphere surrounding the aircraft and on a ground plane below the aircraft's trajectory.

TILTROTOR NOISE REDUCTION THROUGH FLIGHT TRAJECTORY MANAGEMENT AND AIRCRAFT CONFIGURATION CONTROL

by

Marc Gervais

Dissertation submitted to the Faculty of the Graduate School of the
University of Maryland, College Park in partial fulfillment
of the requirements for the degree of
Doctor of Philosophy
2004

Advisory Committee:

Professor Fredric H. Schmitz, Chairman/Advisor
Associate Professor James D. Baeder
Professor Inderjit Chopra
Associate Professor Darryll J. Pines
Professor Ricardo H. Nochetto, Dean's Representative

Dedication

To Laila

Acknowledgments

I would like to thank my advisor Dr. Fred Schmitz for his advice and encouragement during the past five years. His support, whether work related or not, has been invaluable to me and has allowed me to enjoy my work while continually being challenged to excel. I have gained much knowledge about engineering while at the University of Maryland and I owe a great deal of this knowledge to Dr. Schmitz.

I would also like to thank the other members of my committee: Drs. Inderjit Chopra, Jim Baeder, Darryll Pines, and Ricardo Nochetto for their review of this Dissertation and for the excellent feedback which they provided.

This work was made much more relevant and focused by the support and guidance of industry experts, in particular Bryan Edwards and John Brieger of Bell Helicopter, Dave Conner of NASA Langley, and Bill Decker of NASA Ames. Their assistance is greatly appreciated.

The great atmosphere at the University of Maryland's Rotorcraft Center is also to be credited. The excellence of the faculty, coupled with the many bright and interesting students, made for an exciting work environment. I would especially like to acknowledge the late Dr. Alfred Gessow for his incredible spirit and love of teaching. I would also like to acknowledge Dr. Marat Tishchenko for his depth of knowledge and

passionate teaching attitude. It was truly an honor to be able to work with and learn from these two great individuals. This research benefited tremendously from the assistance and feedback from Dr. Ben Sim, whose willingness to help was at times a true saving grace. The many discussions with fellow graduate student Gaurav Gopalan also proved invaluable.

I would also like to thank my family for their encouragement throughout my academic "career." This work would not have been possible without their love and support. And I also would like to thank my parents-in-law for the many supportive conversations.

Finally, I would like to thank my wife, Laila. Her unwavering support kept me going when times were difficult and her intelligence and wonderful personality helped me keep in mind life's true priorities. Thank you for everything Laila.

Table of Contents

List of Tables

List of Figures

Nomenclature

a	Airfoil lift curve slope, rad^{-1}
a	Neural network output
a_0	Speed of sound in air, ft/s (a_0 = 1,110 ft/s)
A	Rotor disk area, ft^2 ($A = \pi R^2$)
b	Neural network bias
c	Blade chord, ft
c_{do}	Airfoil profile drag coefficient
c_{ref}	Reference blade chord, ft
C_D	Total airframe drag coefficient
$C_{D\ base}$	Baseline airframe drag coefficient
$C_D\|_{\delta e}$	Airframe drag coefficient correction due to elevator deflection
$C_D\|_{\delta f}$	Airframe drag coefficient correction due to wing flap deflection
$C_D\|_{iN}$	Airframe drag coefficient correction due to nacelle tilt
C_H	Individual rotor H-force coefficient
C_L	Total airframe lift coefficient
$C_{L\ base}$	Baseline airframe lift coefficient
$C_L\|_{\delta e}$	Airframe lift coefficient correction due to elevator deflection
$C_L\|_{\delta f}$	Airframe lift coefficient correction due to wing flap deflection
$C_L\|_{iN}$	Airframe lift coefficient correction due to nacelle tilt

C_M	Total airframe moment coefficient
C_T	Individual rotor thrust coefficient
dD	Blade element drag, lb/ft
df	Blade element force, lb/ft
dL	Blade element lift, lb/ft
dM_A	Elemental rotor aerodynamic moment, ft lb
dr	Elemental radius, ft
dx	Elemental position along blade, ft ($dx = dr/R$)
d_τ	Distance between acoustic source and observer at emission time, ft
$D_{airframe}$	Total drag of airframe, lb
E	Beddoes induced inflow constant, rad ($E = \chi/2$)
g	Gravitational constant, = 32.2 ft/s^2
h	Altitude, ft
h_{ref}	Reference altitude, ft
h_{rotor}	Distance between aircraft center-of-gravity and hub in z-body axis, ft
i, **j**, **k**	Unit vectors
I_b	Blade flapping moment of inertia, slug ft^2
I_{xx}, I_{yy}, I_{zz}	Mass moment of inertia about x, y, and z body-axis, slug ft^2
I_{xz}	Product of inertia about x- and z-body axes, slug ft^2
i_N	Nacelle tilt, rad (0° = airplane mode and 90° = helicopter mode)
K	Flapping restraint stiffness, lb ft/rad
l_{rotor}	Distance between aircraft center-of-gravity and hub in x-body axis, ft
$L_{airframe}$	Total lift of airframe, lb

M	Pitching moment about y body-axis, lb ft
M_A	Rotor aerodynamic pitching moment about the hub, ft lb
$M_{airframe}$	Pitching moment due to airframe about the y body-axis, ft lb
M_{AT}	Advancing tip Mach number
M_{rotor}	Individual rotor moment about the y body-axis, ft lb
M_{TR}	Trace Mach number
M_x, M_z	Horizontal and vertical aircraft Mach number in earth-fixed coordinates
N	Number of data points in neural network
N_b	Number of blades
p_n	n-th neural network input
p, q, r	Angular velocity components in the x, y, and z body-axis, rad/s
R	Blade radius, ft
S_{ref}	Reference wing area, ft^2
r_{mic}	Distance between microphone and acoustic source at observer time, ft
r_p	Radial location of point p on a blade, ft
t	Time, sec.
t	Neural network target output
u, v, w	Freestream velocity components in the x, y, and z body-axis, ft/s
U_P, U_T, U_R	Perpendicular, tangential and radial blade velocities, ft/s
U_x, U_y, U_z	Blade velocity components in rotating frame, ft/s
V	Airspeed, ft/s
V_x, V_z	Horizontal and vertical aircraft velocity in earth-fixed coordinates, ft/s
$\mathbf{V}_{\text{blade}}$	Total velocity vector at blade in arbitrary coordinate system, ft/s

$\mathbf{V}_{\infty}$	Freestream component of velocity vector at blade, ft/s
$\mathbf{V}_{\beta}$	Flapping component of velocity vector at blade, ft/s
$\mathbf{V}_{vi}$	Induced inflow component of velocity vector at blade, ft/s
W	Gross weight, lb
x	Position along blade, ft ($x = r/R$)
x, y, z_{mic}	Acoustic source location w.r.t. observer in Cartesian coordinates, ft
$X, Y, Z_{airframe}$	Aerodynamic forces due to airframe in the x, y, and z body-axis, lb
$X, Y, Z_{hemisphere}$	Noise hemisphere Cartesian coordinates, ft
X, Y, Z_{rotor}	Individual rotor force components in the x, y, and z body-axis, lb
α_F	Fuselage angle-of-attack, rad
α_{blade}	Blade angle-of-attack, rad
$\alpha_{F\ stall}$	Fuselage stall angle-of-attack, rad
β	Blade flapping angle, rad
β_0	Rotor coning angle, rad
β_F	Fuselage sideslip angle, rad
β_{1c}	Longitudinal flapping coefficient, rad
β_{1s}	Lateral flapping coefficient, rad
β_p	Rotor pre-cone angle, rad
χ	Wake skew angle, rad
δ_e	Elevator deflection, deg. (positive down)
δ_f	Wing flap deflection, deg. (positive down)

δ_3	Pitch-flap coupling, rad
ϕ	Inflow angle, rad
ϕ_F	Fuselage roll angle, rad
ϕ_{mic}	Lateral noise hemisphere elevation, rad
γ	Flight path angle, rad (positive in climb)
γ	Lock number ($\gamma = \rho acR^4/I_b$)
γ_b	Blade-vortex interaction angle, rad
λ	Total inflow (positive up through the rotor)
$\overline{\lambda}$	Average inflow (positive up through the rotor)
λ_0	Uniform inflow (positive up through the rotor)
λ_i	Induced inflow (positive up through the rotor)
μ	Advance ratio ($\mu = V/\Omega R$)
μ_x	Advance ratio parallel to TPP ($\mu_x = V\cos\alpha_{TPP}/\Omega R$)
μ_z	Advance ratio perpendicular to TPP ($\mu_z = V\sin\alpha_{TPP}/\Omega R$)
ν_i	Induced inflow velocity, ft/s (positive up through the rotor)
ν_β	Rotor flapping frequency, rad/sec
θ	Fuselage pitch angle, rad (positive nose up from horizon)
θ_{blade}	Blade pitch angle, rad
$\theta_{cylindrical}$	Hemisphere cylindrical elevation, rad
θ_{mic}	Longitudinal noise hemisphere elevation, rad
θ_0	Rotor collective angle, rad
θ_{1c}	Rotor lateral cyclic coefficient, rad

θ_{1c}	Rotor longitudinal cyclic coefficient, rad
θ_{TW}	Blade twist, rad/ft
$\dot{\theta}_{hub}$	Total rotor pitch rate, rad/s ($\dot{\theta}_{hub} = \dot{\theta} + di_N / dt$)
ρ	Sea level standard air density, slug/ft^3
τ	Retarded (or emission) time, sec
ψ	Blade azimuth angle, rad
ψ_H	Hemisphere azimuth angle, rad
Φ_H	Hemisphere elevation angle, rad
Ω	Rotational velocity of the rotor, ft/s
$\dot{x}$	Time derivative of x

Abbreviations

AGL	Above Ground Level
ART	Acoustic Repropagation Technique
ATB	Advanced Technology Blades
BET	Blade Element Theory
BVI	Blade-Vortex Interaction
CAMRAD	Comprehensive Analytical Model of Rotorcraft Aerodynamics and Dynamics
CFD	Computational Fluid Dynamics
DATCOM	Data Compendium

DNW	Duits-Nederlandse Windtunnel
FAA	Federal Aviation Administration
FWD	Forward
GTRS	Generic TiltRotor Simulation
HAI	Helicopter Association International
HHC	Higher Harmonic Control
HNM	Heliport Noise Model
HP	Hub Plane
HSI	High-Speed Impulsive
IBC	Individual Blade Control
IFR	Instrument Flight Rules
IRAP	In-Flight Rotorcraft Acoustic Program
IW	Input Weight
LaRC	Langley Research Center
LW	Layer Weight
MIC	Microphone
MSE	Mean Square Error
NASA	National Aeronautics and Space Administration
OASPL	Overall Sound Pressure Level
PE	Processing Element
Q-SAM	Quasi-Static Acoustic Modeling
QTR	Quad TiltRotor
RIA	Runway Independent Aircraft

RNM	Rotorcraft Noise Model
ROD	Rate of Descent
RPM	Rotation Per Minute
RTA	Rotor Test Apparatus
SEL	Sound Exposure Level
SH(CT)	Short-Haul (Civil Tiltrotor)
SPL	Sound Pressure Level
TPP	Tip-Path-Plane
TRAC	TiltRotor Aeroacoustic Code
TRAM	Tilt Rotor Aeroacoustic Model
TRRA	TiltRotor Research Aircraft
VMS	Vertical Motion Simulator
V/STOL	Vertical or Short Takeoff and Landing
VTOL	Vertical Takeoff and Landing
UAV	Unmanned Aerial Vehicle
USAF	United States Air Force

Chapter 1

Introduction

This chapter does not only provide a roadmap for the Dissertation, but also serves as the foundation upon which this work has been built. A brief introduction to the tiltrotor aircraft is first presented, followed by a clear problem statement and a short exposition of the history of tiltrotor aircraft. A concise introduction to the particularities of tiltrotor external noise is then presented, followed by an extensive review of the literature pertinent to this work. Finally, the main research objectives are introduced and a brief outline of the Dissertation is presented.

1.1 Background

Tiltrotors are a unique type of aircraft that combine the main advantages of rotorcraft and fixed-wing vehicles. They can hover, takeoff, and land vertically as well as cruise at high-speed and fly long distances. This aircraft is truly a mix between a helicopter and an airplane. Large proprotors (highly twisted rotors) are mounted on wing-tip nacelles that are rotated to achieve the conversion between helicopter mode and airplane mode. In

helicopter mode, the nacelles are vertical and the aircraft operates as a side-by-side helicopter, whereas in airplane mode the nacelles are horizontal and the aircraft then functions as a fixed-wing turboprop airplane. The tiltrotor can perform the conversion while in-flight, within a range of different airspeeds. Figure 1.1 shows the V-22 Osprey in the airplane, conversion, and helicopter modes. The nacelle tilt is 0° in airplane mode and 90° in helicopter mode. Note that because of the large size of the proprotors, the vehicle cannot land in airplane mode, as the rotors would strike the ground.

Figure 1.1. V-22 Osprey in airplane, conversion and helicopter modes (from Ref. 1).

Since the aircraft must fulfill the extreme requirements of two very different modes of flight, the rotors are sized with compromise in mind. The rotors are smaller than would be desired in helicopter mode – causing higher hover power required, higher downwash velocities, and poor autorotation capabilities – and are larger than required for airplane mode flight, thus causing decreased propulsive efficiency and a higher gust sensitivity. In addition, the aircraft has a variable RPM capability for the two different modes of flight. The RPM is set to 589 rotations-per-minute at nacelle tilts above 60°, and 517 rotations-per-minute at lower nacelle tilts. This reduction of the RPM in airplane mode flight improves the rotor performance in cruise.

The unique capabilities of the tiltrotor make it suitable for many different missions both, civil and military. In civil service, the tiltrotor is envisioned as a solution to the imminent problem of air transport gridlock. Indeed, short-haul aircraft operations account for approximately 40-percent of the total aircraft operations at hub airports although they are responsible for only 20-percent of the passenger transport (Ref. 2). It is therefore believed that Runway Independent Aircraft (RIA), in particular tiltrotors, could be used to alleviate congestion at hub airports by simultaneously operating on stub runways, on helipads or from smaller regional airports. In military service, tiltrotors have the potential to fulfill many different types of scenarios that range from special warfare to transport and even to intelligence gathering missions.

1.1.1 Problem Statement

One of the main obstacles to the acceptance of tiltrotors as either a commercial or military aircraft is the high level of externally radiated noise associated with rotorcraft. This issue could become a determining factor for the viability of commercial tiltrotors since one of their key selling points is their ability to operate from regional airports, which are much closer to noise sensitive residential areas than major airports. Fortunately, tiltrotors spend most of their flight time in cruise, where they operate at higher altitudes in airplane mode and radiate relatively low levels of noise to the ground, a characteristic typical of conventional turboprop airplanes. The takeoff phase (climb in helicopter mode) has also been identified by previous research as a rather quiet segment (Refs. 3-6).

In terms of noise, the critical portion of flight for tiltrotors is the approach phase. During this segment, the aircraft is susceptible to experiencing a phenomenon known as Blade-Vortex Interaction (BVI), which leads to BVI noise (see section 1.1.3). Since BVI occurs mostly during descent (or sometimes during maneuvering flight), BVI noise is usually produced at fairly low altitudes, within the terminal area and close to neighboring communities. Consequently, for years BVI noise has been at the center of many noise reduction efforts for conventional helicopters. Some researchers have also identified thickness noise as a possible high noise mechanism for a tiltrotor during an approach procedure. Indeed, an extreme case of thickness noise called High-Speed Impulsive noise (HSI) can potentially set the level of annoyance during flight conditions where BVI is not prevalent. A deeper understanding of tiltrotor approach noise and systematic flight procedures for noise abatement approaches are key to the successful integration of tiltrotors in the commercial air system.

1.1.2 Tiltrotor History

The advent of the airplane fulfilled the dream of human flight only to a certain extent. Airplanes need at least a strip of grass to takeoff and to land. Also, airplanes cannot hover over a fixed point like a hummingbird can. When helicopters were first flown successfully it seemed the problem was solved: humans achieved the capability to hover, and to takeoff and land vertically. However, obvious limitations were soon discovered. Due to their basic nature, helicopters are far more limited than airplanes in terms of forward flight speed, range, and endurance. Thus, a new type of vehicle was envisioned, one that could consolidate the capabilities of both fixed-wing and rotary-wing vehicles.

Such aircraft are known as V/STOL vehicles (Vertical or Short Takeoff and Landing), or in their purest form, VTOL (Vertical Takeoff and Landing). The many different concepts for V/STOL aircraft imagined by engineers and inventors were illustrated by the McDonnell Aircraft Company in the 1960s and subsequently modified (see Figure 1.2). This illustration is sometimes dubbed the "Wheel of Misfortune." Because of its low disk loading (compared with other V/STOL vehicles), the tiltrotor appeared to be one of the most promising designs.

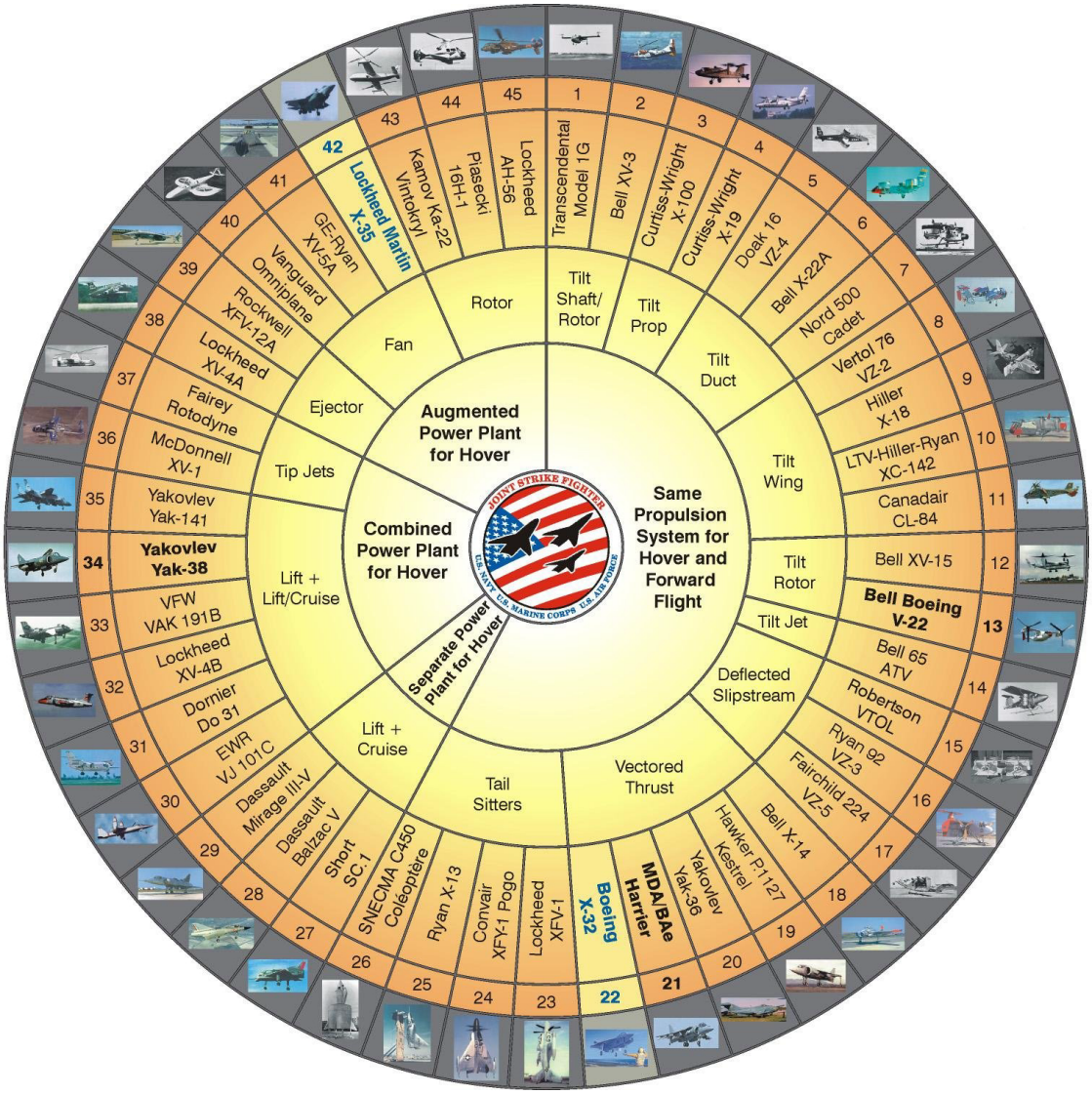

Figure 1.2. Wheel of V/STOL aircraft and propulsion concepts (from Ref. 7).

One of the first aircraft to be configured similarly to a modern tiltrotor is the Berliner tilt-propeller aircraft of the early 1920's. It was a side-by-side helicopter that could tilt its propellers forward from the horizontal. However, the vehicle could not fully operate in pure airplane mode since its propellers could not be tilted completely forward.

Between the 1930s and the late 1940s, many tiltrotor designs, or convertiplanes had been on the drawing boards in the United States, Great Britain, and Germany. One of the first true tiltrotors is the Transcendental Model 1-G that first flew in 1954 and made many successful flights before crashing in 1955 (Ref. 8). The aircraft came within ten degrees of achieving a full conversion to airplane mode.

The first truly successful tiltrotor aircraft was the XV-3, or Bell Model 200. In 1959, the XV-3 was the first tiltrotor to achieve a full conversion from helicopter mode to airplane mode. The XV-3 accumulated a total of 125 hours of flight tests, including 110 full conversions between 1955 and 1968 (Ref. 8). However, the state of technology in the fifties and sixties did not allow the aircraft to achieve the predicted performance in either mode of flight. Also, the aeroelastic instability caused by the rotor/pylon/wing system was not yet fully understood. Despite those limitations, the safe and successful conversions of the XV-3 secured a place for the tiltrotor in the future of manned atmospheric flight.

A continued interest in V/STOL vehicles led to the design and development of the XV-15 TRRA (Tilt Rotor Research Aircraft). In 1977, the XV-15 made the first flight of what was to become its long life of research service. Over the years, the two aircraft (tail numbers N702NA and N703NA) have accumulated over eight hundred flight hours, and over fifty hours of full-scale testing in the NASA Ames 40-by-80 feet wind tunnel. The last operational XV-15, tail number N703NA, was finally retired and donated to the

National Air and Space Museum in the fall of 2003 and is on display at the new Udvar-Hazy Center in Dulles, Virginia.

Figure 1.3. The XV-15 tiltrotor arriving at the National Air and Space Museum's Udvar-Hazy Center (from Ref. 9).

The JVX program, later named the V-22 Osprey, was set underway in 1981 using the XV-15 as a proof-of-concept. Although the program experienced several setbacks the aircraft made its first flight in 1989, and the first production V-22 was delivered to the U.S. Marine Corps in 1999. After two fatal crashes, the operational testing of the V-22 by the Marines was stopped, but it resumed after a Blue Ribbon Panel advised that it could proceed with caution. Many aircraft are now taking part in an aggressive flight test program aimed at exploring the entire flight envelope of the V-22.

Another tiltrotor aircraft that has flown for many years is Bell Helicopter's 7/8-scale Eagle Eye UAV (Unmanned Aerial Vehicle) that first flew in 1993. The US Coast Guard recently selected the aircraft for the Integrated Deepwater System contract, with deliveries scheduled to begin in 2006.

Figure 1.4. Bell Helicopter's 7/8-scale Eagle Eye UAV (from Ref. 10).

Because tiltrotors can potentially reduce air traffic gridlock, they are envisioned as an effective commodity on the civil market. In 1994, Bell initiated a program for the vehicle now known as the Bell-Agusta Model 609. The aircraft achieved its first flight in March of 2003 (see Figure 1.5 below).

Figure 1.5. First flight of the BA-609 commercial tiltrotor (from Ref. 11).

Another project that has recently attracted considerable attention is the Bell QTR (Quad-TiltRotor). This huge aircraft is based on the V-22 but is designed to carry well over 100,000 pounds and has four tilting rotors (two on a front wing and two on a rear wing).

The future of tiltrotor aircraft seems to be in better shape today than ever before, with many simultaneous projects in the industry. Other advanced concepts, such as tiltrotors with variable diameter rotors or stop-fold rotors are under consideration. Most experts agree that tiltrotors have their place both on the battlefield and in commercial airports. However, many obstacles still prevent a wider use of tiltrotors. Technological and operational challenges have not been fully investigated or resolved. And, one of the most

important challenges is to reduce noise levels emitted by the vehicle during an approach to land.

1.1.3 Introduction to Tiltrotor Noise

Noise sources present on a rotorcraft in flight are generally categorized as follows: impulsive noise, harmonic loading noise, broadband noise, engine noise, and gearbox noise. When it occurs impulsive noise is by far the loudest and most annoying type of noise. Note that a tiltrotor does not require a tail rotor to provide anti-torque, a fact that readily eliminates an important source of harmonic noise on conventional helicopters. This research will focus on reducing tiltrotor impulsive noise during an approach, in particular BVI noise. Thickness noise will also be discussed in relation to flight regimes where it dominates the noise spectrum. For a tiltrotor in hovering or near-hovering flight, noise is also generated due to a *fountain flow* effect that is caused by re-circulating flow deflected upwards by the wing and back through the rotors. However, hover noise will not be considered in this Dissertation.

Blade-Vortex Interaction (BVI) Noise

During the descent phase, the aircraft experiences a widely known phenomenon called BVI noise. BVI noise is caused when one or more of the rotating blades encounter a tip vortex shed by a preceding blade and large impulsive loads are induced onto the surface of the blade thus causing rapid changes in blade surface pressures, which ultimately leads

to large acoustic pressures. BVI produces a very loud popping or slapping sound that contains a lot of acoustic energy and radiates efficiently to the acoustic far-field.

Different techniques have been devised and tested in order to reduce BVI noise. These techniques can be grouped into three general categories that deal with the strength and the size of the shed vortices, the response of the blade to the shed vortices and finally, the distance between the shed vortices and the rotor blades at the time of the interaction.

In the first category, some methods have been field-proven (reducing disk loading, reducing tip speed, and modifying the design of the blade tip shape) and some methods, although effective in various experiments, are still in the research phase (Higher-Harmonic Control (HHC), Individual Blade Control (IBC), blade tip air mass injection and blade sub-wing).

In the second category, passive methods (airfoil design and leading-edge design) have been implemented with a certain degree of success, while active methods (active flap and fluidic control) are still being investigated.

The last category, which is the focus of this research, deals with what is commonly known as *miss-distance*. Miss-distance is defined as the perpendicular distance between the vortex core and the rotor blade at the time of the interaction. It is known that the larger the miss-distance, the lesser the strength of the blade-vortex interaction or even the likelihood of occurrence of a significant interaction. Methods that have been investigated

to increase the miss-distance are Higher-Harmonic Control, Individual Blade Control and active flaps. However, this research will focus on using trajectory and configuration controls to increase miss-distance and thus reduce BVI noise. These two noise reduction methods involve piloting techniques and are mainly known as flight path management procedures. As this Dissertation will show, a tiltrotor aircraft has a variety of different controls that allow it to benefit from a broader range of trajectory and configuration controls than a conventional, single main rotor/tail rotor helicopter.

In terms of BVI noise, there are two main differences between a conventional helicopter and a tiltrotor. The first and most obvious difference is the unique configuration of the tiltrotor: its wing can offload the rotors in forward flight, causing a change in the rotor operating condition that leads to different noise characteristics. Therefore, the pitch angle of the fuselage plays a very important role in determining the acoustics of a tiltrotor, whereas the fuselage pitch of a conventional helicopter plays a lesser role. In addition, the ability to incline the rotors in a wide range of angles can significantly alter the BVI geometry and resulting noise strength.

The second main difference between a tiltrotor and a helicopter's BVI noise characteristics is due to the high twist of the tiltrotor's blades that can cause the tip of the blades to become negatively loaded in helicopter mode forward flight. As a result, this generates a secondary vortex (inboard of the tip) that changes the BVI noise directivity and strength.

Thickness Noise and High-Speed Impulsive Noise (HSI)

Thickness noise is caused by the thickness of a blade and how it displaces a volume of air as it moves through the medium. As velocity increases, a shock pocket forms on the blade that eventually extends past the tip of the blade. This phenomenon, called *delocalization*, results in a drastic increase in the impulsive noise strength since it causes the shock to be efficiently radiated to the far-field. When delocalization occurs thickness noise is referred to as High-Speed Impulsive (HSI) noise. HSI noise rapidly increases with respect to the advancing tip Mach number and as such is usually considered a problem in high-speed forward flight, not in descent. The maximum noise level directivity is forward and in the plane of the rotor. For a conventional helicopter, this often means that noise is propagated towards the horizon and eventually absorbed by the atmosphere before it is perceived on the ground. Common methods to reduce thickness noise are to decrease the thickness of the blades and to reduce the tip speed of the rotor. Since today's new generation of helicopters operate at lower tip speeds, HSI noise is much less likely to occur in typical commercial operations. However, tiltrotors have high tip speeds and fairly thick blades because of the compromise made between airplane and helicopter modes of flight. Furthermore, in a descent a tiltrotor can operate at fairly high airspeeds in conversion mode, which can cause the rotors' in-plane directivity to be pointed towards the ground. This makes thickness noise during a descent a potentially more important issue for a tiltrotor than for a conventional helicopter (see section 1.2.2). Although this research will mainly focus on avoiding strong BVI noise, the analysis of the final noise abatement approach profiles developed herein will discuss both BVI noise and thickness noise.

1.2 Survey of Tiltrotor Acoustics Research

1.2.1 Tiltrotor Acoustic Reviews and Tiltrotor Noise Reduction

The acoustic characteristics of tiltrotors and the potential for noise reduction through flight path control are first addressed in 1971 (Refs. 3, 12-14). As the XV-15 emerged so did more opportunities to characterize tiltrotor noise. Limited estimates of anticipated noise footprints can be found in the Tilt Rotor Research Aircraft Familiarization Document (Ref. 15) as well as a more extensive discussion of tiltrotor acoustics in Ref. 16. Limited results are presented for hover noise trends with respect to tip speed and some approach and departure ground noise contours are shown. A paper by George et al. (Ref. 5) gives a good summary of previous tiltrotor acoustic studies and clearly identifies the main factors that influence tiltrotor acoustics. It also reinforces the notion that the tiltrotor has a unique potential for noise reduction techniques. George acknowledges that more research is necessary in terms of theoretical analysis and acoustical flight tests. The paper identifies the descent phase as the most problematic acoustic phase for tiltrotors and states that the way the aircraft is flown through the conversion corridor (from airplane mode to helicopter mode) is critical to noise ground exposure levels. A paper by Huston and Golub also presents some noise considerations for tiltrotors (Ref. 17). A presentation by Maisel gives an account of all existing XV-15 acoustics data up to 1991 and again emphasizes the importance and potential of flight trajectory management in terms of tiltrotor noise reduction (Ref. 18). A presentation by Cox highlights the tiltrotor's low cruising flight noise and states that delaying the conversion from airplane

mode to helicopter mode during approach can reduce noise contour areas by thirty percent (Ref. 19). A summary of a tiltrotor aircraft noise workshop held in 1991 is presented in (Ref. 20). Many areas of future research are identified at this meeting, such as: understanding and prediction capability of tiltrotor BVI noise, simulation models for trajectory management efforts, instrumented small-scale models for blade airloads and a more extensive noise measurement database for existing tiltrotors. In terms of tiltrotor noise metrics, Sternfeld et al. presents the results of a subjective noise test where participants rated the annoyance level of simulated tiltrotor sounds (Ref. 21). It was found that combining A-weighted and overall sound pressure levels resulted in better agreement than using A-weighted sound pressure level alone. The NASA Short Haul (Civil Tiltrotor) program, SH(CT), contained objectives pertaining to noise reduction for tiltrotors. An outline of the acoustic elements of the program is found in (Ref. 22). For information on tiltrotor interior noise and structural acoustics, which are not discussed in this Dissertation, see Refs. 23-25.

1.2.2 Tiltrotor Acoustic Flight Tests

In 1981, outdoor hover flight tests were performed on the XV-15, providing an opportunity for tiltrotor hover noise characterization (Ref. 26). The main goal of this test was to establish the horizontal noise directivity of the aircraft in hover. This study was followed by limited level-flight experiments in 1982 and then more extensive flight tests in 1986 (Ref. 4). The later results were the first to confirm that nacelle tilt combined with flight path management had the potential to lead to significant noise alleviation benefits. A paper by Edwards gives the results of a 1988 flight test of the XV-15 and once again

emphasizes the possibility for significant noise reduction through careful nacelle tilt versus airspeed schedules (Ref. 6). The paper identifies regions of minimum, moderate and maximum noise within the XV-15's flight envelope as well as assesses the noise characteristics of "mid-envelope" and "upper envelope" transitions, with mid-envelope transitions performed at slower airspeeds, see Figure 1.6.

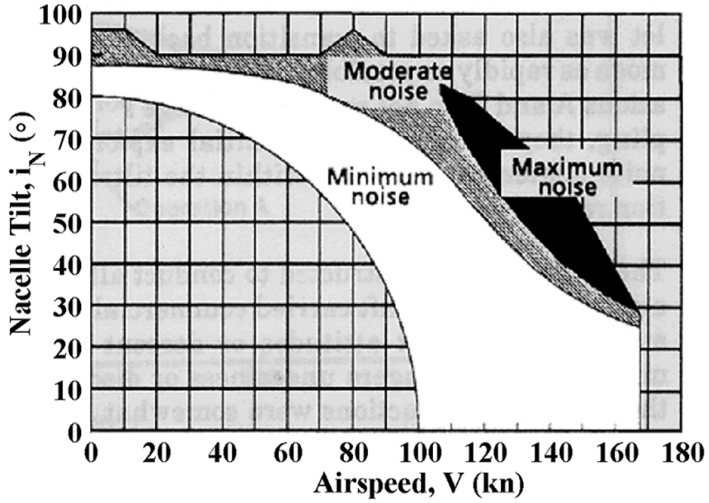

Figure 1.6. Regions of maximum, moderate, and minimum noise within the XV-15 flight envelope (adapted from Ref. 6).

This paper also presents noise contours measured for two different takeoff and approach profiles using a large area microphone array. This provided an initial assessment of the tiltrotors' actual potential for noise abatement flight profiles (also see Refs. 27 & 28). It was shown that by instructing the pilots to begin the airplane-to-helicopter mode at a slower airspeed, the ground contour areas exposed to higher levels of noise was reduced somewhat. In 1990, an XV-15 hover test was conducted at Moffett field in California. The results are presented in Refs. 29-31. A paper by Santa Maria discusses the results of

a 1991 flight test of the XV-15, with Advanced Technology Blades (ATB) (Ref. 32). The results from this test were compared to the results from the 1988 test to investigate the effect of the new blades but no apparent acoustic advantages were found. These flight tests paved the way for the most recent series of flight tests, which were carried out in 1995 (Refs. 33 & 34), 1997 (Refs. 35 & 36) and 1999 (Ref. 37). The following section details these flight tests.

NASA/Army/Bell XV-15 Tiltrotor Low Noise Terminal Area Operations Flight Research Program

This series of XV-15 acoustics flight tests had the following objectives (Ref. 35):

- "1995: Define broad characteristics of tiltrotor approach noise at a matrix of operating conditions, provide high-quality dataset for tiltrotor acoustic prediction model validation, and perform a limited set of approaches for preliminary review."
- "1997: Demonstrate approach profiles incorporating Instrument Flight Rule (IFR) handling qualities constraints and tradeoffs with sound. Investigate broad range of approach procedures and develop "short list" of promising ones."
- "1999: Refine the "short list" of approach procedures produced by the previous testing. Fly optimal approaches to develop and demonstrate most practical, quietest flight procedures."

A paper by Conner et al. summarizes and presents the results from the three phases of the flight research program (Ref. 38). The first flight test examined takeoff, level flight, and approach conditions on the XV-15 and determined that the approach condition was the most critical in terms of noise. The acoustic and performance results from this test are

used in this research to build a performance/acoustic model of the tiltrotor (see Chapters 3 and 4). The 1997 flight test used an improved flight director that allowed better approach repeatability. The test explored five different approach profiles: 3º, 6º, 9º descents and two different 3º to 9º descents. The shallowest approach was found to be one of the quietest while the steepest approach was found to be the loudest. One of the two-segment approaches yielded the least noise out of all the approaches. The most promising approaches from the 1997 test were refined for testing in the 1999 trials. Some approach profiles developed from the Rotorcraft Noise Model (RNM) were also tested in 1999 (see Ref. 39). All approaches were flown IFR using the flight director and more emphasis was placed on handling characteristics and pilot workload. During this test the use of high flap deflections (75º) was shown to improve handling qualities during steep approaches. One of the 3º to 9º segmented approaches was, again, the quietest approach. It was suggested that the nacelle tilt had to be maintained at a low angle for as long as possible as the helicopter mode of flight is generally the loudest. It was also concluded that the approach profile had to be tailored to the specifics of the landing site since ground noise exposure varied greatly with different profiles. Using the improved flight director, the potential for noise reduction using airspeed/glideslope/nacelle angle scheduling seemed promising but the high pilot workload hinted at fully automated approaches. Six of the approaches from the flight test were further test-flown by nine pilots for handling qualities evaluation at the NASA Ames Vertical Motion Simulator (VMS), (Ref. 40).

An important issue to point out is the methodology that was used in the previous references to design and refine the low-noise approach procedures. For the 1997 test, the approaches were basically designed through trial-and-error, based on the basic knowledge of the aircraft's acoustic characteristics obtained through the 1995 flight test. As Ref. 38 states: "…a set of 10 initial candidate profiles were developed using a somewhat *ad hoc* approach based on the phase I results." For the 1999 test, RNM was used in combination with a commercial optimizer to design approaches that minimize noise at three distinct points on the ground, along the flight track of the tiltrotor. This was an improvement, however RNM uses only *steady-state* vehicle performance to predict the acoustics associated with a particular *decelerating* approach. In this Dissertation, a methodology is introduced that takes into account the first-order effects of deceleration to systematically design low-noise approaches that directly reduce the vehicle's acoustic emission.

In-Flight Rotorcraft Program Acoustics (IRAP)

In order to provide validation for upcoming full-scale wind tunnel acoustics tests of the XV-15 rotor, a few flights were performed in 1995 with the XV-15 and a YO-3A airplane flying in close formation (Ref. 41, see Figure 1.7 below).

Figure 1.7. The XV-15 in formation with the YO-3A (from Ref. 41).

Two microphones were located on the YO-3A and the aircraft flew in a way as to capture prominent BVI noise. Only helicopter mode flights were performed. In this test, the rotor gimbal angle and the aircraft pitch attitude were measured. The gimbal angle yields the rotor's flapping angle with respect to the shaft, which allows for an accurate estimate of the rotor tip-path-plane angle. In the test, strong BVI noise was measured at an advance ratio of 0.159 and a tip-path-plane of -2° (nose-up from the incoming freestream velocity). For that case, the acoustic time-history revealed that two BVI pulses were seen for each blade. It was suggested in Ref. 42 that the presence of multiple pulses could be due to portions of the rotor being negatively loaded and creating a twin shed vortex system.

1.2.3 Tiltrotor Acoustic Wind Tunnel Tests

The first actual measurements of tiltrotor noise were conducted in full-scale wind tunnel tests of the XV-15 at the NASA Ames' 40-by-80 feet facility in 1979 (Ref. 43). The test was performed at a fixed tip Mach number of 0.65 and a fixed airspeed of 80 knots. The nacelle tilt was varied from airplane mode to helicopter mode. It was shown that the nacelle tilt was a major governing parameter in the noise radiation of the aircraft since both the noise levels and the noise characteristics changed appreciably with respect to the nacelle tilt. In truth, the tip-path-plane angle that results from the nacelle tilt is in this case the main governing acoustic parameter. The highest levels and most impulsive noise were experienced in helicopter mode.

Fifteen-Percent Scaled JVX Rotor Acoustics Wind Tunnel Tests

From June to August of 1994, an aerodynamic and acoustic test of a fifteen-percent scaled JVX rotor (the precursor to the V-22) was conducted in the NASA Langley 14-by-22 feet wind tunnel (Ref. 44). Because the model had 60º to 95º nacelle tilting capability, it offered a good opportunity to quantify the variation of noise level and directivity with nacelle tilt. In order to match the isolated rotor test conditions to the complete aircraft flight conditions, a trim code was used to determine the specific rotor test conditions. Sixteen microphones were used and positioned on two traversing wings 1.75R below the rotor hub. The test's major conclusion was that the noise levels were higher for a higher nacelle tilt, which is closer to helicopter mode. However, the authors caution that inferring a simple relationship between nacelle tilt and noise is not possible. Yet, the

paper also suggests that an acoustic benefit is obtained by maintaining a lower nacelle angle for a given flight condition.

Full-Scale Isolated XV-15 Rotor Acoustics Wind Tunnel Tests

The XV-15 rotor system was tested extensively at the 80-by-120 feet wind tunnel at NASA Ames Research Center. For these tests, a single full-scale XV-15 rotor was mounted on NASA's Rotor Test Apparatus (RTA). The RTA's angle can be varied from 15 degrees forward to 15 degrees backward (Refs. 45 & 46). This setup was used to determine the baseline BVI noise characteristics of the XV-15 during descent flights. For noise measurement, four microphones were placed on the advancing side and 1.8R below the rotor on a traverse with variable longitudinal placement (Refs. 42 & 47). A fifth microphone was placed in the same relative position as the starboard wing microphone in the IRAP tests (see above, Ref. 41) and a sixth microphone was placed as a mirror image. The rotor was operated at a fixed tip Mach number and thrust coefficient while the tip-path-plane angle and advance ratio were varied. Some of the runs were performed for validation with the IRAP XV-15 tests for which case the Mach number, advance ratio, tip-path-plane angle, and torque coefficient were matched with the in-flight test. Because of the small size of the microphone "array" (created by moving the traverse incrementally) the peak noise level for most BVI conditions was not captured by the traversing microphones. Some results from the tests indicate that the far-field characteristics of the acoustic waveforms do not change much with small changes in tip-path-plane angles, but that the near-field is very sensitive to those small changes. The test also studied, in no great detail, the effects of varying the thrust coefficient.

The measured wind tunnel acoustic data differs significantly from the in-flight data. One of the main problems of the test was that the torque coefficient, rather than the thrust coefficient, was matched between wind tunnel and flight tests Ref. 48. Since the thrust coefficient plays such an important role in BVI noise generation, this parameter must be matched more precisely. The importance of an accurate trim methodology is emphasized in Ref. 46.

A second phase of this program was performed to expand the operating envelope of the previous test and to study noise reduction concepts such as blade-tip subwings and Higher Harmonic Control (HHC), see Ref. 48 & Ref. 49. For this test, the longitudinal traverse was comprised of eight microphones and a ninth microphone was placed in the far-field. In the first part of the test, three noise-reducing techniques were tested: reduction in tip Mach number, blade-tip subwings, and the addition of a fourth blade (Ref. 48). A reduction in the tip Mach number produced a reduction in noise of 4dB at the maximum BVI noise condition. The use of a subwing to diffuse the vortex core actually increased the noise and was detrimental to the performance. Noise reductions were found to be possible by adding a fourth blade when used in conjunction with a lower RPM. In the second part of the test, higher harmonic control was used to reduce BVI noise and vibration levels (Ref. 49). Using HHC, the test showed a reduction of up to 12dB in peak noise levels, mostly for the lower BVI condition. The test results were compared with the TiltRotor Aeroacoustic Code (TRAC) prediction system in Ref. 50, which is discussed in the TRAC section of this chapter.

Tilt Rotor Aeroacoustic Model (TRAM)

The TRAM project involves the development and testing of an isolated rotor system and a full-span tiltrotor aircraft, both representing a ¼-scale V-22 Osprey tiltrotor aircraft. A good introduction to the TRAM project is provided in Ref. 51. The two systems work together; the isolated rotor components become part of the full-span model when assembled. The isolated rotor was tested in the Duits-Nederlandse Windtunnel (DNW) and the full-span model was tested at the 80-by-120 feet wind tunnel at NASA Ames. The main objectives of the TRAM project were as follows (Ref. 51):

- "Acquisition of isolated proprotor aeroacoustic data, including rotor airloads."
- "Acquisition of full-span aeroacoustic data, including airloads to assess aerodynamic interaction effects."
- "Serve as technology demonstrator for low-noise proprotors."

The TRAM models incorporate rotor and airframe balances, pressure-instrumented blades, ground adjustable nacelle tilt (airplane mode to helicopter mode) and remote-controlled flaps and elevators. An overview of the data acquired during the TRAM isolated rotor DNW test is presented in Refs. 52 & 53. This test mainly focused on low-speed helicopter mode test conditions with data obtained for varying shaft tilt, advance ratio, tip Mach number, and thrust coefficient. The acoustics results from this test are presented in Ref. 54. One of the test's goals was to provide TRAC with a more comprehensive experimental data set in order to validate the results. It is important to note that the rotor tip speed of the model was more then ten percent below the tip speed of the XV-15 or V-22 due to model drive shaft dynamic response limits. Therefore, HSI

noise level, as well as thickness and loading noise levels are lower than for the full-scale aircraft.

Thirteen traversing microphones were used and positioned 1.73R below the rotor hub. The test showed that the glideslopes corresponding to maximum BVI noise are larger than for a conventional helicopter, a fact that is clearly due to the higher disk loading of tiltrotors. For this test, the maximum BVI was obtained at a tip-path-plane angle of approximately 11º, but the true maximum may not have been reached. The test also showed that the trends remain the same for higher thrust coefficient but, as expected, the glideslopes corresponding to maximum BVI noise become even larger for larger thrust coefficients. It was also shown that BVI noise levels increase with an increasing advance ratio, and that the noise contours also change drastically with an increasing advance ratio, thus indicating a possible change in the BVI interaction geometry. The results for changes in thrust were also as expected: as the thrust increases, the BVI miss-distance increases and the BVI noise levels decrease. The paper suggests that although the vortices become stronger for higher thrust, it is the increase in miss-distance that has a larger effect on the resulting BVI noise levels. The paper also presents an analysis of the effect of thrust when compared at equivalent wake geometry. It was found that BVI noise levels increase with increasing thrust due to the stronger vortices. A paper by Burley et al. compares the test results to the TRAC code predictions and is discussed in the TRAC section of this literature survey (Ref. 55).

In addition to aeroacoustic testing, three-dimensional wake geometry data was obtained in the DNW wind tunnel (Ref. 56). It was observed that at low thrust conditions, the high twist of the rotor caused negative loading at the tip of the blade, which leads to a secondary vortex to be shed inboard of the tip. It was revealed that this secondary vortex rotates in the opposite direction of the main tip vortex. In addition, the pressure-instrumented blades also gave the TRAM model airloads measurement capability (Ref. 57). It was shown that over the rotor disk, the region of negative tip loading decreases as the rotor shaft was tilted forward. This surprising result should be analyzed further, since the blades are usually more negatively loaded at lower angles-of-attack. For a given shaft tilt, an increase in thrust coefficient was demonstrated to reduce the azimuth range of negative tip loading, which is an expected result. For BVI, some results were shown where the blade experiences multiple parallel vortex interactions. Comparisons of the test results and CAMRAD II predictions were presented in Refs. 58 & 59. These papers study in more detail the roll-up process of the wake, which appears to be slower than for helicopters. The full-span TRAM model was first tested in the 80-by-120 feet wind tunnel at Ames in late 2000 (Refs. 60 & 61). The data acquired was used to study performance, wing hover download, rotor-on-wing interactions, and acoustics. A total of twelve microphones were used and positioned on traversing wings below the model. This preliminary test provided limited acoustics data and no complete traverse sweep. No acoustic data from this test was published in the open literature.

1.2.4 Tiltrotor Acoustic Prediction

Most known acoustic prediction methodologies apply to both helicopters and tiltrotors, but as mentioned in section 1.1.3, some important considerations must be taken into account when analyzing the tiltrotor. These factors, coupled with the complexities of predicting the rotor operating condition for a certain flight condition, have lead to a slower development of the acoustic prediction capabilities for tiltrotors. Many prediction methodologies use the WOPWOP code to predict acoustics, but different codes are used to predict the aircraft trim and include the fountain flow effect (Refs. 62-70). All of these references stress the importance of correctly predicting the trim of the aircraft since it determines the rotor operating condition. Because hover noise is not considered in this Dissertation, the reader is directed to the references listed above for further information on that subject and to Refs. 71 & 72 for small-scale aeroacoustics testing of the fountain flow effect.

A 1992 paper by Riley describes a noise prediction methodology based on the FAA's Heliport Noise Model (HNM), and states that the proper selection of airspeed and nacelle tilt is effective in minimizing tiltrotor noise (Ref. 73). A paper by Boyd gives a good overview of the current state of rotorcraft noise prediction and outlines areas of future research necessary to improve such predictions (Ref. 74). A tiltrotor case study is presented in which results from the 1995 XV-15 acoustic flight test are compared with predictions from the TRAC code (see section below). Boyd stresses the importance of carefully matching aircraft states and rotor operating conditions between the prediction and flight test. In particular, the paper notes that variations in airspeed and fuselage pitch

can have large effects on wing/rotor lift sharing, thus appreciably changing the rotor operating condition. For further information on this subject, refer to chapters 2, 3 and 4 of this Dissertation.

TiltRotor Aeroacoustic Code (TRAC)

The TiltRotor Aeroacoustic Code (TRAC) consists of a group of different Computational Fluid Dynamics (CFD) and non-CFD modules that predict performance, aerodynamics, wake structure, and acoustics of tiltrotor aircraft (Ref. 75, see also Ref. 76 where results are compared to the 1994 fifteen-percent JVX rotor wind tunnel test of Ref. 44). The performance of the aircraft is predicted using a modified version of CAMRAD and the acoustics are predicted using a modified version of the WOPWOP code (Ref. 77). The results show that poor agreement is obtained for BVI noise levels on the retreating side while slightly better agreement is found for BVI noise levels on the advancing side. A multiple-vortex predicted wake produced better results and showed that the secondary vortex present in many conditions on the advancing side was on the same order of strength as the tip vortex. It is important to note that the TRAC system is not restricted to tiltrotors and has been used to predict non-tiltrotor associated noise (Ref. 78). In this case, it is used to study the effects of blade shape on helicopter BVI noise. TRAC has also been used to predict surface acoustic pressures because of an interest in interior tiltrotor noise (Ref. 79).

A 1999 paper by Burley et al. describes the initial comparisons of TRAC predictions to isolated rotor TRAM results (Ref. 55). A surprising conclusion of this paper is that peak

BVI levels for a tiltrotor occur at lower rotor angles, or shallower descents, than for helicopters. This contradicts TRAM test results (Ref. 54). The explanation provided in the paper is that negative tip loading causes multiple vortices to shed, and that the strong inboard vortices tend to push the tip vortices up towards the rotor. It is clear that more investigation is needed to clarify these trends. Another conclusion is that multiple vortices cause the peak BVI noise region to spread over a larger range of shaft tilt, a fact that was corroborated in the TRAM test (Ref. 54).

Some results from the 1995 acoustics flight test of the XV-15 (Ref. 33) were compared to TRAC predictions in Ref. 80. Three conditions were analyzed, all with the aircraft in helicopter mode: a level, steady-state flight and two steady-state descents. In most cases, the TRAC results under-predicted the noise levels of the measured data, especially at mid and high frequencies. Flight data from the 1995 test were again compared to TRAC results in 2001 (Ref. 81). Four descent cases were analyzed: three descents of varying glideslope at a 60º nacelle tilt and one "BVI" 9º descent at an 85º nacelle tilt. By examining the flight test acoustic data carefully, the authors point out that thickness noise was the dominant noise source on approach, except for cases where BVI was present. This is an important discovery that will be taken into account in this Dissertation. The ability of TRAC to correctly predict noise for the cases chosen was very limited. It is speculated that differences in rotor/wing lift sharing between the test and the predictions are the main cause of the error. The TRAC code was also compared to the wind tunnel test results of Ref. 48 in Ref. 50. Comparing the TRAC predictions to wind tunnel test data has the advantage of relying on steady, repeatable data and known thrust and tip-

path-plane angle conditions. However, this wind tunnel test has a limited range of shaft tilts. The comparison was made with a high BVI case where thrust coefficient and longitudinal flapping were matched. The newer CAMRAD II was used in place of CAMRAD.Mod1, used in prior TRAC predictions. The majority of predictions were compared to a far-field microphone used during the wind tunnel test. Some accuracy was achieved in predicting the amplitude of the BVI pulse but not in predicting the character of the waveform.

1.2.5 Noise Reduction Through Flight Path Management

Early flight tests aimed at reducing BVI noise (then referred to as *blade slap*) in conventional helicopters via careful flight operations showed that there were obvious advantages to flight trajectory control (Ref. 82). These early tests showed that the pilot could fly more quietly by carefully avoiding certain regions of the well known "fried-egg plot", which was constructed through cabin noise measurements and subjective evaluations of the radiated noise by the pilots. The general guidelines obtained during the flight test were expanded and included in the Helicopter Association International's (HAI) *Fly Neighborly Program* (Ref. 83). These voluntary flight procedures designed to reduce the community noise exposure are still used by various operators today. More recently, the development of GPS technology has been explored as a means of implementing flight path management strategies (Refs. 84-86). Recent papers have used a quasi-static performance model to show how X-force control and flight path management can be used to reduce BVI noise on conventional helicopters (Refs. 87 &

88) and tiltrotors (Refs. 89 & 90). The progression of the present research is documented in the literature in Refs. 91-93.

1.3 Survey of Tiltrotor Performance Modeling

A fairly limited number of papers that relate to the performance modeling of tiltrotors are available in the open literature. Analyses of rotors that operate at large tip-path-plane angles can be found early in the literature (Refs. 94 & 95). Both of these references use a modified blade-element analysis to model high inflow conditions. Their main difference lies in their choice of axis system, with the second reference being more applicable to a rigid rotor. A performance analysis based on momentum theory for a descending tiltrotor with moderate nacelle tilt angles can be found in Ref. 3. A model aimed at investigating the dynamics of proprotors operating at different nacelle tilts can be found in Refs. 96-98. In these references, a uniform inflow model is judged as supplying the best results with the limited wind-tunnel test data available. Adding torsion and lag degrees of freedom lead to no improvements in the performance correlations.

Bell Helicopter developed the most widely used mathematical simulation tiltrotor model in support of the XV-15 aircraft (Ref. 99). Over the years, this model was expanded and improved and eventually implemented in the NASA Ames Vertical Motion Simulator (VMS), see Refs. 100-103. This model is usually referred to as the Generic Tilt-Rotor Simulation (GTRSIM). Extensive use of XV-15 aerodynamic look-up tables is made in the model. The rotor inflow is assumed to be uniform over the rotor disk.

1.4 Research Objectives

The goal of this research is to develop a broader understanding of tiltrotor approach noise and noise reduction potential. The specific objectives of the research are as follows:

- To develop a combined performance/acoustic model of a tiltrotor for longitudinal terminal area operations.
- To improve the level of understanding of tiltrotor descent noise and its relation to the aircraft's unique performance capabilities.
- To use measured tiltrotor acoustic flight test data to develop new flight procedures that take advantage of the tiltrotor's distinctive attributes to reduce approach noise, in particular BVI noise.

These objectives are detailed below.

Developing a Performance/Acoustic Tiltrotor Model

This objective involves developing a performance model that can be tied to the tiltrotor's acoustic characteristics. In order to emphasize a basic understanding of the fundamentals of tiltrotor approach profiles, a building-block approach is used to develop the performance model. Complexity is added only when required to capture the physical trends of a descending approach. In the same manner, a simple method is first used to obtain a qualitative BVI noise measure for a tiltrotor in a descent as a function of key

aircraft performance parameters. Acoustic flight test data of the XV-15 aircraft is then used to model the complete noise characteristics of the aircraft.

Improving Tiltrotor Noise Understanding

The main goal here is to establish a relationship between the performance-state of a tiltrotor and its noise emission characteristics. Basic trend studies are conducted to ascertain BVI noise trends as a function of flight parameters and aircraft configuration. The understanding gained from these trend studies are used to propose basic approach guidelines to reduce noise.

Developing Low Noise Tiltrotor Approach Profiles

Using the performance/acoustics tiltrotor model and the basic understanding gained by fulfilling the previous two objectives, specific approach profiles that reduce BVI noise are designed. These approach profiles are designed with practical implementation in mind. The resulting low BVI noise approach procedures are evaluated against a baseline approach profile.

1.5 Outline of Dissertation

The importance of the tiltrotor's approach noise characteristics to its success was emphasized at the beginning of this chapter. A thorough tiltrotor acoustics literature review was given in section 1.2 and highlighted the need for a deeper understanding of

tiltrotor noise and for a systematic methodology for designing low-noise approaches. The remainder of this Dissertation is organized in three main parts: the development of a performance/acoustics tiltrotor model, the design and analysis of low BVI noise approaches, and finally, the conclusions and recommendations.

Chapter 2 presents the derivation and validation of the performance model. Different methodologies for solving the resulting system of equations are discussed and a baseline approach profile is introduced. Chapter 3 introduces the details of the 1995 XV-15 acoustic flight test. Since the results from the test are later used to build an acoustic model, the emphasis is placed on a thorough exposition of the test setup and acoustic and performance measurement methods. The importance of associating the correct aircraft performance parameters with each microphone measurement is highlighted. In Chapter 4, the Quasi-Static Acoustic Modeling (Q-SAM) method is introduced. This method allows a database of steady-state noise predictions or measurements to be mapped to a quasi-static maneuvering flight. A neural network is developed to interpolate the XV-15 acoustic data and tie it to the quasi-static performance model. The network is then used to study the measured noise trends associated with changes in different flight trajectory and aircraft configuration parameters.

Chapter 5 first presents a trend-based analysis that relates an acoustically important performance parameter to the likelihood of strong BVI noise. BVI noise constraints are imposed on the baseline approach by adjusting this performance parameter to match

measured BVI noise trends. Low BVI noise approach profiles are designed and compared to the baseline approach.

Chapter 6 summarizes the results, presents conclusions, and provides suggestions for future research on the topic.

Chapter 2

Quasi-Static Longitudinal Tiltrotor Performance Model

In this chapter, a performance model is developed for a tiltrotor that operates in the longitudinal plane. The goal of the model is to confidently predict performance trends associated with a tiltrotor when a slow decelerating approach maneuver is performed. The predicted performance parameters are subsequently tied to the acoustic characteristics of the aircraft in order to obtain noise predictions for various approach procedures. The performance results are validated in comparison with XV-15 flight test results.

2.1 Quasi-Static Assumption

One of the main assumptions used to derive the performance and acoustic models is that the maneuvers considered in this research can be estimated as quasi-static maneuvers. This implies that during a slow maneuver, the governing force and moment equations are satisfied (including vehicle acceleration) but the effects of unsteady airframe aerodynamics, unsteady rotor aerodynamics, and rotor inflow dynamics are negligible.

For example, between two time steps of a decelerating approach, the inflow through the rotor is assumed to instantaneously achieve the steady-state inflow associated with force and moment balance equilibrium. This assumption implies that the wake system shed from the rotor is that due to a sequence of *steady-state like* conditions, with the rotor in force and moment equilibrium. The quasi-static assumption restricts the modeling validity to slow accelerations/decelerations, typical of commercial flight operations. In the limit, as acceleration/deceleration approaches zero, steady-state tiltrotor performance and acoustics are modeled. For this Dissertation, maximum decelerations of approximately -0.1 g's are considered; thought to be small enough for the quasi-static approximation to be valid.

It is also known that the rotor's coning and flapping dynamic response to input are fast (1/4 to 1/2 of a rotor revolution, see Ref. 103), with respect to the force and moment equations. For this reason, dynamic coning and flapping responses have been neglected and the algebraic equations for steady-state coning and flapping angles can be considered separate degrees of freedom from the rigid body equations.

2.2 Coordinate Systems

In order to derive the equations that govern the quasi-static longitudinal performance of the tiltrotor, it is useful to employ different coordinate systems. For example, the derivation of blade forces and moments is more easily accomplished in an axis system that rotates and flaps with the blades. However, the derivation of the rigid body

equations is typically carried out in a body-axis system. In this section, the different coordinate systems used in this research are presented as well as some useful coordinate transformation matrices.

2.2.1 Body and Wind-Axis Systems

In flight dynamics work, it is customary to use a coordinate system fixed to the aircraft (body-axis) in order to derive the rigid body equations. The body-axis system is fixed to the center-of-gravity of the tiltrotor with its x-axis pointing through the nose of the vehicle along a chosen reference line and the perpendicular z-axis pointing through the floor. Figure 2.1 shows the longitudinal plane body-axis unit vectors, $\mathbf{i}_B$ and $\mathbf{k}_B$. The wind-axis system is oriented with the incoming flow velocity and can be attached to the body or the wing aerodynamic center as shown in Figure 2.1. Its x-axis points in the direction of drag and its z-axis points in the direction of lift. Note that the wind-axis system is undefined in hover where the airspeed is zero. Figure 2.1 also shows the longitudinal plane wind-axis unit vectors, $\mathbf{i}_W$ and $\mathbf{k}_W$. Also defined on the figure are the fuselage pitch angle, flight path angle, and nacelle tilt angle. Observe that the flight path angle is shown negative, which corresponds to a descent angle.

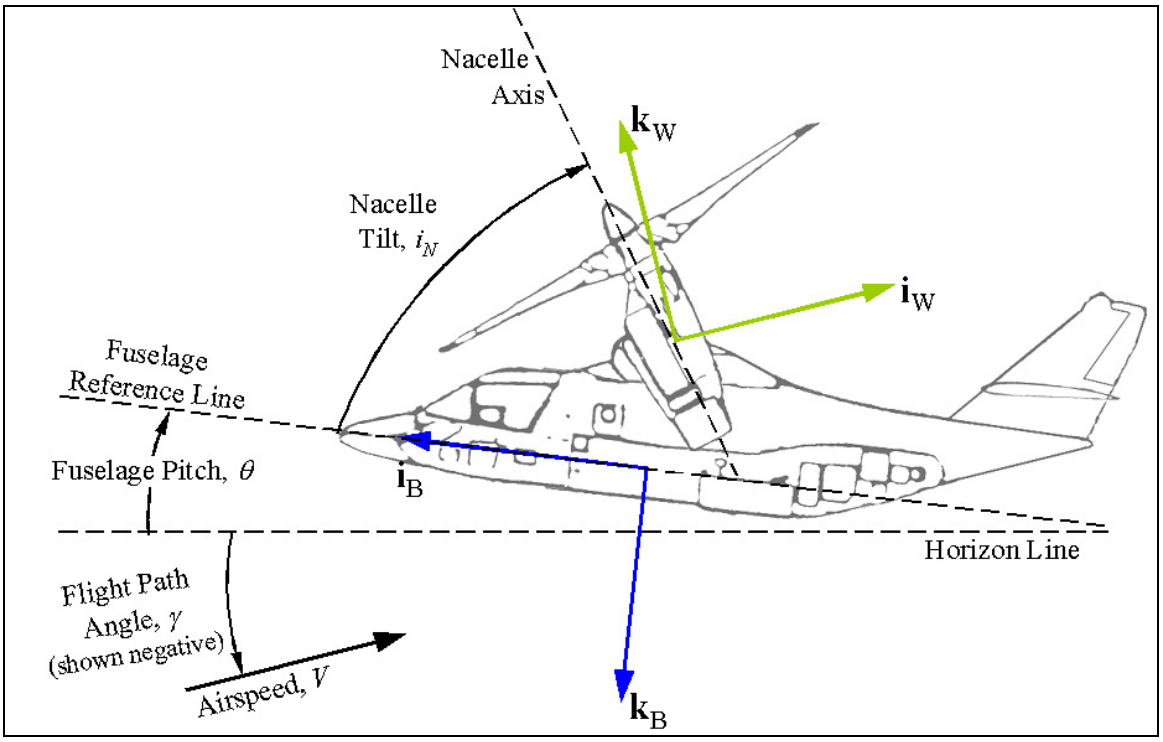

Figure 2.1. Body and wind-axis systems.

2.2.2 Blade Coordinate Axes

Using different axis systems and coordinate transformations often greatly simplify the derivation of blade forces and moments, which can be quite complex. Figure 2.2 shows three rotor coordinate axis systems often used to describe rotor forces and moments. The coordinate system represented by the unit vectors $\mathbf{i}_{NR}$, $\mathbf{j}_{NR}$, and $\mathbf{k}_{NR}$ is aligned with the nacelle axis (shaft axis) and does not rotate with the blades. The unit vectors $\mathbf{i}_R$, $\mathbf{j}_R$, and $\mathbf{k}_R$ correspond to the rotating frame axis system, which rotates about the shaft axis at the same angular velocity as the rotor. Finally, the flapped-axis system is represented by the unit vectors $\mathbf{i}_F$, $\mathbf{j}_F$, and $\mathbf{k}_F$. It is fixed to the blade and follows its rotation through the azimuth angle, ψ, and its flapping through the flapping angle, β, which is a function of ψ.

These axis systems are centered at the rotor hub and follow the aircraft motion and configuration changes (tilt of the nacelles).

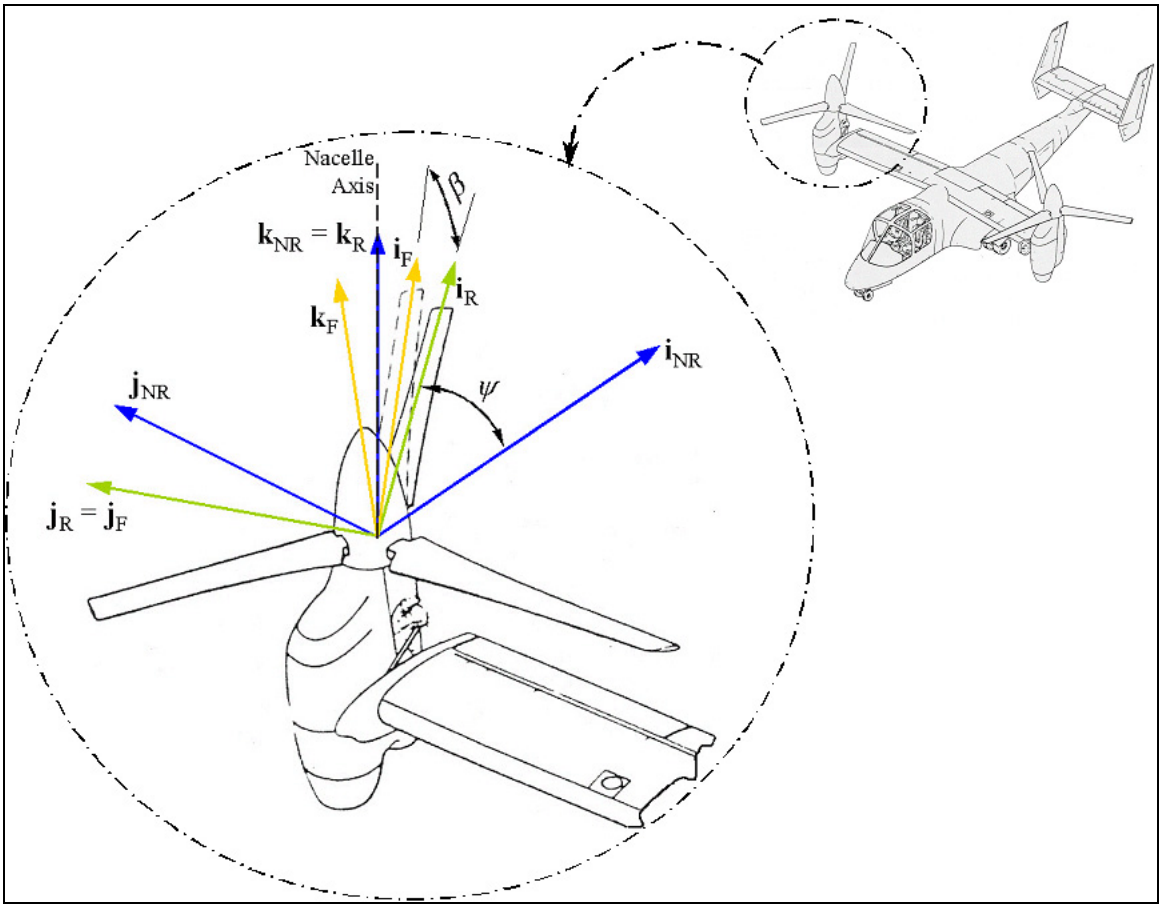

Figure 2.2. Blade coordinate axes.

2.2.3 Rotor Reference Planes

The main rotor planes used herein are the tip-path-plane and the hub plane. The first harmonic tip-path-plane is used to describe the orientation of the rotor forces in space. It is assumed that the resultant rotor thrust and H-force are respectively perpendicular and parallel to the tip-path-plane. The hub plane is perpendicular to the nacelle axis (shaft

axis) and is used to define the longitudinal flapping and cyclic of the blade, β_{1c} and θ_{1s}. Figure 2.3 defines the tip-path-plane and the hub plane as well as the rotor coning, rotor flapping, and tip-path-plane angles with the latter being shown negative. Note that the hub plane is formed by the $\mathbf{i_{NR}}$ and $\mathbf{j_{NR}}$ unit vectors of the non-rotating axis system described above in section 2.2.2.

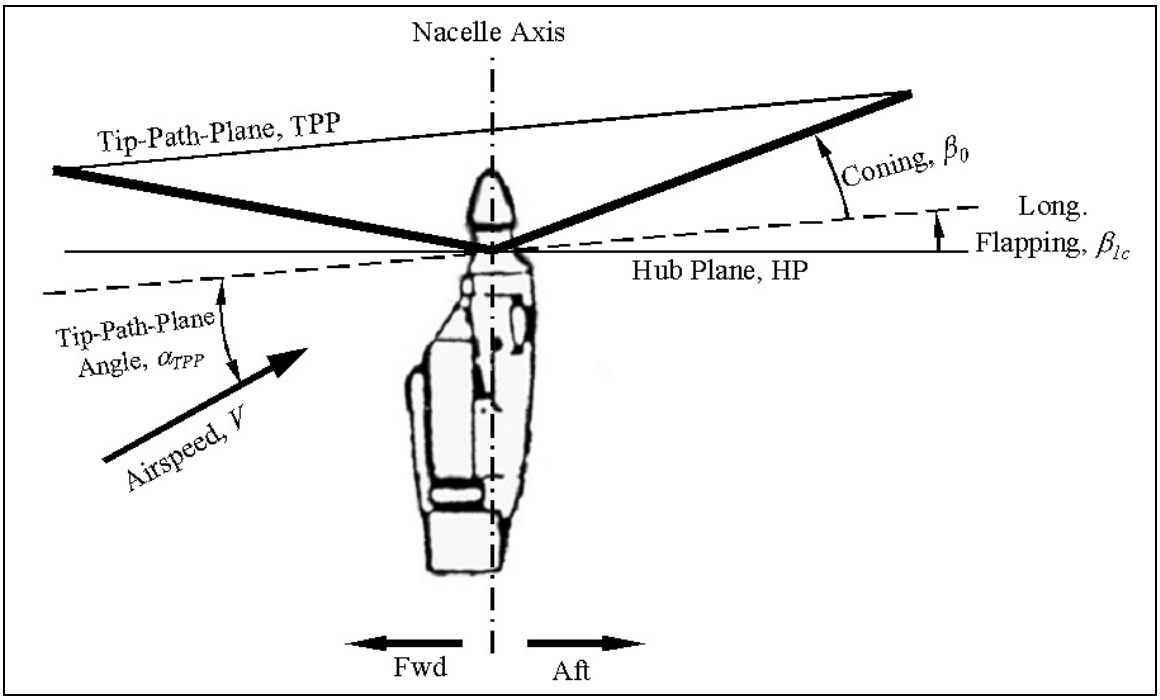

Figure 2.3. Rotor reference planes.

2.2.4 Coordinate Transformation Matrices

The following useful transformation matrices are derived using Figure 2.1 and Figure 2.2. Note that the inverse transformation can be obtained by taking the inverse of the original transformation matrix. The flapping angle, β, is assumed to be small ($\cos\beta \approx 1$).

1) Non-Rotating Shaft Axis to Body Axis:

$$\begin{pmatrix}\mathbf{i}\\ \mathbf{j}\\ \mathbf{k}\end{pmatrix}_{\mathbf{B}} = \begin{bmatrix}-\sin i_N & 0 & \cos i_N\\ 0 & 1 & 0\\ -\cos i_N & 0 & -\sin i_N\end{bmatrix}\begin{pmatrix}\mathbf{i}\\ \mathbf{j}\\ \mathbf{k}\end{pmatrix}_{\mathbf{NR}} \tag{2.1}$$

2) Rotating Shaft Axis to Non-Rotating Shaft Axis:

$$\begin{pmatrix}\mathbf{i}\\ \mathbf{j}\\ \mathbf{k}\end{pmatrix}_{\mathbf{NR}} = \begin{bmatrix}\cos\psi & -\sin\psi & 0\\ \sin\psi & \cos\psi & 0\\ 0 & 0 & 1\end{bmatrix}\begin{pmatrix}\mathbf{i}\\ \mathbf{j}\\ \mathbf{k}\end{pmatrix}_{\mathbf{R}} \tag{2.2}$$

3) Rotor Flapping to Rotating Shaft Axis:

$$\begin{pmatrix}\mathbf{i}\\ \mathbf{j}\\ \mathbf{k}\end{pmatrix}_{\mathbf{R}} = \begin{bmatrix}1 & 0 & \beta\\ 0 & 1 & 0\\ -\beta & 0 & 1\end{bmatrix}\begin{pmatrix}\mathbf{i}\\ \mathbf{j}\\ \mathbf{k}\end{pmatrix}_{\mathbf{F}} \tag{2.3}$$

4) Rotor Flapping Axis to Body-Axis:

$$\begin{pmatrix}\mathbf{i}\\ \mathbf{j}\\ \mathbf{k}\end{pmatrix}_{\mathbf{B}} = \begin{bmatrix}-\cos\psi\sin i_N + \beta\cos i_N & \sin\psi & -\cos\psi\cos i_N - \beta\sin i_N\\ \sin\psi\sin i_N & \cos\psi & \sin\psi\cos i_N\\ \beta\cos\psi\sin i_N + \cos i_N & -\beta\sin\psi & \beta\cos\psi\cos i_N - \sin i_N\end{bmatrix}\begin{pmatrix}\mathbf{i}\\ \mathbf{j}\\ \mathbf{k}\end{pmatrix}_{\mathbf{F}} \tag{2.4}$$

2.3 Longitudinal Rigid Body Equations

Three nonlinear Euler rigid body equations of motion govern the longitudinal flight of the tiltrotor. These are the X and Z force equilibrium equations and the pitching moment equation that are derived below in the aircraft body axis.

The main assumption in simplifying the rigid body equations is that the longitudinal motion of the aircraft is uncoupled from the lateral motion. This assumption is perfectly valid for a tiltrotor because of its counter-rotating side-by-side rotor configuration and the absence of a tail rotor. In addition, the aircraft's center-of-gravity is assumed to lie on the longitudinal axis. The roll angle, roll rate, yaw rate, and sideward velocity are all zero. Note that the pitching moment of inertia, I_{yy}, is assumed to vary linearly with the nacelle tilt but that the rate of change of the pitching moment of inertia, $\dot{I}_{yy}$, is neglected.

Force equilibrium equations:

$$X = \frac{W}{g}(\dot{u} + qw) + W\sin\theta \tag{2.5}$$

$$Z = \frac{W}{g}\left(\dot{w} + \cancel{pv}^{0} - qu\right) - W\cos\theta\,\cancel{\cos\phi}^{1} = \frac{W}{g}(\dot{w} - qu) - W\cos\theta \tag{2.6}$$

Moment equilibrium equation:

$$M = I_{yy}\dot{q} + (I_{xx} - I_{zz})\cancel{pr}^{0} + I_{xz}\left(\cancel{p^2}^{0} - \cancel{r^2}^{0}\right) = I_{yy}\dot{q} \tag{2.7}$$

Assuming that the fuselage angle-of-attack and the fuselage pitch are small, the following substitutions can be made:

$$\begin{aligned} &\alpha_F = \theta - \gamma \\ &u = V\cos\alpha_F \approx V \quad \text{and} \quad \dot{u} \approx \dot{V} \\ &w = V\sin\alpha_F \approx V\alpha_F = V(\theta - \gamma) \quad \text{and} \quad \dot{w} \approx \dot{V}\alpha_F + V\dot{\alpha}_F = \dot{V}(\theta - \gamma) + V(\dot{\theta} - \dot{\gamma}) \end{aligned} \tag{2.8}$$

Using these assumptions and substituting the kinematic relation, $q = \dot{\theta}$, for zero roll and yaw angles, in the force and moment balance equations gives the following:

Force equilibrium equations:

$$X = W \sin\theta + \frac{W}{g}\left(\dot{V} + V\dot{\theta}(\theta - \gamma)\right) \tag{2.9}$$

$$Z = \frac{W}{g}\left(\dot{V}(\theta - \gamma) - V\dot{\gamma}\right) - W \tag{2.10}$$

Moment Equilibrium equation:

$$M = I_{yy}\ddot{\theta} \tag{2.11}$$

The left-hand side of each of the previous equations is comprised of airframe and rotor contributions resolved in the body-axis system and can be written as:

$$X = X_{airframe} + 2X_{rotor} \tag{2.12}$$

$$Z = Z_{airframe} + 2Z_{rotor} \tag{2.13}$$

$$M = M_{airframe} + 2M_{rotor} + 2X_{rotor} \cdot h_{rotor} - 2Z_{rotor} \cdot l_{rotor} \tag{2.14}$$

The airframe contributions are obtained from wind tunnel test results of a full-scale XV-15 aircraft (see section 2.4). These airframe contributions vary with fuselage angle-of-attack, nacelle tilt, flap deflection, and elevator deflection. However, airframe/rotor

interactions are assumed negligible since the flight regimes considered in this Dissertation consist of airspeeds greater than 40 knots and nacelle tilts greater than 60 degrees.

The rotor forces and moments are derived using blade element theory (BET) in section 2.5. The pitching moment terms caused by the rotor hub offset with respect to the aircraft's center-of-gravity are depicted graphically in Figure 2.4. Note that the rotor hub offset terms, h_{rotor} and l_{rotor}, and the longitudinal center-of-gravity position of the aircraft both vary with the nacelle tilt.

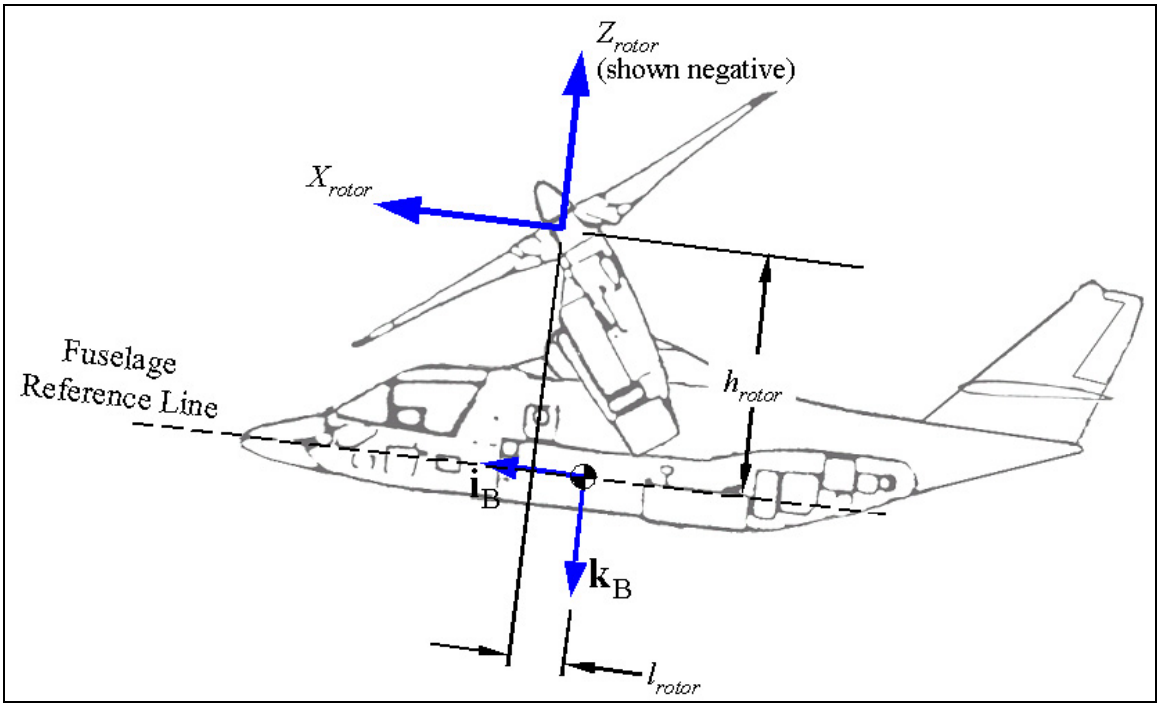

Figure 2.4. Rotor hub offset with respect to center-of-gravity.

2.4 Airframe Equations

As previously mentioned, the airframe contributions to equations (2.12), (2.13), and (2.14) are obtained from wind tunnel test results of a full-scale XV-15 aircraft (Ref. 104). Since rotor/airframe interactions are neglected in this analysis, only power-off results were used. The total airframe lift, drag, and pitching moment are expressed as:

$$L_{airframe} = \frac{1}{2}\rho V^2 S_{ref} C_L \tag{2.15}$$

$$D_{airframe} = \frac{1}{2}\rho V^2 S_{ref} C_D \tag{2.16}$$

$$M_{airframe} = \frac{1}{2}\rho V^2 S_{ref} c_{ref} C_M \tag{2.17}$$

The lift, drag, and pitching moment coefficients are functions of the angle-of-attack, nacelle tilt, flap deflection, and elevator deflection. The following sections describe how the coefficients were derived from the wind-tunnel test data.

2.4.1 Airframe Lift Coefficient

The total airframe lift coefficient is obtained by adding nacelle tilt, flap deflection and elevator deflection corrections to the baseline airplane mode lift coefficient:

$$C_L = f\left(\alpha_F, i_N, \delta_f, \delta_e\right) = C_{L_{base}} + C_L\big|_{i_N} + C_L\big|_{\delta_f} + C_L\big|_{\delta_e} \tag{2.18}$$

The baseline lift-curve slope, zero-lift angle-of-attack, and angle of maximum lift were obtained with the aircraft in airplane mode (i_N = 0°) with no flap deflection (δ_f = 0°). Two methods were evaluated to model the baseline lift coefficient past stall: a simple linear lift model and a more complex method based on the USAF Stability and Control DATCOM (Ref. 105). In the simple method, the baseline lift-curve slope is assumed constant up to stall so that lift varies linearly with respect to the angle-of-attack in that particular region. After stall, the lift-curve slope is changed so that the lift coefficient is zero at α_F = ± 90°. The DATCOM method involves choosing and adjusting many empirical factors (see Ref. 105). Figure 2.5 shows the resultant baseline variation of lift coefficient with respect to fuselage angle-of-attack for the simple method and the DATCOM method as well as the measured data.

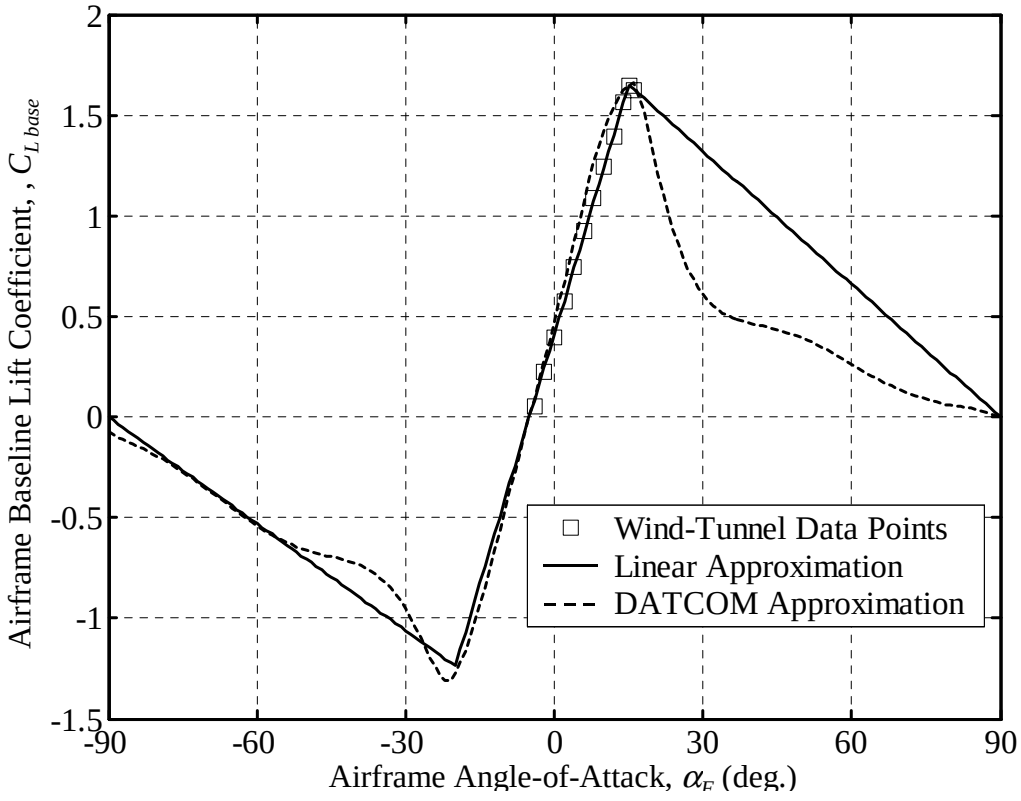

Figure 2.5. Airframe baseline lift coefficient vs. angle-of-attack.

As the figure shows, the simpler method predicts the pre-stall lift behavior of the data quite well but over-predicts the post-stall lift coefficient. Since the flight regimes considered in this research were limited to pre-stall flight, it was deemed more important to accurately model pre-stall lift behavior. Therefore, the simpler stall model was considered acceptable.

Polynomial approximations of the wind tunnel data were developed to obtain the lift coefficient corrections due to nacelle tilt and to flap deflections. The polynomial approximations are presented below, with the nacelle tilt and flap deflection in degrees:

$$C_L|_{i_N} = \left(-2.2742\times10^{-4}\right) i_N - \left(6.8287\times10^{-6}\right) i_N^2 - \left(2.3940\times10^{-7}\right) i_N^3 \tag{2.19}$$

$$C_L|_{\delta_f} = \left(2.5125\times10^{-2}\right) \delta_f - \left(2.3059\times10^{-4}\right) \delta_f^2 \tag{2.20}$$

The lift coefficient correction due to elevator deflection was obtained directly from Ref. 104, where the elevator deflection angle is expressed in degrees:

$$C_L|_{\delta_f} = \left(0.01\right) \delta_e \tag{2.21}$$

2.4.2 Airframe Drag Coefficient

The expression for the total airframe drag coefficient is similar to the lift coefficient expression of section 2.4.1:

$$C_D = f\left(\alpha_F, i_N, \delta_f, \delta_e\right) = C_{D_{base}} + C_D\big|_{i_N} + C_D\big|_{\delta_f} + C_D\big|_{\delta_e} \tag{2.22}$$

The baseline drag coefficient is obtained by fitting two polynomial approximations that represent the pre-stall and post-stall drag behavior to the wind tunnel data, where the fuselage angle-of-attack is in degrees:

$$\begin{aligned}
\alpha_F \le \alpha_{F_{STALL}} \Rightarrow C_{D_{base}} &= 1.1636\times10^{-1} - \left(5.4015\times10^{-4}\right)\alpha_F \\
&\quad + \left(5.7391\times10^{-4}\right)\alpha_F^2 - \left(2.4114\times10^{-6}\right)\alpha_F^3 \\
\alpha_F > \alpha_{F_{STALL}} \Rightarrow C_{D_{base}} &= \left(-1.1122\times10^{-2}\right)\alpha_F + \left(1.7634\times10^{-3}\right)\alpha_F^2
\end{aligned} \tag{2.23}$$

Figure 2.6 shows the baseline drag modeling.

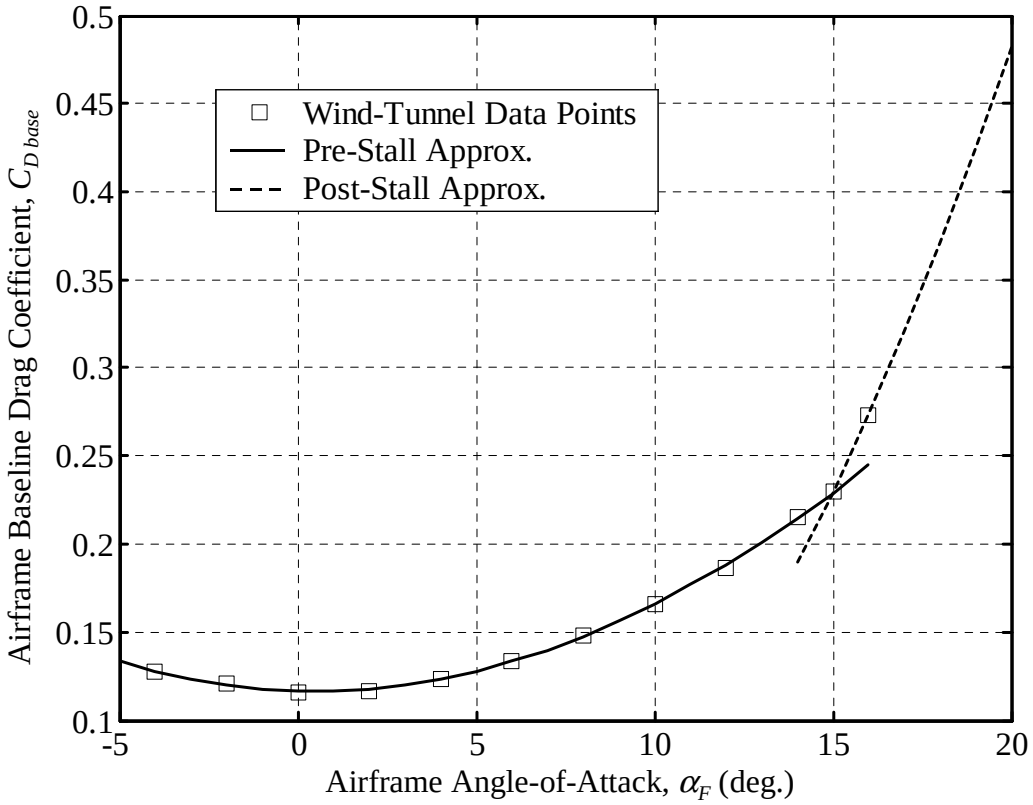

Figure 2.6. Airframe baseline drag coefficient vs. angle-of-attack.

Polynomial approximations of the wind tunnel data were again obtained to model the drag coefficient corrections due to nacelle tilt and to flap deflections. The drag increase due to elevator deflection is small and therefore neglected. The following approximations were used, with the nacelle tilt and flap deflection in degrees:

$$C_D|_{i_N} = \left(3.6402\times10^{-3}\right) i_N - \left(1.8810\times10^{-5}\right) i_N^2 \tag{2.24}$$

$$C_D|_{\delta_f} = \left(8.4030\times10^{-4}\right) \delta_f + \left(3.4100\times10^{-5}\right) \delta_f^2 \tag{2.25}$$

2.4.3 Airframe Pitching Moment Coefficient

The total airframe pitching moment coefficient is given by:

$$C_M = f\left(\alpha_F, i_N, \delta_f, \delta_e\right) = C_{M_{base}} + C_M\big|_{i_N} + C_M\big|_{\delta_f} + C_M\big|_{\delta_e} \tag{2.26}$$

Based on the wind tunnel data, the baseline pitching moment variation was modeled as a linear function of the angle-of-attack of the fuselage (see Figure 2.7):

$$C_{M_{base}} = 1.6643\times10^{-1} - \left(2.9404\times10^{-2}\right)\alpha_F \qquad (\alpha_F \text{ in degrees}) \tag{2.27}$$

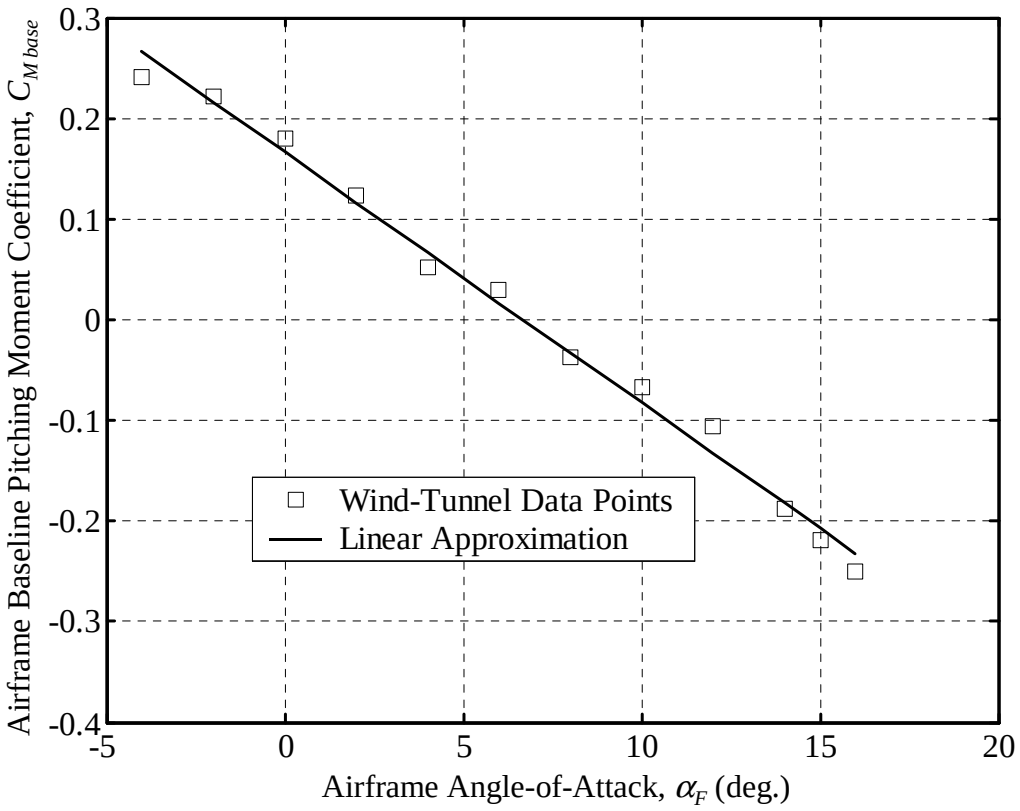

Figure 2.7. Airframe baseline pitching moment coefficient vs. angle-of-attack.

The following polynomials were fitted to the test data in order to approximate the nacelle tilt and flap deflection corrections (with nacelle tilt and flap deflection in degrees):

$$C_M\big|_{i_N} = \left(1.4510\times10^{-3}\right) i_N - \left(1.0896\times10^{-4}\right) i_N^2 + \left(2.9666\times10^{-6}\right) i_N^3 - \left(2.0228\times10^{-8}\right) i_N^4 \tag{2.28}$$

$$C_M\big|_{\delta_f} = \left(5.8393\times10^{-3}\right) \delta_f + \left(9.5420\times10^{-5}\right) \delta_f^2 \tag{2.29}$$

The pitching moment coefficient correction due to elevator deflection was obtained directly from Ref. 104 (where the elevator deflection angle is expressed in degrees):

$$C_M\big|_{\delta_f} = \left(0.0375\right) \delta_e \tag{2.30}$$

2.4.4 Rotor/Wing Interactions

In certain regimes of flight, the rotors' downwash velocities impinge on the aircraft and can alter the airframe lift, drag, and pitching moment. In hover and in slow helicopter mode forward flight, the forces produced on the wing and fuselage can be considerable (Refs. 106-108). Similarly, in airplane mode cruise flight, the wing is immersed in the wake of the proprotors and the resultant velocity vector is a combination of freestream and rotor induced velocities. However, airplane mode cruise flight and helicopter mode hover are not cases considered in this research. Indeed, the range of nacelle tilts of interest for BVI noise during an approach is between 60° and 90° (conversion mode to

helicopter mode) and the minimum velocity considered is 40 knots. Therefore, the rotor/airframe interaction effects are assumed to be negligible. A simple analysis based on momentum theory reinforced this assumption in Ref. 91

2.4.5 Airframe Forces in Body-Axis System

Using the transformation from the wind-axis system to the body-axis system developed in section 2.2.4 yields the final expressions for the airframe X and Z force equations:

$$X_{airframe} = L_{airframe} \sin(\theta - \gamma) - D_{airframe} \cos(\theta - \gamma) \tag{2.31}$$

$$Z_{airframe} = -L_{airframe} \cos(\theta - \gamma) - D_{airframe} \sin(\theta - \gamma) \tag{2.32}$$

2.5 Rotor Equations

The goal of this section is to derive expressions for the rotor forces and moments, as well as for the longitudinal flapping and coning angles. The analysis closely follows that of Ref. 109. Assumptions and simplifications are discussed along with the derivations.

2.5.1 Blade Velocities

The first step in deriving the rotor forces and moments is to obtain the total velocity vector at a point on an individual blade. In order to maintain generality, the velocity vector is derived with respect to an arbitrary fixed coordinate axis, and then expressed in

any desired coordinate axis by using the coordinate transformations introduced in section 2.2.4.

The total velocity vector is separated into components due to 1) freestream velocity, $\mathbf{V}_\infty$, 2) rotor induced inflow, $\mathbf{V}_{v_i}$, and 3) blade flapping, $\mathbf{V}_\beta$:

$$\mathbf{V}_{blade} = \mathbf{V}_\infty + \mathbf{V}_{v_i} - \mathbf{V}_\beta \tag{2.33}$$

The velocity component due to the freestream velocity is given with respect to the body-axis as:

$$\mathbf{V}_\infty = -u\mathbf{i_B} - v\mathbf{j_B} - w\mathbf{k_B} \tag{2.34}$$

Using the transformation matrix from the body-axis to the non-rotating shaft axis:

$$\begin{aligned}\mathbf{V}_\infty &= u\sin i_N\mathbf{i_{NR}} - u\cos i_N\mathbf{k_{NR}} - v\mathbf{j_{NR}} + w\cos i_N\mathbf{i_{NR}} + w\sin i_N\mathbf{k_{NR}} \\ &= \left(u\sin i_N + w\cos i_N\right)\mathbf{i_{NR}} - v\mathbf{j_{NR}} + \left(w\sin i_N - u\cos i_N\right)\mathbf{k_{NR}}\end{aligned} \tag{2.35}$$

The velocity components can now be expressed in the rotating shaft axis using the appropriate transformation matrix:

$$\begin{aligned}\mathbf{V}_\infty = \left(u\sin i_N + w\cos i_N\right)\left(\mathbf{i_R}\cos\psi - \mathbf{j_R}\sin\psi\right) - v\left(\mathbf{j_R}\cos\psi + \mathbf{i_R}\sin\psi\right) \\ + \left(w\sin i_N - u\cos i_N\right)\mathbf{k_R}\end{aligned}$$

or:

$$\begin{aligned}\mathbf{V}_\infty = &\left(u\sin i_N\cos\psi + w\cos i_N\cos\psi - v\sin\psi\right)\mathbf{i_R}\\ &+\left(-u\sin i_N\sin\psi - w\cos i_N\sin\psi - v\cos\psi\right)\mathbf{j_R}\\ &+\left(w\sin i_N - u\cos i_N\right)\mathbf{k_R}\end{aligned} \tag{2.36}$$

A small angle assumption is now applied to the fuselage angle of attack, α_F, and the sideslip angle, β_F, is set to zero:

$$\begin{aligned}u &= V\cos\alpha_F\,\cancel{\cos\beta_F}^{\,1} = V\cos\alpha_F \approx V\\ v &= V\,\cancel{\sin\beta_F}^{\,0} = 0\\ w &= V\sin\alpha_F\,\cancel{\cos\beta_F}^{\,1} = V\sin\alpha_F \approx V\alpha_F\end{aligned} \tag{2.37}$$

Using these expressions for *u*, *v*, and *w*, the freestream velocity component is expressed as:

$$\begin{aligned}\mathbf{V}_\infty = &V\left(\sin i_N\cos\psi + \alpha_F\cos i_N\cos\psi\right)\mathbf{i_R}\\ &+V\left(-\sin i_N\sin\psi - \alpha_F\cos i_N\sin\psi\right)\mathbf{j_R}\\ &+V\left(\alpha_F\sin i_N - \cos i_N\right)\mathbf{k_R}\end{aligned} \tag{2.38}$$

Assuming that the blade flapping is small, the blade velocity component due to the induced inflow (which is defined as positive *upward* through the rotor) is given in the rotating frame as:

$$\mathbf{V}_{v_i} = v_i \mathbf{k}_\mathbf{R} \tag{2.39}$$

Assuming that the center-of-gravity of the aircraft lies on the nacelle axis and that the flapping angle is small, the velocity vector at a point r_p on the blade due to flapping can be written in the rotating frame as (see Ref. 109):

$$\begin{aligned}\mathbf{V}_\beta = &\left(\dot{\theta}_{hub}\cos\psi(R_H + r_p\sin\beta) - r_p\dot{\beta}\sin\beta\right)\mathbf{i}_\mathbf{R} \\ &+\left(\Omega r_p\cos\beta - \dot{\theta}_{hub}\sin\psi(R_H + r_p\sin\beta)\right)\mathbf{j}_\mathbf{R} \\ &+\left(r_p\beta\cos\beta - \dot{\theta}_{hub}r_p\cos\beta\cos\psi\right)\mathbf{k}_\mathbf{R}\end{aligned} \tag{2.40}$$

In the previous equation, the total hub pitch rate, $\dot{\theta}_{hub}$, is the sum of the fuselage pitch rate and the nacelle tilt-rate.

The total velocity vector at a point on the blade in the rotating frame is then:

$$\mathbf{V}_{blade} = \mathbf{V}_{\infty} + \mathbf{V}_{v_i} - \mathbf{V}_{\beta}$$

$$\mathbf{V}_{blade} = \underbrace{\left[V\left(\sin i_N \cos\psi + \alpha_F \cos i_N \cos\psi\right) - \left(\dot{\theta}_{hub} \cos\psi (R_H + r_p \sin\beta) - r_p \dot{\beta} \sin\beta\right)\right]}_{U_x} \mathbf{i_R}$$

$$+ \underbrace{\left[V\left(-\sin i_N \sin\psi - \alpha_F \cos i_N \sin\psi\right) - \left(\Omega r_p \cos\beta - \dot{\theta}_{hub} \sin\psi (R_H + r_p \sin\beta)\right)\right]}_{U_y} \mathbf{j_R}$$

$$+ \underbrace{\left[V\left(\alpha_F \sin i_N - \cos i_N + \frac{v_i}{V}\right) - \left(r_p \dot{\beta} \cos\beta - \dot{\theta}_{hub} r_p \cos\beta \cos\psi\right)\right]}_{U_z} \mathbf{k_R} \tag{2.41}$$

Assuming that the flapping angle is small, the previous result is transformed into the flapped axis system as follows:

$$\mathbf{V}_{blade} = \underbrace{(U_x + \beta U_z)}_{U_R} \mathbf{i_F} + \underbrace{U_y}_{-U_T} \mathbf{j_F} + \underbrace{(U_z - \beta U_x)}_{-U_P} \mathbf{k_F} \tag{2.42}$$

The components of the velocity vector in the flapped axis system are therefore expressed with respect to the blade as radial (U_R), tangential (U_T), and perpendicular (U_P) velocity components. Substituting equation (2.41) into equation (2.42) yields:

$$U_R = V\left(\sin i_N \cos\psi + \alpha_F \cos i_N \cos\psi\right) - \left(\dot{\theta}_{hub} \cos\psi (R_H + r_p \beta) - r_p \dot{\beta} \beta\right)$$
$$+ \left[V\left(\alpha_F \sin i_N - \cos i_N + \frac{v_i}{V}\right) - \left(r_p \dot{\beta} - \dot{\theta}_{hub} r_p \cos\psi\right)\right] \beta \tag{2.43}$$

$$U_T = V\left(\sin i_N \sin\psi + \alpha_F \cos i_N \sin\psi\right) + \left(\Omega r_p - \dot{\theta}_{hub} \sin\psi (R_H + r_p \beta)\right) \tag{2.44}$$

$$U_P = -V\left(\alpha_F \sin i_N - \cos i_N + \frac{v_i}{V}\right) + \left(r_p\dot{\beta} - \dot{\theta}_{hub} r_p \cos\psi\right)$$
$$+\left[V\left(\sin i_N \cos\psi + \alpha_F \cos i_N \cos\psi\right) - \left(\dot{\theta}_{hub}\cos\psi(R_H + r_p\beta) - r_p\dot{\beta}\beta\right)\right]\beta \tag{2.45}$$

The next step in the derivation of the blade element velocities is to apply an ordering scheme to equations (2.43), (2.44), and (2.45) in order to simplify the expression for U_R, U_T, and U_P by eliminating lower order terms. Each term in the equations is assigned an order of magnitude relative to a small quantity ε, that is 10 to 20-percent of the largest term. Terms of order ε^2 or ε^3 are therefore neglected (corresponding to 0.1-percent to 4.0-percent of the largest term).

$$U_R = \underbrace{V\sin i_N \cos\psi}_{O(1)} + \underbrace{V\alpha_F \cos i_N \cos\psi}_{O(\varepsilon)} - \underbrace{\dot{\theta}_{hub}\cos\psi R_H}_{O(\varepsilon)} - \underbrace{\dot{\theta}_{hub}\cos\psi r_p\beta}_{O(\varepsilon)}$$
$$+ \underbrace{r_p\dot{\beta}\beta}_{O(\varepsilon^2)} + \underbrace{V\alpha_F \sin i_N\beta}_{O(\varepsilon^2)} - \underbrace{V\cos i_N\beta}_{O(\varepsilon)} + \underbrace{v_i\beta}_{O(\varepsilon^2)} - \underbrace{r_p\dot{\beta}\beta}_{O(\varepsilon^2)} + \underbrace{\dot{\theta}_{hub} r_p\cos\psi\beta}_{O(\varepsilon^2)} \tag{2.46}$$

$$U_T = \underbrace{V\sin i_N \sin\psi}_{O(1)} + \underbrace{V\alpha_F \cos i_N \sin\psi}_{O(\varepsilon)} + \underbrace{\Omega r_p}_{O(1)} - \underbrace{\dot{\theta}_{hub}\sin\psi R_H}_{O(\varepsilon)} - \underbrace{\dot{\theta}_{hub}\sin\psi r_p\beta}_{O(\varepsilon^2)} \tag{2.47}$$

$$U_P = -\underbrace{V\alpha_F \sin i_N}_{O(\varepsilon)} + \underbrace{V\cos i_N}_{1} - \underbrace{v_i}_{O(\varepsilon)} + \underbrace{r_p\dot{\beta}}_{O(\varepsilon)} - \underbrace{\dot{\theta}_{hub} r_p\cos\psi}_{O(\varepsilon)} + \underbrace{V\sin i_N\cos\psi\beta}_{O(\varepsilon)}$$
$$+ \underbrace{V\alpha_F \cos i_N \cos\psi\beta}_{O(\varepsilon^2)} - \underbrace{\dot{\theta}_{hub}\cos\psi R_H\beta}_{O(\varepsilon^2)} - \underbrace{\dot{\theta}_{hub}\cos\psi r_p\beta^2}_{O(\varepsilon^2)} + \underbrace{r_p\dot{\beta}\beta^2}_{O(\varepsilon^3)} \tag{2.48}$$

The final expressions for U_R, U_T, and U_P are obtained by neglecting the terms that are two orders of magnitude smaller than the largest order term in each of the three previous equations:

$$U_R = V \sin i_N \cos\psi + V\alpha_F \cos i_N \cos\psi - \dot{\theta}_{hub} \cos\psi R_H - \dot{\theta}_{hub} \cos\psi r_p \beta - V \cos i_N \beta \quad (2.49)$$

$$U_T = V \sin i_N \sin\psi + V\alpha_F \cos i_N \sin\psi + \Omega r_p - \dot{\theta}_{hub} \sin\psi R_H \quad (2.50)$$

$$U_P = -V\alpha_F \sin i_N + V \cos i_N - v_i + r_p \dot{\beta} - \dot{\theta}_{hub} r_p \cos\psi + V \sin i_N \cos\psi\beta \quad (2.51)$$

2.5.2 Hub Reactions

In this section, the aerodynamic forces and moments on a blade element are derived in order to obtain hub reactions that can be included in the rigid body equations. Refer to Figure 2.8 below for an illustration of the blade element lift and drag.

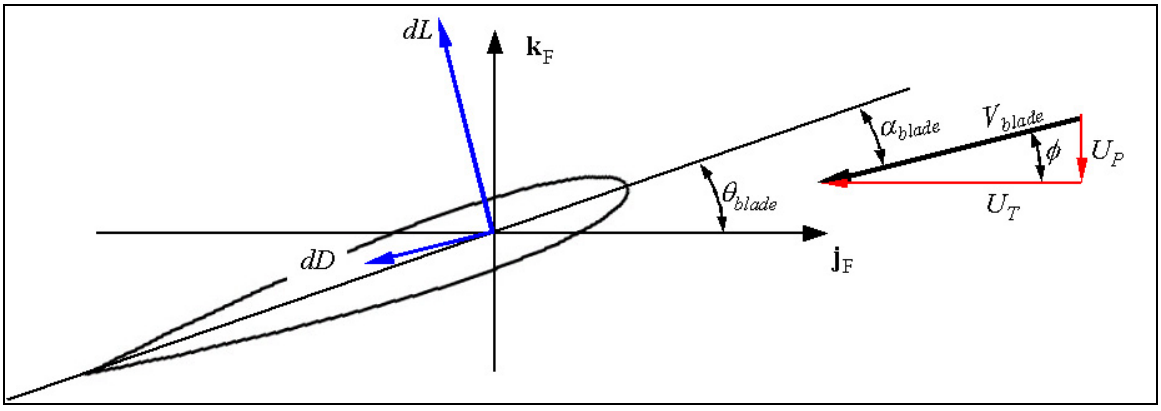

Figure 2.8. Lift and drag of a blade element.

As seen in the above figure, the elemental force components in the $\mathbf{k_F}$ and $\mathbf{j_F}$ directions can be written as a function of the elemental lift and drag and the inflow angle, ϕ.

$$\mathbf{df} = -\left(dL\sin\phi + dD\cos\phi\right)\mathbf{j_F} + \left(dL\cos\phi - dD\sin\phi\right)\mathbf{k_F} \tag{2.52}$$

Assuming that the tangential velocity component is much larger than the perpendicular velocity component (small inflow angle assumption):

$$df_{\mathbf{j_F}} = -\left(dL\sin\phi + dD\cos\phi\right) \approx -dL\phi - dD \approx -dL\frac{U_p}{U_T} - dD \tag{2.53}$$

$$df_{\mathbf{k_F}} = dL\cos\phi - dD\sin\phi \approx dL \tag{2.54}$$

Since the forces are derived in the flapped axis system and the lift and drag forces are assumed to act in the plane of the blade element, there is no component of the force in the blade's radial direction.

Assuming that the blade angle-of-attack is small, the airfoil lift coefficient is assumed to be a linear function of the blade angle-of-attack and the drag coefficient is assumed to be constant. The lift and drag on the blade element are given by:

$$dL = 1/2\,\rho V_{blade}^2 c_\ell c dr \tag{2.55}$$

$$dD = 1/2\,\rho V_{blade}^2 c_{d_o} c dr \tag{2.56}$$

Once again, by invoking the small inflow angle assumption the velocity at the blade can be expressed as:

$$V_{blade}^2 = \left(U_T^2 + U_P^2\right) = U_T^2\left(1+\frac{U_P^2}{U_T^2}\right) = U_T^2\left(1+\frac{O(\varepsilon^2)}{O(1)}\right) \approx U_T^2 \tag{2.57}$$

The lift and drag on a blade element can therefore be written as:

$$dL = 1/2\,\rho U_T^2 c_L c dr = 1/2\,\rho U_T^2\left(a\alpha_{blade}\right) c dr \tag{2.58}$$

$$dD = 1/2\,\rho U_T^2 c_{d_o} c dr = 1/2\,\rho U_T^2 \frac{c_{d_o}}{a} a c dr \tag{2.59}$$

The angle-of-attack at the blade element is small and can be simplified by first expressing it as a Taylor series expansion and then neglecting higher order terms:

$$\alpha_{blade} = \theta_{blade} - \tan^{-1}\frac{U_P}{U_P} = \theta_{blade} - \frac{U_P}{U_P} - \frac{1}{3}\left(\frac{U_P}{U_P}\right)^3 + \ldots \approx \theta_{blade} - \frac{U_P}{U_P} \tag{2.60}$$

The elemental lift can therefore be expressed as:

$$dL = 1/2\,\rho U_T^2 a\left(\theta_{blade} - \frac{U_P}{U_T}\right) c dr = 1/2\,\rho a\left(U_T^2\theta_{blade} - U_P U_T\right) c dr \tag{2.61}$$

The rotor tip speed, ΩR, is now used to non-dimensionalize the velocity components in equations (2.61) and (2.59):

$$dL = 1/2\,\rho a \Omega^2 R^3 c \left[\theta_{blade} \left(\frac{U_T}{\Omega R} \right)^2 - \left(\frac{U_P}{\Omega R} \right) \left(\frac{U_T}{\Omega R} \right) \right] dx \tag{2.62}$$

$$dD = 1/2\,\rho a c U_T^2 \frac{c_{d_o}}{a} \left(\frac{U_T}{\Omega R} \right)^2 dx \tag{2.63}$$

The elemental lift and drag expressions are now substituted in the elemental force equations (2.53) and (2.54):

$$df_{\mathbf{j_F}} = 1/2\,\rho a \Omega^2 R^3 c \left[\left(\frac{U_P}{\Omega R} \right)^2 - \theta_{blade} \left(\frac{U_P}{\Omega R} \right) \left(\frac{U_T}{\Omega R} \right) - \frac{c_{d_o}}{a} \left(\frac{U_T}{\Omega R} \right)^2 \right] dx \tag{2.64}$$

$$df_{\mathbf{k_F}} = 1/2\,\rho a \Omega^2 R^3 c \left[\theta_{blade} \left(\frac{U_T}{\Omega R} \right)^2 - \left(\frac{U_P}{\Omega R} \right) \left(\frac{U_T}{\Omega R} \right) \right] dx \tag{2.65}$$

The elemental force components are now integrated over the span of the blade:

$$dF_{\mathbf{j_F}} = \int_0^1 df_{\mathbf{j_F}} \quad , \quad dF_{\mathbf{k_F}} = \int_0^1 df_{\mathbf{k_F}} \tag{2.66}$$

The individual blade forces are expressed in the body axis by X_R, Y_R, and Z_R:

$$\begin{aligned} d\mathbf{F} &= dF_{\mathbf{j_F}}\,\mathbf{j_F} + dF_{\mathbf{i_F}}\mathbf{k_F} \\ &= dX_{rotor}\mathbf{i_B} + dY_{rotor}\mathbf{j_B} + dZ_{rotor}\mathbf{k_B} \end{aligned} \tag{2.67}$$

Using the flapped-axis to body axis transformation matrix from section 2.2.4, the forces are transformed to the body-axis system:

$$\begin{aligned} d\mathbf{F} = {} & dF_{\mathbf{j_F}}\left[\left(\sin\psi\sin i_N\right)\mathbf{i_B} + \cos\psi\,\mathbf{j_B} + \left(\sin\psi\cos i_N\right)\mathbf{k_B}\right] \\ & + dF_{\mathbf{k_F}}\left[\left(\beta\cos\psi\sin i_N + \cos i_N\right)\mathbf{i_B} - \beta\sin\psi\,\mathbf{j_B} + \left(\beta\cos\psi\cos i_N - \sin i_N\right)\mathbf{k_B}\right] \end{aligned} \tag{2.68}$$

Therefore, the individual blade forces in body-axis system are:

$$dX_{rotor} = dF_{\mathbf{j_F}}\left(\sin\psi\sin i_N\right) + dF_{\mathbf{k_F}}\left(\beta\cos\psi\sin i_N + \cos i_N\right) \tag{2.69}$$

$$dY_{rotor} = dF_{\mathbf{j_F}}\left(\cos\psi\right) - dF_{\mathbf{k_F}}\left(\beta\sin\psi\right) \tag{2.70}$$

$$dZ_{rotor} = dF_{\mathbf{j_F}}\left(\sin\psi\cos i_N\right) + dF_{\mathbf{k_F}}\left(\beta\cos\psi\cos i_N - \sin i_N\right) \tag{2.71}$$

The blade forces integrated over the azimuth in body-axis give the individual rotor forces (where N_b is the number of blades):

$$X_{rotor} = \frac{N_b}{2\pi}\int_0^{2\pi} dX_{rotor} \tag{2.72}$$

$$Y_{rotor} = \frac{N_b}{2\pi}\int_0^{2\pi} dY_{rotor} \tag{2.73}$$

$$Z_{rotor} = \frac{N_b}{2\pi} \int_0^{2\pi} dZ_{rotor} \tag{2.74}$$

If desired, the rotor forces can be expressed in the tip-path-plane axis to obtain the rotor thrust coefficient and H-force coefficient:

$$C_T = \frac{1}{\rho A(\Omega R)^2}\left[X_R \cos(i_N - \beta_{1c}) - Z_R \sin(i_N - \beta_{1c}) \right] \tag{2.75}$$

$$C_H = \frac{1}{\rho A(\Omega R)^2}\left[-X_R \sin(i_N - \beta_{1c}) - Z_R \cos(i_N - \beta_{1c}) \right] \tag{2.76}$$

Note that since the rotor is gimbaled (the three-bladed equivalent of a teetering rotor), there is no moment directly transmitted to the hub. However, a tiltrotor usually has some flapping restraint that introduces a spring stiffness in the rotor system. This stiffness is modeled herein by a rotor pitching moment proportional to the amount of longitudinal flapping:

$$M_{rotor} = K\beta_{1c} \tag{2.77}$$

2.5.3 Rotor Coning and Longitudinal Flapping

The rotor of a tiltrotor is typically gimbaled. A gimbaled rotor behaves like an articulated rotor with no hinge offset for the flapping modes and as a hingeless rotor with high

stiffness for the coning mode. From Ref. 109, the flapping equation of motion for a gimbaled rotor with a pitching hub is as follows:

$$\frac{\ddot{\beta}}{\Omega^2}+\nu_\beta^2\beta=\frac{k_\beta}{\Omega^2 I_b}\beta_p+\frac{M_A}{\Omega^2 I_b}-2\frac{\dot{\theta}_{hub}}{\Omega}\sin\psi+\frac{\ddot{\theta}_{hub}}{\Omega^2}\cos\psi+\left(\frac{\dot{\theta}_{hub}}{\Omega}\right)^2 I_H \tag{2.78}$$

The previous equation is solved for the coning and longitudinal flapping by assuming a periodic solution of the form:

$$\begin{aligned}\beta(\psi)&=\beta_0+\beta_{1c}\cos\psi+\cancelto{0}{\beta_{1s}}\sin\psi\\ \dot{\beta}(\psi)&=-\Omega\beta_{1c}\sin\psi\\ \ddot{\beta}(\psi)&=-\Omega^2\beta_{1c}\cos\psi\end{aligned} \tag{2.79}$$

The blade pitch is also assumed to be periodic:

$$\theta_{blade}(\psi)=\theta_0+\theta_{1c}\cos\psi+\theta_{1s}\sin\psi+\theta_{TW}x-\tan\delta_3\beta \tag{2.80}$$

Because the coning and flapping motions are not periodic during a maneuver, solving equation (2.78) by assuming a periodic solution is not rigorously valid. However, for the slow maneuvers considered in this research, this assumption is suitable (Refs. 103 & 109). Equation (2.78) is solved by a harmonic balance method that equates the constant, sin ψ, and cos ψ terms on each side of the equation. The effects of the higher harmonic terms on the performance of the vehicle are negligible and therefore the second harmonic

term and higher harmonic terms are neglected. Note that even though a flapping spring is present on the XV-15 it is of very low stiffness (225 ft-lb/deg.). The flapping frequency is therefore approximately 1/rev., so that $\nu_\beta^2 \approx 1$. However, the separate hub spring, which adds coning stiffness, is not of low stiffness. From equations (2.78) and (2.79):

Constant Term:

$$\beta_0 = \frac{k_\beta}{\Omega^2 I_b}\beta_p + \frac{M_{A_{const}}}{\Omega^2 I_b} + \left(\frac{\dot{\theta}_{hub}}{\Omega}\right)^2 I_H \tag{2.81}$$

Sine Term:

$$\beta_{1s}\cancelto{0}{\left(\nu_\beta^2 - 1\right)} = 0 = \frac{M_{A_{\sin}}}{\Omega^2 I_b} - 2\frac{\dot{\theta}_{hub}}{\Omega} \tag{2.82}$$

Cosine term:

$$\beta_{1c}\cancelto{0}{\left(\nu_\beta^2 - 1\right)} = 0 = \frac{M_{A_{\cos}}}{\Omega^2 I_b} + \frac{\ddot{\theta}_{hub}}{\Omega^2} \tag{2.83}$$

In order to solve these three equations for the blade coning and longitudinal flapping, an expression for the aerodynamic moment, M_A, must be developed. The elemental blade aerodynamic moment about the rotor hub is depicted in Figure 2.9 below.

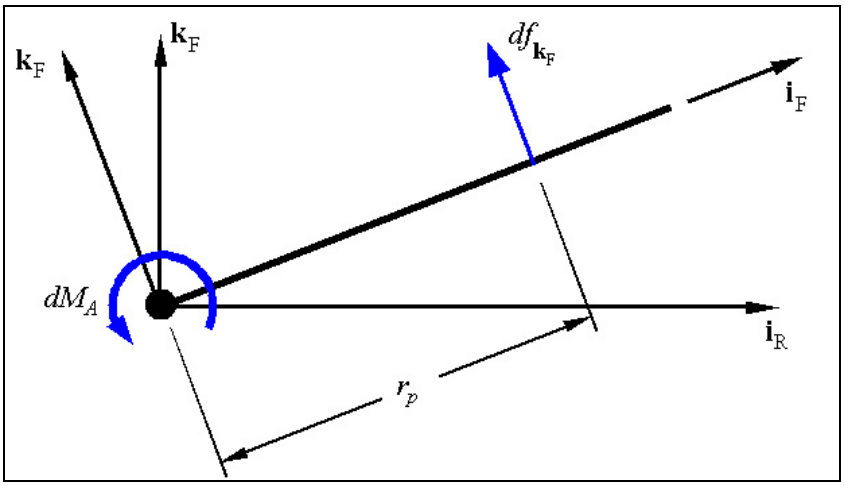

Figure 2.9. Aerodynamic moment of a blade element.

Using the previous figure, the elemental aerodynamic moment about the hub due to a force at a point *p* on the blade is given by:

$$\begin{aligned} dM_A &= r_p df_{\mathbf{k_F}} = r_p dL = 1/2\,\rho a\left(U_T^2\theta_{blade} - U_P U_T\right) c r_p dr \\ &= 1/2\,\rho a\Omega^2 R^4 c\left[\theta_{blade}\left(\frac{U_T}{\Omega R}\right)^2 - \left(\frac{U_P}{\Omega R}\right)\left(\frac{U_T}{\Omega R}\right)\right] x dx \end{aligned} \tag{2.84}$$

Using the value of the lock number, $\gamma = \dfrac{\rho a c R^4}{I_b}$:

$$dM_A = \frac{\gamma}{2}\Omega^2 I_b\left[\theta_{blade}\left(\frac{U_T}{\Omega R}\right)^2 - \left(\frac{U_P}{\Omega R}\right)\left(\frac{U_T}{\Omega R}\right)\right] x dx \tag{2.85}$$

The total aerodynamic moment on a blade is then simply:

$$M_A = \int_0^1 dM_A \tag{2.86}$$

After substitution of the blade velocities, integration over the blade span, and cancellation of higher-order terms, the aerodynamic moment can be split into constant, sine, and cosine components. The cosine component contains lateral flapping terms but no longitudinal flapping terms. It is therefore not reproduced here.

$$\begin{aligned} M_{A_{const}} = \frac{\gamma}{2}\Bigg(& -\frac{1}{4}\tan\delta_3\beta_0 + \frac{1}{6}\theta_{TW}\mu^2\sin^2 i_N + \frac{1}{4}\theta_0\mu^2\sin^2 i_N \\ & + \frac{1}{5}\theta_{TW} + \frac{1}{4}\theta_0 + \frac{1}{2}\theta_0\alpha_F\sin i_N\cos i_N + \frac{1}{3}\theta_{1s}\mu\sin i_N + \frac{1}{3}\lambda_0 \\ & + \frac{1}{3}\theta_{TW}\mu^2\alpha_F\sin i_N\cos i_N + \frac{1}{3}\theta_{1s}\mu\alpha_F\cos i_N + \frac{1}{3}\mu\alpha_F\sin i_N \\ & - \frac{1}{3}\mu\cos i_N \Bigg) \end{aligned} \tag{2.87}$$

$$\begin{aligned} M_{A_{\sin}} = \frac{\gamma}{2}\Bigg(& \frac{3}{8}\mu^2\theta_{1s}\sin^2 i_N + \frac{2}{3}\theta_0\mu\sin i_N + \frac{1}{2}\theta_{TW}\mu\sin i_N \\ & + \frac{1}{2}\lambda_0\mu\sin i_N + \frac{2}{3}\theta_0\mu\alpha_F\cos i_N + \frac{1}{2}\theta_{TW}\mu\alpha_F\cos i_N \\ & - \frac{2}{3}\tan\delta_3\beta_0\mu\sin i_N + \frac{1}{2}\mu^2\alpha_F\sin^2 i_N + \frac{1}{4}\beta_{1c} + \frac{1}{4}\theta_{1s} \\ & - \frac{1}{2}\mu^2\cos i_N\sin i_N - \frac{1}{2}\mu^2\alpha_F\cos i_N \Bigg) \end{aligned} \tag{2.88}$$

Equations (2.87) and (2.88) can now be solved simultaneously for the rotor coning and longitudinal flapping.

2.5.4 Induced Inflow Modeling

The induced rotor inflow is obtained using the Beddoes inflow model (Ref. 110):

$$\lambda_i = \lambda_0 \left(1 + E \cos\psi \frac{r}{R} - E \left| \left(\sin\psi \frac{r}{R} \right)^3 \right| \right) \tag{2.89}$$

The constant E is equal to $\chi/2$ as suggested by Leishman (Ref. 111), as opposed to $E = \chi$ as originally suggested by Beddoes in Ref. 110. The uniform inflow value is obtained from the momentum theory approximation:

$$\lambda_0 = -\frac{C_T}{2\sqrt{\mu_x^2 + \lambda_i^2}} \tag{2.90}$$

The wake skew angle, χ, is given by:

$$\chi = \tan^{-1}\left(\frac{\mu_z}{\mu_x + \lambda_i} \right) \tag{2.91}$$

By assuming a small fuselage pitch rate and nacelle tilt-rate, the total inflow in the tip-path-plane axis is written as (where the inflow is positive upward through the rotor):

$$\lambda = -\frac{V}{\Omega R}\sin\alpha_{TPP} + \lambda_i \tag{2.92}$$

In Chapter 5, an average rotor inflow value, $\overline{\lambda}$, is introduced, corresponding to an average inflow over the rotor advancing side and outboard 40-percent of the blades. The usefulness of this parameter will be discussed in Chapter 5.

2.6 Summary of Equations

The previous sections presented the equations used to characterize the quasi-static longitudinal performance of a tiltrotor. It is now useful to summarize these equations as well as the unknowns that comprise the complete performance model.

Equations:

- Rigid Body Equations
    1) X-Force equilibrium, equation (2.9)
    2) Z-Force equilibrium, equation (2.10)
    3) Pitching moment equilibrium, equation (2.11)
- Rotor Equations
    4) Rotor longitudinal flapping, equation (2.81)
    5) Rotor coning, equation (2.82)
    6) Rotor inflow, equation (2.92)

Unknowns:

- Trajectory Parameters

1) Airspeed, $V(t)$

2) Flight path angle, $\gamma(t)$

3) Fuselage pitch, $\theta(t)$

- Aircraft Configuration Parameters

4) Nacelle tilt, $i_N(t)$

5) Wing flap deflection, $\delta_f(t)$

- Rotor Parameters

6) Rotor longitudinal flapping, $\beta_{1c}(t)$

7) Rotor coning, $\beta_0(t)$

8) Rotor induced inflow, $\lambda_i(t)$

- Pilot Controls

9) Rotor collective, $\theta_0(t)$

10) Rotor longitudinal cyclic, $\theta_{1s}(t)$

Note that the elevator deflection is not an unknown since it is "rigged" to the cyclic pitch control to produce two degrees of deflection for each degree of cyclic pitch. In this analysis, it is assumed that the rigging constant remains unchanged with nacelle tilt, i.e. there is no "phase-out" of the cyclic control as the aircraft converts to airplane mode. Since the minimum upward nacelle tilt considered in this paper is 60°, this assumption is valid. This rigging between longitudinal cyclic and elevator deflection further couples the moment equation and the force equations.

The system is therefore comprised of six equations and ten unknowns – clearly an under-determined system. In order to solve this system, four *control variables* must be prescribed thus leaving six equations and six unknowns. Many different combinations of these controls can solve exactly the system of equations. This characteristic of tiltrotors is referred to as "non-unique performance" or more commonly, "non-unique trim." Moreover, the parameters that allow the aircraft to achieve a non-unique trim are termed "non-unique controls." It is because of the non-uniqueness of its performance-states that the tiltrotor has long been regarded as having greater potential for noise reduction through flight trajectory management than a conventional helicopter. Indeed, the various non-unique controls can possibly be used to change from a "noisy" condition to a "quieter" one without a significant change in the flight trajectory. In order to avoid confusion, it must be pointed out that the term "non-unique controls" refers to mathematical controls that dictate the behavior of the force and moment balance, and not piloting controls such as cyclic and collective. The task of determining which four unknowns to prescribe requires careful consideration and will be discussed in a subsequent section.

2.7 Validation of the Performance Model

The following figures show the correlation between the fuselage pitch predicted by the performance model and the fuselage pitch obtained during the 1995 flight test (Ref. 33). The correlation is presented for flight path angles of 0°, -3°, -6°, -9°, and -12° and various nacelle tilts. In order to obtain these results the airspeed, flight path angle, nacelle tilt,

and flap deflection are prescribed to match the flight test values whereas the fuselage pitch, longitudinal flapping, coning, induced inflow, collective and cyclic are solved for simultaneously by the system. Fuselage pitch results are presented because for a given airspeed, flight path angle, nacelle tilt, and flap deflection, the pitch is the performance parameter that has the strongest effect on the rotor operating condition. This is because the fuselage pitch (along with the flight path angle) determines the airframe angle-of-attack, which in turn determines the airframe lift, drag, and moment coefficient. To ensure an adequate comparison, the flight test data points shown on the graphs were carefully selected: the points shown have very small unsteadiness and a maximum of one degree of roll or yaw.

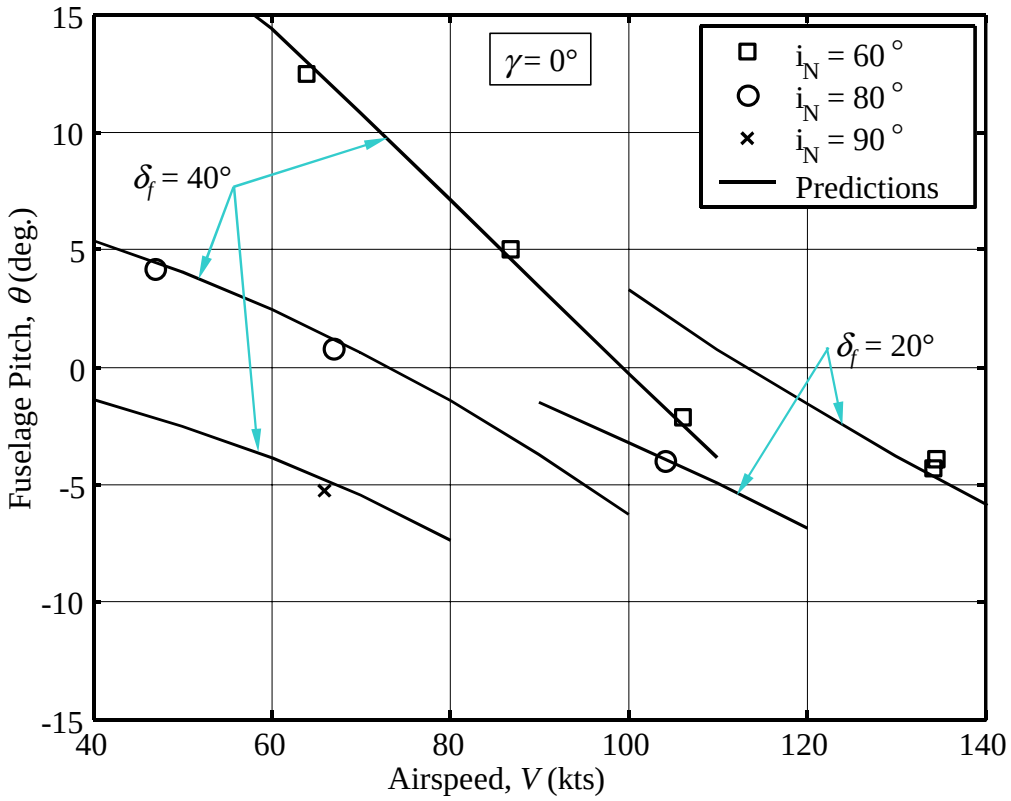

Figure 2.10. Fuselage pitch validation for level flight.

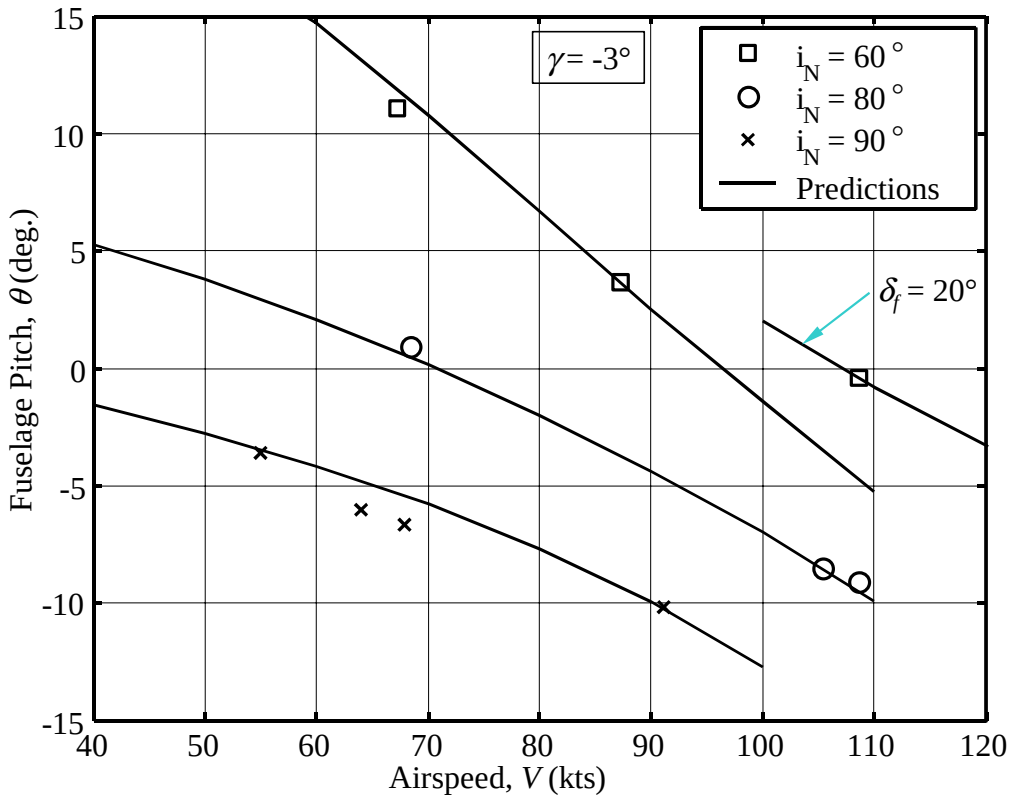

Figure 2.11. Fuselage pitch validation for 3° descent.

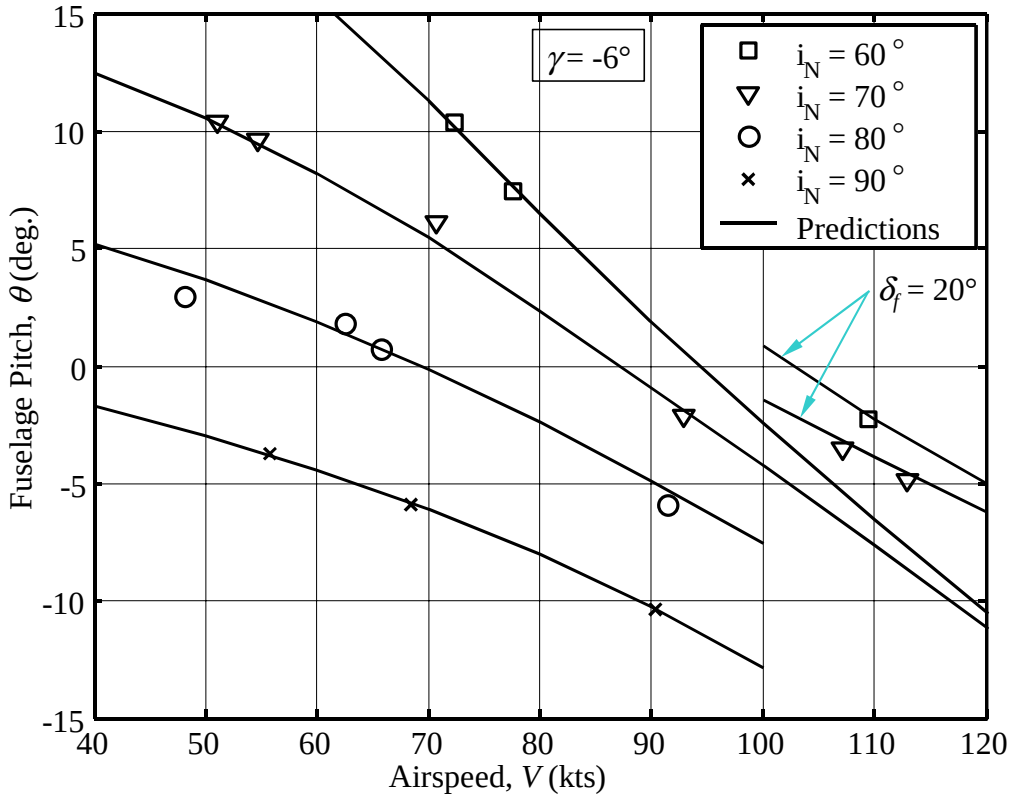

Figure 2.12. Fuselage pitch validation for 6° descent.

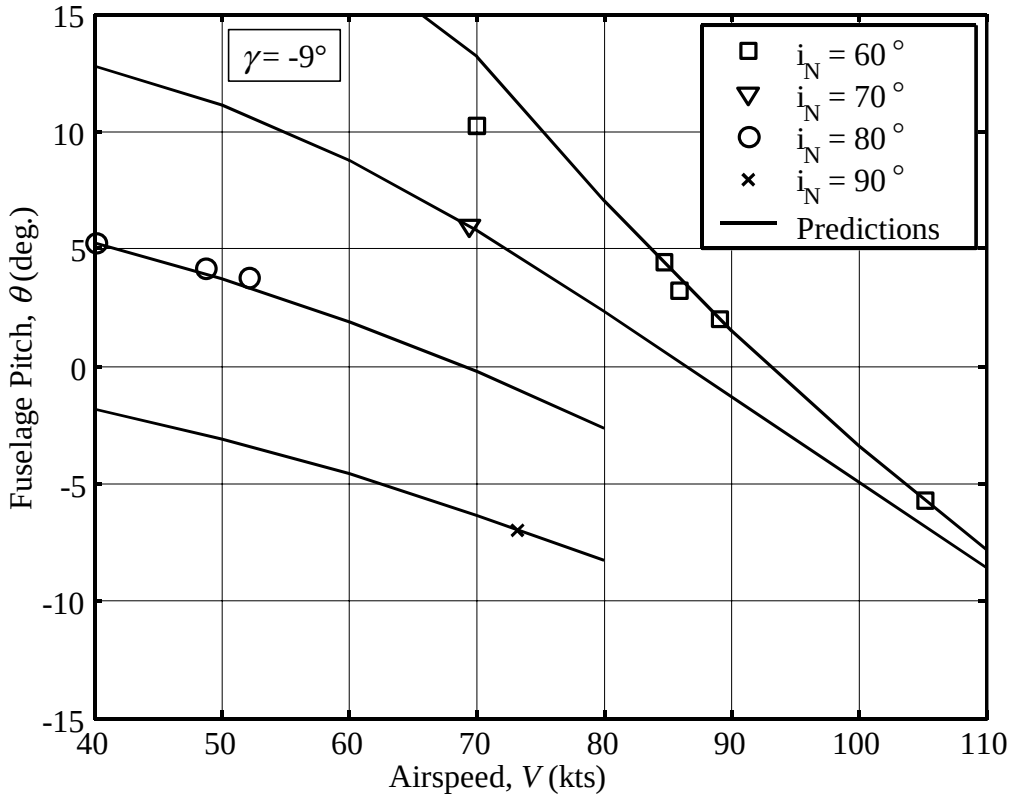

Figure 2.13. Fuselage pitch validation for 9° descent.

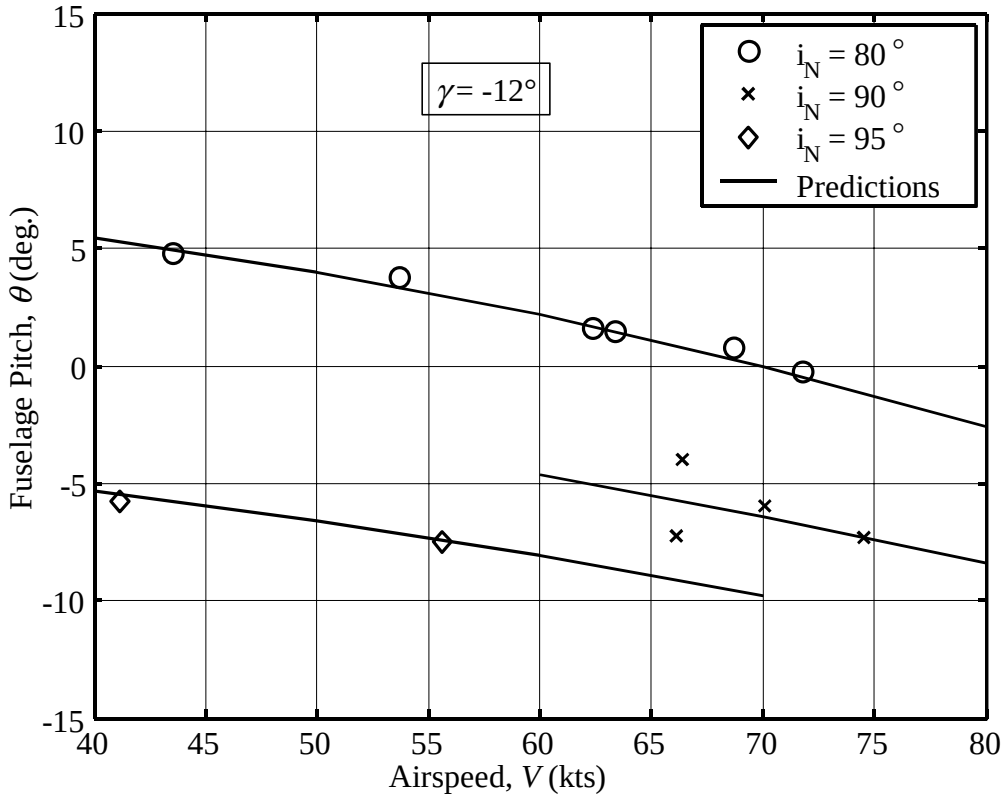

Figure 2.14. Fuselage pitch validation for 12° descent.

The previous figures show that the performance model provides a good estimate of the fuselage pitch especially for the level flight case and the shallower descent angles cases. There are two main factors contributing to the difficulty of correlating steep descent cases. First, the flight test data shows that the pilot has more difficulty holding the flight profile fixed for steeper descents. This yielded approaches that were highly unsteady, at times with large excursions from the desired flight profile. Figure 2.15 shows an example of such an approach by presenting the airspeed, fuselage pitch, longitudinal stick position, and collective stick position as a function of overhead time for a steep helicopter mode approach. Large excursions in airspeed and fuselage pitch can be seen on the figure.

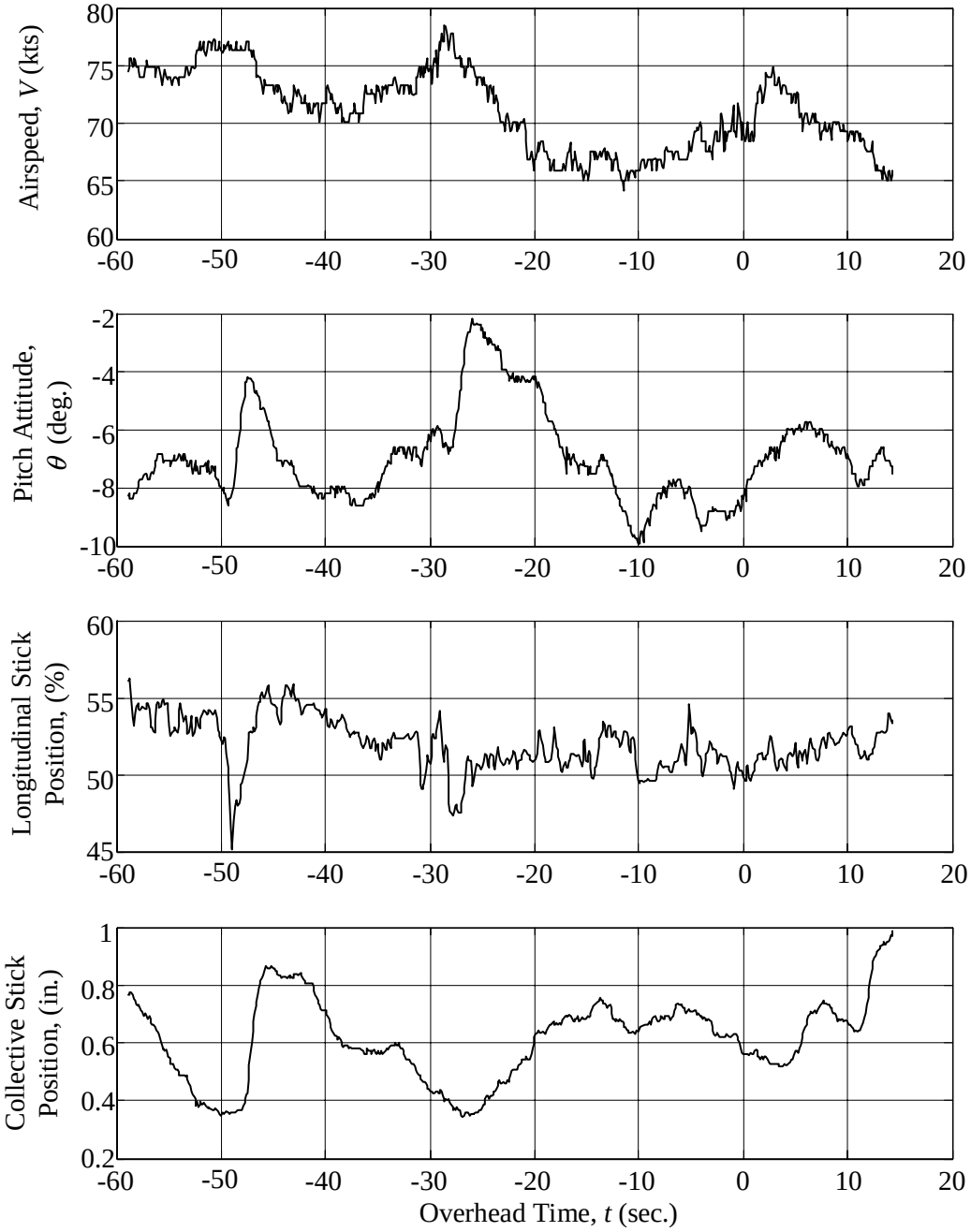

Figure 2.15. Flight test data for steep 12° descent.

The second cause of the higher correlation error at steeper descent angles is due to the aerodynamic modeling used in the performance model (mostly the drag modeling).

Larger descent angles indeed cause higher angles-of-attack and often leading the aircraft to operate close to wing stall. The wind tunnel results used to model the aerodynamics of the XV-15 contained minimal data in the higher angle-of-attack range. A simple extrapolation technique was used to model the stall and near-stall characteristics of the aircraft but in a real flight many factors introduce uncertainty in this regime of flight, such as the effects of the nacelle tilt angle.

2.8 Solution Methodologies and Baseline Approach

This section presents a discussion of the different strategies that can be used to solve the system of equations representing the performance of the tiltrotor (i.e., which unknowns to prescribe and which unknowns to solve for). Each simulation presented in this section is started in steady-state flight, at a 6° descent angle and 60° nacelle tilt angle. The wing flaps are deflected at 40° throughout the simulation. The maneuver begins after ten seconds of steady-state flight when the nacelles are tilted up towards helicopter mode at a constant 1.5 deg./sec. nacelle tilt-rate. The upward tilt of the nacelles is stopped when helicopter mode is reached (i_N = 90°) and the simulation is run for a total of eighty seconds. With the nacelle tilt schedule and flap deflection being prescribed, the system of equations summarized in section 2.6 reduces to six equations and eight unknowns. Two additional unknowns must therefore be prescribed in order to solve the system. The time-histories of the performance variables resulting from various choices of prescribed parameters are presented below.

2.8.1 Prescribed Collective and Cyclic (Stick-Fixed) Conversion

A first method of solution is to "fly" the performance model *stick-fixed* during the conversion to helicopter mode, i.e. keeping the rotor collective and cyclic controls fixed while specifying the nacelle tilt schedule. However, this is not a viable solution because as the nacelles rotate up, the aircraft tends to "rise" and stray from the intended flight path, which causes the fuselage pitch angle to increase in order to maintain an adequate angle-of-attack. This unstable motion is sometimes known as "ballooning" and is well known to tiltrotor pilots, who use longitudinal cyclic inputs to keep the aircraft nose level and collective inputs to maintain the desired flight path angle (Ref. 112). Figure 2.16 shows the resulting time-histories of a stick-fixed conversion to helicopter mode. The unstable motion can clearly be seen from the oscillating nature of the various performance parameters. In fact, it seems that the conversion has excited the long period (or *phugoid*) mode of the aircraft. Indeed, the fuselage angle-of-attack remains fairly constant, and the oscillations represent an exchange of potential and kinetic energy. Note that the extremely high flight path angle and fuselage pitch amplitudes violate many small angle assumptions and aerodynamic modeling assumptions built into the performance model. Clearly, holding the collective and cyclic sticks fixed during a conversion to helicopter mode is not a valid method of solution.

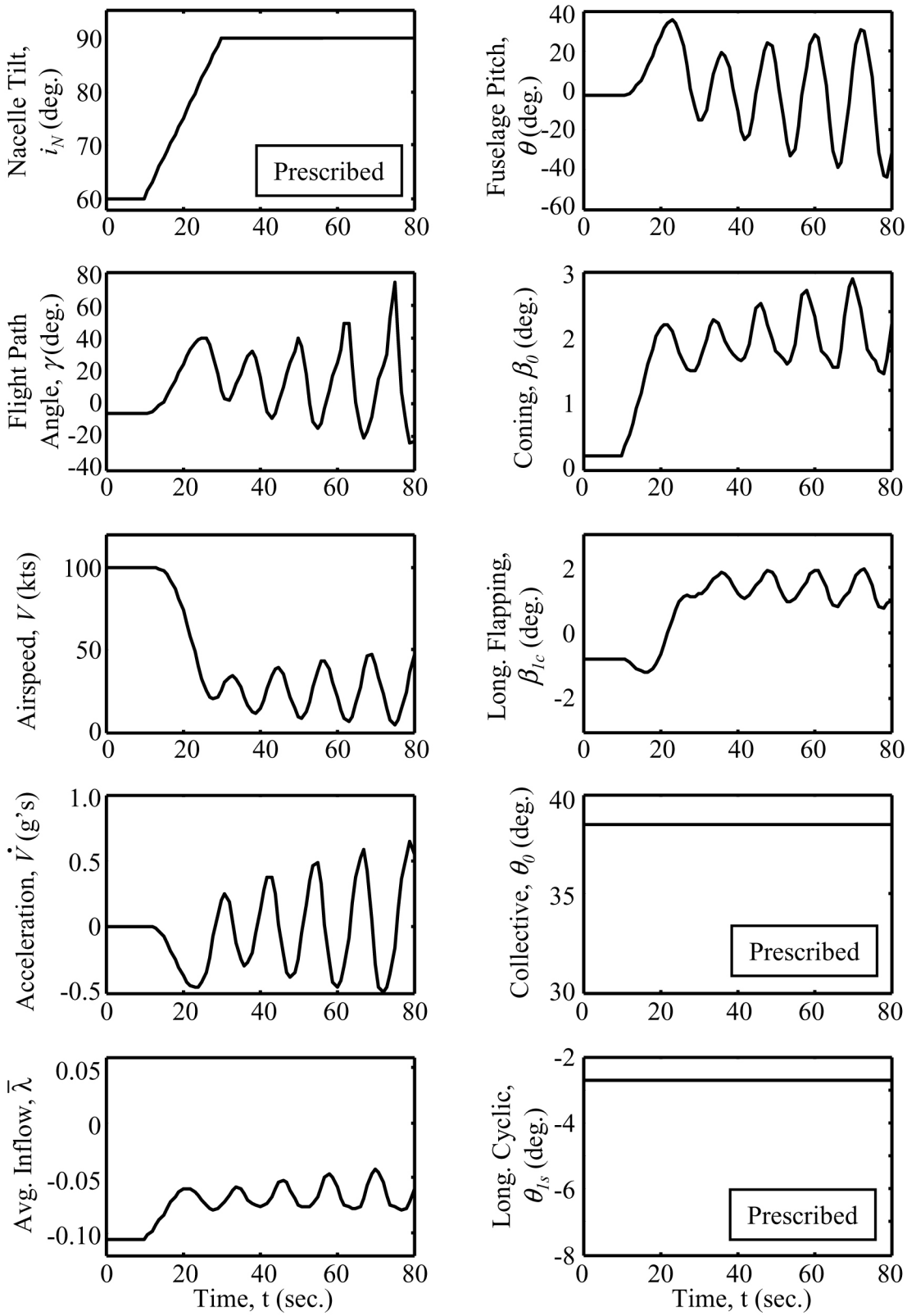

Figure 2.16. Conversion while holding collective and cyclic fixed.

2.8.2 Prescribed Collective and Flight Path Angle Conversion

A second method of solution consists of fixing the flight path angle and the rotor collective and using the longitudinal stick to push the nose of the aircraft down during conversion. This is a valid approach, since pitching the fuselage down as the nacelles tilt up allows to aircraft to maintain a constant flight path angle. However, Figure 2.17 shows that this method can lead to unacceptable pitch attitudes, as low as 16° nose down. Also note that performing the conversion in this manner actually causes the aircraft to accelerate and reach a final steady-state solution at approximately 110 knots. Obviously, this is not a desirable feature of an approach-to-land procedure.

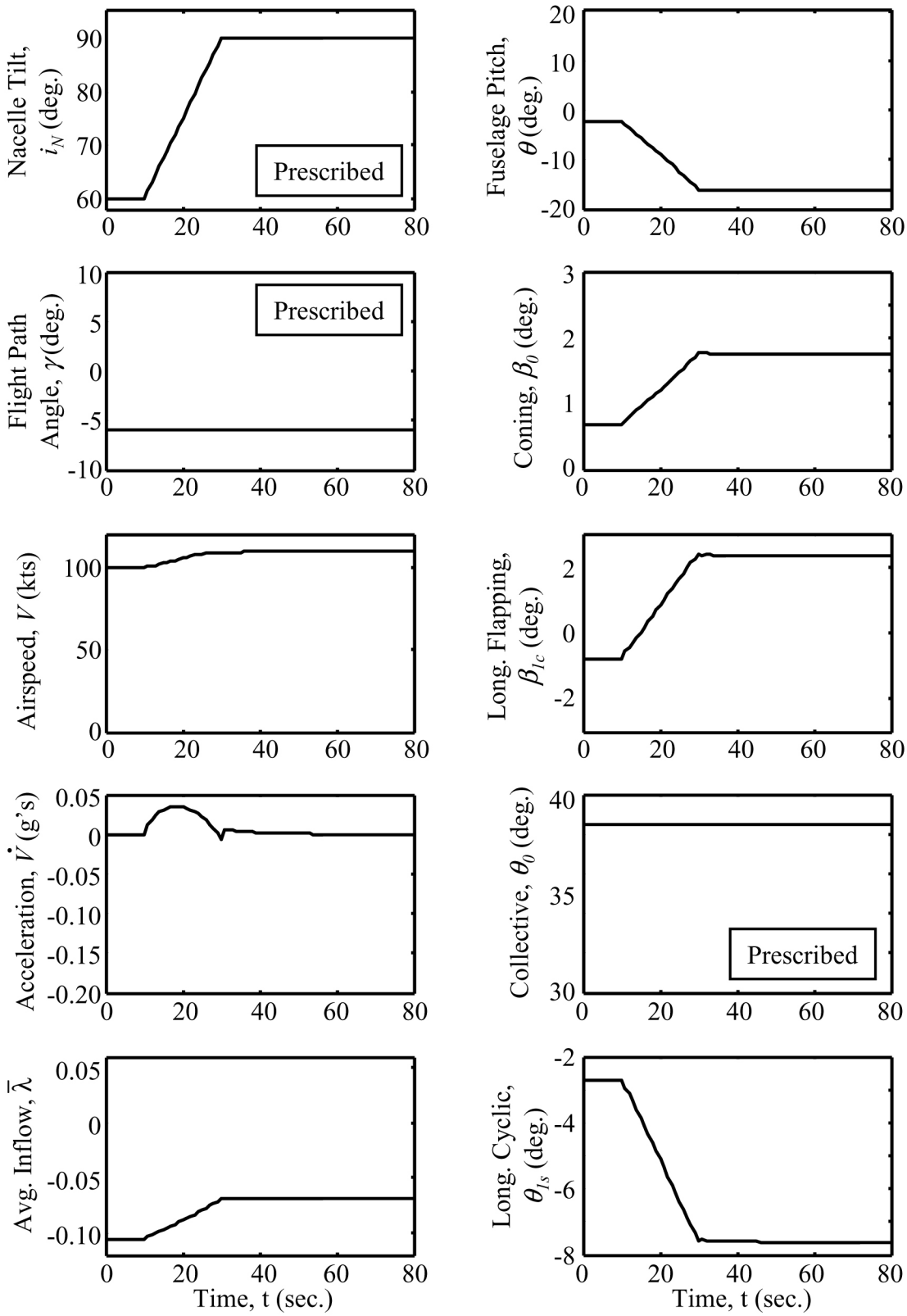

Figure 2.17. Conversion while holding collective and flight path angle fixed.

2.8.3 Prescribed Collective and Fuselage Pitch Conversion

Yet another method of solution is to hold the fuselage pitch and the rotor collective fixed during the conversion. In this approach, the pilot uses only the longitudinal stick to hold the initial fuselage pitch constant. However, this leads to a large increase in flight path angle, coming to a steady-state solution at a 10° climb angle (see Figure 2.18). This shows that the pilot must use collective control in addition to cyclic control in order to fly through the nacelle tilt conversion.

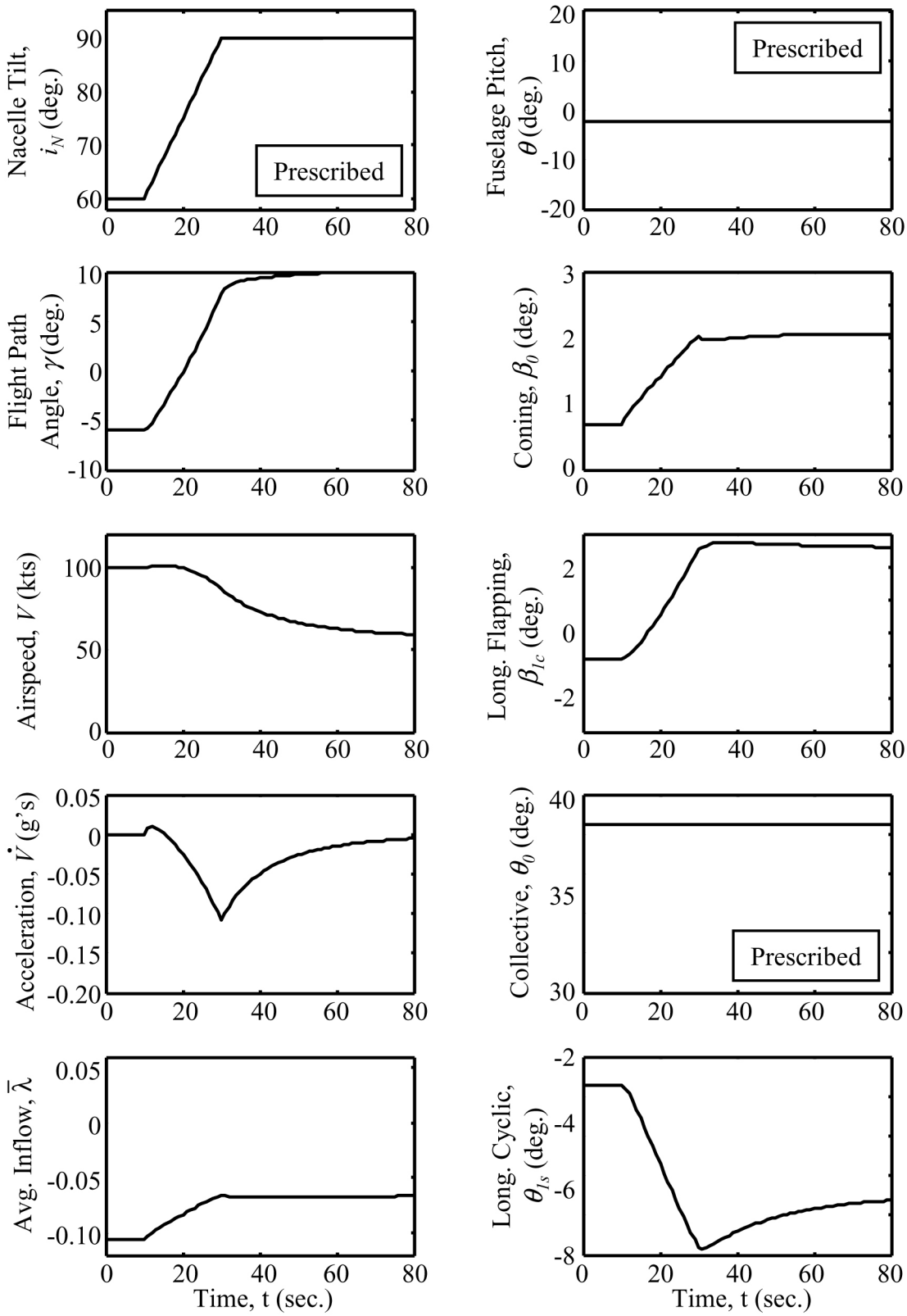

Figure 2.18. Conversion while holding collective and fuselage pitch fixed.

2.8.4 Prescribed Flight Path Angle and Fuselage Pitch: Baseline Approach

The previous sections illustrated the fact that the pilot must control the collective and cyclic sticks throughout a conversion from 60° nacelle tilt to 90° nacelle tilt. Thus, the most plausible method of "flying" the performance model is to prescribe the flight path angle and the fuselage pitch during the conversion to helicopter mode. This solution method is therefore used in this analysis and referred to as the *baseline approach*. Of course, during a real conversion, the actual method of flying the aircraft is not as straightforward, and involves a combination of stick inputs and excursions in pitch and flight path angle. This research assumes that a flight control system is able to perfectly hold the fuselage pitch and flight path angle constant. The baseline approach starts in conversion mode (i_N = 60°), at an airspeed of 100 knots along a 6° descent with the flaps down 40°. The initial fuselage pitch is obtained by solving the system for a steady-state solution with the initial conditions as mentioned above. The conversion to helicopter mode is started at a nacelle tilt-rate of 1.5 deg./sec after ten seconds of steady-state flight in the initial configuration. The nacelles are stopped when the aircraft reaches helicopter mode (i_N = 90°). The fuselage pitch and the flap deflection are held constant throughout the approach. With four prescribed parameters (fuselage pitch, flight path angle, flap deflection and nacelle tilt), the remaining six unknowns are: airspeed, longitudinal cyclic, collective, longitudinal flapping, coning, and rotor inflow. The following figure shows the resulting time-histories of the performance parameters for the baseline approach.

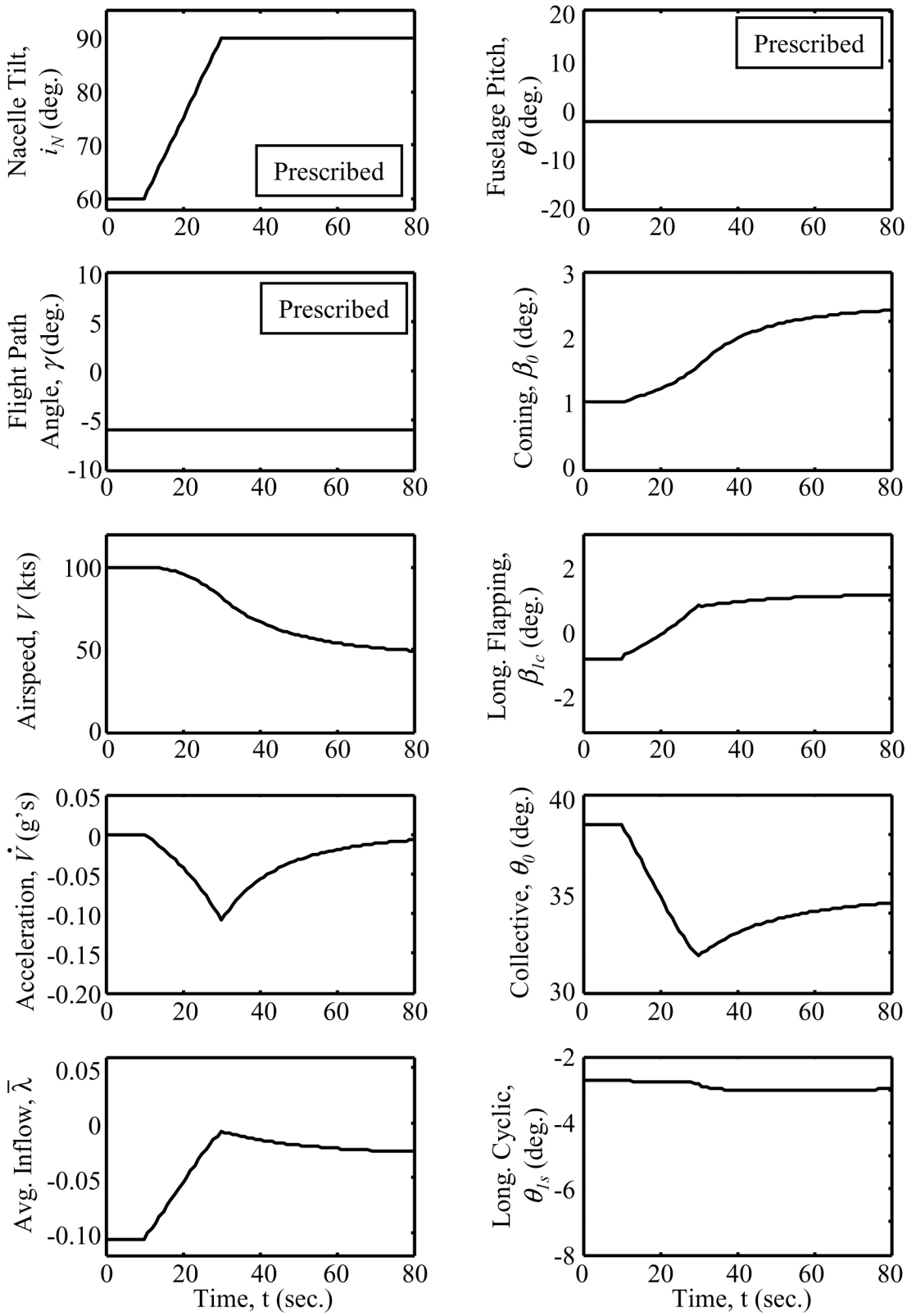

Figure 2.19. Baseline approach.

Figure 2.19 shows that for the baseline converting approach, the resulting airspeed profile is fairly acceptable, but it leads to a large maximum deceleration of 0.10 g's (0.05 g's is usually considered a limit for commercial flight operations). The maximum deceleration is experienced as the helicopter reaches helicopter mode and the nacelle tilt-rate is set to zero. The deceleration is the main consequence of converting to helicopter mode: the rotor thrust used for forward propulsion at 60° nacelle tilt is now redirected upwards at 90° nacelle tilt. In order to maintain the force equilibrium, the aircraft must slow down to decrease the lift on the airframe.

The fuselage pitch is maintained at approximately -2.5°, which is acceptable in terms of pilot and passenger comfort level. The longitudinal cyclic, collective pitch, rotor longitudinal flapping and rotor coning are also all within typical limits. However, often during this flight profile the value of the average inflow is close to zero, indicating that for this baseline approach the rotor wake is in close proximity to the rotor itself and could cause high BVI noise. The relation between this average inflow and the level of BVI noise will be discussed extensively in Chapter 5.

Chapter 3

XV-15 Acoustic Flight Test Data

This chapter describes the XV-15 acoustic flight test conducted in 1995 (Ref. 33). The results from the this test are used to model the aircraft's acoustic characteristics in the following chapters. The flight test was the first in a series of three conducted to define the XV-15's acoustic characteristics during an approach as well as to design low-noise approach profiles. The 1995 flight test consisted of two phases. The main goal of Phase I was to obtain a steady-state mapping of the ground acoustics with respect to variations in airspeed, nacelle tilt, and flight path angle. To achieve this goal, the aircraft was flown over a linear array of microphones at a given nacelle tilt, while the pilot attempted to maintain a constant airspeed and descent angle. On the other hand, the second phase sought to establish preliminary low-noise approach guidelines and used the same microphones but repositioned in a two-dimensional array. Since only results from the first phase are used in this research, all references made to "flight test results" refer to Phase I of the 1995 test.

As explained in the next two sections, the performance data and the acoustic data (already processed and presented in the form of "noise hemispheres") were provided separately. One of the main difficulties in analyzing and interpreting the data is the need to connect each noise level on a hemisphere with the performance-state of the aircraft at the time of the acoustic emission. This involves solving the retarded time equation for each given hemisphere location.

3.1 Details of Flight Test

The flight test was performed in Waxahachie, Texas during the months of October and November in 1995. The terrain at the test site was flat, nearly treeless, and covered with short grass. Seventeen ground microphones were arranged in a linear array perpendicular to the flight track, which ran east to west and was approximately 10,000 feet in length. Three additional microphones were positioned along the flight track at certification locations. Figure 3.1 shows the microphone locations at the test site.

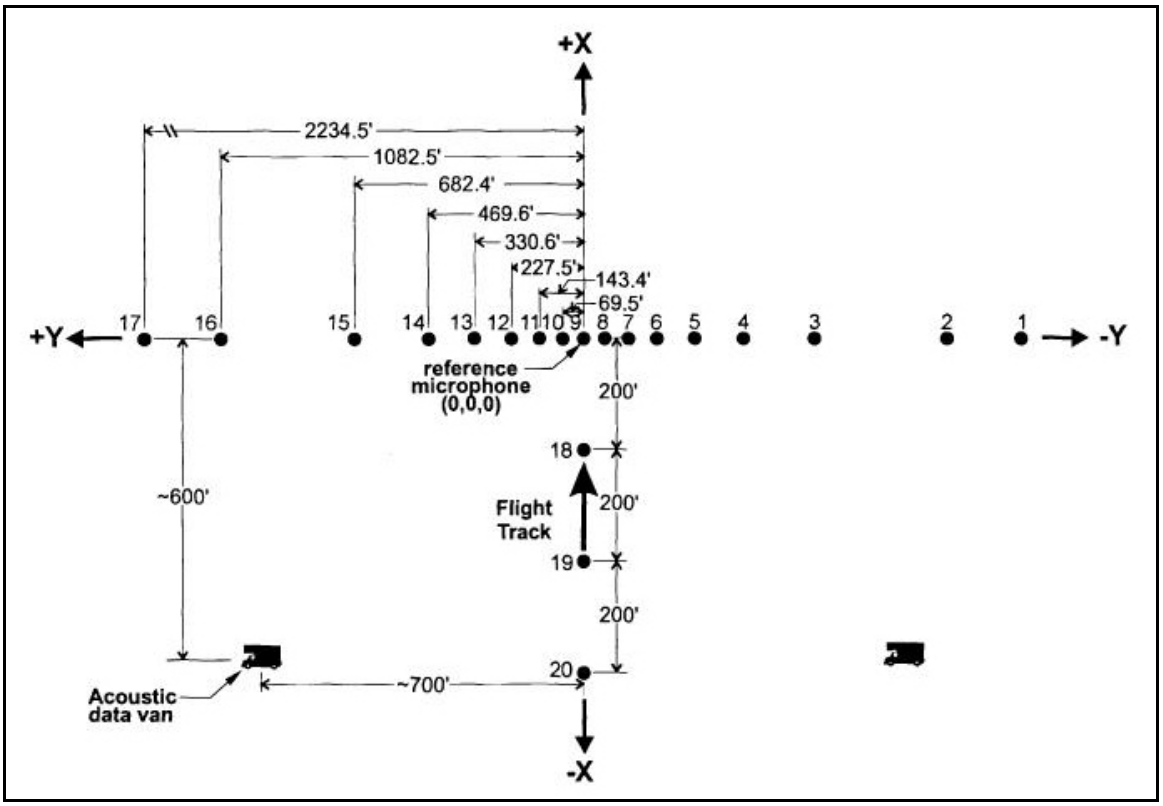

Figure 3.1. Location of microphones for phase I of the 1995 flight test (from Ref. 33).

Figure 3.1 shows that the microphones in the array are not equidistant from one another. In fact, the location of these microphones was chosen to yield "c.g.-to-microphone" elevation angles in increments of ten degrees when the aircraft was at the target altitude of 394 feet over the centerline microphone (#9) (see Figure 3.2). As later discussed in section 3.3, this was done to facilitate the construction of the noise hemispheres corresponding to a given flight condition.

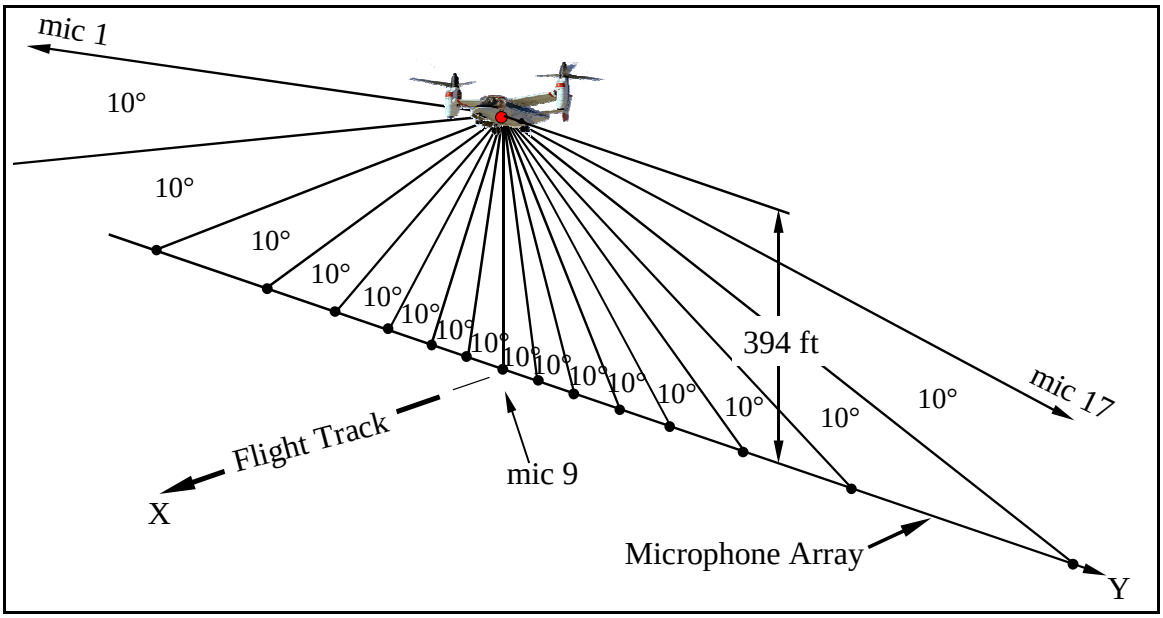

Figure 3.2. Microphone lateral positions in the phase I array.

The following figure shows the matrix of test conditions flown. Also shown in thick lines on each subplot are the boundaries delimiting the normal level, steady-state flight envelope of the XV-15.

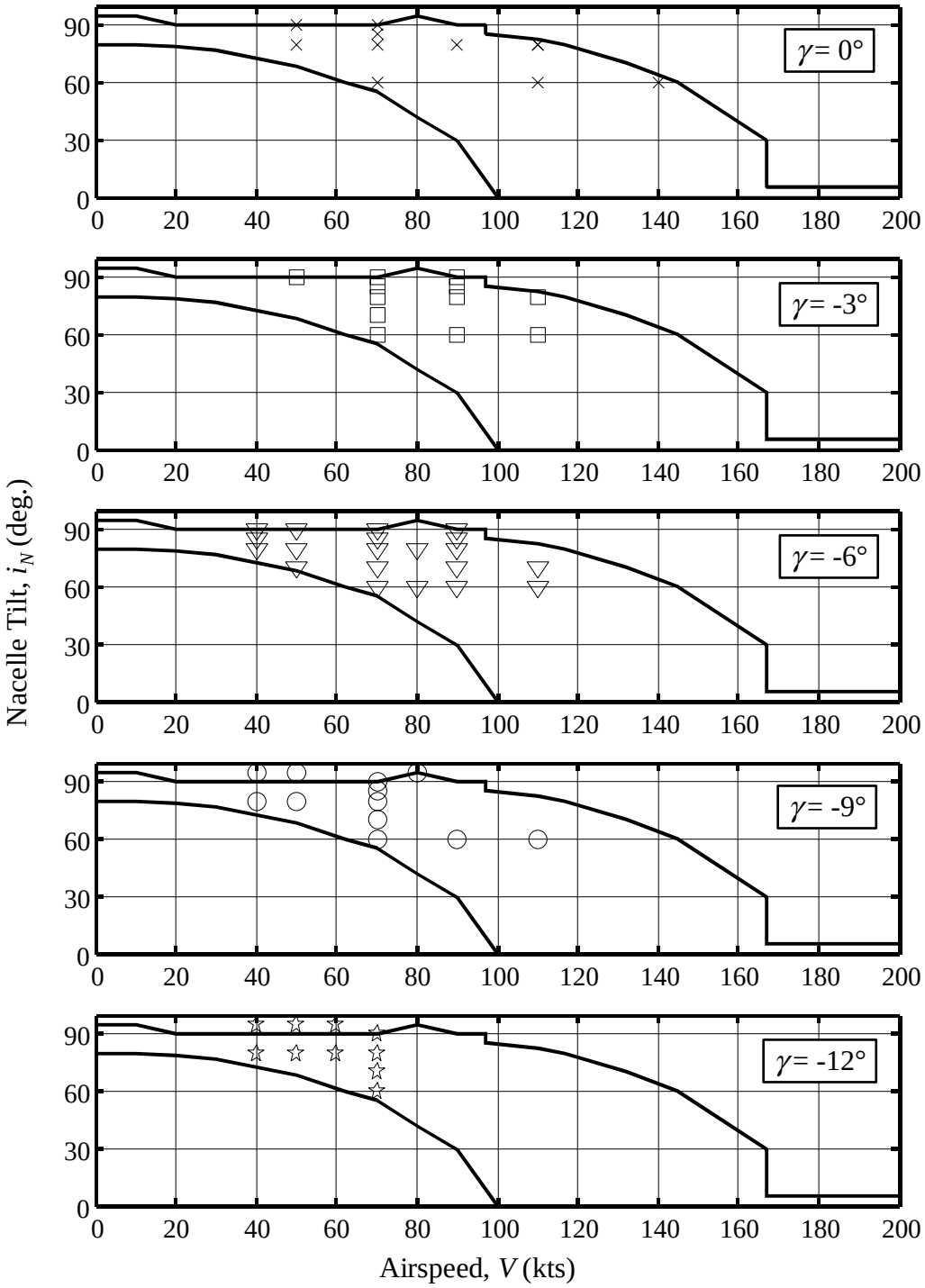

Figure 3.3. Test conditions flown in phase I of the 1995 XV-15 acoustic flight test.

Each flight was initiated approximately two nautical miles uprange of the microphone array and terminated approximately one nautical mile past the array for level flights. For

descending flights, the pilot decided when to terminate the approach based on a safe altitude.

The test gross weight was 13,200 pounds, with the nominal RPM at 98-percent (589 RPM) for nacelle tilts between 60° and 90°. Aircraft N702NA was used and equipped with the original metal blades as opposed to the ATB or Advanced Technology Blades. The landing gear was retracted for all level flights and for descents at airspeeds greater than 90 knots.

3.1.1 Acoustic, Tracking, Aircraft State, and Meteorological Measurements

The microphone measurements were sampled at 20 kHz (equivalent to 2000 acoustic measurements per rotor revolution). Section 3.3 provides details of the format in which the acoustic data was provided to the University of Maryland for this project.

The aircraft tracking data (x, y, and z position with respect to the centerline microphone) was obtained using a laser optical tracking system with a sampling rate of 100 Hz. The accuracy of the system was ± 1 meter. The radar altitude and instrumented boom altitude were also recorded.

The aircraft state data was sampled at 100 kHz and was recorded onboard the aircraft. Table 3.1 shows the state data information that was recorded during each flight.

Table 3.1. Recorded onboard aircraft state data.

Measurement	Units
Instrumented boom altitude, h	ft
Radar Altitude, h	ft
Pitch Attitude, θ	deg.
Angle-of-Attack, α_F	deg.
Yaw Attitude, ψ_F	deg.
Sideslip, β_F	deg.
Roll Attitude, ϕ_F	deg.
Instrumented boom airspeed, V	kts
Rate-of-Descent, ROD	fpm
Fore/aft cyclic stick control position, δ_{lon}	%
Rudder pedals control position, δ_{ped}	%
Power lever control position, δ_{col}	%
Lateral cyclic control position, δ_{lat}	%
Flap position, δ_f	deg.
#1 pylon conversion position, i_N	deg.
#2 pylon conversion position, i_N	deg.
Rotor RPM	%

Weather information was measured by a tethered weather balloon suspended 1000 feet above ground level (AGL). In addition, surface meteorological data was recorded. The main guidelines for testing were as follows: average surface winds less than ten knots, relative humidity less than 95%, no precipitation, visibility greater than three miles, and ceiling greater than 1,500 feet AGL (Ref. 33).

3.2 Aircraft Tracking and State Data

The aircraft tracking and state data was provided by NASA Langley Research Center (LaRC). Studying the state data is extremely instructional as it provides insight into the performance/acoustics relationship. The data shows that a typical flight run is usually far from being steady-state throughout. The following figure shows the airspeed, altitude, flight path angle, and pitch attitude associated with a *nominal* flight of $V = 90$ knots, $i_N = 70°$, and $\gamma = -6°$. Note that a moving average over ten rotor revolutions (1 second) has been applied to the data (equivalent to a low-pass filter). The original un-averaged data is shown in dash lines on the figure. The altitude shown in the figure was obtained from the laser optical tracking system.

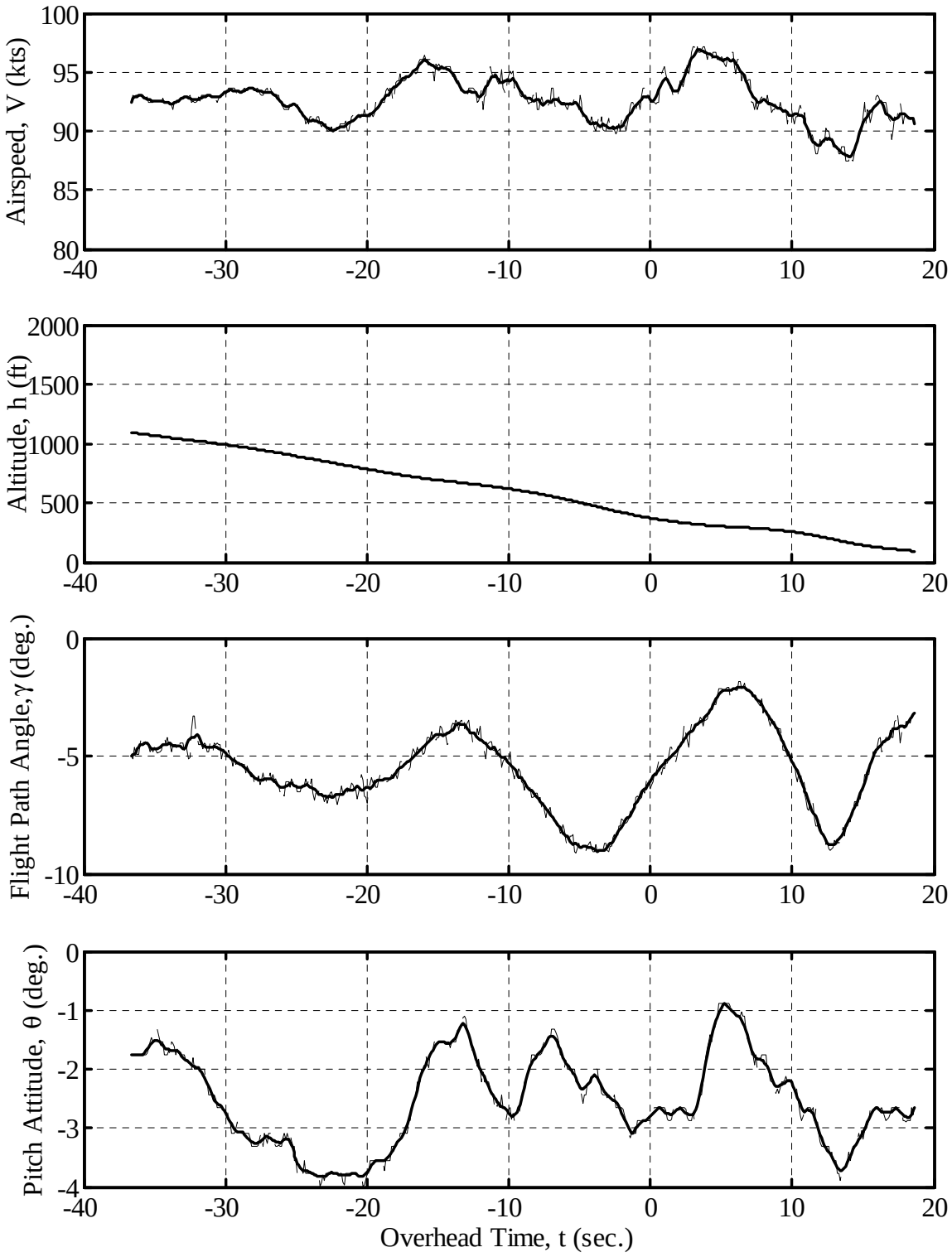

Figure 3.4. Aircraft state data for nominal flight of V = 90 kts, i_N = 70° and γ = -6°.

Figure 3.4 indicates that some segments of the flight are fairly steady-state while others contain large excursions from steady-state flight. Therefore, there does not exist one flight condition for each flight but rather a combination of steady-state flight conditions connected through unsteady flight conditions. For example, at t = -35 seconds, the aircraft flight parameters are as follows: V = 93 knots, γ = -4.5°, and θ = -1.5°. Ten seconds later, at t = -25 seconds, the aircraft is in a different flight condition: V = 91 knots, γ = -6.2°, and θ = -3.8°. These different flight conditions inevitably result in different rotor operating conditions that lead to different measured noise characteristics in terms of both level and directivity. Some flight conditions (large decelerations or changes in flight path angles) are simply too unsteady to be considered a steady-state condition. It is therefore critical to link each microphone measurement to the correct performance condition and to eliminate microphone measurements corresponding to very unsteady performance-states. The following three sections will elaborate upon this point and develop a methodology to take it into account. Note that for a helicopter, defining a flight condition using only airspeed and flight path angle is sufficient to approximate the rotor tip-path-plane angle and thrust (Refs. 87 & 88). On the other hand, it is not sufficient to use airspeed, nacelle tilt, and flight path angle to define a tiltrotor's flight condition. Because of the importance of the fuselage pitch on the airframe aerodynamics, it must also be known in order to approximate the tip-path-plane angle and thrust, two important parameters governing BVI noise.

3.3 Acoustic Data

Bell Helicopter provided the acoustic results used in this research in the form of "noise hemispheres" (see section 3.3.1 below). The noise levels were given in terms of overall sound pressure level (OASPL, in dB), A-weighted sound pressure level (SPL, in dBA), and C-weighted sound pressure level (SPL, in dBC).

Before the data was provided to the University, a bias was applied to the absolute noise levels since the present author did not have the necessary clearance requirements to directly access the original acoustic data. Therefore, the absolute levels on the hemispheres used in this research are not the "true" XV-15 levels. However, the trends of those levels associated with changes in flight parameters are correct. The hemispherical directivity information is also retained. Because of the restriction on available data, no frequency information, such as 1/3-octave bands, was provided to complement the OASPL, dBA and dBC noise hemispheres. This creates difficulties in identifying the type of noise present on a given hemisphere (BVI noise, thickness noise, etc.). However, a careful examination of the flight conditions associated with a noise hemisphere is in most case sufficient to determine with confidence the nature of the resulting noise.

3.3.1 Noise Hemisphere Construction

Noise hemispheres are a convenient way to present steady-state measured acoustic data. They allow for a clear look at noise directivity patterns, such as BVI or thickness noise

hotspots, around the source. The noise hemispheres provided by Bell Helicopter for this research were built from the measured data using a procedure known as ART (Acoustic Repropagation Technique) developed by Wyle Labs (Ref. 113). An explanation of the hemisphere construction process is given below since an understanding of the way the hemispheres are built is instrumental to analyzing the data.

As previously mentioned, the microphones were laterally positioned to produce 10° "slices" when projected back to a point 394 feet above the centerline microphone. Figure 3.5 shows a noise hemisphere and the location of the acoustic measurements after projecting the ground measurements to a 100-meter radius hemisphere centered at the aircraft center-of-gravity and fixed with respect to the horizon. The sound pressure level (SPL) is shown by a colorbar at the right of the hemisphere.

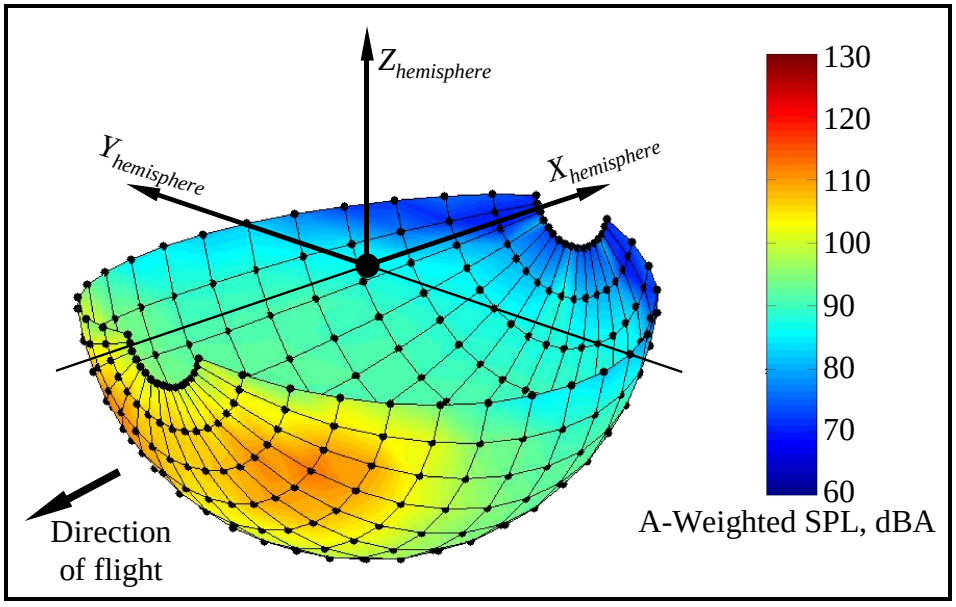

Figure 3.5. Sample noise hemisphere showing measurement locations.

The hemisphere coordinates are given in terms of Cartesian coordinates. The lateral elevation angles, ϕ_{mic}, are spaced 10° apart and each represents a particular microphone. For example, ϕ_{mic} = 0° corresponds to the centerline microphone (#9). The longitudinal elevation angles, θ_{mic}, are spaced 10° apart for the points representing the centerline microphone but are not equally spaced for other points. Points on the front of the hemisphere (negative θ_{mic}) are measured as the aircraft nears the array whereas points on the back of the hemisphere (positive θ_{mic}) represent measurements made after the aircraft has passed the array.

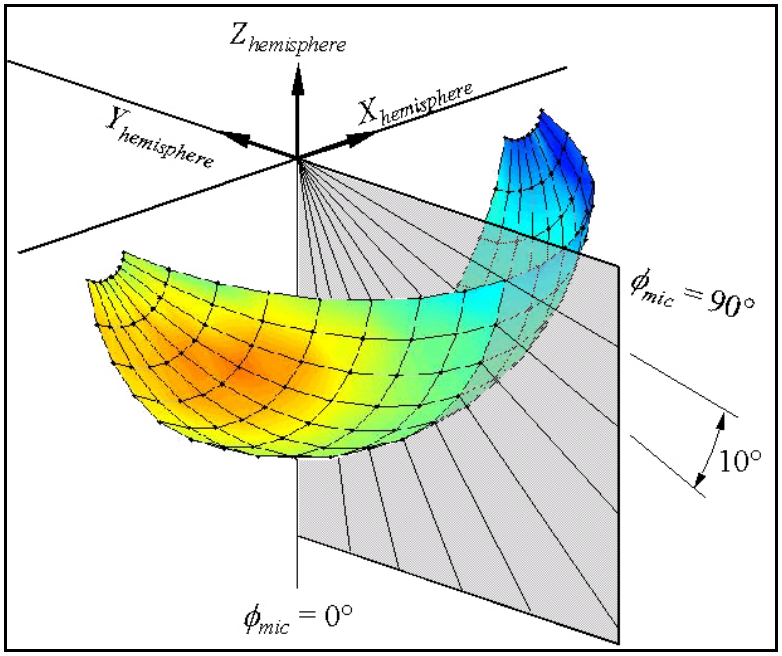

Figure 3.6. Geometry associated with lateral elevation on hemisphere.

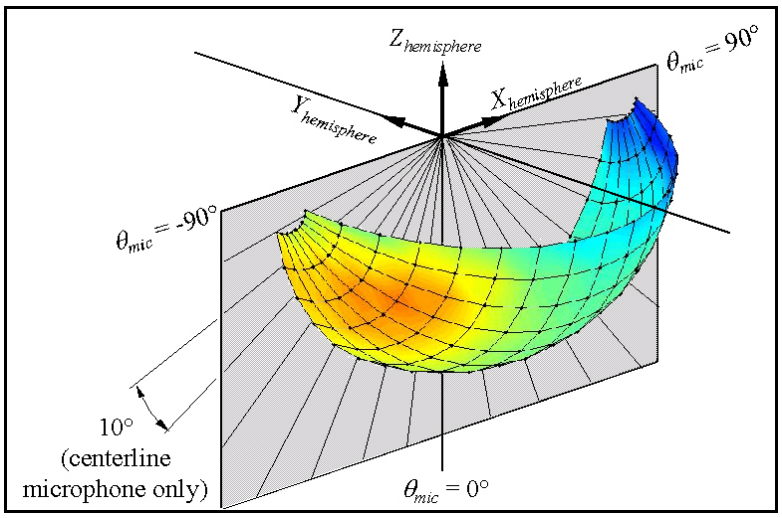

Figure 3.7. Geometry associated with longitudinal elevation on hemisphere.

From Figure 3.6 and Figure 3.7 above, the two elevation angles are given by:

$$\phi_{mic} = \tan^{-1}\left(\frac{-Y_{hemisphere}}{-Z_{hemisphere}}\right) \tag{3.1}$$

$$\theta_{mic} = \tan^{-1}\left(\frac{X_{hemisphere}}{-Z_{hemisphere}}\right) \tag{3.2}$$

Each noise hemisphere was given with an associated nominal flight condition comprising of an airspeed, a nacelle tilt and a flight path angle. For example, the hemisphere of Figure 3.5 was associated with a nominal flight condition of $V = 90$ knots, $i_N = 70°$, and $\gamma = -6°$. It is obvious, however, from the previous discussion of the construction of the hemispheres, that each point on a hemisphere is associated with a different acoustic emission time. For a given flight, points on the front of the hemisphere are measured

long before points on the back of the hemisphere. In addition, points on the rim of the hemisphere (which correspond to the end microphones on the array, numbers 1 and 17) and points at the bottom of the hemisphere (which correspond to the centerline microphone) represent different acoustic emission times because of the different distances the acoustic waves have to travel before reaching the microphones. Therefore, section 3.4 develops a procedure to match each hemisphere position to its associated emission time. The measured state data can then be used to tie a hemisphere location (microphone reading) to its correct flight condition. Clearly, the risk of introducing uncertainty into the measurements would have been reduced had the original ground microphone data been obtained instead of the pre-processed noise hemisphere.

3.3.2 Flat Hemisphere Visualization

It can be instructional to visualize the noise data as a function of hemisphere azimuth angle, ψ_H, and elevation angle, Φ_H. The transformation from the Cartesian hemispherical coordinates is obtained as:

$$\psi_H = \tan^{-1}\left(\frac{Y_{hemisphere}}{X_{hemisphere}}\right) \tag{3.3}$$

$$\Phi_H = -\tan^{-1}\left(\frac{-Z_{hemisphere}}{-X_{hemisphere}}\right) \tag{3.4}$$

Note that in the case of the tiltrotor, the hemisphere azimuth angle does not represent the rotor azimuth angle, because of the twin rotor geometry, see the figure below.

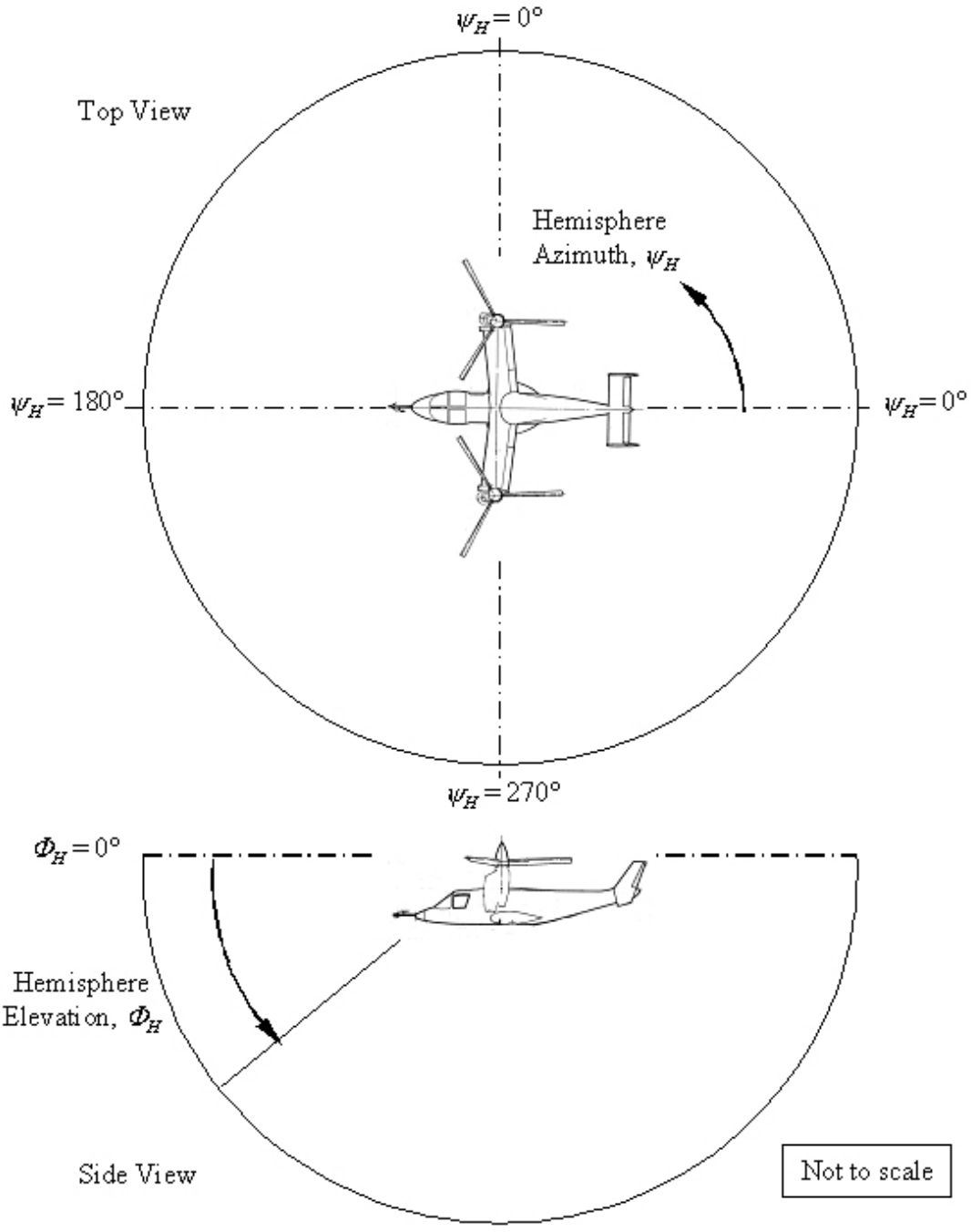

Figure 3.8. Top and side views of hemisphere showing azimuth and elevation angles.

The following figure presents the same acoustic case as shown in Figure 3.5, but this time as a function of hemisphere azimuth and elevation, or as a "flat" hemisphere.

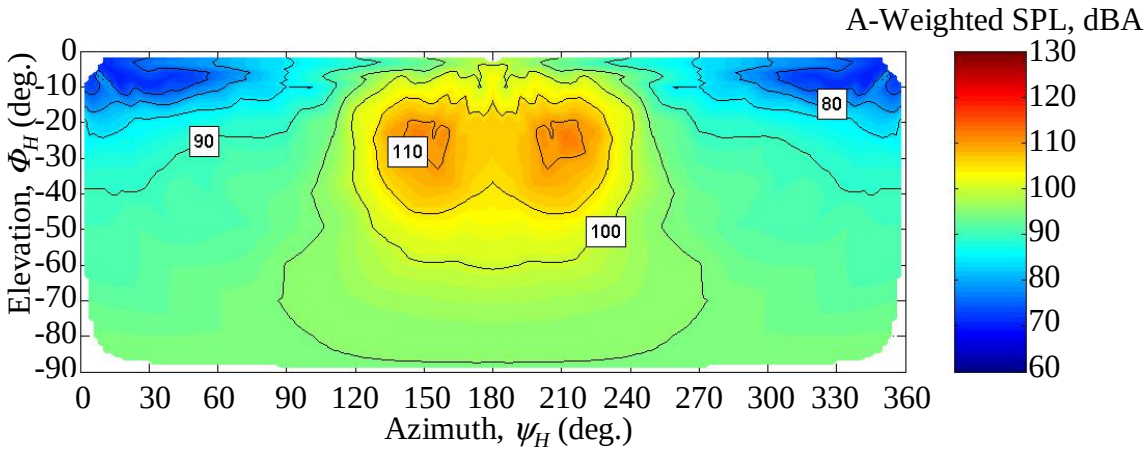

Figure 3.9. Noise data as a function of hemisphere azimuth and elevation ("flat" hemisphere).

3.4 Matching of Performance-State and Acoustic Data

In this section, the assumption is made that the aircraft is on the centerline (Y = 0). The figure shown below illustrates the geometry of the retarded time problem. The figure shows the position of the aircraft at the time of acoustic emission, τ, and at the microphone time, or observer time, t.

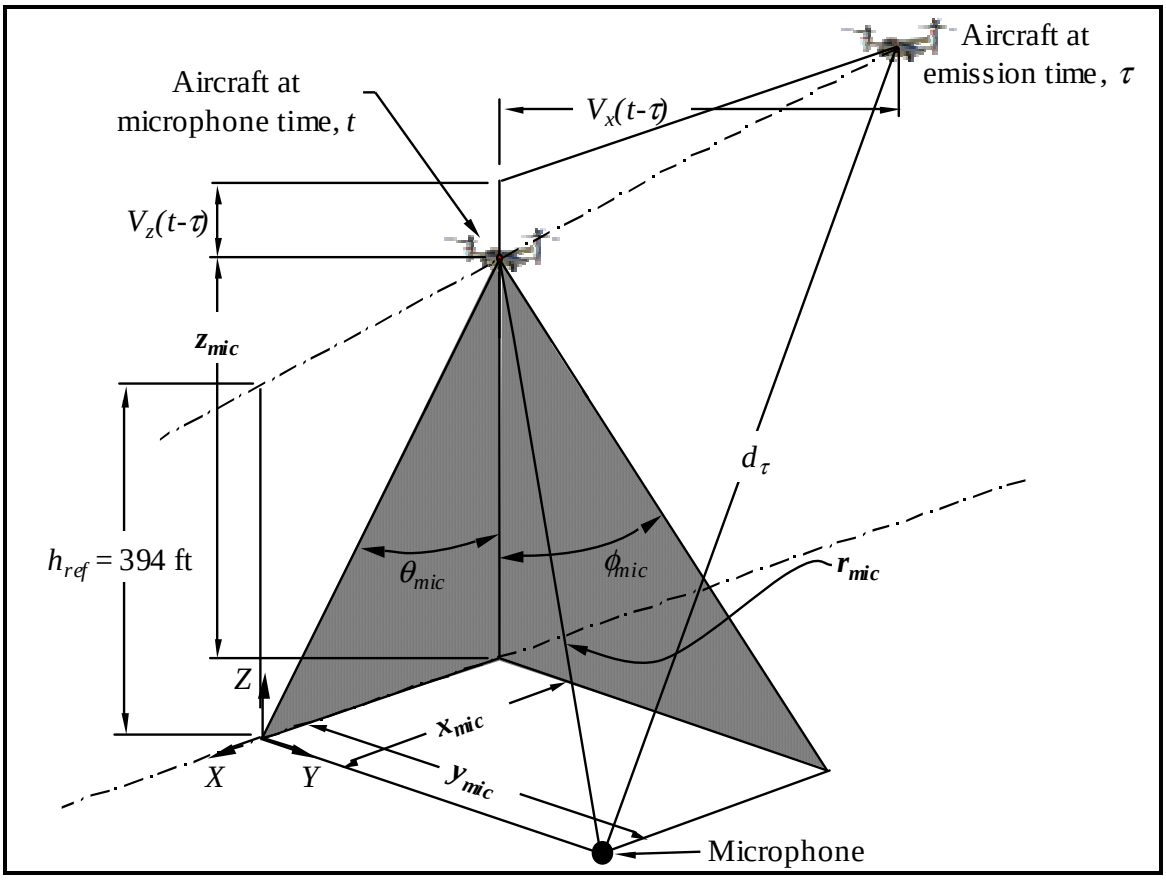

Figure 3.10. Geometry of cg-to-microphone distance.

The goal here is to obtain the emission time of any point given on the hemisphere so that the correct flight condition can be tied to the noise level.

From Figure 3.10, the X, Y, and Z positions of the aircraft at the microphone (observer) time with respect to a microphone are given by (where h_{ref} is equal to 394 feet):

$$x_{mic} = z_{mic} \tan\theta_{mic} \tag{3.5}$$

$$y_{mic} = z_{mic} \tan\phi_{mic} \tag{3.6}$$

$$z_{mic} = \frac{-h_{ref}}{\tan\theta_{mic}\tan\gamma - 1} \tag{3.7}$$

In order to derive an expression for the emission time, τ, the distance between the microphone and the source (aircraft) at the emission time must be found. From Figure 3.10, this distance is given by:

$$\begin{aligned} d_\tau^2 &= \left(x_{mic} - V_x(t-\tau)\right)^2 + y_{mic}^2 + \left(z_{mic} + V_z(t-\tau)\right)^2 \\ &= \left(x_{mic} - M_x d_\tau\right)^2 + y_{mic}^2 + \left(z_{mic} + M_z d_\tau\right)^2 \\ &= x_{mic}^2 - 2x_{mic}M_x d_\tau + M_x^2 d_\tau^2 + y_{mic}^2 + z_{mic}^2 + 2z_{mic}M_z d_\tau + M_z^2 d_\tau^2 \end{aligned} \tag{3.8}$$

$$\Rightarrow \left(1 - M_x^2 - M_z^2\right) d_\tau^2 + 2\left(x_{mic}M_x - z_{mic}M_z\right) d_\tau - \left(x_{mic}^2 + y_{mic}^2 + z_{mic}^2\right) = 0 \tag{3.9}$$

The Mach number components in the x and z directions are given by:

$$M_x = \frac{V_x}{a_0} = \frac{V}{a_0}\cos\gamma \tag{3.10}$$

$$M_z = \frac{V_z}{a_0} = \frac{V}{a_0}\sin\gamma \tag{3.11}$$

Note that the airspeed and flight path angle are assumed constant between the emission and microphone time. The solution to the quadratic equation (3.9) is given by:

$$d_\tau = \frac{-\left(x_{mic}M_x - z_{mic}M_z\right) \pm \sqrt{\left(x_{mic}M_x - z_{mic}M_z\right)^2 + \left(1 - M_x^2 - M_z^2\right)\left(x_{mic}^2 + y_{mic}^2 + z_{mic}^2\right)}}{\left(1 - M_x^2 - M_z^2\right)} \tag{3.12}$$

For M_x <1 and M_z<1, only the positive root of this equation is valid. The emission time is then given by the retarded time equation:

$$\tau = t - \frac{d_\tau}{a_0} \tag{3.13}$$

Using the above equations, each acoustic measurement on a given hemisphere can be associated with the correct performance of the aircraft at the time of the acoustic emission. This methodology will also be used in Chapter 5 to map the hemisphere noise to a ground plane. This methodology is a definite improvement over using just one nominal flight condition to represent acoustic measurements taken over a full flight run, which lasts over a minute and contains many variations in the aircraft performance parameters. However, many assumptions have been used in order to match the acoustic data to the performance data. An additional improvement would be to directly match the ground acoustic measurements to the performance data.

Chapter 4

Quasi-Static Tiltrotor Acoustic Model

In this chapter, a quasi-static neural network model of the XV-15 approach noise characteristics is designed. The goal is to use the measured steady-state noise data introduced in Chapter 3 to obtain a model that predicts noise emitted by a tiltrotor on a hemisphere surrounding the aircraft during an approach maneuver for a range of different flight conditions such as: airspeed, nacelle tilt, flight path angle, and fuselage pitch. In the following chapter, the neural network noise model will be used in conjunction with the performance model in order to design low-noise approach profiles.

4.1 Quasi-Static Acoustic Modeling (Q-SAM)

This research employs the Quasi-Static Acoustic Modeling (Q-SAM) method to predict noise hemispheres for slow maneuvering approach profiles. Gopalan et al. first introduced the Q-SAM method for a conventional helicopter (Ref. 114). The key to the Q-SAM method is that a *steady-state* noise database is used to predict the acoustics of a maneuvering flight in a *quasi-static* manner. This is achieved by using a quasi-static

performance model to predict the performance parameters that govern noise, assuming that those parameters capture the effects of slow maneuvers on the aircraft noise characteristics.

The database of steady-state noise can be obtained from either predictions, steady-state flight test results or wind-tunnel test results. In the paper by Gopalan et al. (Ref. 114), the noise database is comprised of a set of predicted steady-state noise hemispheres that are stored as a function of advance ratio and tip-path-plane angle. In the present research, the steady-state flight test results of the XV-15 are used to build the noise database (see Chapter 3).

The following discussion outlines the steps involved in using the Q-SAM method. The first step is to build a steady-state noise database. Noise can be stored in the database in different ways. In this research however, noise is stored as an A-weighted sound pressure level (SPL in dBA) as a function of the *x*, *y*, and *z* positions on a hemisphere and various measured and predicted performance parameters (see section 4.2.2). Chapter 3 offered the rational for using individual noise hemisphere points and their associated performance-state instead of using one hemisphere per nominal flight condition.

The second step is to devise a method that interpolates between noise data points. This step would be unnecessary if the noise data was obtained from predictions since in that case the noise can be predicted for any flight condition. However, this step is of crucial importance for a discrete noise database like the fairly sparse acoustic flight test database

used herein. In this Dissertation, a neural network model is designed to interpolate between the flight test data points. The next section of this chapter is devoted to developing this neural network model.

The third step in the Q-SAM method is to obtain the performance parameters that govern the acoustics for a selected instant in an approach profile. Chapter 2 described in detail the quasi-static performance model that is used here.

The final step in the Q-SAM method is to link the chosen performance parameters and desired hemisphere location to the noise database through the interpolation procedure in order to obtain the noise level associated with a quasi-static performance-state. The complete Q-SAM procedure is illustrated in the flowchart below.

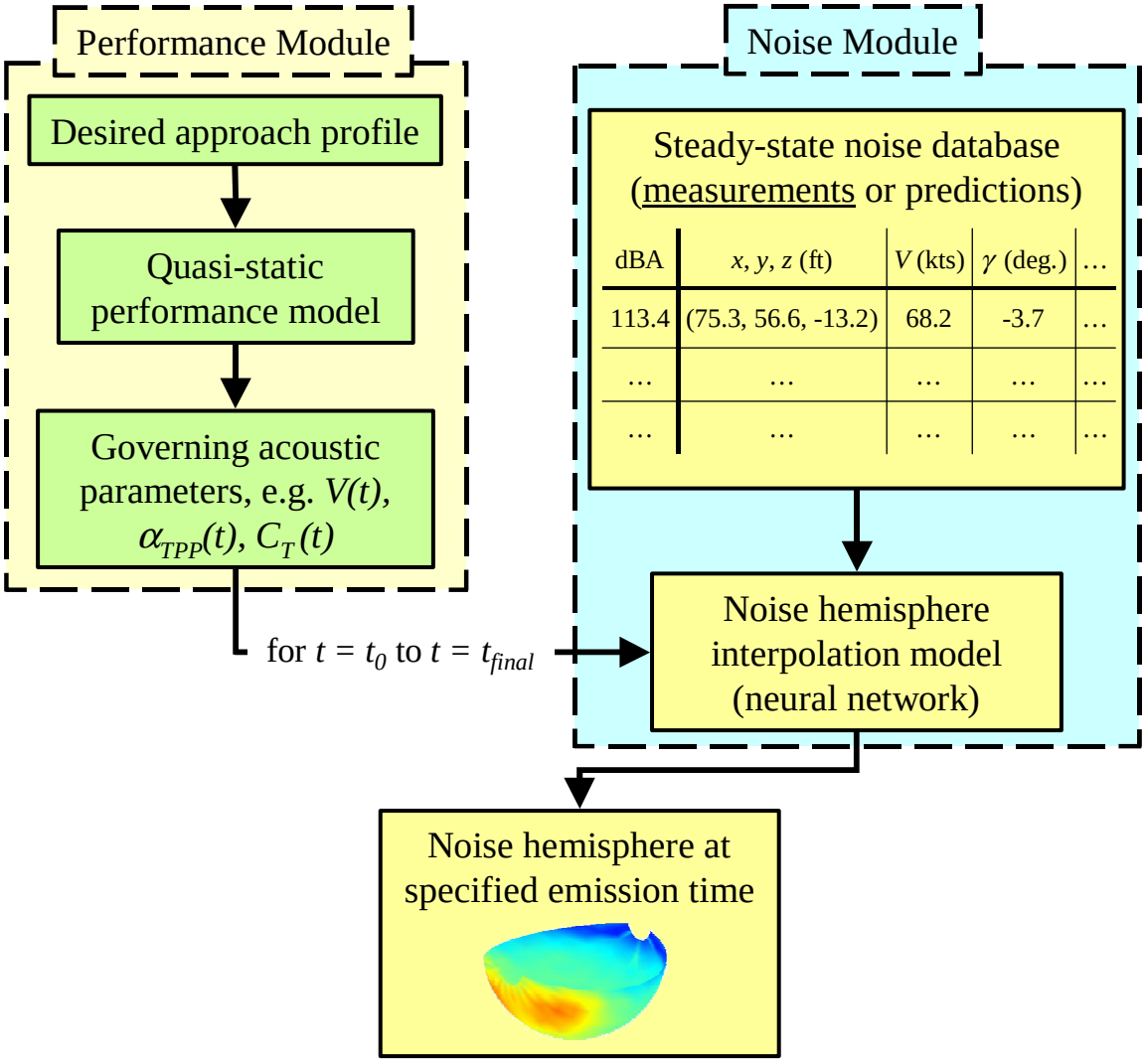

Figure 4.1. Flowchart of the Q-SAM procedure.

4.2 Tiltrotor Acoustic Neural Network

4.2.1 Motivation

A mapping of the 1995 XV-15 flight test acoustic data is sought. A total of 100 noise hemispheres are available, representing the wide range of flight conditions that were tested (see Figure 3.3). Using the technique discussed in section 3.4, each point on a

given hemisphere is tied to a set of performance parameters that represent the state of the aircraft at the time of the acoustic emission. In order to map the hemisphere noise levels to the entire range of possible descent conditions, a relationship between the hemisphere noise (level and directivity) and the performance parameters is necessary. This is not a simple relationship. The noise on a hemisphere represents many sources such as BVI, thickness, loading, broadband, engine, and gearbox noise. These different noise sources are related to the performance parameters in different ways. For example, BVI noise level and directivity are mainly governed (in a highly nonlinear manner) by the advance ratio, hover tip Mach number, tip-path-plane angle, and thrust coefficient. It is therefore difficult to obtain a direct functional relationship between the performance parameters and the noise at a given point on the hemisphere. This fact makes it problematical to use either a linear or nonlinear regression to curve-fit the data. A table look-up procedure is also not the best approach because of the fairly sparse data set and the many parameters involved in the problem. Therefore, it was decided that a neural network model of the acoustic/performance data set would yield the best noise mapping results.

In this research, the desired neural network model is designed to serve as a function approximation or curve-fitting tool that approximates the noise level at a point on the hemisphere as a function of the performance parameters. The main advantage in using a neural network for function approximation is that the model is able to *learn* the highly nonlinear relationships between the network inputs and the desired outputs from a training data set. A carefully designed network is able to *generalize* to new data and is also tolerant of uncertainty in the data set. On the other hand, one of the main

disadvantages in using a neural network is that it can be challenging to make use of existing knowledge and known general trends relevant to the problem. A judicious choice of network inputs and design parameters can ensure a robust neural network model. The neural network used herein is implemented in MATLAB, using the Neural Networks Toolbox (Ref. 115). A solid introduction to the design of neural networks is presented in Ref. 116.

A neural network representation of measured tiltrotor noise acquired in the 1998 isolated full-scale rotor acoustic test is presented in Ref. 117. In this case, the neural network was first used to assess the quality of the measured data. It was then used to predict noise on a traverse below the rotor with inputs being the shaft angle-of-attack, thrust coefficient, advance ratio, traverse location, and microphone location. The neural network was used to predict the noise at the microphone traverse for a limited number of cases and was able to successfully predict the noise within ±1 dB.

4.2.2 Acoustic Neural Network Design

Adapted from Ref. 115 the following figure illustrates the architecture of a simple neural network comprised of p_1 through p_R inputs, three neurons in the first hidden layer, two neurons in the second layer and a single output, a_{final}. On the figure, the neurons are identified as PE or Processing Elements. Each input to a particular layer is assigned a weight (IW – Input Weight and LW – Layer Weight). Furthermore, each neuron is assigned a bias, b. The network is trained by iteratively adjusting the weights and the biases that correspond to each neuron. As the network is trained, the neurons learn the

nonlinear relationships inherent in the data and the error between the network output and the target output is minimized. A transfer function, *f*, is used to scale the summations of weights and biases and to produce an output, *a*.

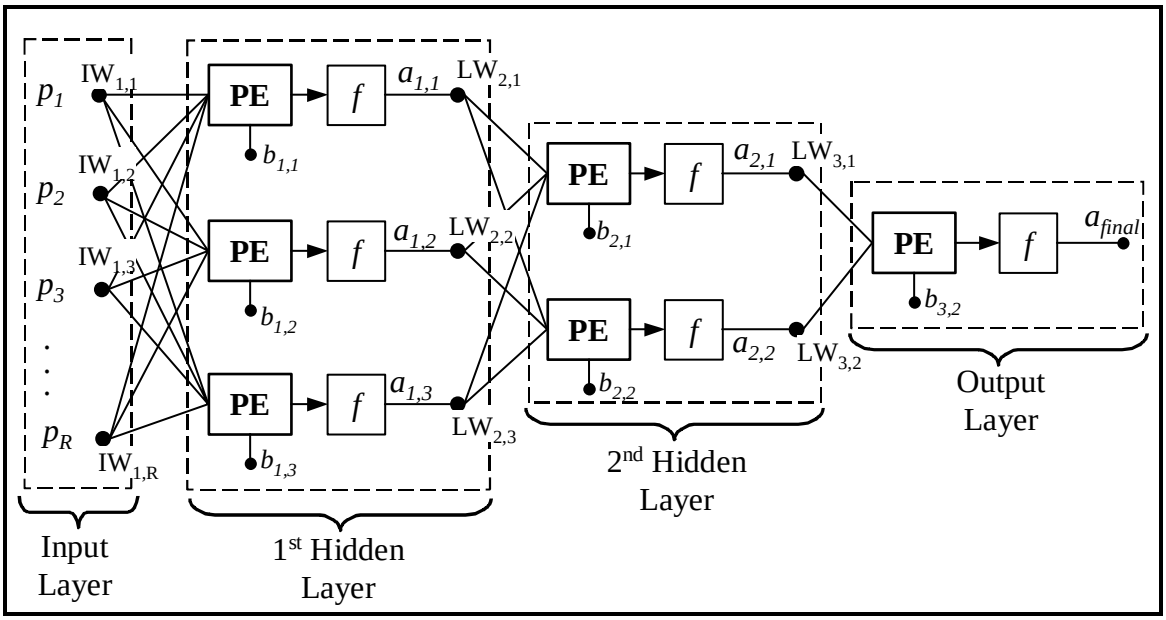

Figure 4.2. Example of a simple neural network architecture.

The design of a neural network involves multiple decisions such as: choosing a type of network, a type of training algorithm, a type of learning algorithm, a type of transfer function between layers, the number of hidden layers, the number of neurons in each layer, as well as the input and the output parameters. These decisions are very specific to the problem at hand and are thus most often made by trial-and-error.

For this application, a feed-forward neural network was chosen, along with error backpropagation as the way to implement the network (see Ref. 115). The network is trained by a Levenberg-Marquardt scheme and the learning algorithm is a gradient-based

method with momentum. Two hidden layers were chosen, both of which use a *sigmoid* transfer function. The output layer uses a linear transfer function that allows the output to scale to the correct magnitude.

In this dissertation, a particular network is identified using the following nomenclature:

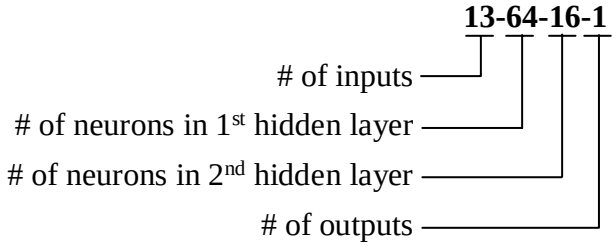

Training Methodology

As mentioned above training a network involves iteratively modifying neuron weights and biases to improve the network's performance, which is generally a measure of the error between the trained network's outputs and its target outputs. In this Dissertation, the mean sum of squares of the network error (*MSE*) is used as a measure of the network performance. The following is the expression for the *MSE*, where *t* is the target output and *a* is the network output.

$$MSE = \frac{1}{N}\sum_{i=1}^{N}\left(t_i - a_i\right)^2 \tag{4.1}$$

To ensure good generalization or, the ability of the network to simulate data not contained in the training set, a method called *early-stopping* is used when training the

network (Ref. 115). Only a portion of the entire available data is used as a training set with this method. At each step in the iterative training, the network simulates data contained in a separate validation set and the *MSE* is calculated. As network training progresses, the validation set error typically reduces with the training set error but as the network begins to memorize or "over-fit" the training set, the validation error increases. Training is then stopped and the network is considered to have reached its optimum performance. Figure 4.3 shows the results of a typical training session, where one *epoch* corresponds to one iteration in the training process.

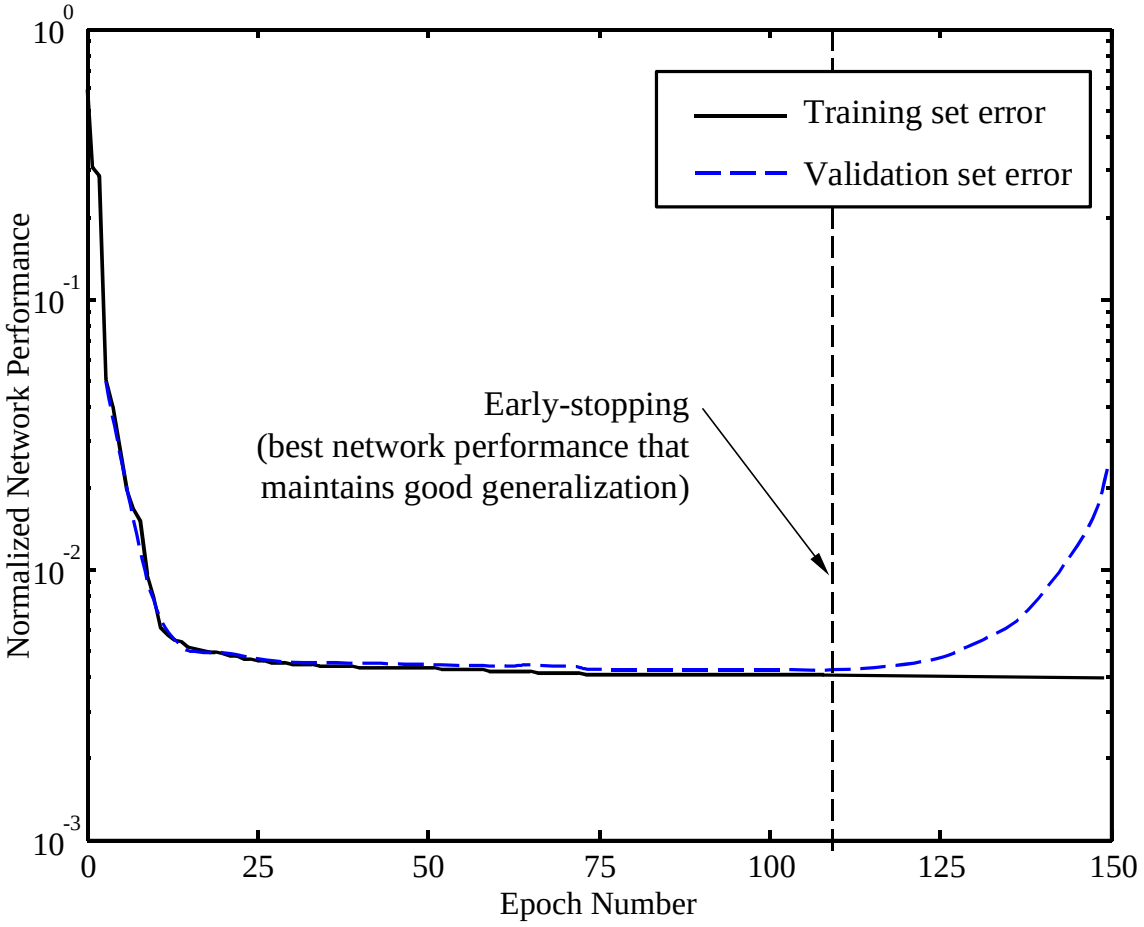

Figure 4.3. Sample training session with early-stopping.

The size and content of the training and validation sets is important. In this research, approximately 80% of the entire data set is used for training, 15% is reserved for validation and 5% is used as a test set that evaluates the final network performance. To ensure that the content of the training, validation, and test sets are not biased (e.g. not enough training data at 60° nacelle tilt), a candidate network is trained repeatedly using random portions of the entire data array to build each set. Repeatedly training a network also provides a better assessment of the network's capabilities. Indeed, before training begins the weights and biases of the individual neurons are initialized at random, meaning that a given network will achieve a slightly different final performance each time it is trained. In this research, each candidate network is trained ten times until early-stopping occurs. A network's performance is then judged based on its average final *MSE*.

Choice of Input and Output Parameters

The neural network's desired output is the noise level at a point on a hemisphere that surrounds the tiltrotor. The data provided for this research contained both A-weighted and overall sound pressure levels (SPL). Because the A-weighted SPL generally gives a more accurate estimate of the human ear's response to noise, it is used in this research.

The network performance is greatly influenced by the choice of input parameters. A judicious choice of inputs will result in a network that is capable of achieving good performance and generalizing to new data. The most obvious set of inputs to provide the

network with is the Cartesian hemisphere positions and the nominal flight conditions for a particular noise level (output). However, as mentioned in section 3.4 the actual flight conditions can appreciably differ from the nominal flight condition between points on a same hemisphere. Also, additional parameters that were not measured in the flight test more directly govern noise generation (such as the rotor tip-path-plane angle and the rotor thrust coefficient).

In order to analyze the neural network performance with respect to the choice of inputs, a parametric study was conducted. Two different sets of inputs characterizing the observer position on a hemisphere and five different sets of inputs characterizing the performance-state of the aircraft were studied for a total of ten complete input sets. Table 4.1 shows the different potential input sets. Note that some of the performance input sets are comprised of measured data as well as computed data obtained through the performance model.

In the Table 4.1, the variable named $\theta_{cylindrical}$ represents the elevation angle of a cylindrical coordinate system with its longitudinal axis aligned with the y-hemisphere Cartesian coordinate. Although one cylindrical angle and three Cartesian coordinates yields redundant information about the position of a point on the hemisphere, it can provide the neural network an important geometrical relationship. This is because the cylindrical elevation angle is defined with respect to the velocity vector, and as such can represent the projection of the tip-path-plane angle on the hemisphere. For example, for a point on the hemisphere, if $\theta_{cylindrical}$ is equal to the tip-path-plane angle, then that point is

in the plane of the rotor's projection on the hemisphere. Since thickness noise radiates most strongly in the plane of the rotor, the neural network can more easily establish the thickness noise directivity trends.

Table 4.1. Potential hemisphere position and aircraft performance inputs.

Set #	**Hemisphere Position Inputs**
Pos.1	Cartesian coordinates (x, y, z)
Pos.2	Combined Cartesian and cylindrical coordinates (x, y, z, $\theta_{cylindrical}$)
Set #	**Aircraft Performance Inputs**
Perf.1	($V_{nominal}$, i_N, $\gamma_{nominal}$)
Perf.2	($V_{measured}$, i_N, $\gamma_{measured}$, $\theta_{measured}$)
Perf.3	($V_{measured}$, i_N, $\gamma_{measured}$, $\theta_{measured}$, $\phi_{F\ measured}$, $\beta_{F\ measured}$)
Perf.4	($V_{measured}$, i_N, $\gamma_{measured}$, $\theta_{measured}$, $\phi_{F\ measured}$, $\beta_{F\ measured}$, $\alpha_{TPP\ comp}$, $C_{T\ comp}$, $M_{AT\ comp}$)
Perf.5	($V_{measured}$, $\alpha_{TPP\ comp}$, $C_{T\ comp}$, $M_{AT\ comp}$)

Each complete input set was used to build an X-16-8-1 network (where X is the total number of inputs) that was trained, validated, and tested ten times. The performances of the ten networks were then averaged to yield a representative neural network performance for each input set. The following figure presents the results of the parametric study and shows the average performance of the network in terms of the mean square error in dBA for each combination of the input sets.

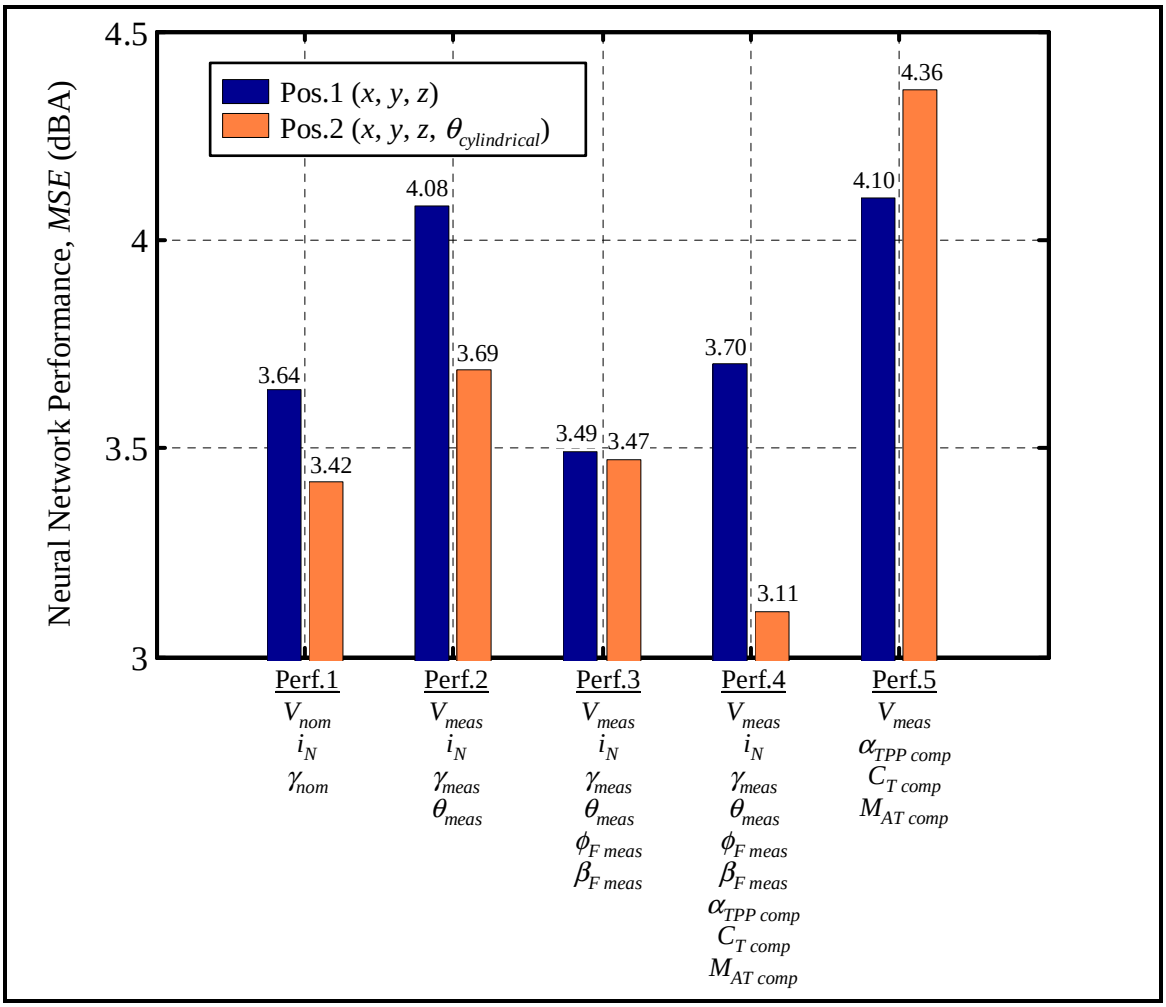

Figure 4.4. Neural network performance as a function of input parameters.

As the previous chart shows, in all but one of the complete input sets, better results are obtained with the combined Cartesian/cylindrical coordinates hemisphere position input set (Pos.2). The network is indeed able to establish a relationship between the noise directivity and the tip-path-plane angle. The best combined input set uses Pos.2 with the set containing the most information about the measured performance parameters of the aircraft as well as the computed tip-path-plane angle, thrust coefficient, and advancing tip Mach number (Perf.4). The network is able to achieve a fairly good performance using

only the nominal flight conditions as inputs. However, adding the correct measured inputs and some computed quantities improves the network performance by approximately 10-percent. It is believed that using the direct ground acoustic measurements instead of "de-propagating" a hemisphere would lead to much greater improvement because many possible sources of errors would be removed.

Hidden Layers Sizing

Determining the number of neurons in each layer is not an easy task. In general, more neurons are needed to approximate very complex functions. However, a compact network is more desirable as it is easier to train, simulate, and analyze.

A general rule of thumb is to use at least the same number of neurons in the first layer as there are inputs. The size of the second layer is usually smaller than the first layer. A parametric study was conducted to identify the number of neurons in each layer required to achieve a target performance of approximately *MSE* = 1.5 dBA. A smaller target *MSE* was judged unnecessary due to the uncertainty already contained in the measured acoustic data set. The following table shows the final network performance (after early-stopping) for a number of different network sizes that are averaged over ten training sessions. Although a more extensive study was conducted the results of only eight network sizes are shown.

Table 4.2. Neural network sizing results.

Number of Neurons		Average Final Network Performance		
L1	L2	Epoch Number	Training Time	*MSE* (dBA)
8	4	97	107	4.43
16	8	71	277	3.34
32	8	91	1061	2.25
32	16	55	1244	2.25
32	32	67	3128	2.09
64	8	72	2862	2.49
64	16	55	4042	1.62
64	32	70	11928	1.34

As the table shows, the MSE decreases as the network size increases. However, as mentioned before, building a very large network is undesirable in terms of training and simulation time, and attempting to attain a very small *MSE* is ill-advised considering the uncertainty already contained in the measured acoustic and performance data. A neural network with 64 neurons in the first hidden layer and 16 neurons in the second hidden layer is therefore judged to be adequate, with an acceptable training time and sufficiently good average performance. The average *MSE* of the ten training sessions for that particular network is *MSE* = 1.62 dBA.

Training Results

The acoustic neural network model designed in the previous section was retrained once until early-stopping occurred. The network achieved a *MSE* of 1.42 dBA after 72 epochs, or iterations. The training time was 5,470 seconds. The following figure shows the predicted noise versus the measured noise for the entire data set, which is comprised of over 15,000 data points.

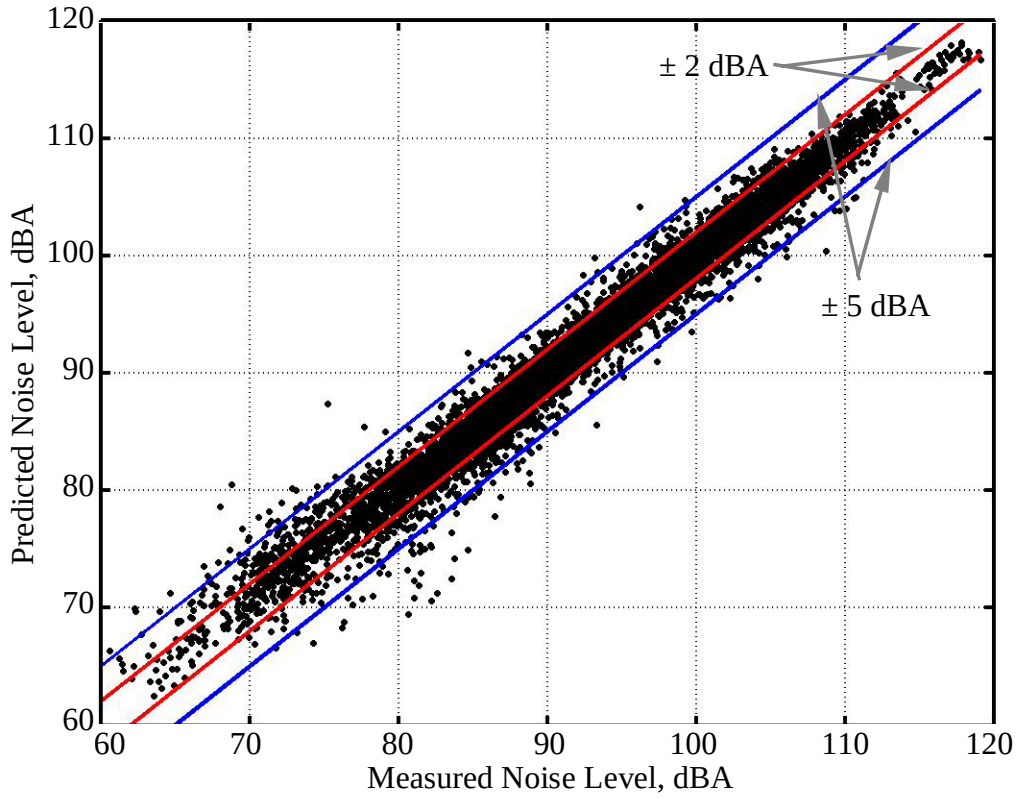

Figure 4.5. Measured vs. predicted noise levels for 13-64-16-1 neural network with *MSE* = 1.42 dBA.

As the previous figure shows, most of the predictions fall within ± 2 dBA of the measurements. In general, the error is largest at the lower noise levels, which implies

that the neural network is performing very well in predicting the level and the directivity of hotspots due to BVI and to thickness or HSI noise. However, some points have a very large error, lying far from the "prediction = target" line. The next section will discuss this matter further.

Study of Outliers

To improve the neural network's performance, it is useful to study the individual target data points that the network seems to have a greater difficulty in predicting (points that have the largest deviations from the *MSE*). In many cases, these outliers correspond to erroneous data measurements or performance predictions and can distract the network from identifying underlying trends during the training iterations. In this research, outliers are typically caused by faulty microphones, highly unsteady vehicle performance, and high winds. In these cases it is useful to remove the outliers from the data set and to retrain the network without the outliers. Figure 4.5 showed the results of training the 13-64-16-1 network until early-stopping. The individual data points that have an error larger than ± 5 dBA are considered to be possible outliers. The performance and noise data of each possible outlier was individually studied to determine the cause of the large error between predicted and measured noise levels. A data point remained in the data set if deemed acceptable and removed from the data set if the prediction error was deemed to be due to measurement error or other sources of uncertainty. In this data set 211 points out of approximately 15,000 were identified as outliers.

The network was re-trained with the outliers removed and an improved performance of *MSE* = 1.15 dBA was obtained, an improvement of 19-percent over the original network performance. Figure 4.6 shows the difference between the predicted and measured values.

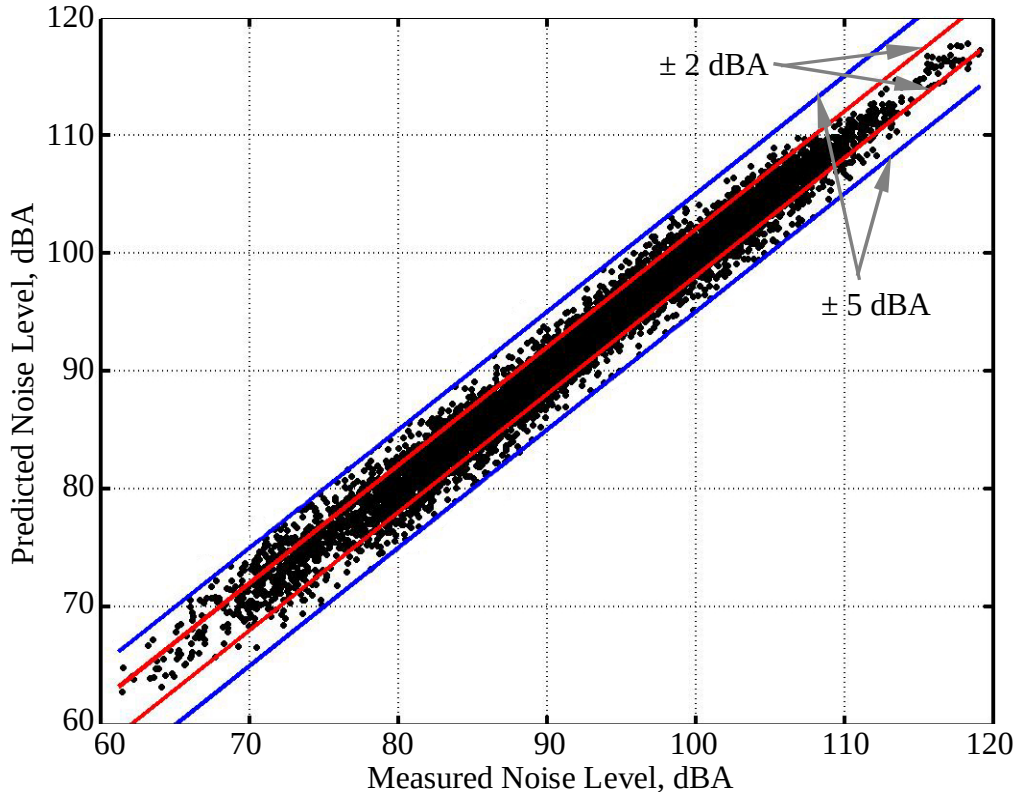

Figure 4.6. Measured vs. predicted noise levels for improved 13-64-16-1 neural network with *MSE* = 1.15 dBA, outliers removed.

The next figure shows a histogram of the prediction errors and illustrates that most of the nearly 15,000 data points lie within a ±2 dBA boundary.

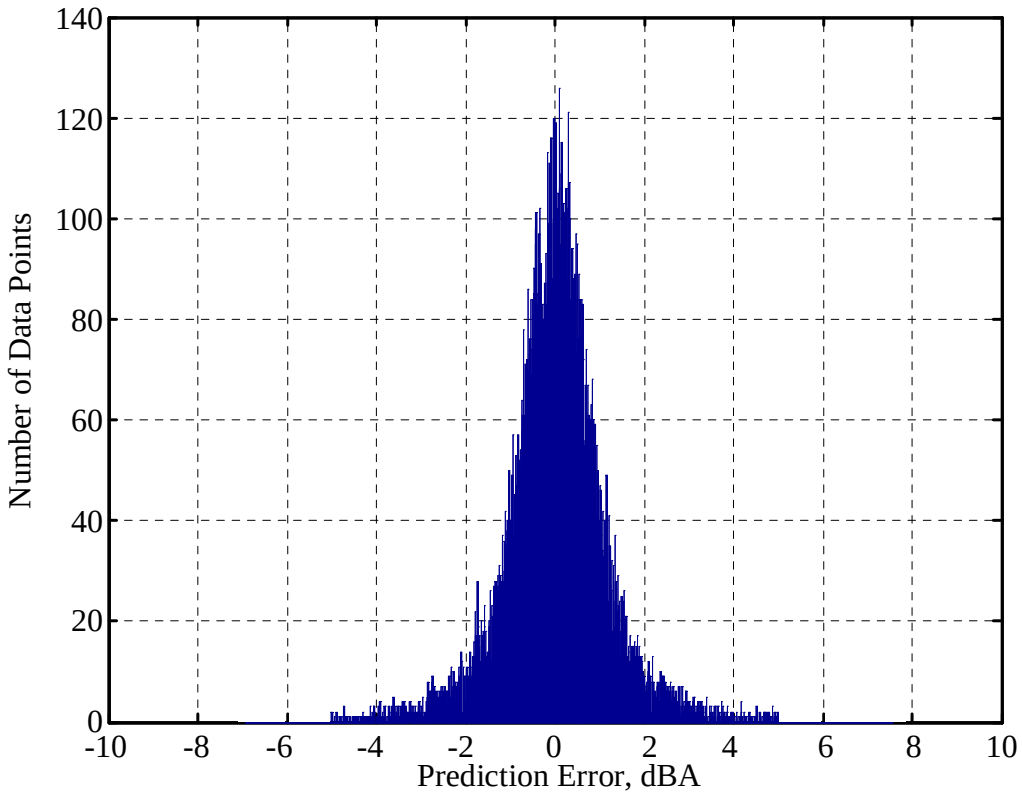

Figure 4.7. Histogram of the prediction errors for 13-64-16-1 neural network.

The following table summarizes the architecture of the acoustic neural network.

Table 4.3. Summary of acoustic neural network architecture.

Position Inputs	x, y, z, $\theta_{cylindrical}$
Performance Inputs	V_{meas}, i_N, γ_{meas}, θ_{meas}, $\phi_{F\ meas}$, $\beta_{F\ meas}$, $\alpha_{TPP\ comp}$, $C_{T\ comp}$, $M_{AT\ comp}$
# of Neurons in 1st Hidden Layer	64
# of Neurons in 2nd Hidden Layer	16
Ouput	A-Weighted SPL @ x, y, z on hemisphere
Network Performance (*MSE*)	1.15 dBA

4.2.3 Acoustic Neural Network Results

Comparison of Predicted vs. Measured Noise Hemispheres

In this section, the neural network model is used to obtain predicted noise hemispheres that correspond to measured noise hemispheres. The model is also used to predict noise hemispheres that correspond to flight conditions that were not obtained in the flight test, thus highlighting the model's ability to generalize to new input data. Note that since the measured noise hemispheres were very nearly symmetrical along the longitudinal plane, only one half of each hemisphere was used for training, comprised of the average of both halves of the hemisphere. Therefore, the noise hemispheres presented below are symmetrical about the longitudinal axis.

Figure 4.8 shows a descent case where strong BVI noise is present. The "flat hemisphere" visualization technique is used for clarity.

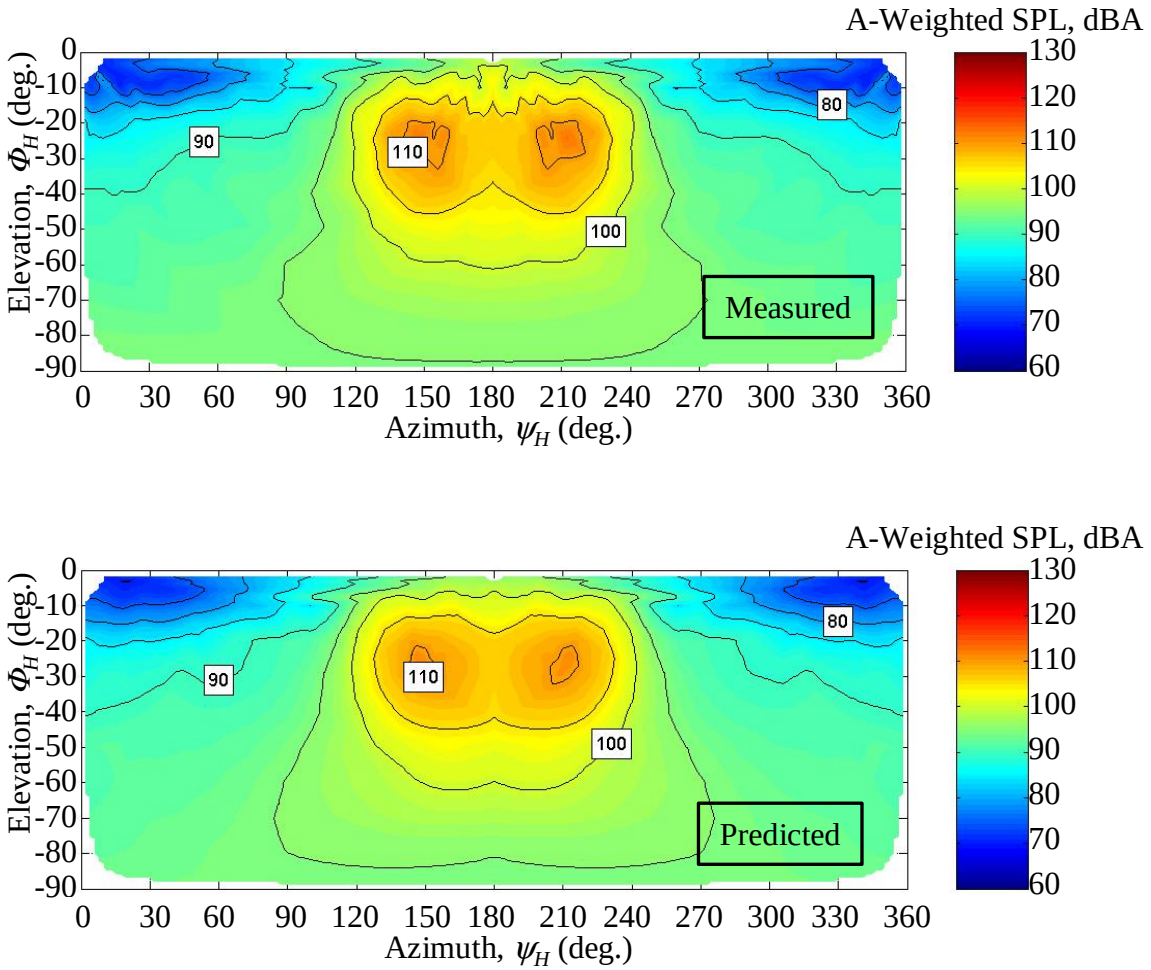

Figure 4.8. Comparison of measured and predicted noise on a flat hemisphere for a BVI case, V = 92 knots, i_N = 70°, and γ = -6°.

The figure above shows that the neural network model captures both the level and the directivity of BVI noise hotspots very well. The next figure shows a high-speed impulsive noise case.

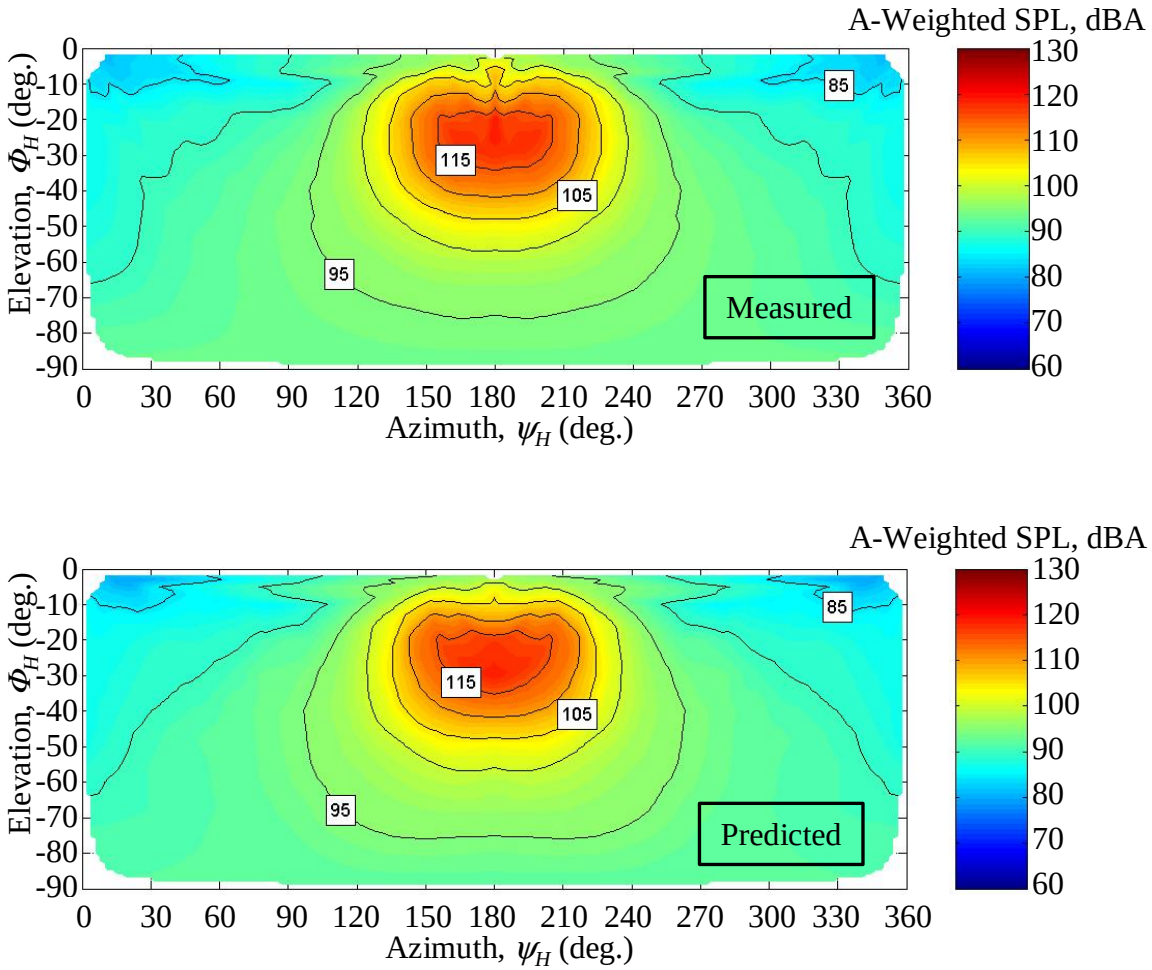

Figure 4.9. Comparison of measured and predicted noise on a flat hemisphere for a HSI case, V = 135 knots, i_N = 60°, and γ= 0°.

Figure 4.9 shows that once again the neural network model is successful in capturing the level and the directivity of the HSI noise hotspot, which, like BVI, is a highly nonlinear noise source. Since the measured noise hemisphere is comprised of noise with different emission times (hence different performance-states), it is not possible to show the tip-path-plane angle on the previous figures. However, for HSI noise, the hotspot is generally in the projection of the tip-path-plane. On the previous figure, the general

orientation of the projection of the tip-path-plane with respect to the hemisphere is at approximately Φ_H = -25°.

In order to better assess the ability of the neural network model to generalize to new data, the network was retrained with one full noise hemisphere omitted from the training set. The comparison between the measured and predicted noise hemisphere that was omitted in the training set is shown in the next figure.

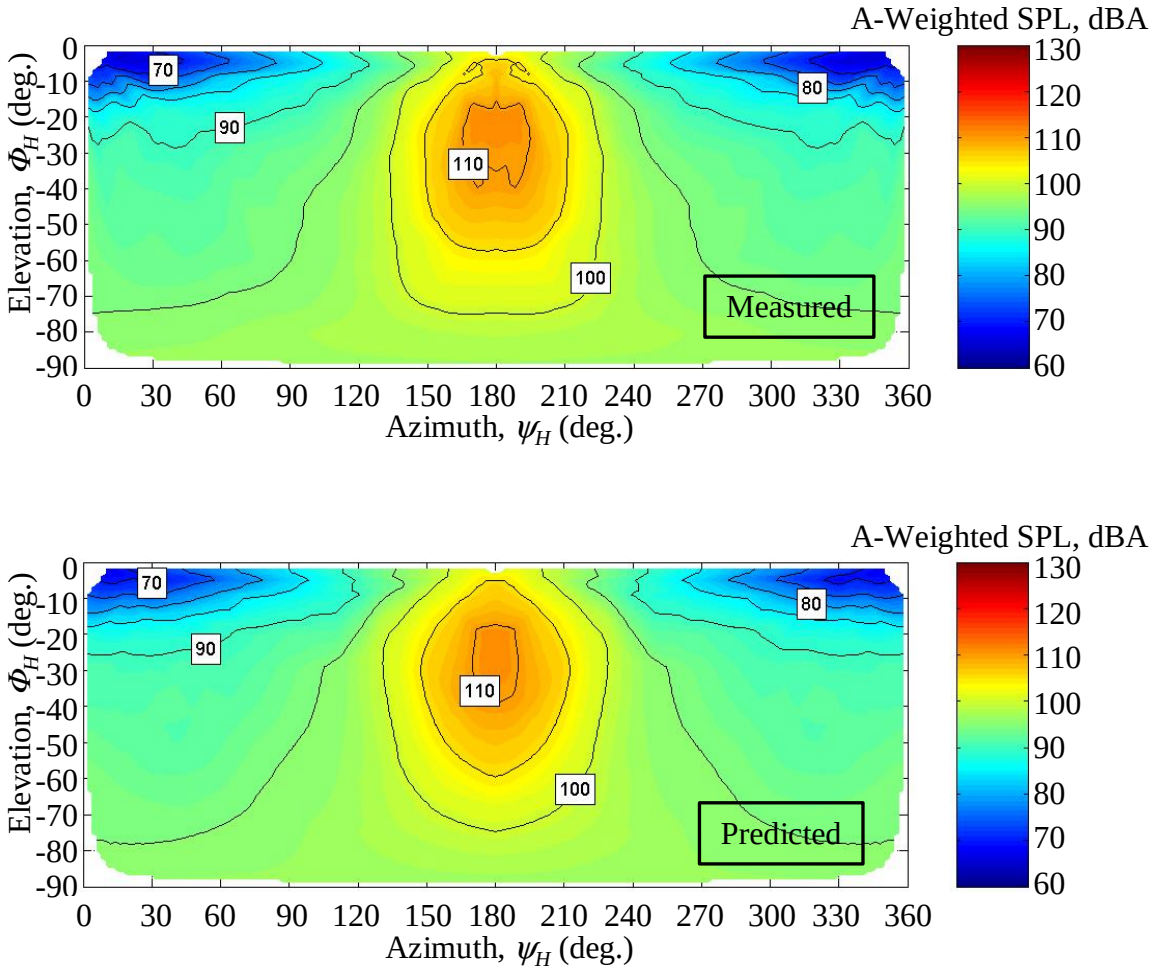

Figure 4.10. Comparison of measured and predicted noise on a flat hemisphere for a BVI case, V = 68 knots, i_N = 90°, and γ= -6°, case omitted from training data set.

The previous figure shows that even though the neural network was never trained on the particular noise hemisphere being shown, it can still adequately predict the noise levels. This shows that the network can identify the correct trends and relationships within the training data set.

Measured Noise Trends

The neural network noise model was shown to adequately model the XV-15 acoustic data set. In this section, the neural network is used to simulate and to present the steady-state noise hemispheres associated with a range of airspeeds, flight path angles, and nacelle tilts. The resulting noise level and directivity trends are then discussed.

The next three figures show the noise hemispheres for nacelle tilts of 70°, 80°, and 90°; airspeeds of 60, 80, and 100 knots; and flight path angles of 0°, -3°, -6°, -9°, and -12°. The projection of the computed tip-path-plane angle is shown on a hemisphere by a black line at the front of the hemisphere. Flight conditions that are far outside of conditions tested in the experiment are not shown.

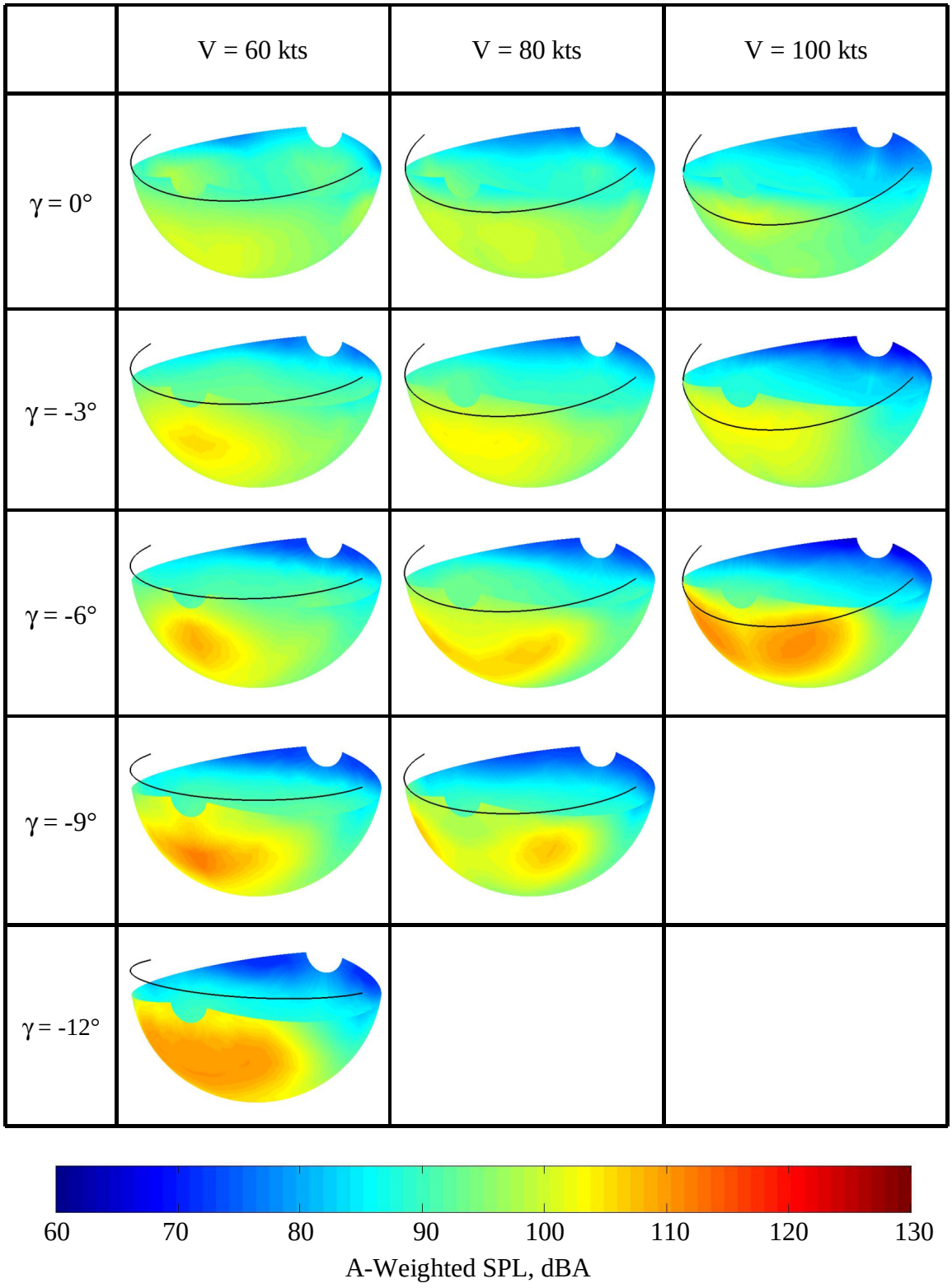

Figure 4.11. Noise hemispheres for 70° nacelle tilt.

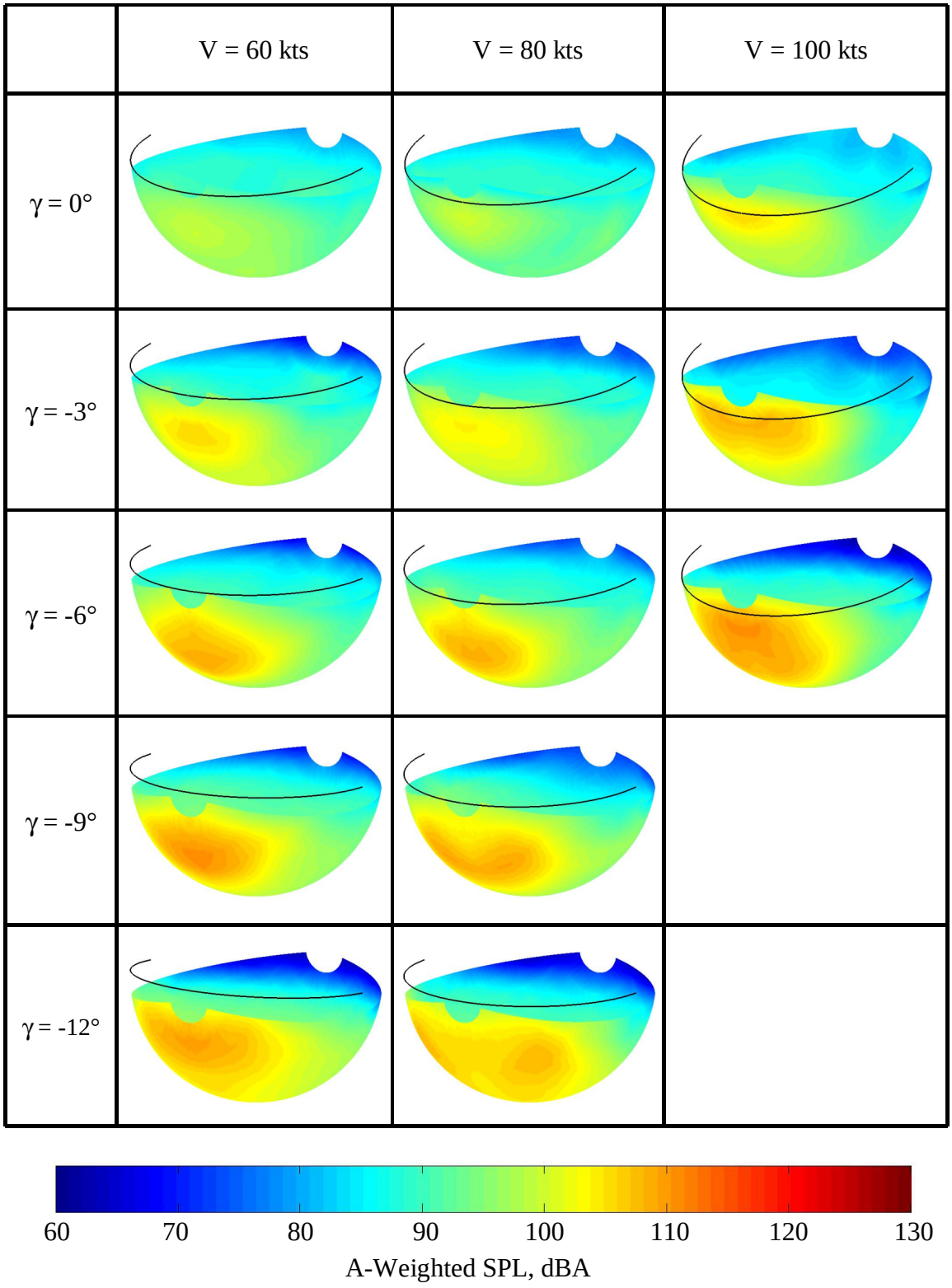

Figure 4.12. Noise hemispheres for 80° nacelle tilt.

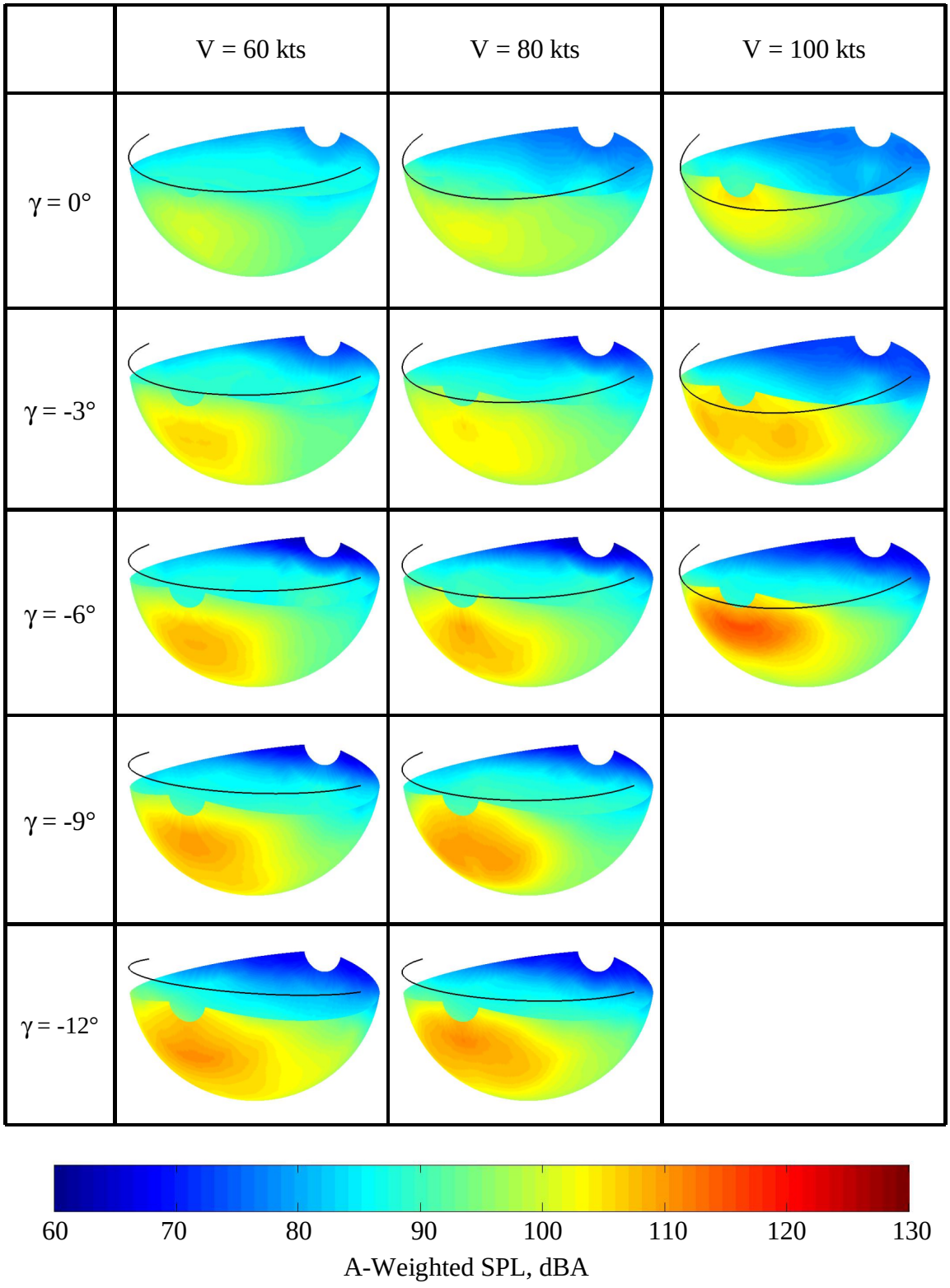

Figure 4.13. Noise hemispheres for 90° nacelle tilt.

By analyzing the three previous figures, some observations about the descent noise characteristics of the XV-15 can be made:

1) BVI noise dominates most of the descent cases as shown by the location of the hotspot(s) below the plane of the rotor. HSI noise occurs mostly in level flight cases and at the highest airspeed. However, an indication of strong thickness noise or HSI noise can be seen for level flight cases at 100 knots for all nacelle tilts.
2) The clearest trend is that BVI noise strength increases with steeper decent angles. From the available data, it seems that the rotor wake has not been pushed above the rotor for the steepest descents, since the noise levels are still increasing. The high disk loading of the tiltrotor explains this fact. This has been seen in wind-tunnel results of the TRAM model where an equivalent descent angle of 11° was not sufficient to push the wake above the rotor (Ref. 54). In a conventional helicopter with a moderate disk loading, BVI noise levels increase with steeper descent angles until the wake moves above the rotor, whereupon the noise decreases as the wake is pushed further above the rotor.
3) The directivity of the BVI hotspot also changes with respect to the descent angle. For shallow descent angles, the hotspot is located directly in front of the aircraft and below the tip-path-plane angle. As the descent angle is made steeper, the hotspot tends to spread and move upward, eventually splitting into two distinct hotspots. This is a characteristic of BVI acoustic phasing effects and represents different *types* of interactions. Chapter 5 discusses this subject in more detail (see also Ref. 118).

4) The BVI noise level is seen to increase as the nacelles near helicopter mode. This is due to a decrease in the rotor inflow, which leads to a decrease in BVI miss-distances. However, note that even flight conditions leading to a large rotor inflow (such as i_N = 70°, γ = -6°, and V = 100 knots) can lead to strong BVI noise generation. This is explored further in Chapter 5.

5) Finally, the maximum BVI noise level on a hemisphere for a given flight path angle and nacelle tilt increases with respect to the airspeed in most cases.

As mentioned above, the cases presented in figures 4.11, 4.12, and 4.13 showed no indication that thickness noise or high-speed impulsive noise are dominant during a descent. In level flight however, the advancing tip Mach number, M_{AT}, tends to be fairly high at higher airspeeds. This leads to a higher level of thickness noise. The following figure shows four cases in level flight at 70° nacelle tilt, with high airspeeds of 100, 110, 120, and 130 knots.

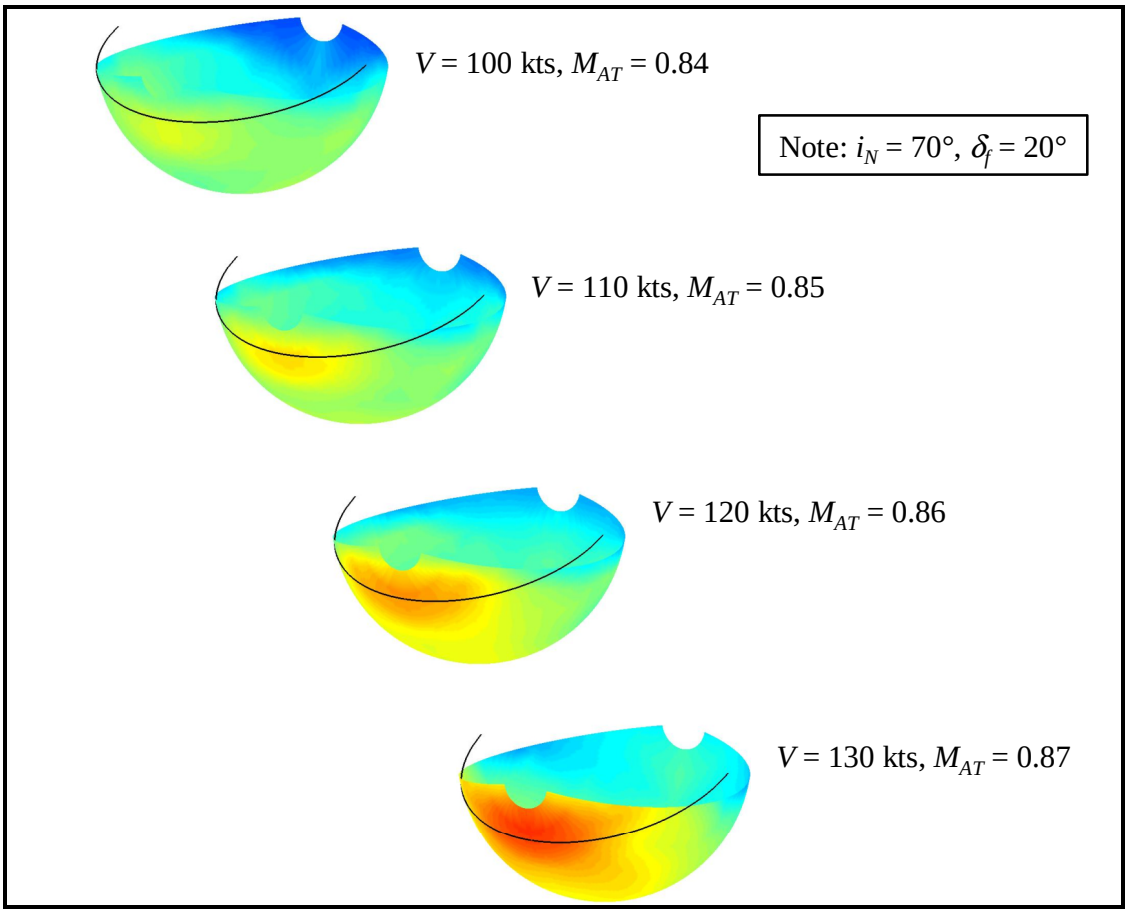

Figure 4.14. Development of thickness noise and HSI noise in level flight.

On the previous figure, the development of strong thickness noise and even HSI impulsive noise can clearly be seen by the hotspot, which is in the plane of the rotor and forward. It is possible to avoid strong thickness noise by avoiding high advancing tip Mach numbers. This can be achieved by keeping the nacelle tilt lower in high speed level flight. Therefore, before beginning a descent, the airspeed should be reduced as much as possible while in airplane mode. This can be accomplished by using larger wing flap deflections, which increases the percentage of the total lift carried by the airframe. In the baseline approach profile used in this research, the initial velocity is 100 knots. Therefore, high-speed impulsive noise is not a dominant source of noise.

Chapter 5

Design and Analysis of Low BVI Noise Approaches

Chapter 4 described a neural-network used to model the measured XV-15 descent acoustic characteristics, which can be used in conjunction with the performance model developed in Chapter 2 to obtain a series of noise hemispheres for any descent profile within the limits of the model. This combined performance/acoustics model is very useful to assess the noise associated with a particular approach profile, but it does not directly provide an insight into potential noise abatement techniques.

In this chapter, a trend-based analysis is developed in order to gain an understanding of the main trajectory and aircraft configuration parameters that govern the likelihood and strength of BVI noise. This crucial understanding is then used to develop low BVI noise approach profiles, which are then validated and analyzed using the neural network noise model.

5.1 Miss-Distance and Inflow as a Measure of BVI Noise

The strength of BVI noise is governed by three main factors: 1) the miss-distance between the vortex and the blade at the time of interaction, 2) the phasing of the acoustic pulses which is governed by the top-view geometry of the blade-vortex interaction and 3) the strength of the vortex (Ref. 118). The rotor operating condition (advance ratio, hover tip Mach number, thrust coefficient, and tip-path-plane angle) determines these three factors.

In order to simplify the present analysis and develop concrete noise reduction techniques, only the miss-distance is considered to govern the strength of BVI noise. In reality, the effects of interaction geometry and vortex strength are not secondary. However, this analysis will show that using the miss-distance as an indicator of BVI noise strength provides the correct measured BVI noise trends.

In order to accurately predict the miss-distance associated with a particular interaction, the position of the tip vortex must be known at the time of the interaction. This requires an accurate prediction of the rotor wake, which is very difficult to achieve for a conventional helicopter's rotor let alone for a highly twisted proprotor system. Since the goal of this research is not to accurately predict BVI noise but to develop BVI noise trends associated with the tiltrotor's performance-state, a simplified approach is used to obtain a measure of the miss-distance based on the rotor inflow.

For a given vortex, the downward distance traveled away from the rotor disk is governed by the rotor inflow, which is the non-dimensional velocity through the rotor. In this research, the rotor inflow is defined as negative when pointing down through the disk and is a function of the blade radial position and azimuth location. Since advancing side BVIs are known to radiate much more noise than retreating side BVIs (Ref. 118), an average value of the inflow over the advancing side is used. The inflow is also averaged over the outer 40-percent of the blade since the larger velocities at the blade tips lead to the generation of most of the acoustic energy. From equation 2.92, the expression for the average inflow, $\bar{\lambda}$, is:

$$\bar{\lambda} = \left(-\frac{V}{\Omega R}\sin\alpha_{TPP} + \lambda_i \right) \begin{array}{l} \text{for } \psi = 0° \text{ to } 180° \\ \text{for } r_p = 0.6R \text{ to } 1.0R \end{array} \tag{5.1}$$

The value of the average inflow presented in the previous equation governs the general magnitude of the miss-distances on the advancing side for all blade-vortex interactions. A large negative value implies that the vortices are being pushed far below the rotor, a small positive or negative value implies that the vortices are close to the rotor disk, and a large positive value means that the vortices are pushed far above the rotor. It is clear that using an average inflow value captures the general miss-distance trends on the advancing side but does not account for interaction geometry or vortex strength effects. Therefore, in order to ensure that the main BVI noise trends are represented correctly by the average inflow, it is important to establish a correlation between the average inflow and the measured BVI noise. The next section demonstrates this correlation.

5.1.1 Average Inflow Trends vs. Measured BVI Noise Trends

The previous section postulates that it is possible to capture measured BVI noise trends by considering an average inflow over the advancing side of the rotor. Intuitively, the trends should correlate since the average inflow is a measure of the average miss-distance, which strongly influences BVI noise strength (Ref. 118). The next graph shows the maximum BVI noise on a hemisphere as a function of descent angle for the XV-15 in helicopter mode at 60 knots. The value of the maximum BVI noise is obtained by using the neural network model developed in Chapter 4; therefore it represents *measured* BVI noise trends. Also shown on the graph is the predicted value of the average inflow for the same airspeed and range of descent angles (note the different axis scales).

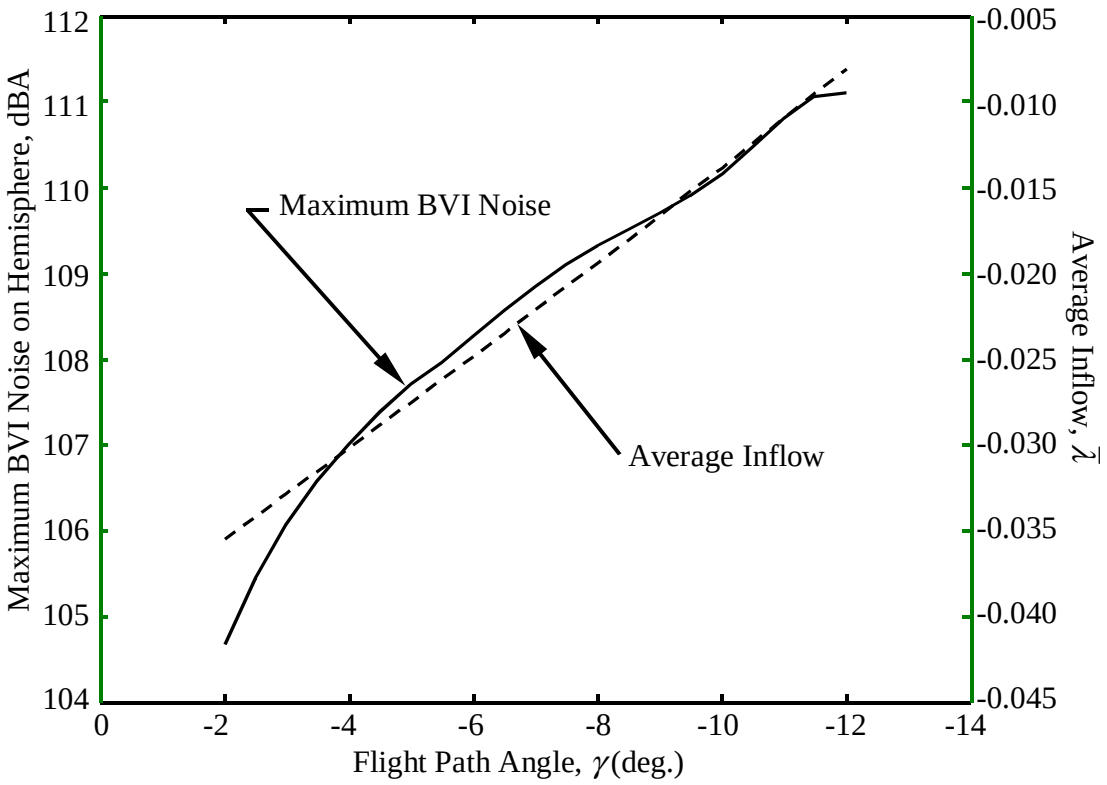

Figure 5.1. Maximum BVI noise and average inflow vs. descent angle for i_N = 90° and V = 60 kts.

Figure 5.1 clearly shows that the trend of increasing noise with an increasing descent angle is matched very well by the trend of decreasing inflow with an increasing descent angle. Indeed, as the descent angle becomes steeper, the vortices are pushed up closer to the rotor disk, thereby reducing the miss-distances of all interactions and increasing the strength of the BVI noise. The average inflow value is therefore an adequate measure of BVI noise *for this particular nacelle tilt and airspeed*. The next step shows that the trend seen in Figure 5.1 is also observed for different nacelle tilts and airspeeds.

The following three figures represent the maximum measured BVI noise on the hemisphere as a function of the predicted average inflow for nacelle tilts of 70, 80, and 90 degrees and airspeeds of 60, 80, and 100 knots. On the figures, the labels "No BVI" represent average inflow conditions that lead to BVI noise levels that are below the levels of the other non-impulsive noise sources present on a hemisphere (i.e., no BVI hotspots). Note that on the figures, the measured BVI noise usually reaches a peak, and then reduces somewhat before increasing again. This indicates a change in the directionality of the BVI hotspots caused by a change in the BVI *type*. As Figures 4.11, 4.12, and 4.13 showed, a strong hotspot is generally seen at the front of the hemisphere at shallow descent angles. As the descent angle is increased, the BVI hotspot can separate to form two distinct hotspots. Thus, for gradually increasing descent angles, the maximum BVI noise on a hemisphere usually decreases slightly as a forward hotspot morphs into two side hotspots, and then increases as the distinct hotspots gain in strength.

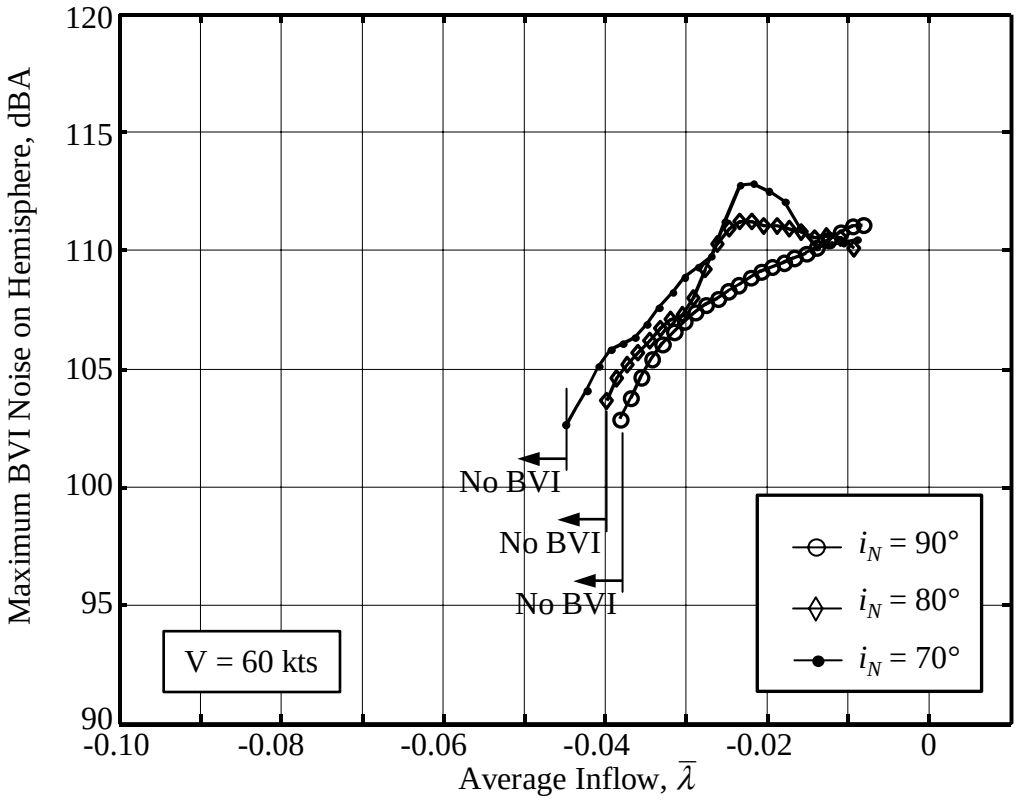

Figure 5.2. Correlation of measured BVI noise and average inflow for V = 60 kts.

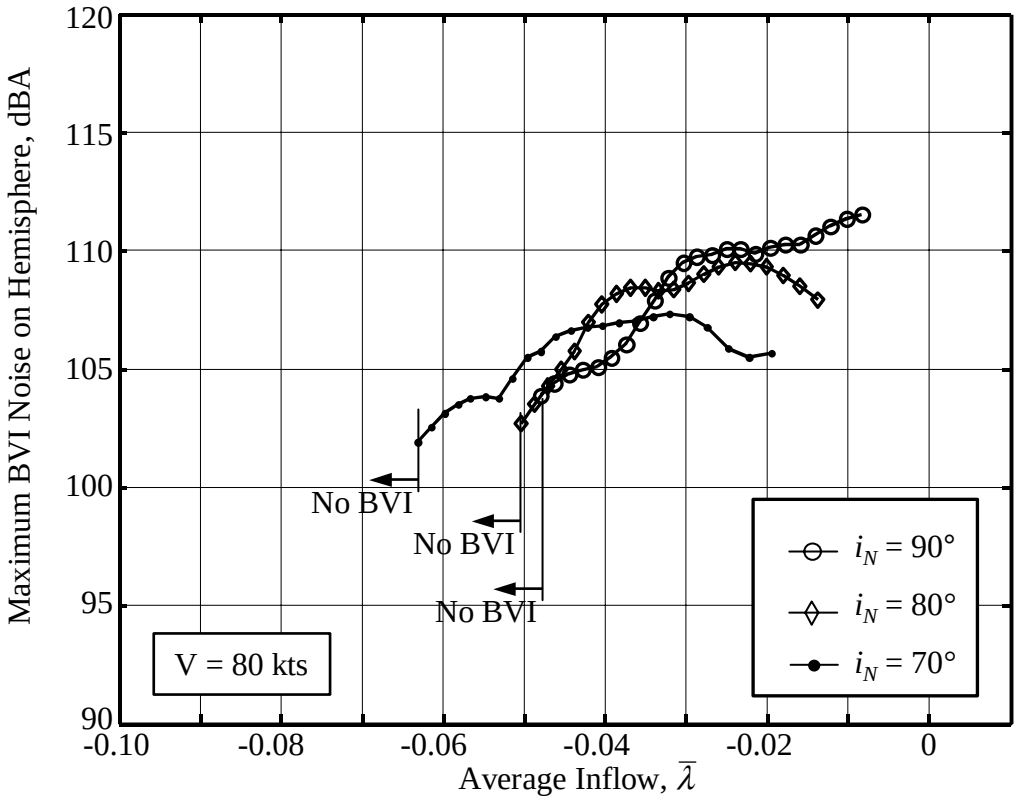

Figure 5.3. Correlation of measured BVI noise and average inflow for V = 80 kts.

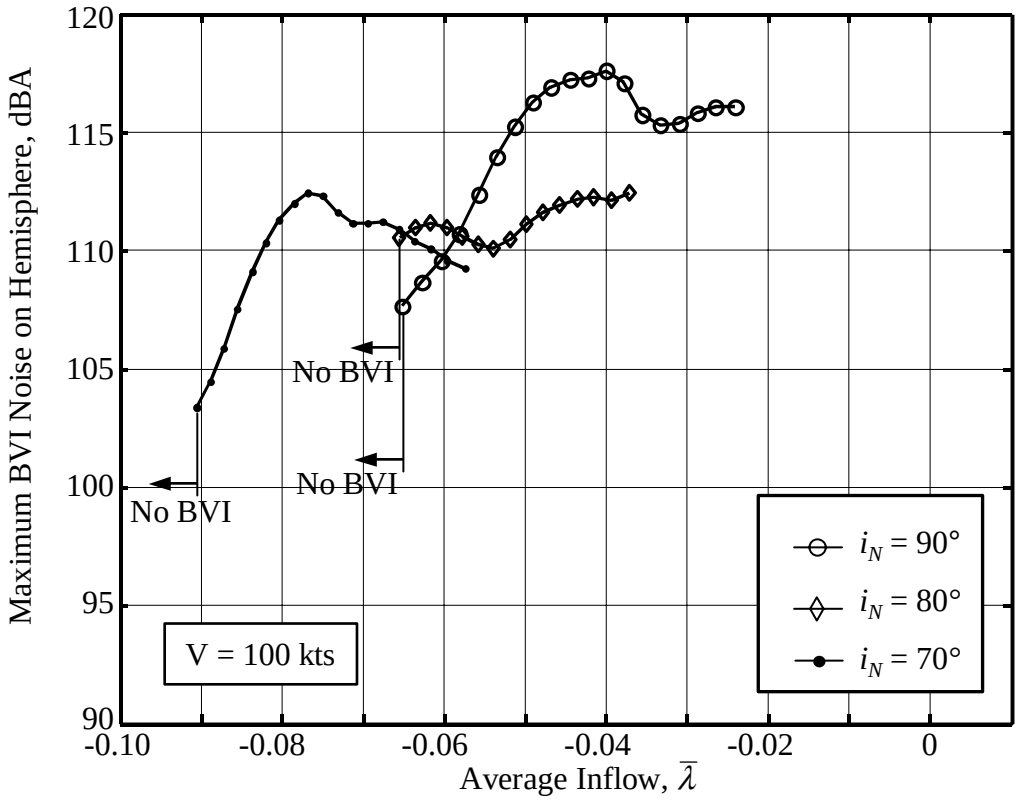

Figure 5.4. Correlation of measured BVI noise and average inflow for V = 100 kts.

The three previous graphs show that the general correlation between measured BVI noise and average inflow is consistent: a decrease in inflow corresponds to an increase in BVI noise level for various nacelle tilts and airspeeds. However, the graphs indicate that this relationship between average inflow and measured BVI noise changes in amplitude with respect to the airspeed and nacelle tilt (to a lesser degree). This shift in the BVI noise/average inflow correlation with respect to airspeed is mostly due to a change in the geometry of the blade-vortex interactions.

At first it is surprising to see that BVI noise hotspots are present on the hemisphere at average inflow values as large as -0.09. However, it is the shift in the BVI noise/average

inflow correlation with respect to airspeed that causes strong BVI to occur at such a large inflow condition. This serves to illustrate the fact that the average inflow does not capture all factors that contribute to strong BVI. Indeed, as will be discussed in section 5.1.2, the geometry of the blade-vortex interactions is a strong function of the airspeed and affects the strength of BVI noise.

Presented in the figure below is an example of a case where strong BVI noise occurs for a large average inflow. In this case, the aircraft is descending at γ = -6°, the nacelles are tilted at i_N = 70° and the airspeed is 90 knots. Clearly, this flight condition leads to a large average inflow through the rotor. Indeed, the predicted average inflow is large in magnitude: $\bar{\lambda} = -0.060$. However, the figure presented below clearly shows that strong noise hotspots are present in the front of the hemisphere.

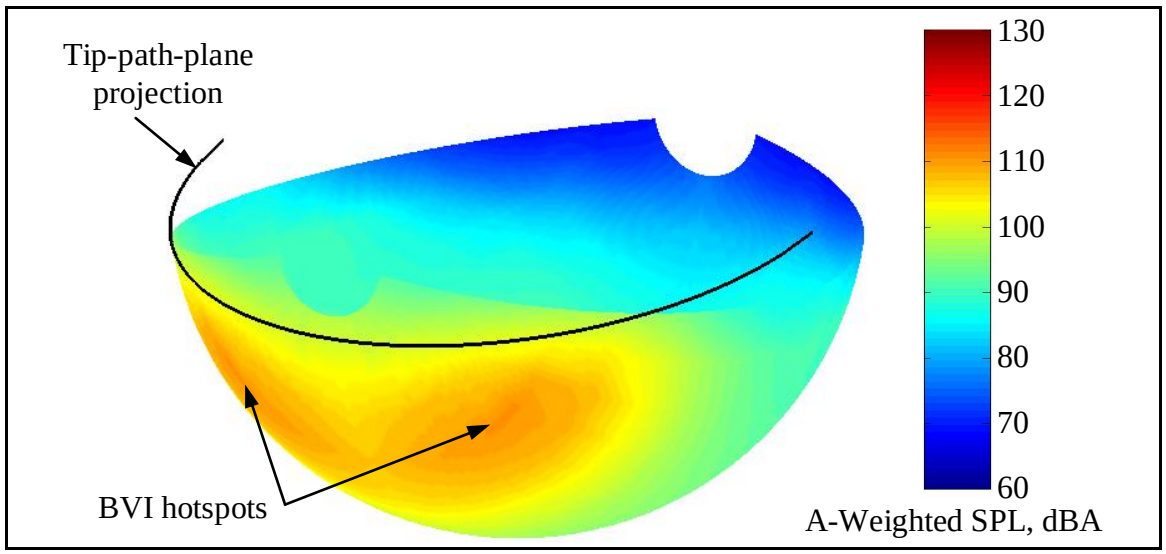

Figure 5.5. Noise hemisphere for i_N = 70°, V = 90 kts, and γ = -6°.

In the previous figure, the noise hotspots are well below the plane of the rotor defined by the black line. Therefore, it is very unlikely that high-speed impulsive noise is the cause of the hotspots. BVI geometry arguments are presented in the next section in order to determine if BVI is the source of the hotspots in Figure 5.5 and similar high inflow cases.

5.1.2 BVI Geometry and Acoustic Phasing

As previously mentioned, blade-vortex interaction occurs when a blade interacts with a previously shed vortex. A top view of a three-bladed rotor with a simple epi-cycloidal wake shows possible interactions that occur for a particular blade at a given airspeed, tip-path-plane angle, and hover tip mach number (see Figure 5.6). The wake is represented by a single rolled-up tip vortex. On the figure, the advancing side interactions are labeled #1 through #6 with the #1 interaction being the youngest. The retreating side interactions are labeled #R1 through #R3.

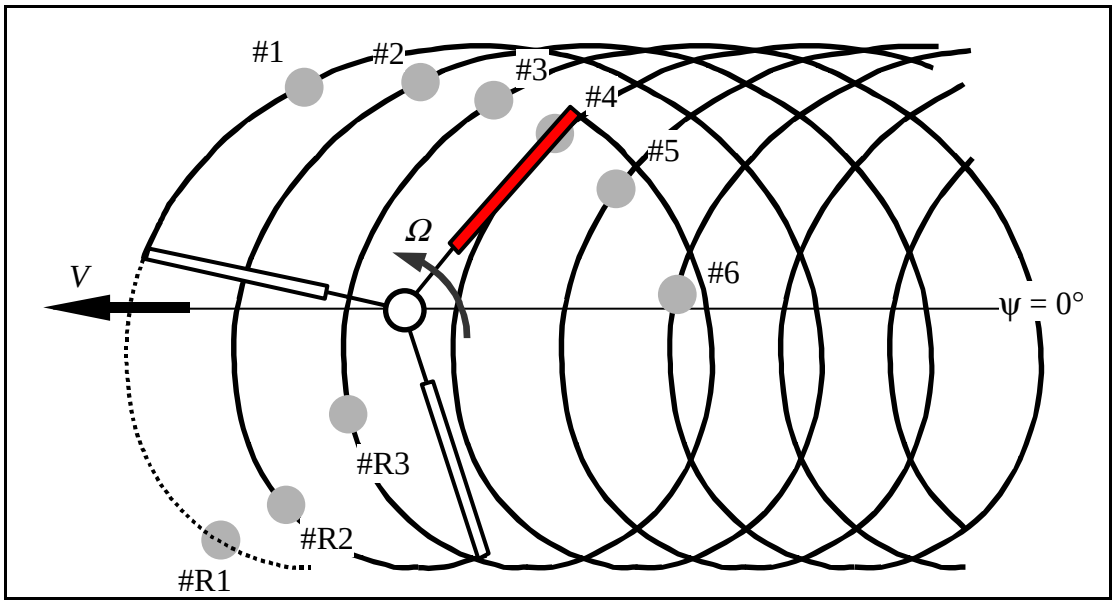

Figure 5.6. Possible BVIs at r_b = 0.9R for an epi-cycloidal wake of a three-bladed rotor operating at μ_x = 0.20.

At the instant shown on Figure 5.6, the blade at the 60° azimuth location has so far experienced two interactions on the advancing side and is currently encountering a third interaction termed a "parallel" interaction. Parallel, as opposed to an "oblique" interaction, is known to cause high levels of BVI noise. As the rotor continues to rotate and to move forward, other interactions will occur on the advancing and the retreating side. In the case shown, a blade encounters a total of six interactions on the advancing side and three on the retreating side during one rotor revolution. The top-view geometry of the interactions is mainly governed by the advance ratio component parallel to the disk, μ_x, but is also somewhat influenced by the tip-path-plane angle. The spread out tip vortex pattern at high advance ratios results in fewer interactions whereas the more closely spaced tip vortex arrangement at low advance ratios results in more interactions.

As Figure 5.6 shows, the younger BVIs are those that interact with a vortex that has a smaller wake age (the amount of time elapsed since the vortex has been shed). This implies that the vortex has not had the time to convect downward very much: thus, the miss-distances associated with younger BVIs are usually fairly small even when the average inflow is large. In part, this explains how a strong BVI can occur when the average inflow is large in magnitude.

The radiation efficiency of a BVI depends on the way in which the acoustic waves accumulate following the interaction. Assuming that the entire wake lies in a plane parallel to the tip-path-plane and that the vortex strength is constant, it is possible to study the accumulation of the acoustic disturbances as a function of only the top-view interaction geometry. Each BVI intersection point can be treated as a spherically spreading acoustic source (BVI wavelet) triggered by the geometric interaction between the blade and a vortex. An example of this analysis is shown in the figure below (from Ref. 118).

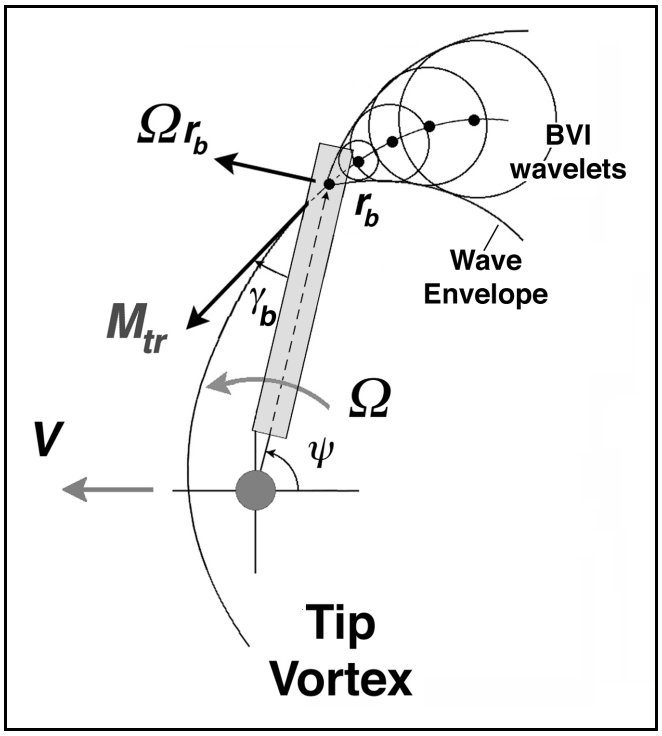

Figure 5.7. Triggering of BVI wavelets (from Ref. 118).

The previous figure shows BVI wavelets triggered by a blade that interacts with a tip vortex. The wavelets spread at the speed of sound, a_0, and accumulate to form a wave front that dictates the radiation efficiency and direction of the resulting BVI noise. The trace Mach number, M_{tr}, depicted on the figure, determines the way in which the wavelets accumulate in space. The trace Mach number is defined as the speed at which the trace of a BVI travels with respect to a fixed observer and is given by (where γ_b is the interaction angle):

$$M_{tr} = \frac{\Omega r_b + V \cos\alpha_{TPP} \sin\psi_b}{a_0 \sin\gamma_b} \tag{5.2}$$

In Ref. 118, it is shown that four different types of BVIs are possible on the advancing side of a rotor and correspond to four different trace Mach number profiles. The different BVI types (labeled α, β, γ, and δ) have different in-plane wavelet radiation characteristics. The next figure shows the classification of the advancing side BVIs with respect to their trace Mach number profile. Also shown on the figure are the associated in-plane wavelet accumulation and radiation patterns.

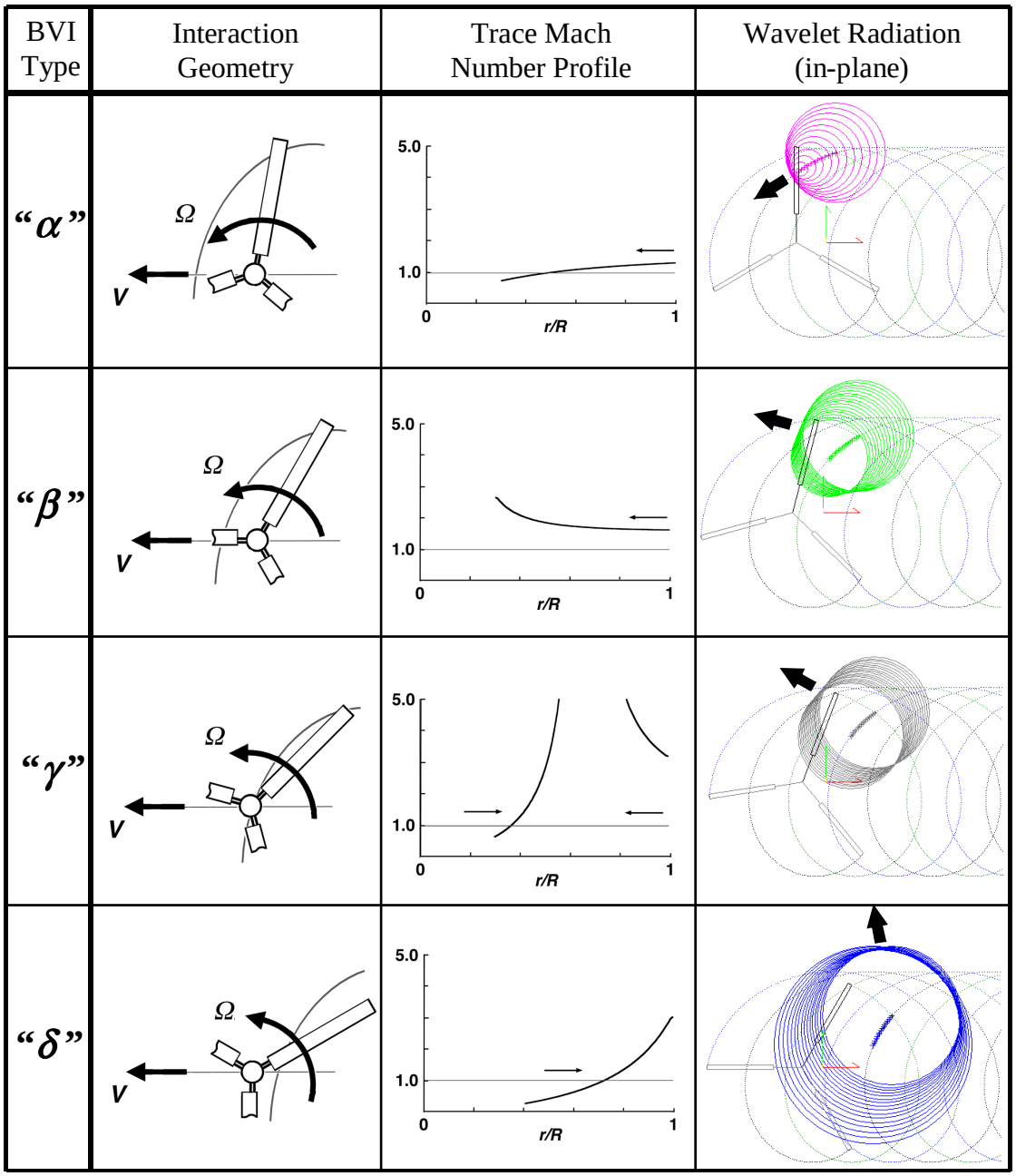

Figure 5.8. Classification of advancing side BVIs by trace Mach number and in-plane wavelet radiation patterns (adapted from Ref. 118).

Figure 5.8 shows that the Type α interaction radiates towards the front of the aircraft whereas the directivity of Type β, γ, and δ interactions progressively shift towards the 90° azimuth direction. The figure also shows that each type of interaction has a very

different trace Mach number profile. For example, Type α starts at a transonic trace Mach number near the blade tip and decelerates as the BVI moves toward the root of the blade. Type γ is known as a parallel interaction because the blade intersects the vortex in a near-parallel fashion.

In terms of noise level, it has been shown that for a given miss-distance Type γ usually contains the most acoustic energy followed by Type β, Type δ, and finally Type α (Ref. 118). This is directly related to the trace Mach number profile associated with the interaction type. However, in some situations, a Type α or β interaction can produce a trace Mach number profile that leads to strong BVI noise. In this case, the trace Mach number remains very close to M_{tr} = 1.0 over the tip portion of the blade and the acoustic waves efficiently radiate to the far-field.

In light of the previous discussion, an analysis was conducted to determine the type of BVI interaction that was shown in Figure 5.5. This was done in order to explain the presence of strong BVI noise at such a large average inflow condition. It was determined that the interaction is most likely a Type β, with a trace Mach number close to 1.0 over the tip portion of the blade. This phenomenon, combined with reasonably small miss-distance due to the small wake age of the interaction, is the probable cause of the BVI hotspots seen in Figure 5.5. This analysis highlights the fact that the average inflow alone is not sufficient to completely capture BVI noise level trends (since the trace Mach number profile can play an important role). Nonetheless, due to the complexities and the unknowns associated with the tiltrotor wake, this research uses the average inflow as a

measure of BVI noise trends. In Section 5.3.5, the measured noise data is used to account for effects *not* captured by the value of the average inflow.

5.2 Parametric Study of Average Inflow Trends

The previous section showed that the value of the average inflow could indeed be used as a representative measure of the level, or the occurrence, of BVI noise. In this section, average inflow results are presented with respect to variations in airspeed, nacelle tilt, flap deflection, flight path angle, and deceleration. This is done in order to identify the flight trajectory and aircraft configuration parameters that could be utilized to reduce BVI noise by increasing the absolute value of the average inflow. This analysis is similar to the one presented in Ref. 91.

5.2.1 Effect of Airspeed on Average Inflow

The following figure shows the effect of airspeed on the average inflow through the rotor for the helicopter mode case at a 6° descent angle with the flaps deflected at 40°.

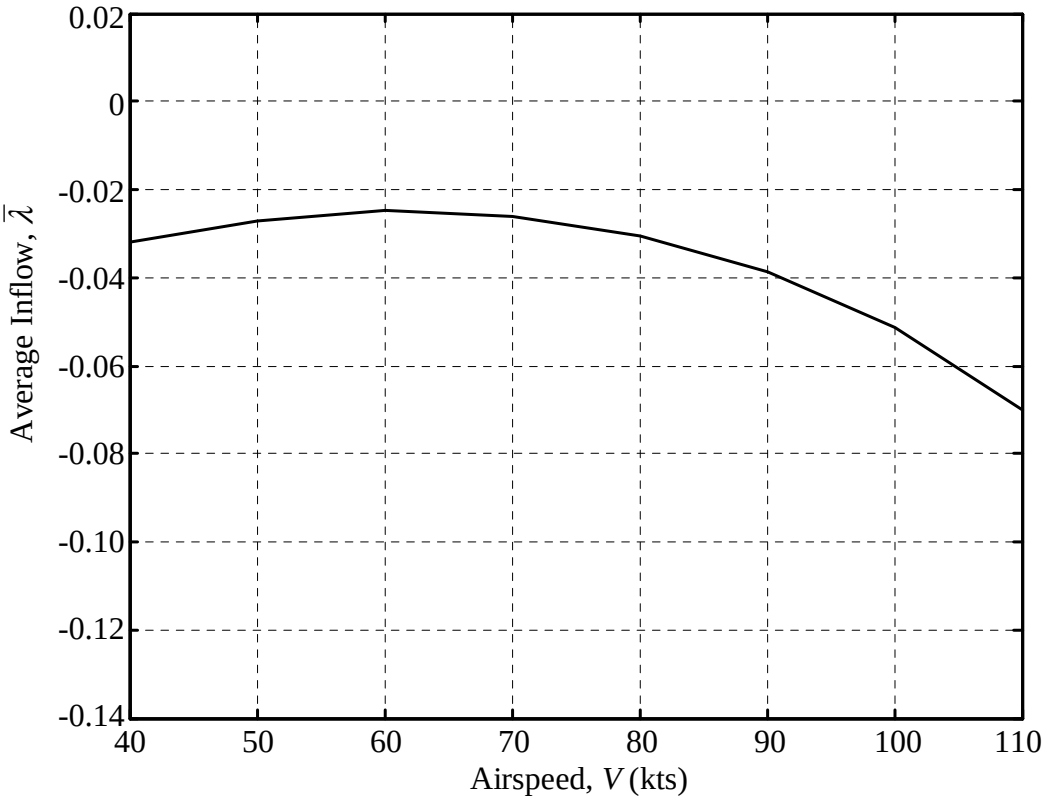

Figure 5.9. Average inflow vs. airspeed for i_N = 90°, γ= -6°, and δ_f = 40°.

Figure 5.9 shows the effect of airspeed on the average inflow value. The curve represents the typical helicopter result: the induced inflow term dominates at low airspeeds, while the freestream velocity inflow term dominates at higher airspeeds. Therefore, an increase in thrust at low airspeeds is favorable in order to push the wake further below the rotor and a forward tilt of the tip-path-plane at high airspeeds leads to a higher absolute value of the inflow.

5.2.2 Effect of Nacelle Tilt on Average Inflow

The tiltrotor's capability to tilt its nacelles in a wide range of angles is an important configuration control that is not available on conventional helicopters. Tilting the nacelles has a large effect on the vehicle trim solution since it changes the airframe drag and moment coefficients in an appreciable way and, more importantly, reorients the rotors' thrust vectors. Because of this change in the trim solution due to the tilting of the nacelles, it is expected that the resulting average inflow be strongly affected by the nacelle tilt. The next figure shows the change in average inflow for different nacelle tilts.

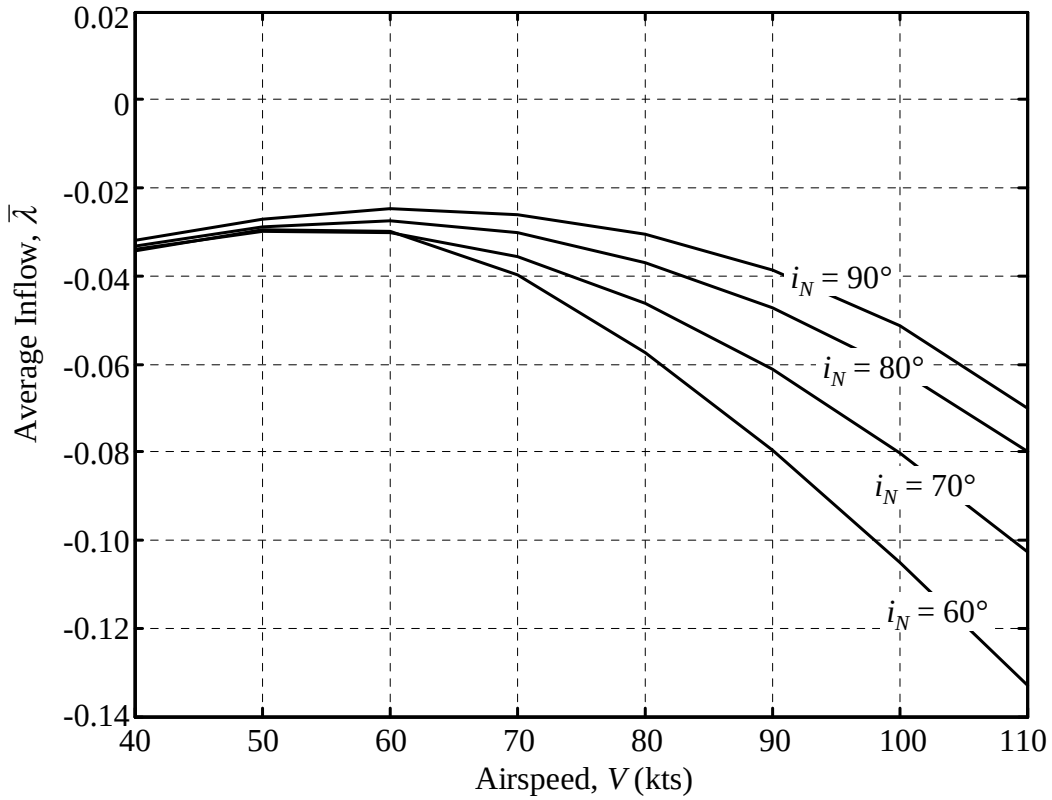

Figure 5.10. Effect of nacelle tilt on average inflow for γ= -6° and δ_f = 40°.

The previous figure shows that the nacelle tilt does indeed have a large influence on the average inflow value, especially at a higher airspeed. At slower airspeeds, the rotor carries most of the total lift and a change in the nacelle tilt is accompanied by a change in fuselage pitch in order to maintain a fairly constant tip-path-plane angle. The resulting average inflow is therefore similar between the different configurations since the tip-path-plane angle is approximately the same. At higher airspeeds however, the airframe carries a larger portion of the total lift, and as such a change in the nacelle tilt does not require that the tip-path-plane remain constant. Therefore, tilting the nacelles down increases the inflow through the rotor. The large inflow values associated with lower nacelle tilt angles lead to a larger average miss-distance but as mentioned in section 5.1.2, can also lead to strong BVI noise when the interaction geometry is conducive to efficient acoustic radiation. Since the goal of an approach procedure is to fully convert to helicopter mode at slow speed, it is not practical to use nacelle tilt alone to maximize the magnitude of the inflow. Yet, it should be kept in mind that a lower tilt of the nacelles at higher airspeed greatly increases the average inflow through the rotor, thereby reducing the likelihood of strong BVI noise generation.

5.2.3 Effect of Flap Deflection on Average Inflow

Another aircraft configuration parameter that significantly affects the trim is wing flap deflection. In typical flights, the use of flaps is predetermined for certain combinations of airspeed and nacelle tilt. Changing the flap angle alters the wing's aerodynamics and thus affects the trim angle of the fuselage pitch. The following figure shows the effects

of different flap deflection angles on the average inflow for a given nacelle tilt and descent angle.

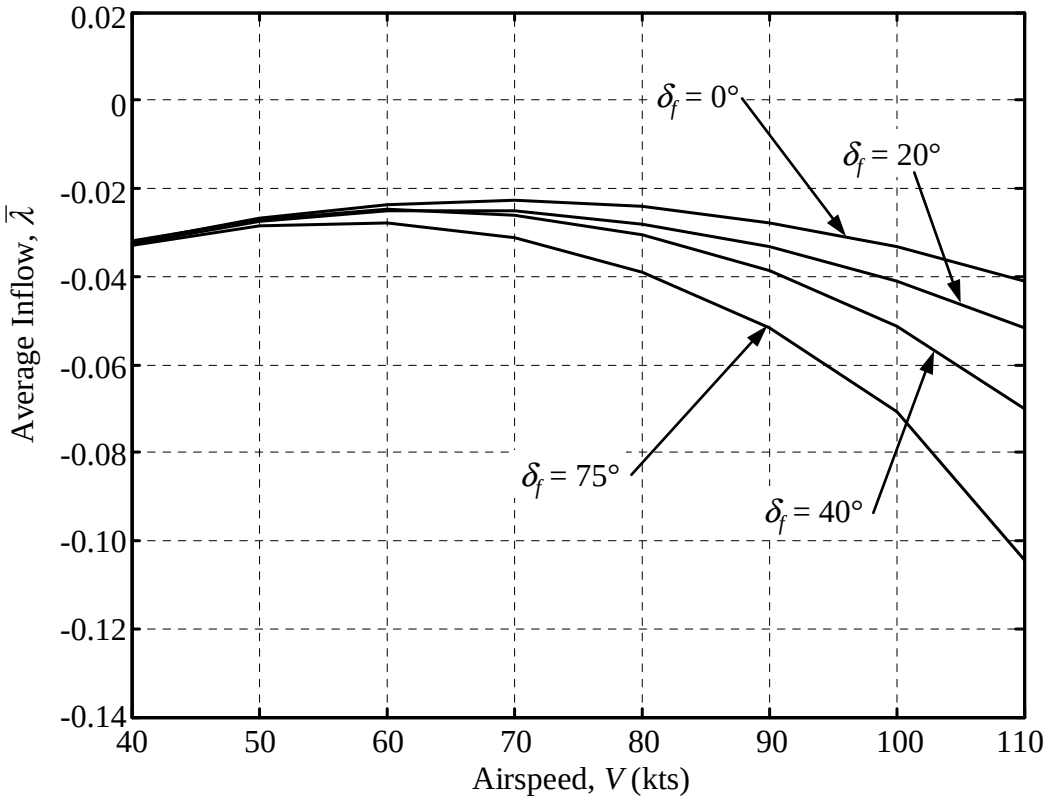

Figure 5.11. Effect of flap deflection on average inflow for i_N = 90° and γ = -6°.

The previous figure demonstrates that different flap deflections do not change the average inflow appreciably at lower airspeeds. This is because the flaps are not as effective in creating lift and drag at low airspeeds. However, as the airspeed is increased, the wing flaps become more effective and larger flap deflections become more effective. For large flap deflections, both the airframe lift and drag are increased, which causes the fuselage pitch to be reduced in order to maintain force and moment equilibrium. This causes a

forward tilt of the tip-path-plane, which increases the absolute value of the inflow through the rotor.

In this research, the flap deflection is held fixed at 40° for all approaches since the fuselage pitch is held fixed, thereby mitigating the effects of flap deflection. However, pilots have noted that a 75° flap deflection can be beneficial because it lowers the nose of the aircraft down during steep, low-powered descents (Ref. 40). Large flap deflections also allow the aircraft to fly at lower nacelle tilt settings at much lower airspeeds, since the wing can carry more lift. This can be beneficial in terms of BVI noise. The use of flaps to reduce noise and improve handling qualities is highly dependent on limits imposed on pilot workload and is subject to further research.

5.2.4 Effect of Flight Path Angle on Average Inflow

The flight path angle is expected to significantly affect the average inflow. In fact, flight path management is the most utilized BVI noise control mechanism on conventional helicopters (for example, see Refs. 3, 12, 82, 84-88, or 118). During a climb, level flight, or shallow descent in helicopter or near-helicopter mode the wake of the rotor is generally well below the rotor, thus leading to a low likelihood of strong BVI noise. As the descent angle is increased, the rotor wake is pushed closer to the rotor disk, resulting in a higher likelihood of strong BVI noise. For yet a steeper descent, the wake can actually be pushed above the rotor disk and thereby increase the miss-distances and reduce the strength of BVI noise. The actual descent angles for which the rotor is above or below the disk depends mostly on the disk loading. As mentioned, high disk loadings

associated with tiltrotors require very steep descent angles to push the wake above the rotor. Figure 5.12 shows the variations of average inflow with respect to the flight path angle.

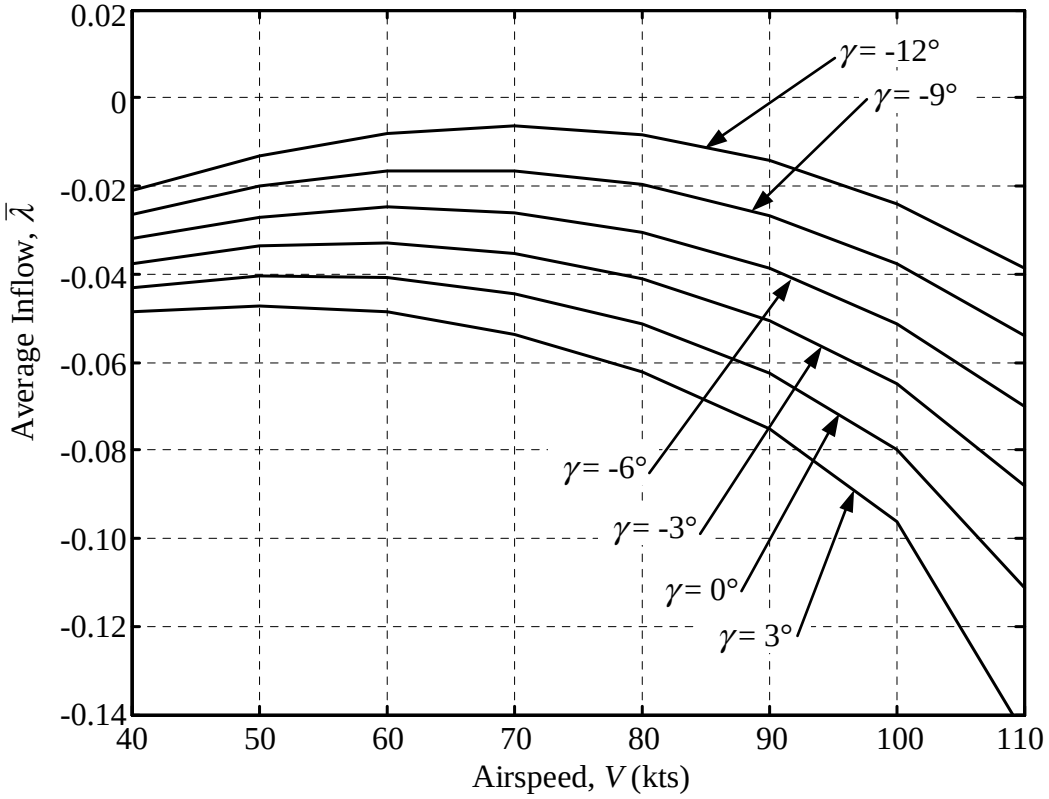

Figure 5.12. Effect of flight path angle on average inflow for i_N = 90° and δ_f = 40°.

As expected, the flight path angle exerts strong influence on the rotor's average inflow. For a given nacelle tilt and airspeed, a flight path angle that is steeper by 3° leads to an average inflow magnitude that is smaller by approximately 0.005 at 40 knots to 0.015 at 110 knots. The flight path angle is therefore a very useful means of controlling the average inflow through the rotor.

5.2.5 Effect of Deceleration on Average Inflow

In this section, the effect of deceleration on the average inflow is studied in a quasi-steady manner. The solution to the system of equations representing the longitudinal performance of the tiltrotor is still a steady-state solution, with the airspeed and deceleration specified independently of one another. This is equivalent to studying the effects of an added force, $F_{\dot{V}} = m\dot{V}$, acting in the direction opposite to drag for a deceleration. Previous research on helicopters has shown that a given deceleration can be used to push the wake above the rotor during a descent (Ref. 87). Figure 5.13 shows the effects of different decelerations on the average inflow.

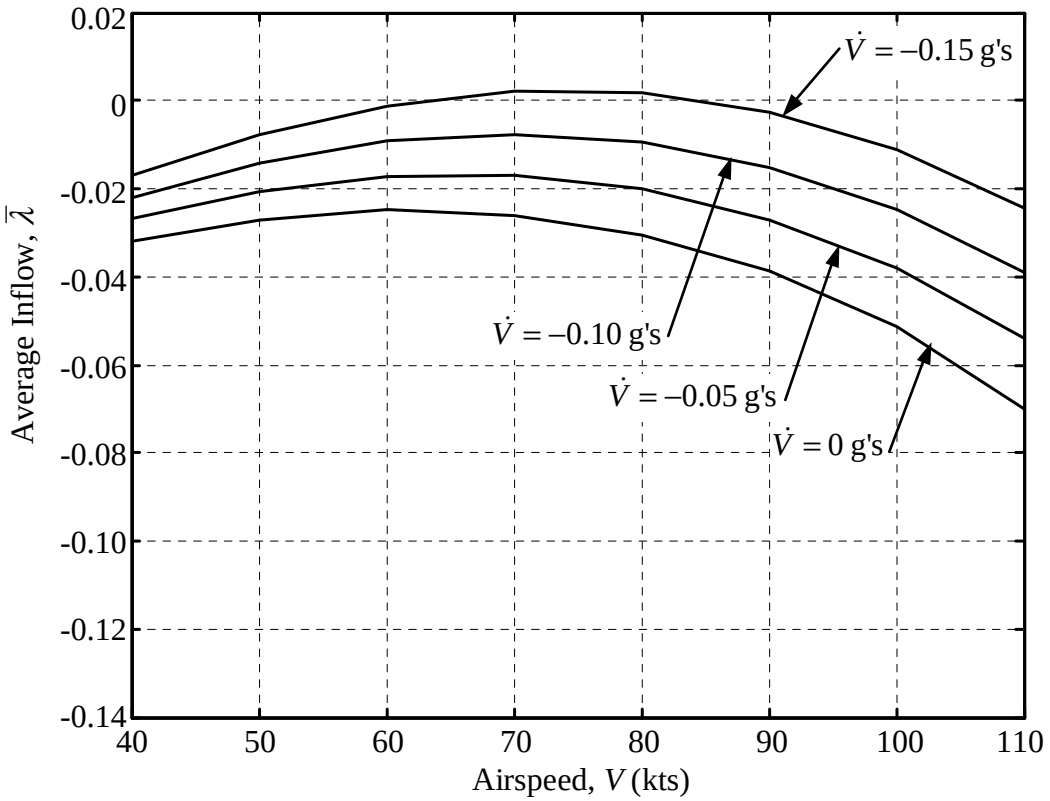

Figure 5.13. Effect of deceleration on average inflow for i_N = 90°, γ= -6°, and δ_f = 40°.

The previous figure illustrates that deceleration has a significant effect on the average inflow value for i_N = 90° and γ = -6°. In fact, the effect of deceleration is very similar to the effect of a change in flight path angle. Indeed, Ref. 87 showed that a simple equivalence between flight path angle and deceleration can be obtained for conventional helicopters (0.1 g's of deceleration is equivalent to a 5.7° decrease in the flight path angle). In regards to the tiltrotor, such a simple equivalence is more difficult to create due to the strong coupling between the airframe aerodynamics and the rotor operating condition. However, Figures 5.12 and 5.13 show that for this XV-15 in helicopter mode, the relationship still holds true: 0.1 g's of deceleration is equivalent to approximately a 6° decrease of the flight path angle. Still, because of the tiltrotor's high downwash velocities, very large decelerations would have to be used in order to push the wake above the rotor. Therefore, it is concluded that high decelerations should be avoided during an approach to land, especially when the nacelle tilt is near 90° (helicopter mode).

5.3 Design of Low BVI Noise Approaches

The previous section explored the effects of various flight parameters on the trim state of the aircraft and in particular on the average inflow value, which in section 5.1.1 was proven to capture the general trends of measured BVI noise. In this section, inflow and deceleration constraints will be applied to the baseline approach based on knowledge gained in the previous sections.

5.3.1 Constrained Approach Methodology

The baseline approach profile considered in this research was presented in Chapter 2 and is repeated here for convenience.

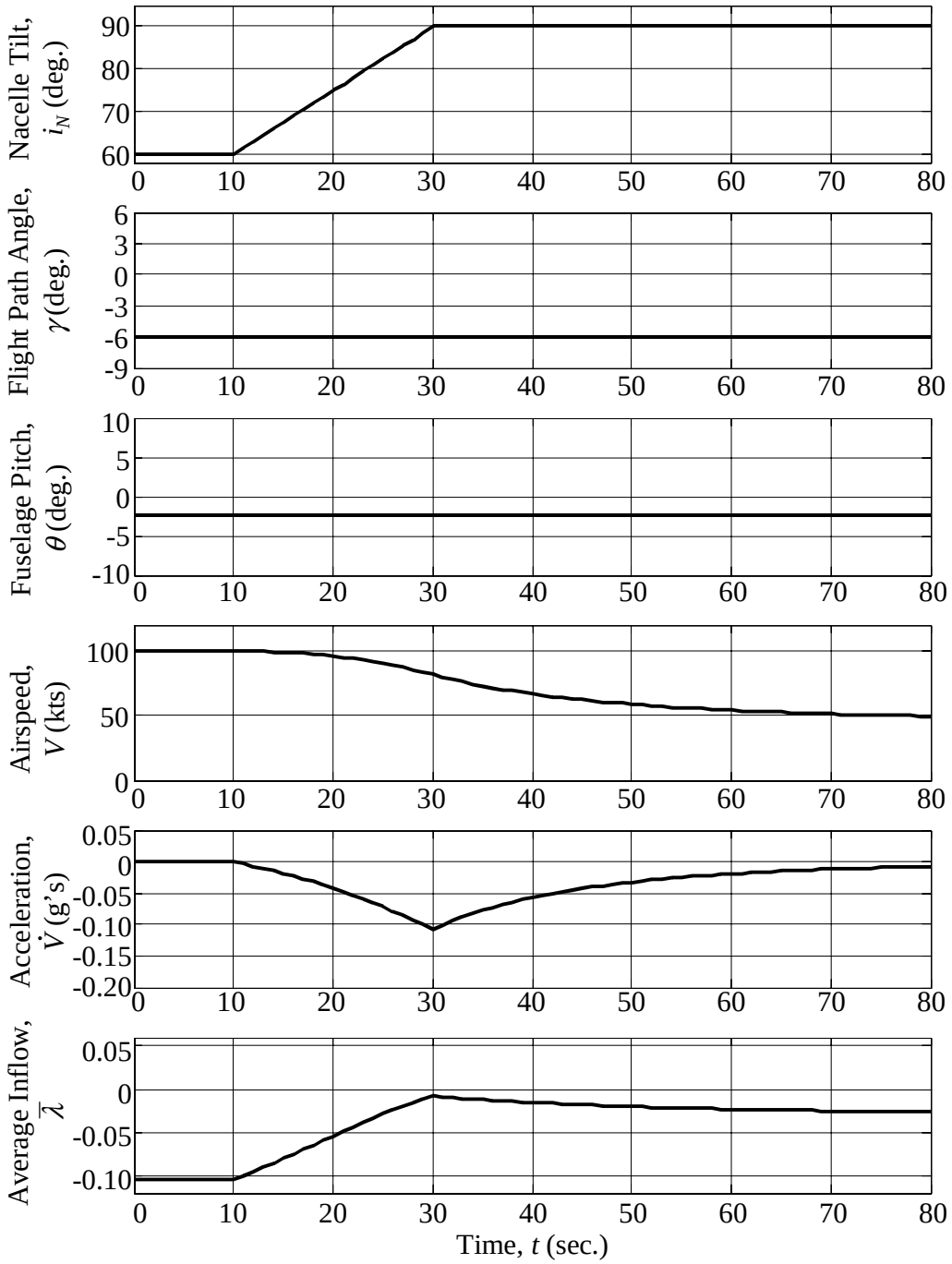

Figure 5.14. Baseline approach profile.

As Figure 5.14 shows, the value of the average inflow changes drastically during the conversion maneuver. At a 60° nacelle tilt, the magnitude of the inflow is large but as the nacelles are rotated upward the inflow reduces and eventually reaches a minimum value at t = 30 seconds. It remains fairly small for the remainder of the simulation. Clearly, the average inflow values in this particular approach profile are undesirable in terms of BVI noise.

In order to constrain the inflow, an inequality constraint equation ($|\bar{\lambda}| \geq \bar{\lambda}_{limit}$) is included in the system of equations that represents the aircraft's performance. If this constraint condition is violated, the minimum inflow is enforced in the form of an additional equation in the system ($\bar{\lambda} = \bar{\lambda}_{limit}$) and the system becomes over-specified: there are now seven equations, six unknowns and four prescribed variables. One of the prescribed variables can no longer be specified in order to solve the system. It was shown in the previous section that the most effective way to control the inflow for a given nacelle tilt was to reduce the descent angle. Therefore, the flight path angle is no longer prescribed: it is solved for by the system in order to enforce the constraint. The flight path angle then becomes the BVI noise control mechanism. The nacelle tilt schedule, fuselage pitch, and flap deflection remain fixed.

Figure 5.14 also shows that the maximum deceleration caused by tilting the nacelles is approximately -0.10 g's. This maximum deceleration is high because -0.05 g's is usually considered the limit for passenger comfort in commercial operations. In order to ensure

that the approach profiles designed in this research are suitable for commercial operations, constraints are also imposed on the deceleration.

Furthermore, constraining the maximum deceleration helps to maximize the inflow through the rotor (see section 5.2.5). How the deceleration constraint is implemented in the performance model is similar to the implementation of the inflow constraint: an inequality constraint equation is included in the system ($|\dot{V}| \leq \dot{V}_{limit}$). Once again, if this constraint condition is violated, the maximum deceleration is enforced in the form of an additional equation in the system ($|\dot{V}| = \dot{V}_{limit}$) and the system becomes over-specified. Since the nacelle tilt schedule, or nacelle tilt-rate, was shown to be the most effective in constraining the deceleration (Refs. 91-93), it is no longer prescribed and becomes an unknown solved for by the system when the deceleration constraint becomes enforced. Indeed, tiltrotor pilots use the tilt of the nacelles to reorient the thrust vector of the rotors and obtain powerful decelerations or accelerations (Ref. 112). Therefore, if the solution of the system leads to a larger deceleration than desired during the conversion to helicopter mode, the nacelle tilt-rate is reduced and tilt up of the nacelles is slowed down.

5.3.2 Approaches Constrained by Constant Inflow Limits

In this section, a constant average inflow constraint is applied to the baseline approach. This allows for the study of the change in flight path angle required to enforce a given inflow constraint. As section 5.1.2 showed, a simple average inflow limit does not ensure the complete elimination of BVI noise for all flight conditions but can drastically reduce

BVI noise over an entire approach profile. Three constant inflow limits are presented: $\bar{\lambda}_{limit} = -0.01$, $\bar{\lambda}_{limit} = -0.02$, and $\bar{\lambda}_{limit} = -0.03$. The next figure presents the first case.

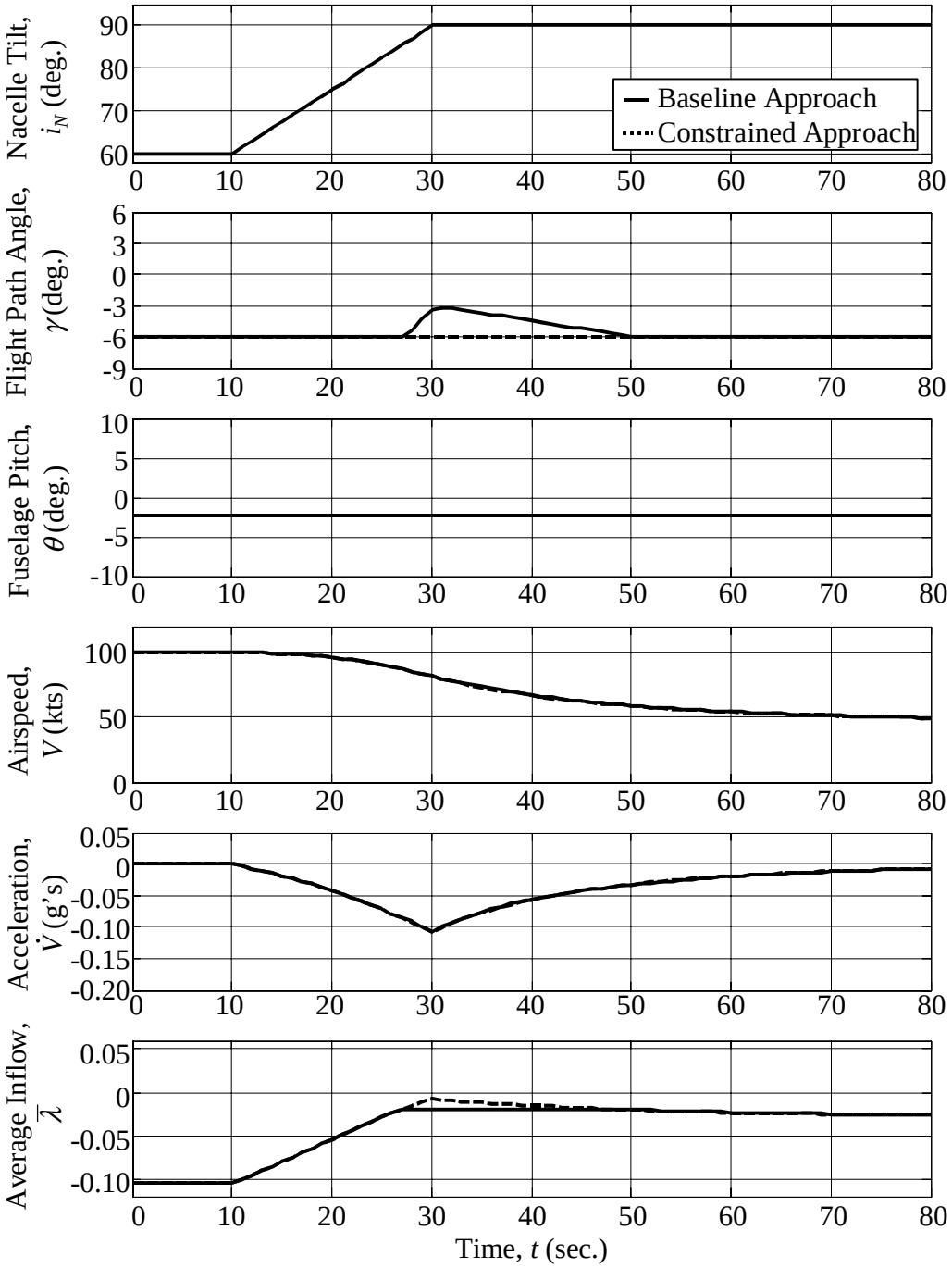

Figure 5.15. Constrained approach with $\bar{\lambda}_{limit} = -0.02$.

Figure 5.15 shows the change in flight path angle required to enforce an inflow constraint of $\bar{\lambda}_{limit} = -0.02$ on the baseline approach. The inflow constraint is enforced at t = 28 seconds. At that time, the descent angle must be flattened in order to keep the average inflow from violating the constraint. The result is a change in the flight path angle from the original γ = -6° to approximately γ = -3° and then back to γ = -6° when the inflow constraint is no longer enforced. The inflow constraint remains enforced for approximately 20 seconds. The required change in flight path angle is small and could be easily implemented in a typical flight procedure. However, the inflow constraint is not very stringent and could still yield significant BVI noise. The next figure shows the result of a much stricter inflow constraint of $\bar{\lambda}_{limit} = -0.035$.

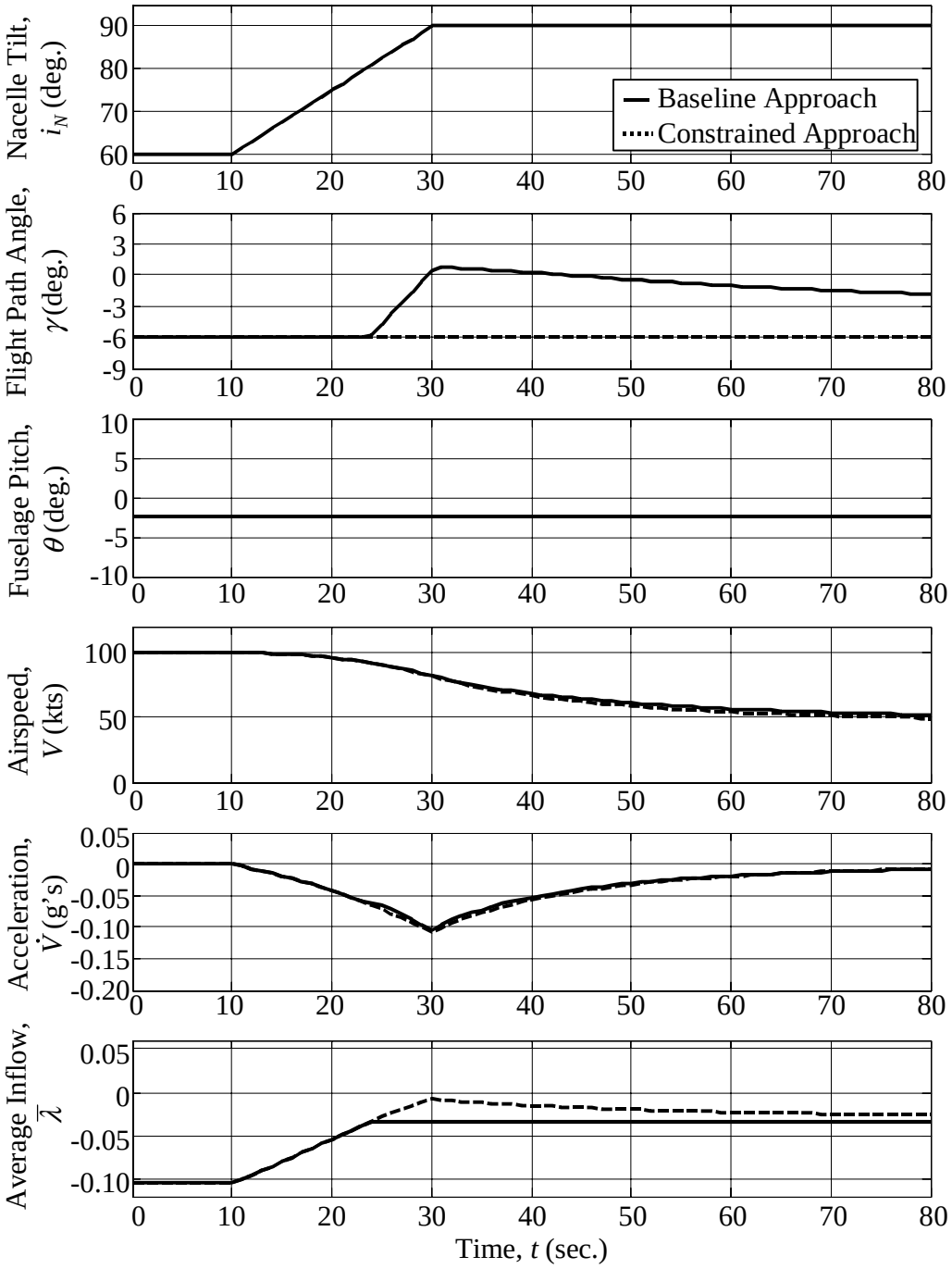

Figure 5.16. Constrained approach with $\bar{\lambda}_{limit} = -0.05$.

The previous figure shows that in order to achieve a more stringent average inflow constraint, the flight path angle must be changed appreciably. Indeed, even a short climb

segment is necessary. At the end of the 80 seconds of simulation, the inflow constraint is still enforced and the flight path angle is at approximately –1.5°. This highlights the fact that during a converting approach, a tiltrotor inevitably experiences flight conditions that lead to small absolute values of the average inflow. To avoid strong BVI noise, it is key to fly through small inflow regions with caution, i.e. with shallow flight path angles and small decelerations. The next figure shows a very stringent inflow constraint of $\bar{\lambda}_{limit} = -0.05$.

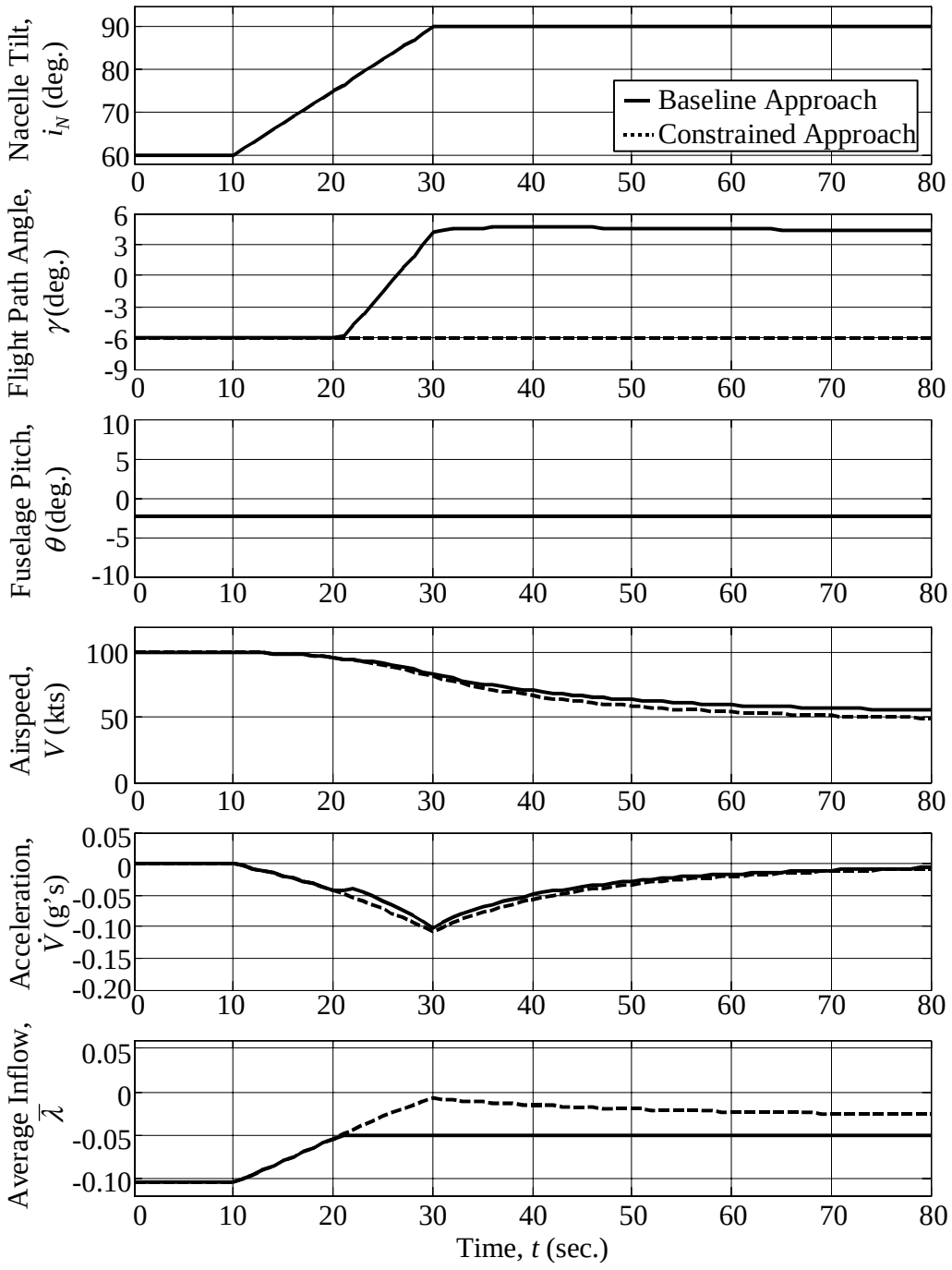

Figure 5.17. Constrained approach with $\bar{\lambda}_{limit} = -0.05$.

As Figure 5.17 shows, the application of a very strict constant average inflow constraint of $\bar{\lambda}_{limit} = -0.05$ means that the aircraft cannot descend in helicopter mode. In fact, in

order to achieve this constraint the tiltrotor must climb at approximately $\gamma = 5°$ for most of the flight. It is obvious that such a stringent constant inflow constraint is not acceptable, since the goal of the approach is to eventually land.

5.3.3 Approaches Constrained by Deceleration Limits

The baseline approach profile (Figure 5.14) contains a large maximum deceleration due to the upward tilting of the nacelles. In this section, three different approach profiles constrained by a maximum deceleration value are presented. The first deceleration constraint is shown in Figure 5.18 below, for $\dot{V}_{limit} = -0.075$.

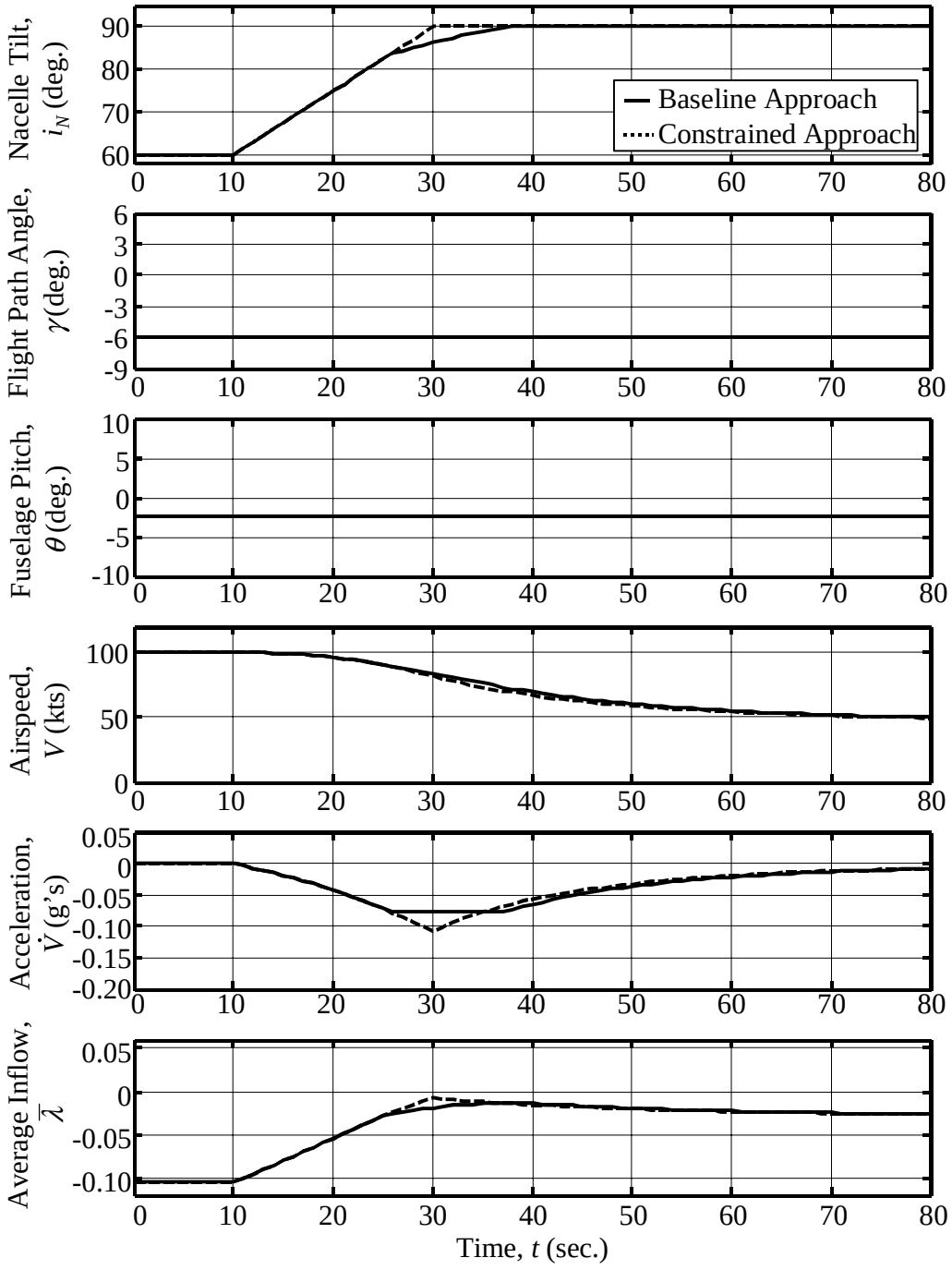

Figure 5.18. Constrained approach profile with $\dot{V}_{limit} = -0.075$.

As the previous figure shows, the constrained deceleration was achieved by slightly reducing the nacelle tilt-rate, starting at t = 26 seconds. The helicopter mode

configuration was reached 7 seconds later than in the baseline approach. Note that in the XV-15, the pilot cannot control the nacelle tilt-rate in-flight. Therefore, the approach profiles presented in this section would have to be approximated by carefully scheduling the nacelle tilt. This implementation issue is subject to further research.

The next figure shows a deceleration constraint of $\dot{V}_{limit} = -0.050$, which is considered a typical limit for passenger comfort during commercial flight operations.

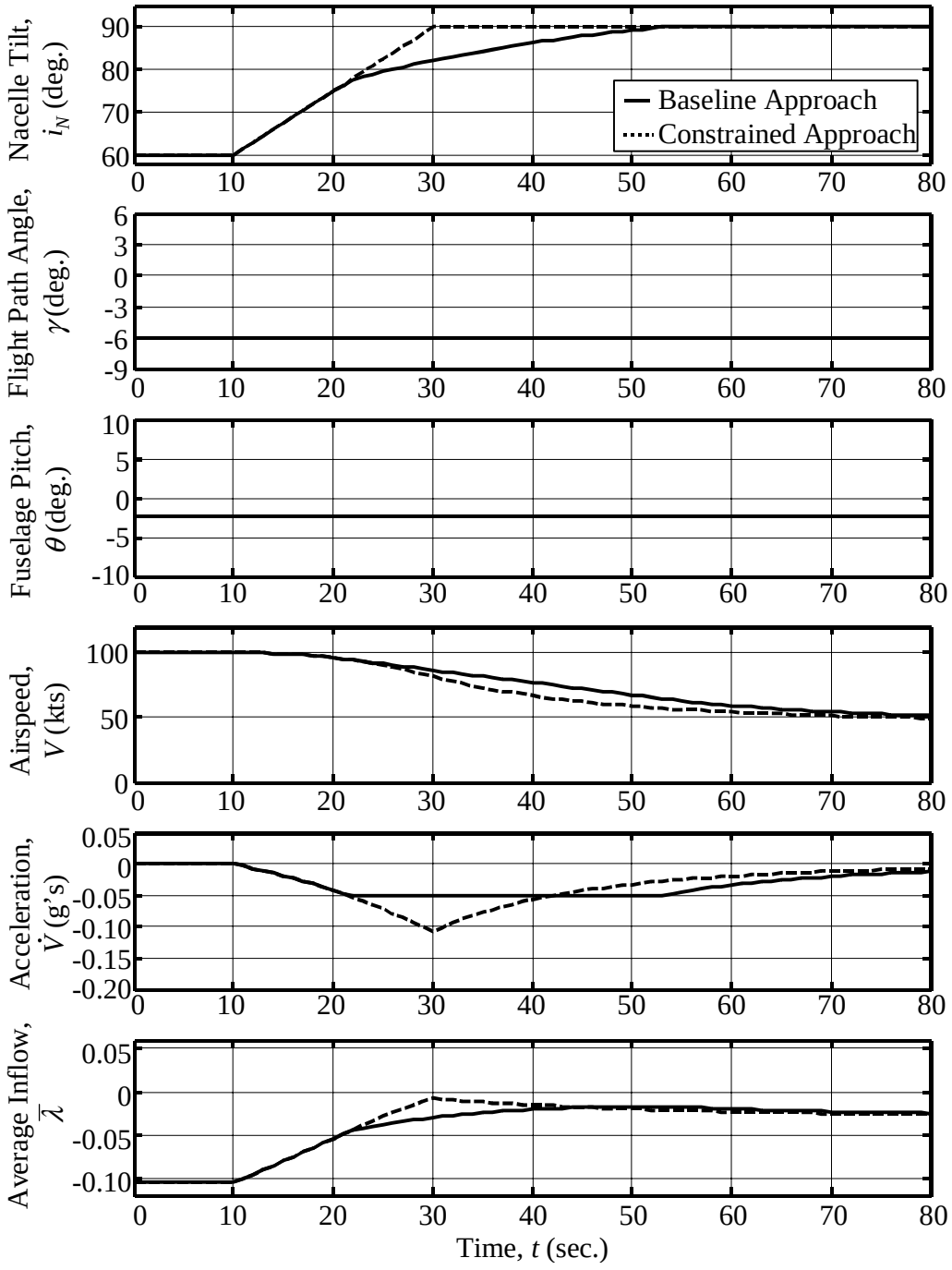

Figure 5.19. Constrained approach profile with $\dot{V}_{limit} = -0.050$.

Figure 5.19 shows that a more stringent deceleration constraint means conversion to helicopter mode is completed approximately 30 seconds later than in the baseline case. It

is also important to note that the deceleration constraint increases the absolute value of the average inflow during certain portions of the flight, particularly at t = 30 seconds. It was shown in section 5.2.5 that larger decelerations tend to push the wake up, as evidenced by the smaller value of the inflow. Thus, constraining the deceleration has the beneficial effect of slightly increasing the average miss-distances. However, using tilt-rate alone to increase the inflow above a certain threshold would yield very small values of the tilt-rate throughout the conversion and would lead to impractical and lengthy conversion times. The next figure shows a very stringent deceleration constraint of $\dot{V}_{limit} = -0.025$.

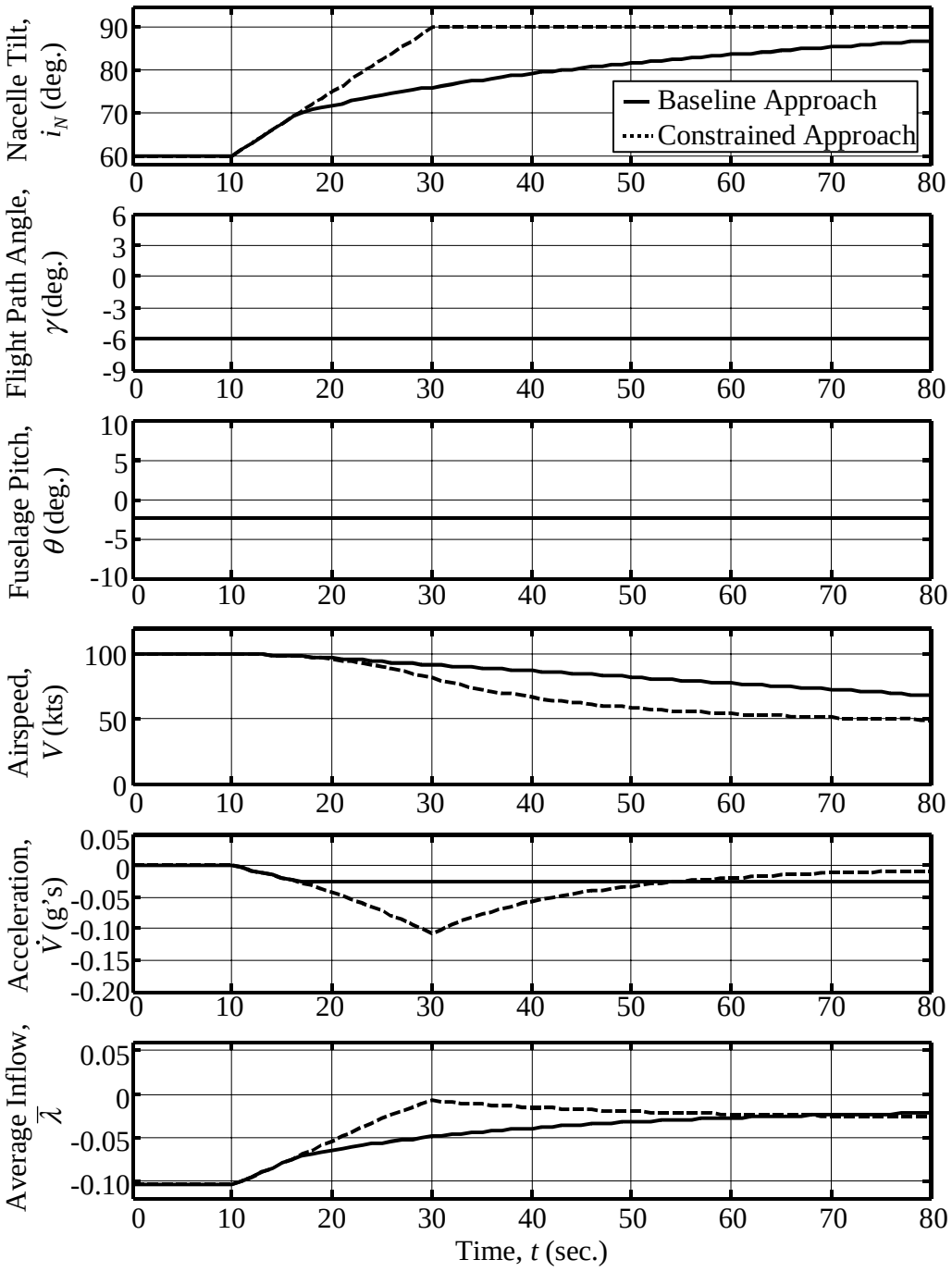

Figure 5.20. Constrained approach profile with $\dot{V}_{limit} = -0.025$.

Figure 5.20 shows that in order to achieve this strict deceleration constraint ($\dot{V}_{limit} = -0.025$), a large change in the nacelle tilt-rate is required. The average tilt-rate

during the constrained part of the simulation is approximately 0.2 deg./sec. as opposed to the initial 1.5 deg./sec. At the end of 80 seconds of simulation, the aircraft has not yet reached helicopter mode. This deceleration constraint is therefore too stringent to be practically implemented. The average inflow is increased for a large portion of the flight but still remains fairly small in the later flight segment.

5.3.4 Approach Constrained by Constant Inflow and Deceleration Limits

The next figure shows an approach profile resulting from: $\bar{\lambda}_{limit} = -0.035$ and $\dot{V}_{limit} = -0.050$. In this case, both the flight path angle and the nacelle tilt-rate are used to enforce the constraints. Figure 5.21 shows the results of this constrained approach.

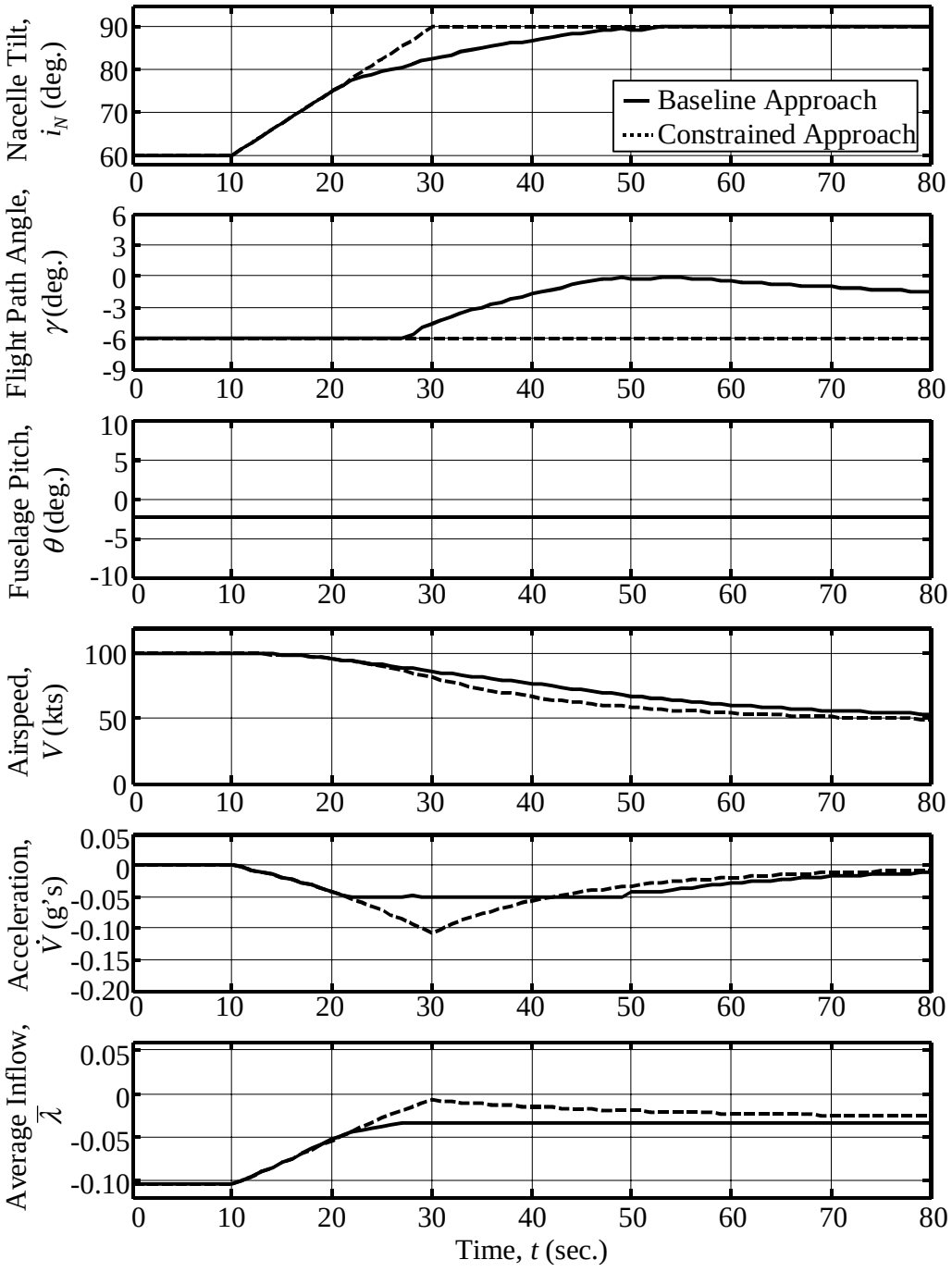

Figure 5.21. Constrained approach profile with $\bar{\lambda}_{limit} = -0.035$ and $\dot{V}_{limit} = -0.050$.

The previous figure demonstrates that both constraints were successfully enforced. A very short level flight segment was necessary and after 80 seconds, with the average

inflow still constrained, the required flight path angle was approximately equal to -1.5°. The nacelle tilt-rate was constrained to approximately 0.4 deg./sec. at t = 22 seconds in order to maintain an acceptable deceleration.

The approach profile shown in Figure 5.21 is a feasible noise abatement approach that maintains acceptable passenger comfort and average inflow values that decrease the likelihood of strong BVI noise. However, section 5.1.1 showed that the average inflow limits that correspond to different levels of measured BVI noise are dependent on the airspeed and nacelle tilt. Therefore, it is expected that a constant average inflow constraint will successfully reduce BVI noise only for portions a complete approach. The next section develops and then implements average inflow constraints based on measured noise in order to refine the low noise approach presented in this section.

5.3.5 Approaches Constrained by Inflow Limits Based on Measured Noise

Figures 5.2, 5.3, and 5.4 illustrated the relationship between average inflow and measured BVI noise for various airspeeds and nacelle tilts. From this relationship, it is possible to identify inflow limits that correspond to different levels of BVI noise on the hemisphere. The following three tables present the inflow limits that lead to: 1) a maximum measured BVI noise of 107 dBA, 2) a maximum measured BVI noise of 105 dBA and 3) no measured BVI noise (meaning no BVI noise levels above other non-impulsive noise levels). The results are presented as a function of airspeed and nacelle tilt.

Table 5.1. Average inflow limits leading to 107 dBA maximum measured BVI noise.

	V = 40 kts	V = 60 kts	V = 80 kts	V = 100 kts
i_N = 70°	-0.0272	-0.0348	-0.0480	-0.0860
i_N = 80°	-0.0240	-0.0332	-0.0420	-0.0750
i_N = 90°	-0.0209	-0.0302	-0.0357	-0.0651

Table 5.2. Average inflow limits leading to 105 dBA maximum measured BVI noise.

	V = 40 kts	V = 60 kts	V = 80 kts	V = 100 kts
i_N = 70°	-0.0408	-0.0408	-0.0514	-0.0888
i_N = 80°	-0.0320	-0.0370	-0.0454	-0.0760
i_N = 90°	-0.0246	-0.0355	-0.0427	-0.0651

Table 5.3. Average inflow limits leading to no measured BVI noise.

	V = 40 kts	V = 60 kts	V = 80 kts	V = 100 kts
i_N = 70°	-0.0432	-0.0450	-0.0615	-0.0905
i_N = 80°	-0.0392	-0.0399	-0.0540	-0.0760
i_N = 90°	-0.0375	-0.0382	-0.0480	-0.0651

The inflow limits presented in the previous tables were obtained by using the neural network noise model to predict noise as a function of flight condition. Curves can be plotted for the three different average inflow limits by parametrically simulating a range of airspeed and nacelle tilt cases. The next three figures show the resulting average inflow curves.

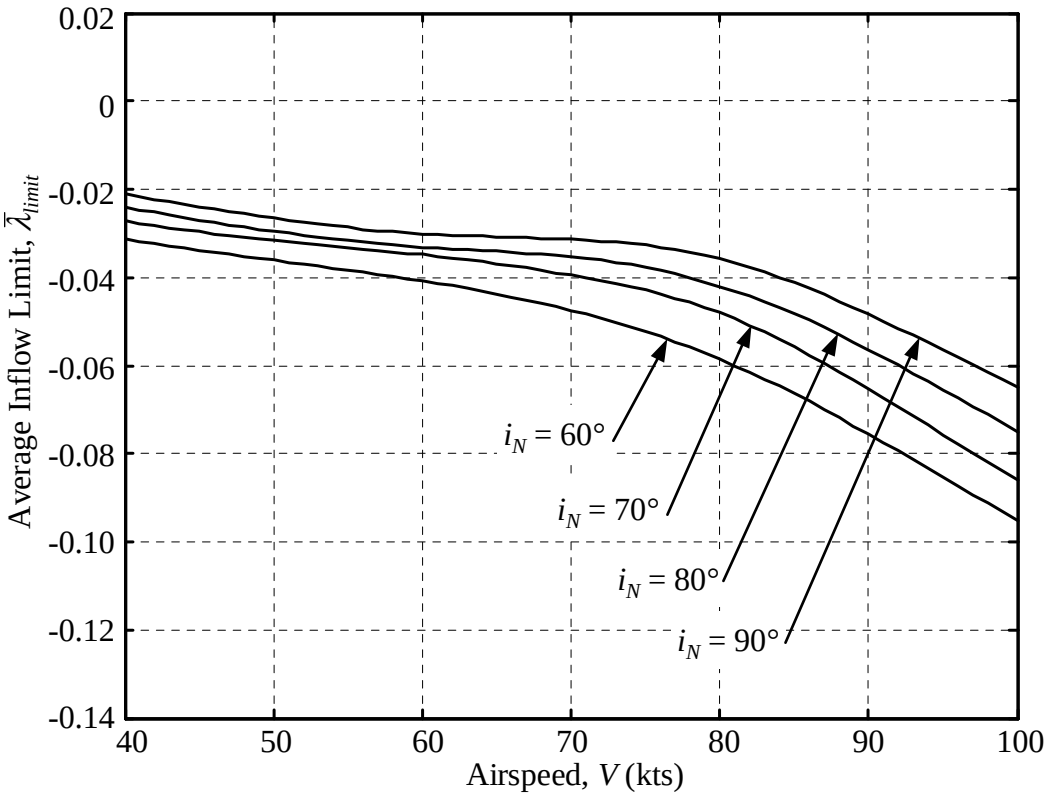

Figure 5.22. Average inflow limits leading to 107 dBA maximum measured BVI noise.

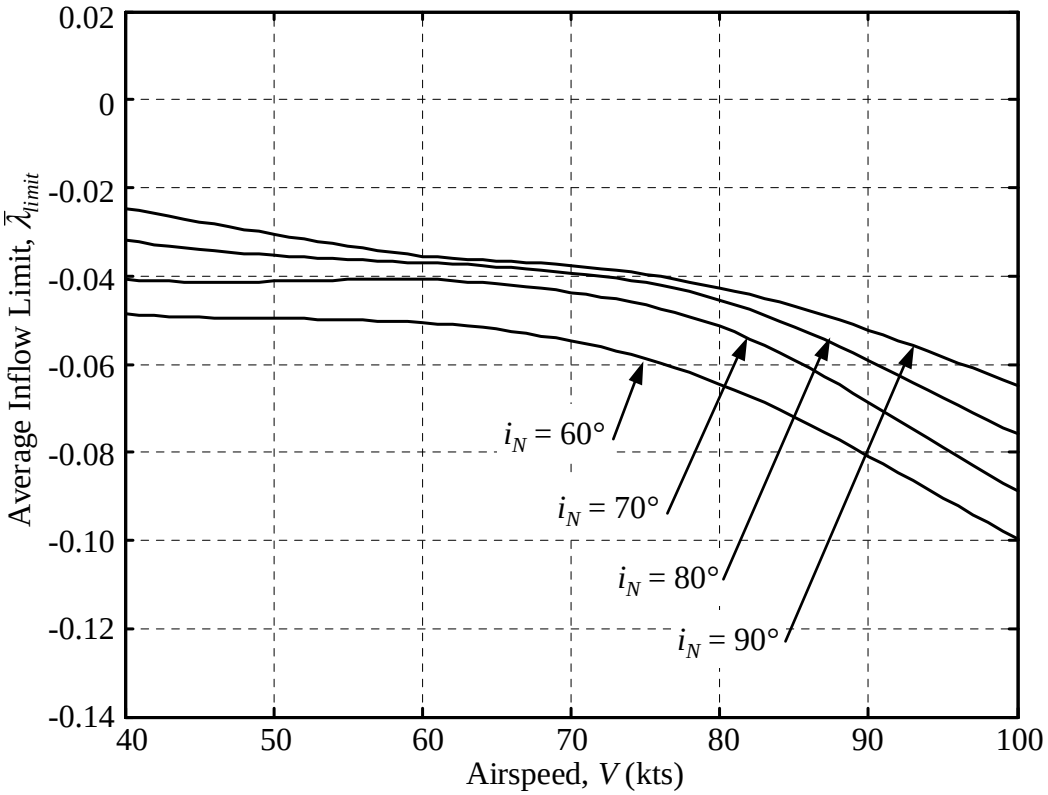

Figure 5.23. Average inflow limits leading to 105 dBA maximum measured BVI noise.

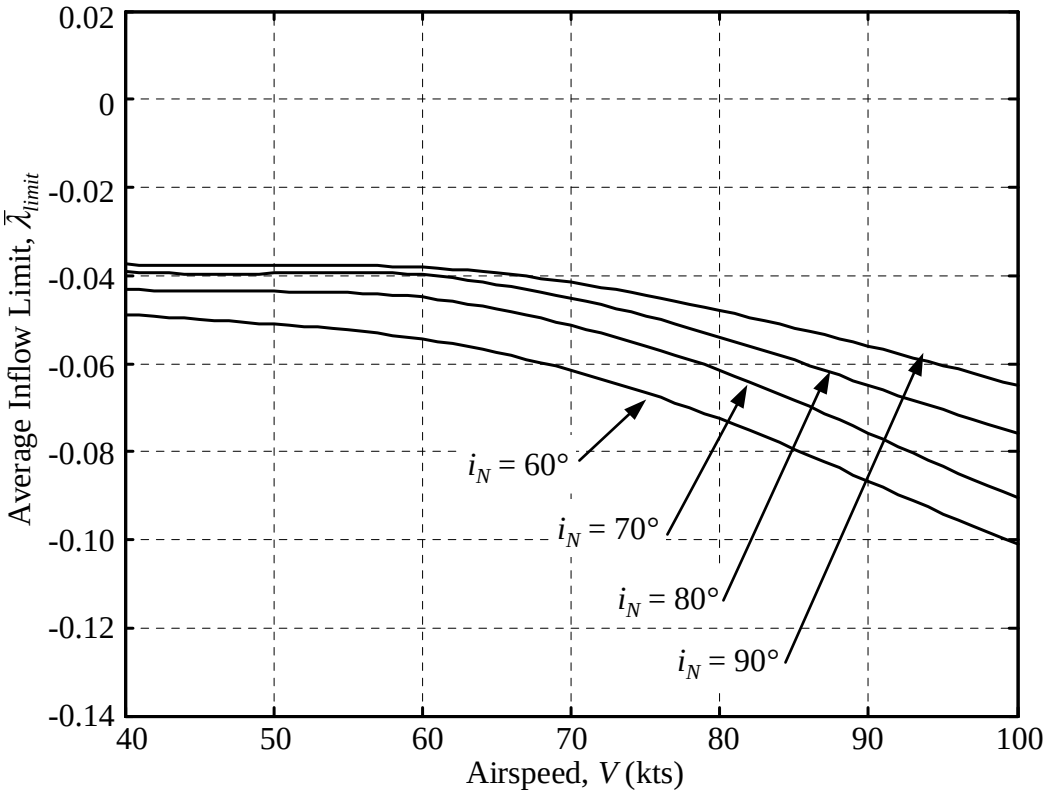

Figure 5.24. Average inflow limits leading to no measured BVI noise.

The inflow limit curves presented in the previous three figures can now be used to design approach profiles that reduce BVI noise levels below a certain known level or, possibly, eliminate BVI noise completely. The next figure shows an approach profile constrained by $\dot{V}_{limit} = -0.050$ and an inflow limit that leads to a maximum BVI noise of 107 dBA on the hemisphere.

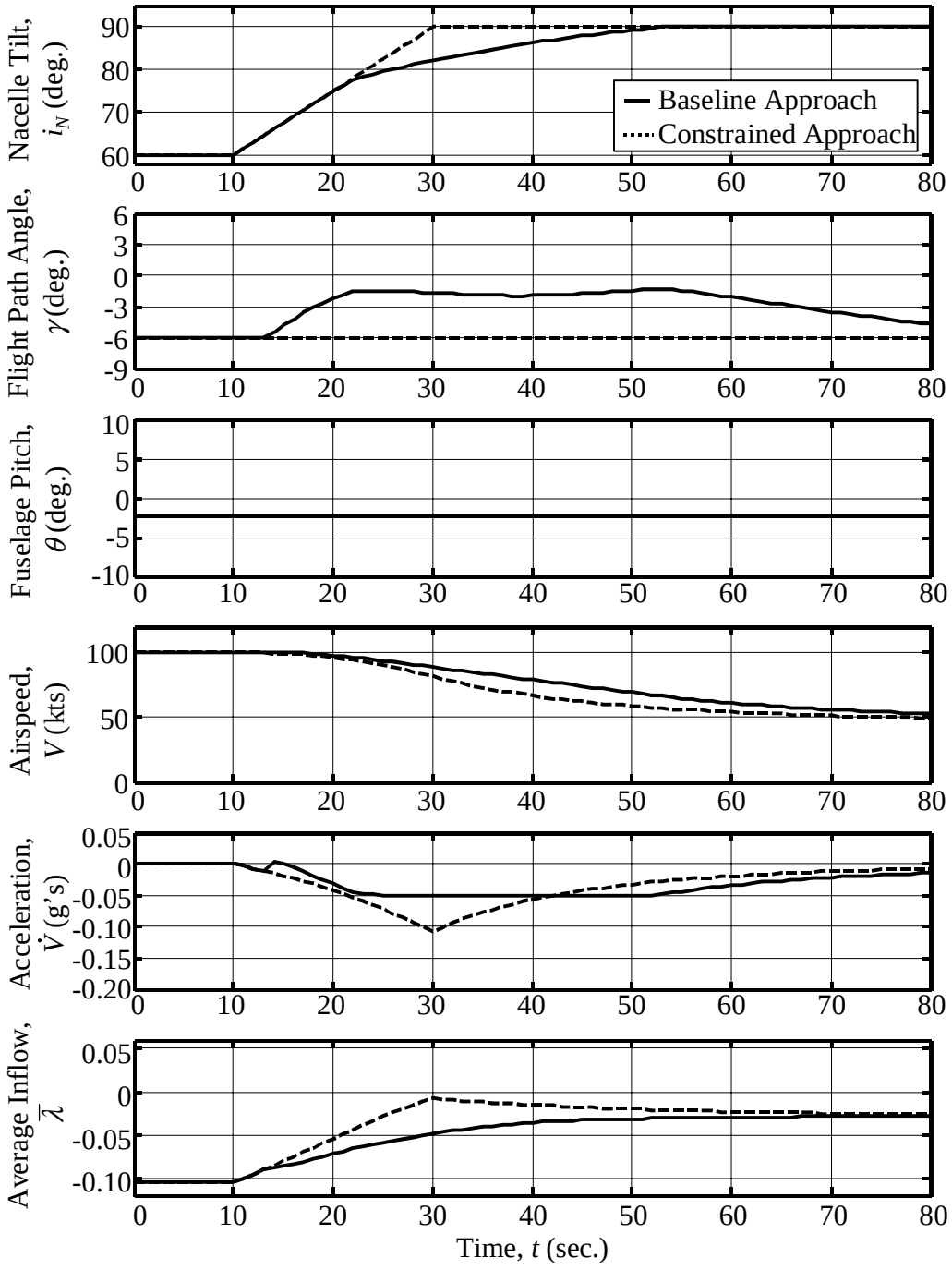

Figure 5.25. Approach profile leading to a maximum measured BVI noise of 107 dBA.

Figure 5.25 shows that it is possible to achieve the required BVI noise constraint with a relatively small change in the intended trajectory. The descent angle is reduced to

approximately –1.5° at t = 25 seconds and is almost back to the original descent angle at t = 80 seconds. This low BVI noise approach profile would therefore be fairly easy to implement. The next figure shows an approach profile constrained by a maximum measured BVI noise of 105 dBA.

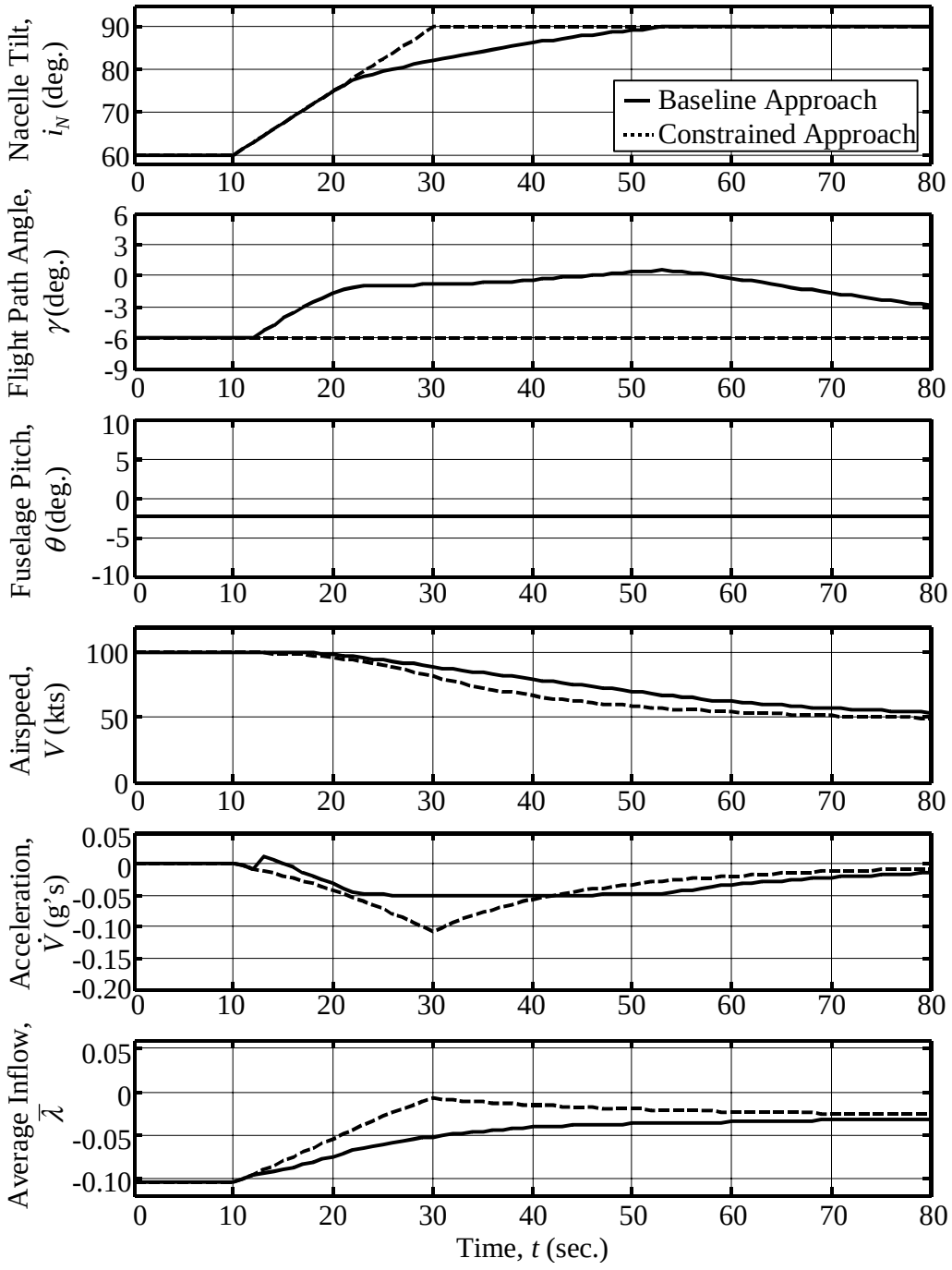

Figure 5.26. Approach profile leading to a maximum measured BVI noise of 105 dBA.

The previous figure shows that an approach profile that limits BVI noise to a maximum of 105 dBA is entirely feasible. This approach requires a segment of very shallow flight

path angle for approximately 30 seconds, from t = 25 seconds to t = 55 seconds. A short climb segment of 0.5° is also necessary between t = 46 seconds to t = 56 seconds After t = 56 seconds, the descent angle can be increased back toward the original, γ = -6°. The deceleration limit also ensures adequate passenger comfort throughout the conversion to helicopter mode. This approach profile yields a better BVI noise reduction than the one shown in Figure 5.22 but it requires a larger modification of the intended flight trajectory. The next figure shows a stringent constraint that leads to no BVI noise throughout the approach profile.

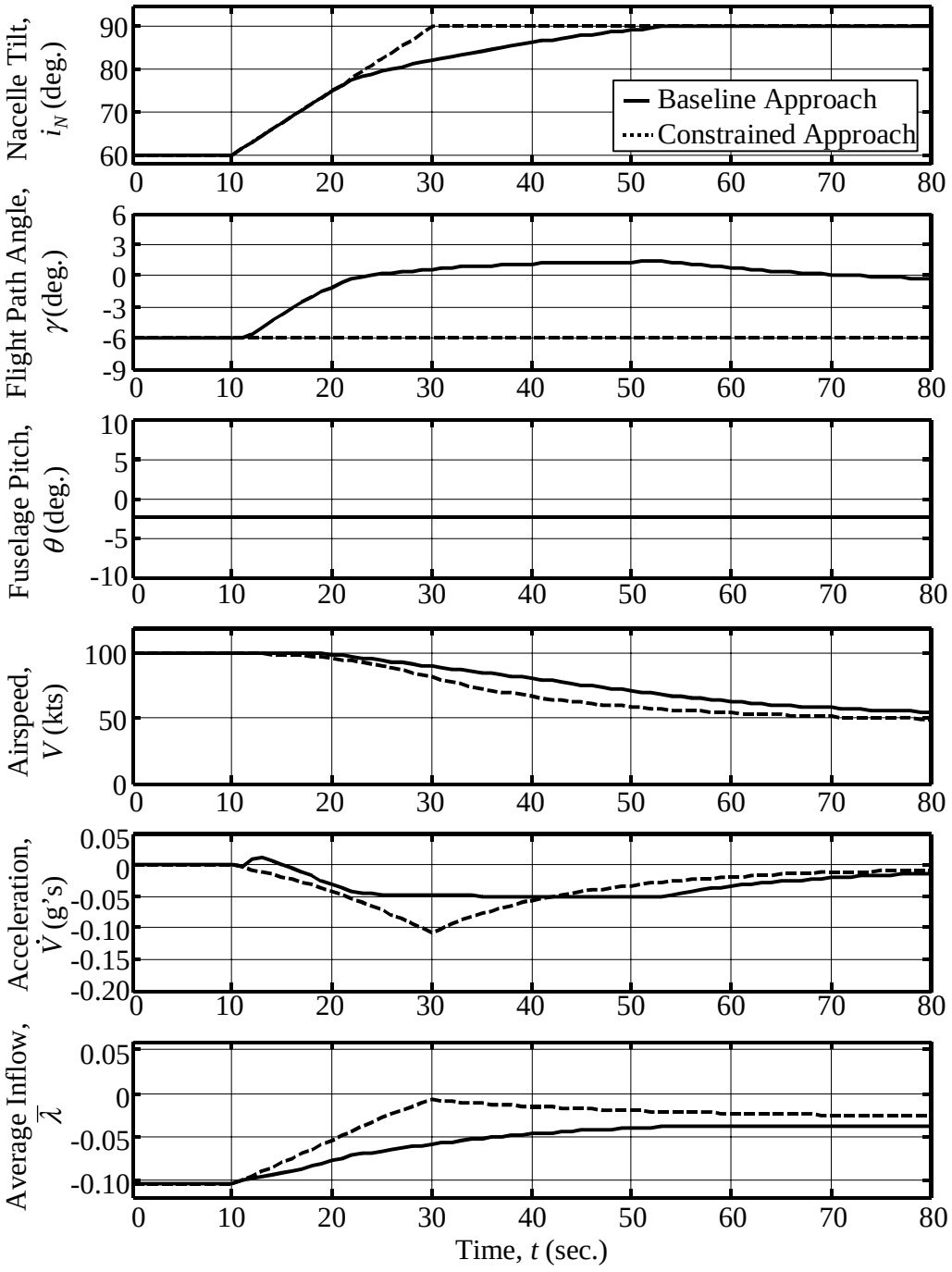

Figure 5.27. Approach profile leading to no measured BVI noise.

As the previous figure shows, attempting to reduce BVI noise levels below the level of other non-impulsive noise levels throughout a converting approach is not feasible,

because it requires the aircraft to climb for most of the flight. This noise constraint is therefore too stringent.

5.4 Integrated Noise Measures

In section 5.5, the various approach profiles developed in the last three sections (5.3.3, 5.3.4, and 5.3.5) will be evaluated by using the acoustic neural network to predict the noise produced by selected approaches. In this section, different measures of noise that can capture the relative *amount* of noise generated during an entire approach are developed.

Sound exposure level (SEL) is a noise metric that accounts for both the level and the duration of a noise event observed at a particular location. With SPL_i being the A-weighted sound pressure level (SPL) in dBA at a particular time step and *dt* being the size of the time step, the SEL can be computed as:

$$SEL = 10\log_{10}\left[\sum_{t} 10^{SPL_i/10} \cdot dt\right] \tag{5.3}$$

In this research, the SEL metric is used to obtain "hemisphere SEL" and "ground plane SEL" representations of the noise produced by a given approach profile.

5.4.1 Hemisphere Sound Exposure Level

The neural network noise model can be used to obtain noise hemispheres at each time step of a given approach profile, like the baseline approach presented in Figure 5.14. In order to obtain a single SEL hemisphere that represents a complete approach profile, equation (5.3) is used at each point on the hemisphere. The presentation of "SEL hemispheres" is unconventional, but it provides a means to compare the relative increase or decrease of the noise at the source for different approach profiles.

5.4.2 Ground Plane Sound Exposure Level

The potential low-noise approach profiles developed in this chapter were designed to reduce BVI noise on a hemisphere surrounding the aircraft. This corresponds to reducing source noise. However, in most instances the observer is located on the ground. Therefore, it is useful to analyze the ground noise impact of the various approach procedures.

In order to propagate a noise level from the source to a particular ground observer location, the retarded time equation must be solved. This equation determines the difference between the observer time and the acoustic emission time. This procedure was described in section 3.4 when it was used to link a ground microphone noise level to the aircraft's performance-state at the time of emission. However, the effect of spherical spreading on the noise level is taken into account in the present case. The following

relation gives the decrease in noise from a point on a hemisphere (at radius $r_{hemisphere}$ from the source) to a point on the ground (at radius r_{ground} from the source):

$$10^{\frac{SPL_{ground}}{10}} = \left(\frac{r_{hemisphere}}{r_{ground}} \right) \cdot 10^{\frac{SPL_{hemisphere}}{10}} \tag{5.4}$$

The spherical spreading term corresponds to a decrease of approximately 6 dBA per doubling of the distance.

Because no frequency information is available for the noise data, the effects of atmospheric absorption, Doppler shift, and diffraction are neglected. These effects do not change the general conclusions presented herein.

Using the procedure outlined above, the noise on a ground plane can be calculated as a function of time for a given approach profile. The results are then presented in terms of a ground plane SEL computed from equation (5.3). In this Dissertation, the results are shown on a ground plane that measures 12,000 feet in length and 4,000 feet in width.

An average SEL metric is also used in this research. It represents a measure of the relative merit of a candidate low-noise approach through a single number given by (where N is the number of hemisphere or ground plane positions):

$$SEL_{avg} = 10\log_{10}\left[\frac{1}{N}\sum_{i} 10^{\frac{SEL_i}{10}}\right] \tag{5.5}$$

In the next section, the different noise metrics introduced here are used to analyze the best candidate low-noise approach profiles and compare them to the baseline approach profile.

5.5 Analysis of Low BVI Noise Approaches

In sections 5.3.2 through 5.3.5, potential low-noise approaches were designed by applying average inflow and deceleration constraints. Both constant inflow constraints and inflow constraints based on measured noise were presented. In this section, three of the potential low-noise approaches are compared to the baseline approach profile. The candidate noise abatement profiles are identified as follows:

Approach 1: Approach with $\bar{\lambda}_{limit} = -0.02$ and $\dot{V}_{limit} = -0.050$.

Approach 2: Approach leading to a maximum BVI noise of 107 dBA on the hemisphere.

Approach 3: Approach leading to a maximum BVI noise of 105 dBA on the hemisphere.

5.5.1 Comparison of Sound Exposure Level on Hemisphere

The following figure shows the hemisphere SEL results for the four approach profiles. Each result is presented on a flattened hemisphere. The figure gives an indication of the

benefits of the various low-noise approaches with regards to the noise levels at the source.

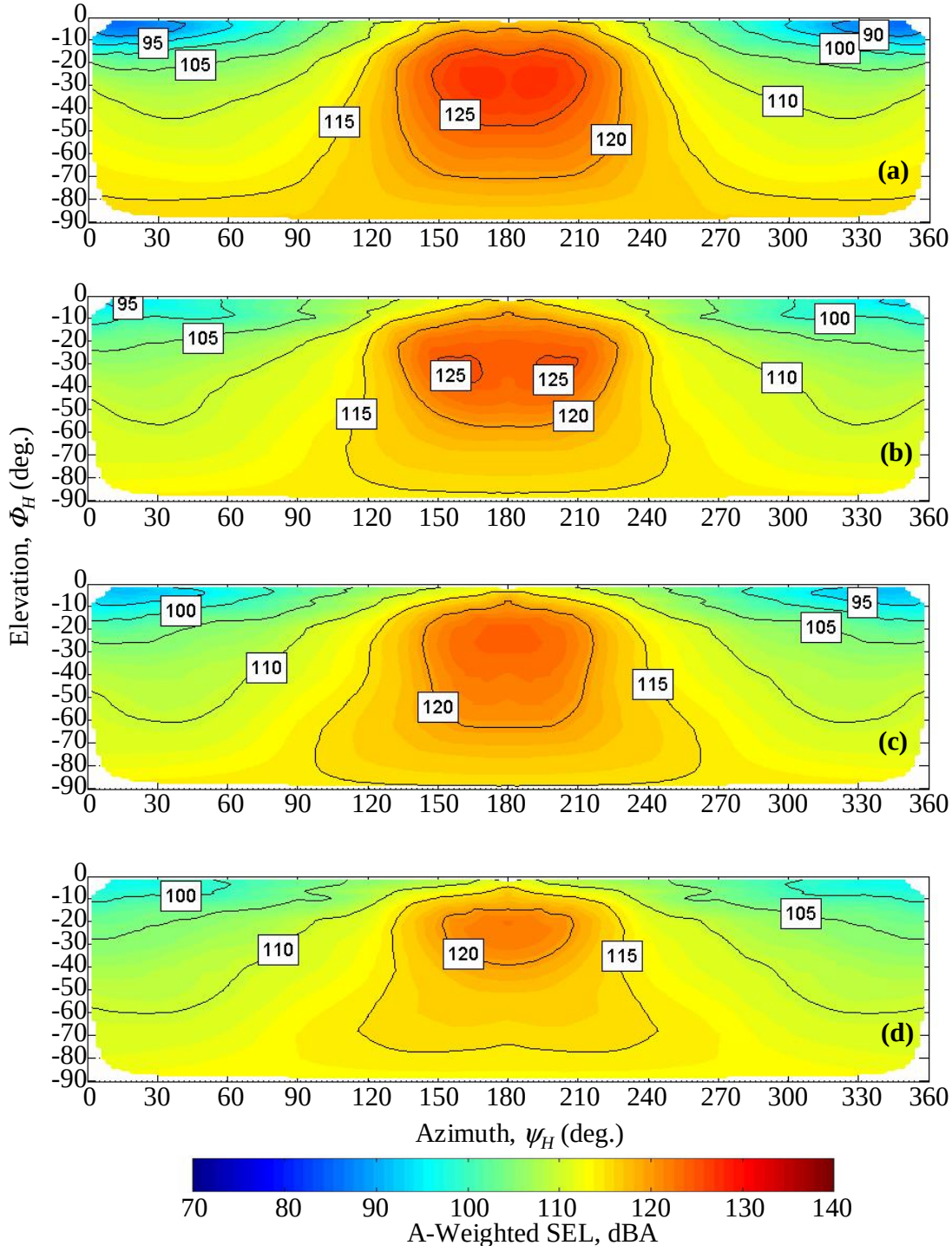

Figure 5.28. Hemisphere SEL for (a) baseline approach, (b) approach 1, (c) approach 2 and (d) approach 3.

The hemisphere SEL for the baseline approach is shown in Figure 5.28(a). A strong hotspot can be seen at 180° azimuth and -25° elevation. Approach 1 applies a constant inflow constraint and a deceleration constraint to the baseline approach. An appreciable decrease in the strength of the hotspot is evident. Approach 2 was designed to avoid a SPL greater than 105 dBA on the hemisphere during the entire approach. In this case the reduction in the strength of the SEL hotspot is much more pronounced. The last approach profile shows a drastic SEL reduction over the baseline approach. The 120 dBA contour line covers an area on the hemisphere approximately five times smaller than for the baseline approach.

The next figure compares the resulting average and maximum SEL on the hemisphere, as well as the peak SPL during each of the four approaches, and thereby summarizes the source noise reductions achieved by the different low-noise approaches.

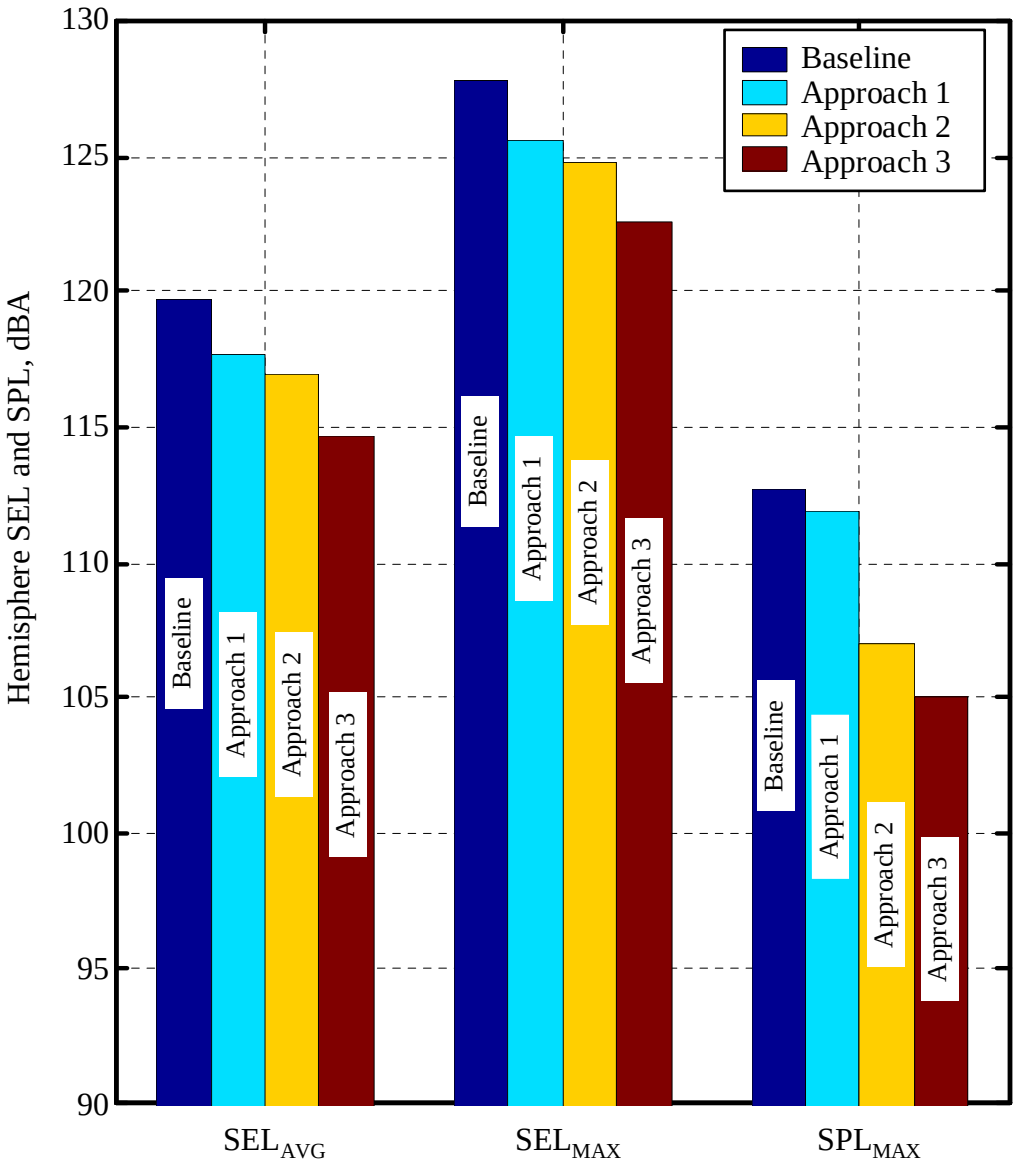

Figure 5.29. Summary of hemisphere noise results.

As the previous figure indicates, all of the constrained approaches successfully reduce noise at the source as compared to the baseline approach. Clearly, approach 3 is the best in terms of noise reduction; it provides an approximately 5 dBA noise reduction for both SEL noise measures and an 8 dBA reduction in peak SPL. This is a large reduction in the

noise on the hemisphere considering that a 6 dBA reduction corresponds to a halving of the acoustic pressure.

5.5.2 Comparison of Sound Exposure Level on Ground Plane

The previous section showed that the low-noise approach profiles were successful in reducing the noise level on a hemisphere surrounding the tiltrotor. To assess the acoustic characteristics of the potential noise abatement procedures on the ground, this section shows ground plane contours for each of the four approach profiles.

The ground plane presented herein is 17,000 feet long by 4,000 ft wide. The aircraft is "flown" for 70 seconds at i_N = 60°, γ = -6°, and V = 100 knots prior to reaching the x = 0 feet ground plane location. This is done to obtain a representative noise summation at the ground plane that accounts for noise that was emitted before the aircraft reached the ground plane. At x = 0 feet, all of the four approaches intercept an altitude of 1,500 feet. At the end of 130 seconds of simulation, each approach therefore results in a different final range and altitude. Section 5.5.3 discusses the results obtained when all approaches are forced to achieve the same final range and altitude.

The following figure shows the aircraft's trajectory for each approach, with markers indicating the start of the conversion towards helicopter mode, as well as the 70°, 80°, and 90° nacelle tilt positions. The aircraft's flight direction is from left to right.

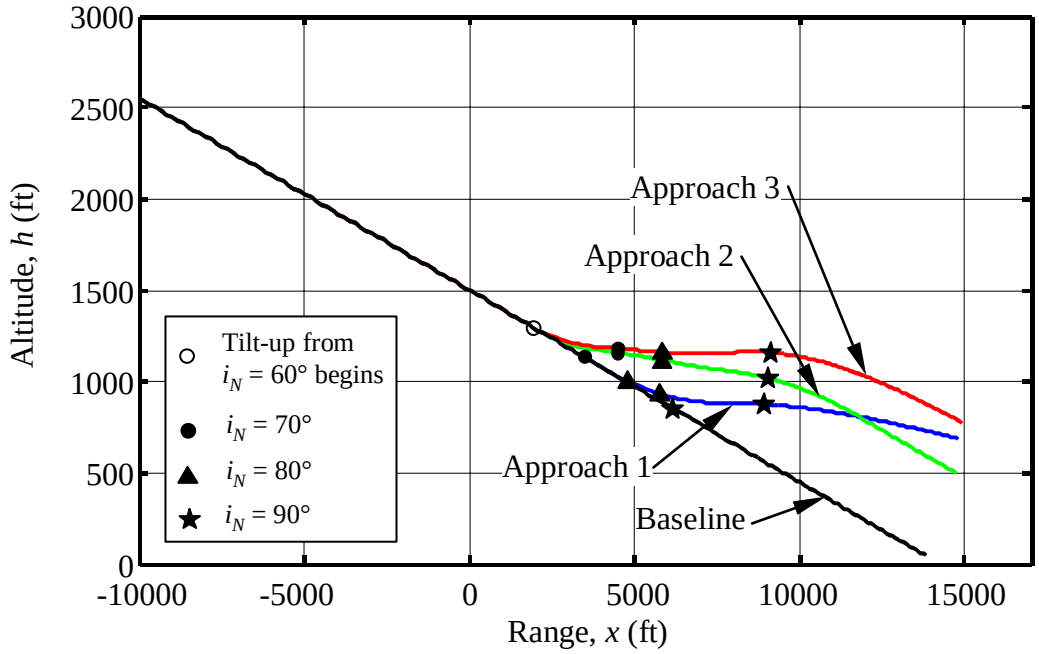

Figure 5.30. Trajectories for the four approach profiles.

The following figure shows the ground SEL contours for the baseline and the low-noise approaches.

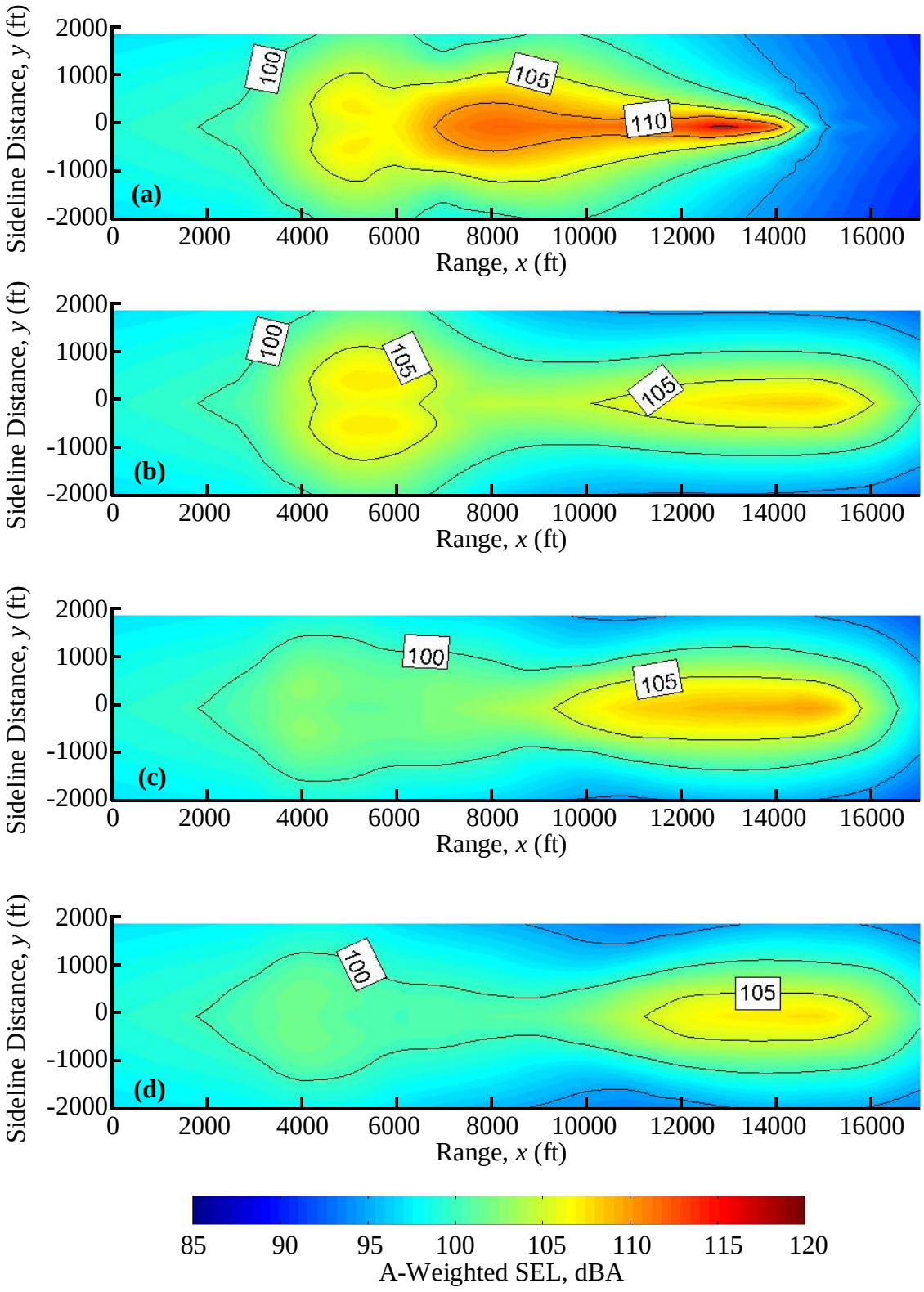

Figure 5.31. Ground SEL contours for (a) baseline approach, (b) approach 1, (c) approach 2 and (d) approach 3.

The previous figure shows that each of the three constrained approaches provides a definite ground SEL reduction over the baseline approach. The reduction in noise is the most dramatic for approach 3. Note that because of the flattening of the flight path angle that occurs for the low-noise approaches, altitude effects tend to improve noise reduction results (since the low-noise approaches are flown at a higher altitude than the baseline approach for the majority of the flight). This is discussed further in section 5.5.3.

The following bar chart summarizes the results of the four approaches.

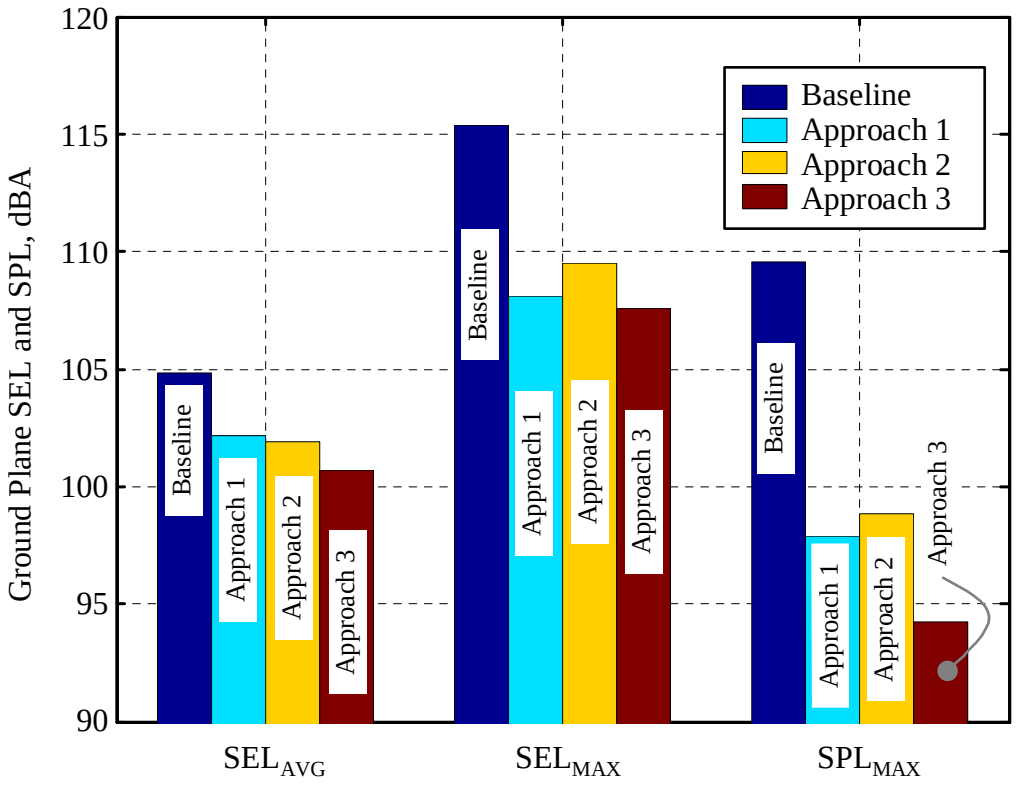

Figure 5.32. Summary of ground noise results.

From the previous chart, it is evident that each of the low-noise approach profiles provide at least a 3 dBA reduction in the SEL_{AVG}, SEL_{MAX}, and SPL_{MAX} values. Approach 3 reduces the average SEL value on the ground plane by approximately 5 dBA, which means that the acoustic pressure was reduced by almost half from the baseline.

The ground plane area covered by the different SEL noise contours is an interesting indicator of the merits of a low-noise approach profile that assists in land development near airports. The following table shows the ground plane area encompassed by an SEL of 1) 100 dBA and higher, 2) 105 dBA and higher and 3) 110 dBA and higher for the four different approach profiles.

Table 5.4. Ground area for various SEL contours.

	Percentage of the ground plane area where the SEL is…		
	≥110 dBA	≥105 dBA	≥ 100 dBA
Baseline Approach	5.4	23.6	52.7
Approach 1	0	13.9	52.9
Approach 2	0	10.4	47.7
Approach 3	0	5.7	38.7

As the previous table shows, using one of the low-noise approaches significantly reduces the ground area exposed to high levels of noise. In fact, all of the noise abatement profiles eliminate zones of ground noise with an SEL of 110 dBA and higher. The table shows that the area covered by a ground noise of 100 dBA is reduced from 52.7-percent for the baseline approach to 38.7-percent for approach 3.

Time Histories of Noise at Particular Centerline & Sideline Ground Observers

In this section, the noise on the ground at two different observer locations is presented as a function of time for the four approach profiles. The two locations are labeled A and B and correspond to a centerline location at a range of x = 10,000 feet and a sideline location (y = -1,500 feet), also at a range of 10,000 feet. The two locations are shown below in Figure 5.33 on the ground SEL plot corresponding to the baseline approach.

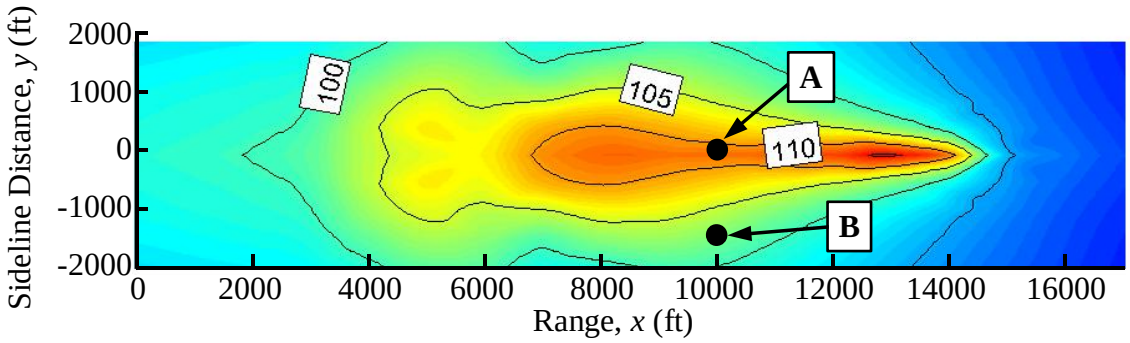

Figure 5.33. Location of observer points A and B on ground plane.

Figure 5.34 shows the SPL time histories at location A for the four approaches.

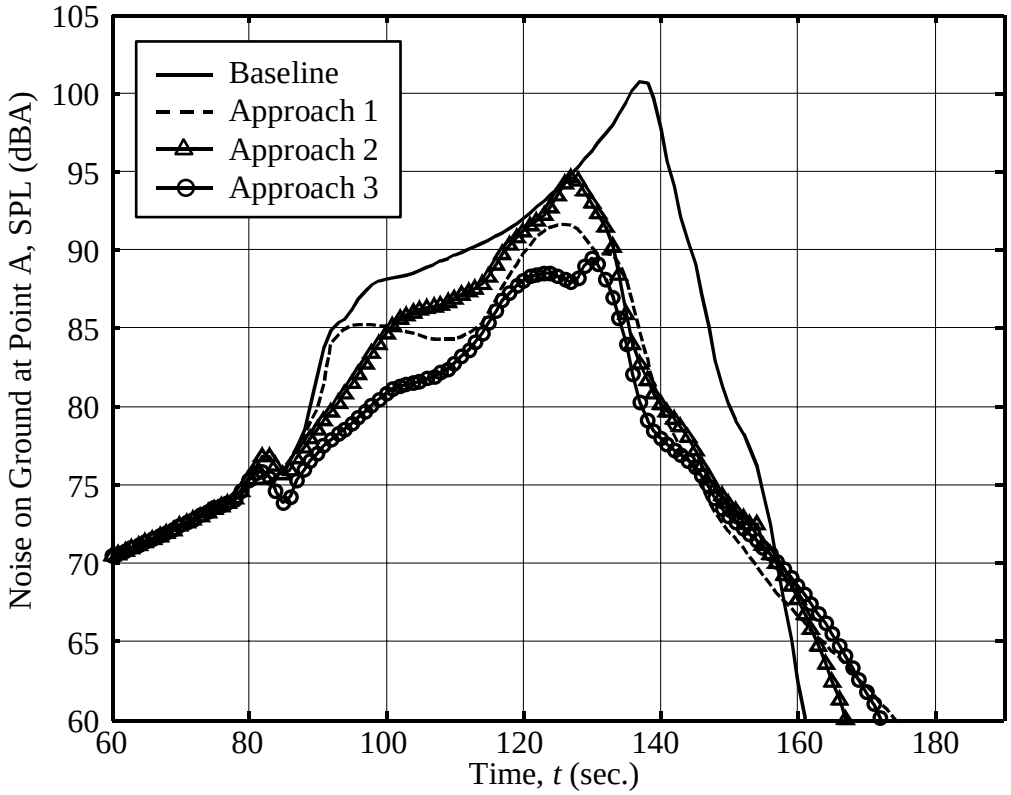

Figure 5.34. SPL time histories at observer location A.

As the previous figure shows, the baseline approach causes the largest peak noise (101 dBA) at ground location A. All of the constrained approaches provide a peak noise reduction of at least 6 dBA, with approach 3 providing an 11 dBA reduction in the peak noise level. This is a tremendous reduction of the peak noise at this particular ground location. However, note that in the baseline approach case the aircraft is at an altitude of 449 feet when it passes over point A whereas in the case of approach 3, the aircraft is at an altitude of 1,137 feet. Section 5.5.3 presents the results obtained for each approaches, with the aircraft being forced to achieve the same final altitude and range.

The next figure shows the SPL time histories at the sideline observer location, B.

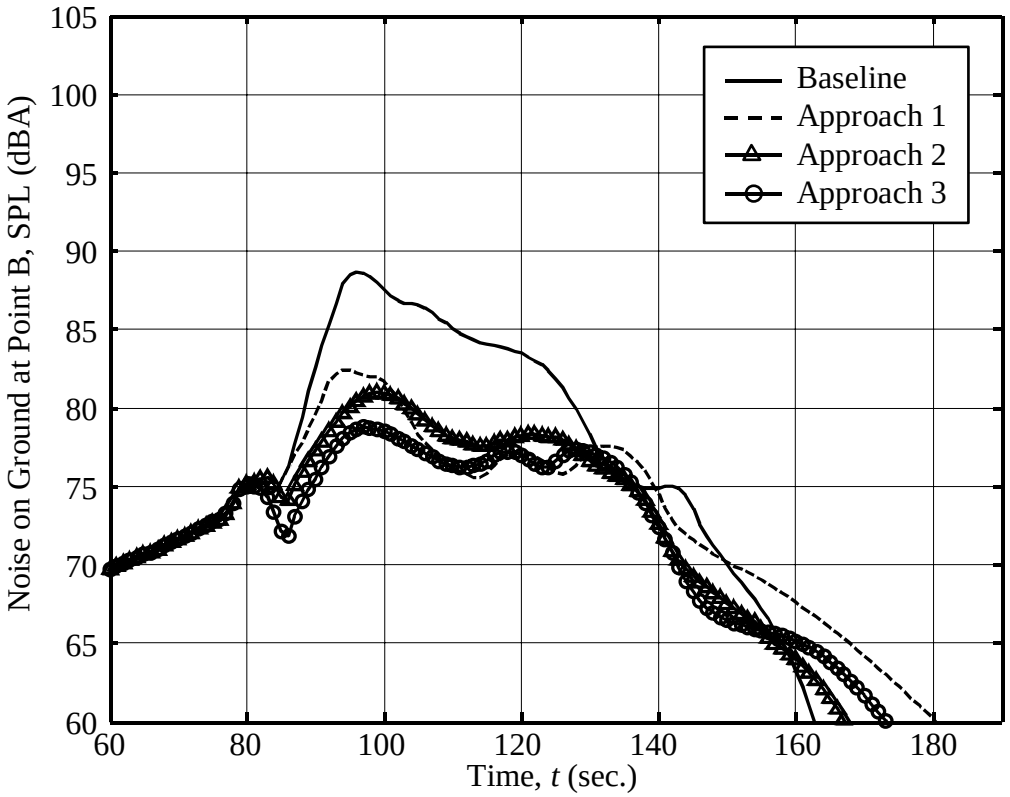

Figure 5.35. SPL time histories at observer location B.

Once again, a large peak noise reduction can be seen for all low-noise approaches, especially approaches 2 and 3. At this particular observer location, approach 3 provides a 10 dBA peak noise reduction over the baseline approach. The following chart summarizes the peak SPL results for the four approach profiles at observer locations A and B.

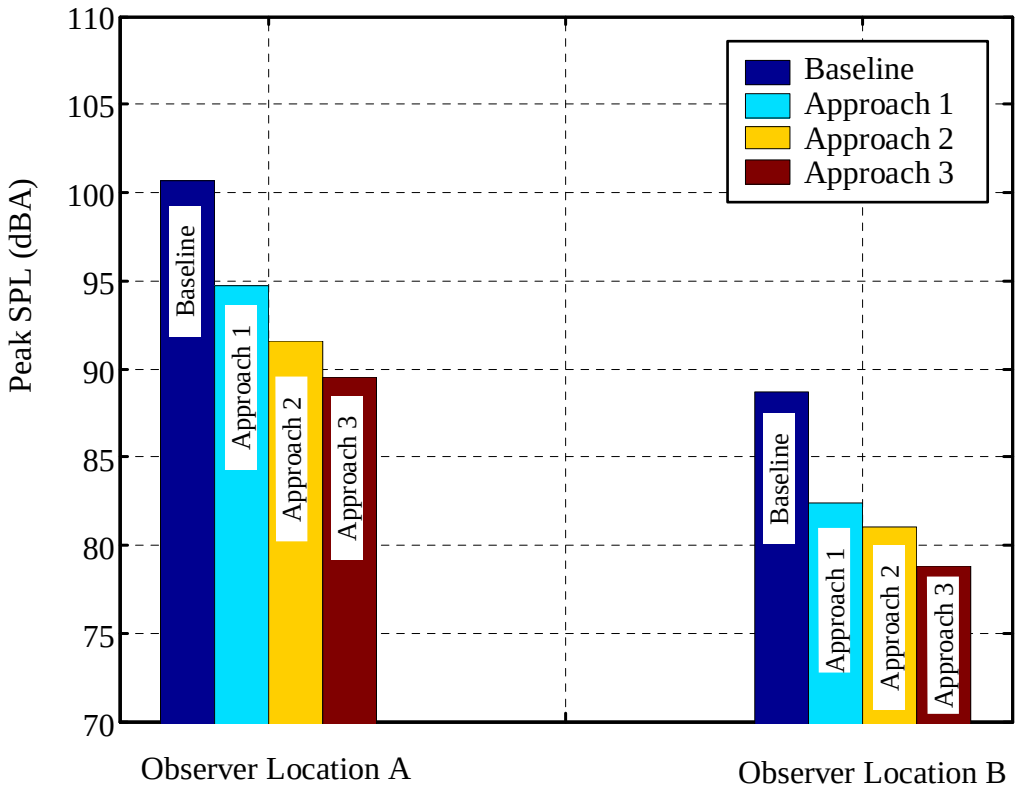

Figure 5.36. Peak SPL at observer locations A and B.

5.5.3 Comparison of Sound Exposure Level on Ground Plane for Approaches Terminated at the Same Altitude and Range

In this section, comparisons between the baseline approach and the three low-noise approaches are again presented. This time however, the approaches are simulated so that the aircraft achieves a final altitude of 100 feet at a range of x = 15,000 feet. These comparisons are useful in that they show that a low-noise approach can be flown to the same target altitude and range as the baseline approach and still achieve its goal of noise abatement.

Figure 5.37 shows the trajectories for the baseline approach and the low-noise approaches. Note that all the approaches are terminated at the same altitude and range. Also note that the low-noise approaches are flown at lower altitudes than the baseline approach for most of the flight time due to the required flattening of the flight path angle.

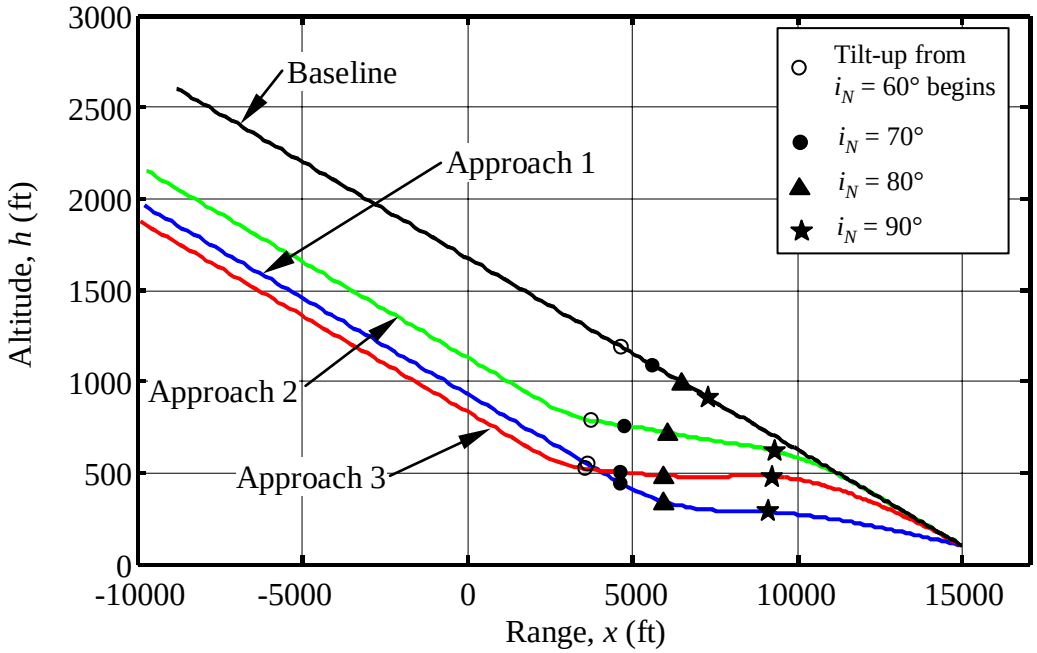

Figure 5.37. Trajectories for the four approach profiles (same final altitude and range).

The following figure shows the ground SEL contours for the baseline and the low-noise approaches, when flown such that the final altitude and range are identical.

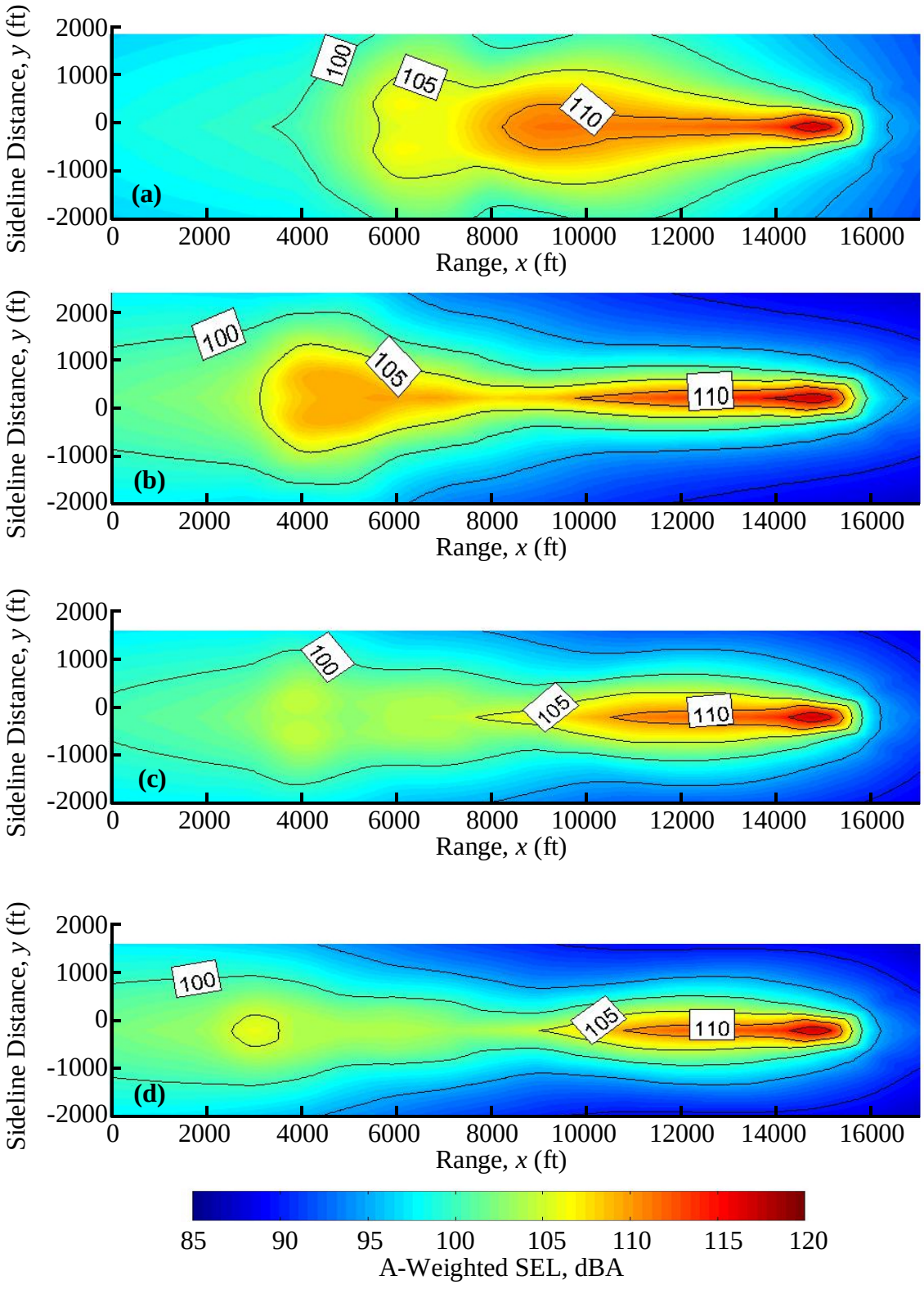

Figure 5.38. Ground SEL contours for (a) baseline approach, (b) approach 1, (c) approach 2 and (d) approach 3 (same final altitude and range).

As the previous figure shows, the noise reduction benefits due to the low-noise approaches are less dramatic when the approaches are flown such that they achieve the same target location. This is because the low-noise approaches were designed to reduce BVI noise at the *source*, which requires a flattening of the flight path angle. Thus, the aircraft is flown closer to the ground in the noise abatement cases as compared to the baseline case. However, note that the segment of the approach flown before the aircraft reaches x = 0 feet is not optimal in terms of noise reduction. As previously discussed, it would be more desirable to fly this segment at lower airspeeds and at nacelle tilts closer to airplane mode. This would considerably reduce the ground SEL contour levels in the region between x = 0 feet and approximately x = 6,000 feet, and therefore emphasize the noise benefits of the three low-noise approaches. Also, the aircraft can be considered to be over the airport or vertiport between x = 14,750 feet and x = 15,250 feet (where the noise levels are maximum). The noise in this region is not as critical as the noise over residential areas. Again, this factor tends to increase the noise reduction benefits of the low noise approaches. It is clear that further research is necessary to determine the optimum tradeoff between noise reduction at the source and on the ground.

The main feature of the ground SEL plots shown in Figure 5.38 is that the noise contours are much narrower for the constrained approaches than for the baseline approach. This is due mainly to the reduction of the size and strength of the BVI hotspot(s) at the source, but it is also due to the fact that the aircraft is closer to the ground. Approaches resulting in narrow ground noise profiles can be desirable in cases where the final approach can be

flown over a narrow strip of unpopulated land (e.g., railway track, highway, etc). The following table shows the noise reduction benefits of approaches 1-3 in terms of ground plane area.

Table 5.5. Ground area for various SEL contours (same final altitude and range).

	Percentage of the ground plane area where the SEL is…		
	≥110 dBA	≥105 dBA	≥ 100 dBA
Baseline Approach	5.4	24.9	54.8
Approach 1	2.2	16.3	42.0
Approach 2	2.2	9.4	45.4
Approach 3	1.8	6.6	37.0

Time Histories of Noise at Particular Centerline & Sideline Ground Observer for Approaches Terminated at the Same Altitude and Range

The next two figures show the time history of the SPL at the ground observer locations A and B, for cases where all approaches are flown to achieve the same final range and altitude.

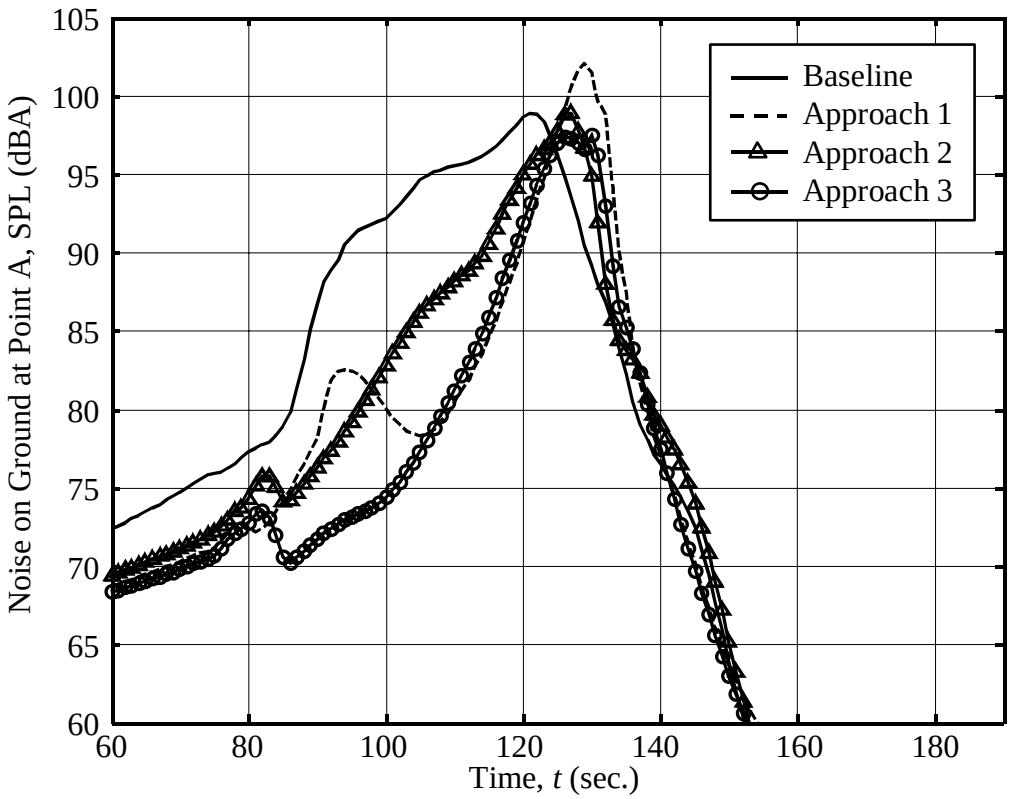

Figure 5.39. SPL time histories at observer location A for equivalent altitude approaches.

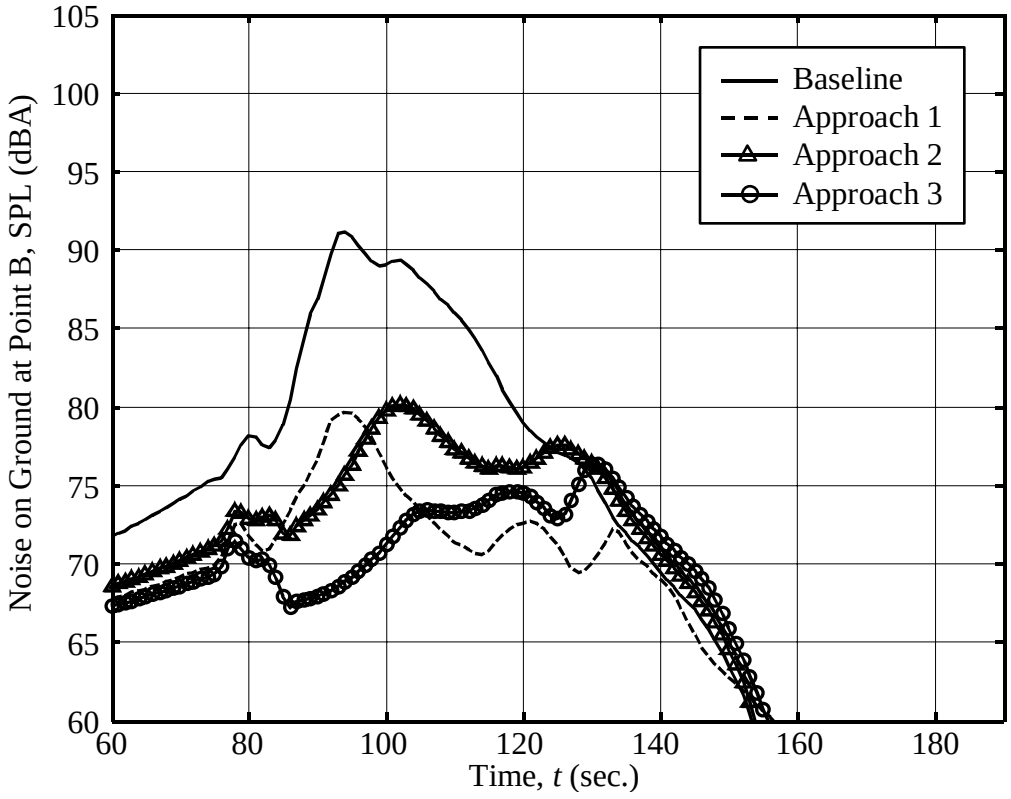

Figure 5.40. SPL time histories at observer location B for equivalent altitude approaches.

As the previous two figures show, the low BVI noise approaches offer the most benefits at the sideline observer location. At ground observer A, the peak SPL is approximately the same, or greater, for the low-noise approaches and the baseline approach. However, at ground observer B, each of the low BVI noise approaches offer a peak SPL reduction of at least 11 dBA., which is substantial. The following chart summarizes the results at observer A and B when all of the approaches are flown so as to achieve the same final altitude and range.

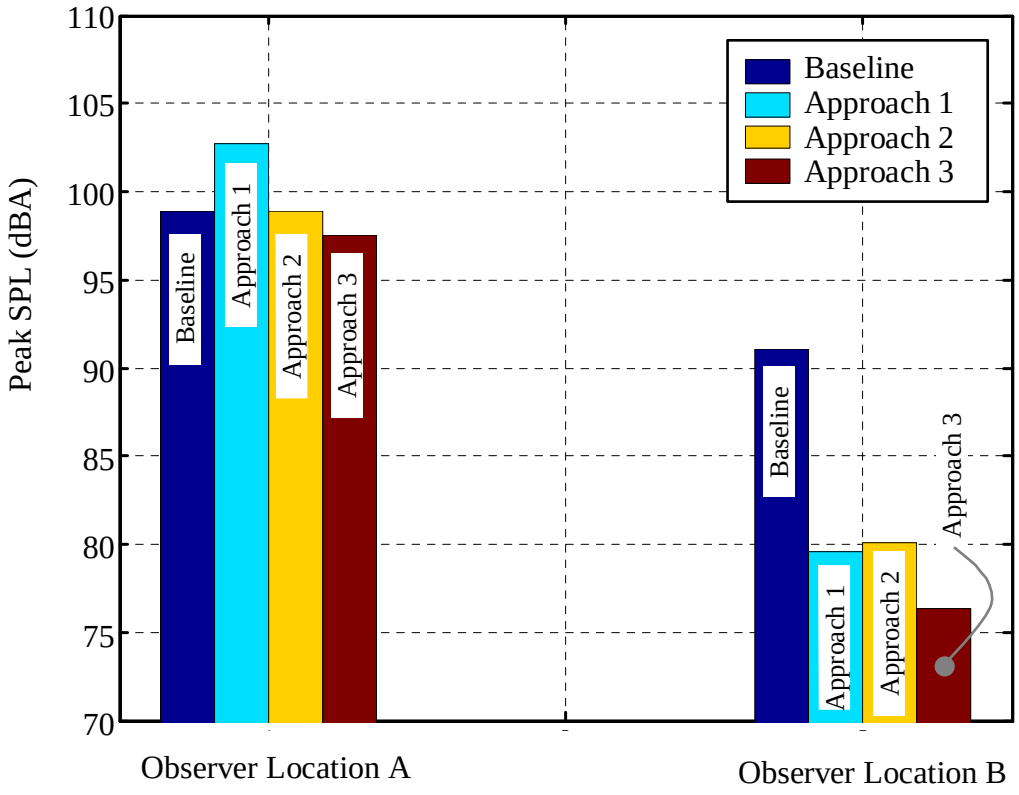

Figure 5.41. Peak SPL at observer locations A and B, same final altitude and range.

The results presented in this section showed that feasible low BVI noise approaches could be designed by constraining the average inflow through the rotor. The reductions in the noise on the ground obtained from the low-noise approaches proved that careful management of the flight path angle and nacelle tilt-rate during a converting descent was indeed essential.

One of the most important observations from this study is that in order to reduce BVI noise it is not necessary to apply flight trajectory management throughout the approach. Rather, the technique can be used only when needed, i.e. when the wake of the rotor becomes very close to the rotor itself. This leads to a better use of noise abatement

strategies. For example, a shallow flight path angle is known to yield a quieter approach (Ref. 4). However, flying shallower implies flying closer to the ground for a longer time, which is not a desirable feature when flying over a residential area. This research has shown that steeper descents can be flown quietly by flattening the flight path angle only when needed to avoid critical inflow conditions.

5.5.4 Comparison of Quasi-Static vs. Steady-State Ground Acoustic Mapping Methods

In this research, the first-order effects of a deceleration on the noise during an approach are captured through the Quasi-Static Acoustic Modeling (Q-SAM) method. In section 5.2.5, the deceleration was shown to have an important effect on the value of the average inflow. In this section, the ground plane noise results of the quasi-static baseline approach are compared to the results obtained through a steady-state baseline approach. This approach is obtained by assembling a series of steady-state performance solutions corresponding to the same time-history of airspeed and nacelle tilt as the quasi-static baseline approach, but with the deceleration set to zero. The following figure shows the resulting ground planes for the quasi-static and steady-state baseline approaches.

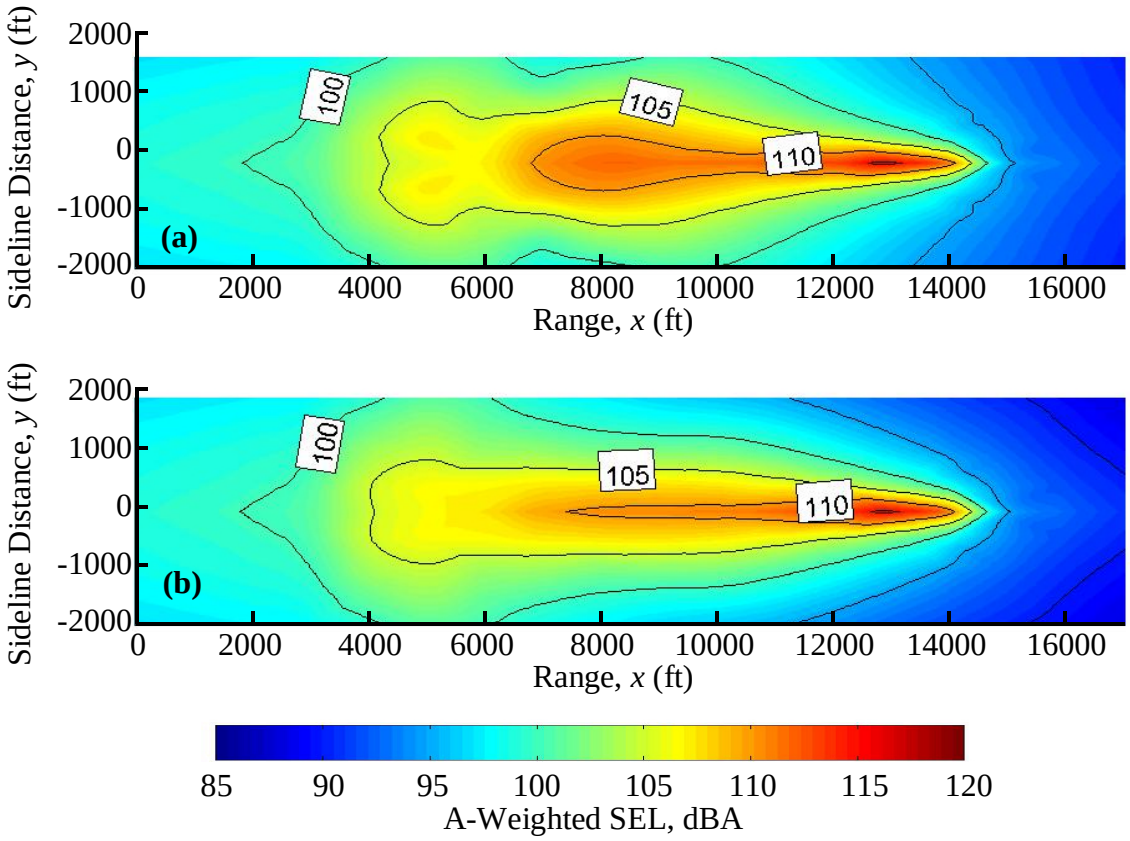

Figure 5.42. Comparison of baseline approach obtained through (a) quasi-static acoustic mapping, and (b) steady-state acoustic mapping.

As the previous figure shows, the general characteristics and levels of the ground contours are similar for both mapping methods. However, in the region where most of the deceleration occurs (between x = 4,000 feet and x = 11,000 feet), significant differences can be observed. Indeed, the ground noise contours obtained through the steady-state method are noticeably smaller in size and levels than those obtained through the quasi-static method. As was previously discussed, this is due to the fairly large decelerations, which cause the wake to be pushed up closer to the rotor and create stronger BVI noise. Therefore, including the first-order effects of deceleration is crucial to an adequate mapping of the BVI noise during a decelerating approach profile.

Chapter 6

Summary & Conclusions

Tiltrotors are an innovative type of rotorcraft that have the potential to alleviate airport congestion. However, the high noise levels produced during an approach to land are a foreseeable impediment to the community acceptance of commercial tiltrotors. With the upcoming introduction of the BA-609 tiltrotor on the civil market, the reduction of descent noise levels is a crucial priority. Therefore, the contributions made by this work are critical in this stage of tiltrotor development.

6.1 Summary

The main focus of this Dissertation was to develop approach profiles that minimize BVI noise during a conversion maneuver. To achieve this end a quasi-static longitudinal performance model was developed that captures the performance effects of relatively slow decelerating maneuvers. Results of a 1995 XV-15 tiltrotor acoustic flight test that measured steady-state descent noise were then used to design a neural network that models the acoustic characteristics of a tiltrotor. The neural network was used to study

measured noise trends with respect to the airspeed, nacelle tilt, and flight path angle of the aircraft. Next, a trend-based analysis was performed to identify the effects of certain flight trajectory and aircraft configuration parameters on the rotor inflow, which gives an indication of the levels of BVI noise. The knowledge gained from that analysis was used to design and to study approach profiles that reduce BVI noise.

The understanding of tiltrotor noise characteristics developed in this Dissertation provides a clear methodology for the design of low-noise approaches. The systematic design of the approach procedures is a definite improvement over the current state-of-the-art of tiltrotor low-noise approach design. Indeed, the noise abatement procedures presented in Ref. 39 were obtained mostly by trial-and-error and by implementing different nacelle tilt and flight path angle scheduling combinations into the Rotorcraft Noise Model (RNM) and assessing the resulting ground noise. In this Dissertation, steady-state noise measurements are used in a quasi-static manner to predict noise during a converting approach, including the effects of the deceleration and the rate-of-change of flight path angle on the performance solution. This is an improvement to the steady-state RNM method, which does not take into account the effects of deceleration on the performance solution.

6.2 Conclusions

In this section, the six main conclusions are presented first, followed by the sub-conclusions, which are organized into three categories that correspond to the three

research objectives introduced in the first chapter. The major conclusions of this work are:

1. ***BVI noise is the dominant noise source during an approach***. This has been observed in previous research (e.g., Ref. 5), but this work showed that strong BVI noise is not limited to flight in the helicopter mode. For example, strong BVI noise was observed at 70° nacelle tilt. The measured noise data showed that BVI noise levels increase sharply with steeper descent angles. Attempting to reduce BVI noise by pushing the wake far above the rotor through a very steep descent is not a viable option because of the tiltrotor's high disk loading.

2. ***Including the effects of deceleration on the rotor operating condition is critical to accurately representing the noise emitted by a tiltrotor during a typical converting approach***. The quasi-static performance model introduced in this work captures the first-order effects of the deceleration created by tilting the aircraft's nacelles upward during a conversion to helicopter mode. It was shown that in terms of the vehicle's force and moment equilibrium, a 0.1 g deceleration is approximately equivalent to a 6° decrease in the flight path angle. The use of a quasi-static acoustic mapping method is a definite improvement over a steady-state acoustic mapping method, which was shown to significantly under-predict BVI noise in flight conditions where the decelerations are fairly large (such as during a conversion to helicopter mode).

3. ***A neural network can successfully be designed to model a tiltrotor's noise characteristics***. In this research, a combination of measured and computed performance and configuration parameters were used as inputs to the network in order to predict the measured XV-15 noise to within a mean square error of 1.2 dBA.

4. ***An average inflow through the rotor adequately represents the general trends of measured BVI noise level***. It was discovered, however, that due to BVI geometry and phasing effects, the correlation between inflow and BVI noise level shifts in magnitude with respect to the airspeed, and to a lesser degree with respect to the nacelle tilt. This is subject to further research.

5. ***During a typical converting approach at a constant descent angle and nacelle tilt-rate, the rotor inevitably experiences a segment of small average inflow values that can lead to strong BVI noise***. This is due to the combination of nacelle tilt, flight path angle, airspeed and deceleration. The region of small inflow is critical in terms of the likelihood of strong BVI noise.

6. ***A low-order mathematical model, combined with measured steady-state noise data, can be used to systematically design realistic approach profiles that considerably reduce BVI noise***. In this research, flight path management was used to reduce the level of BVI noise produced by the aircraft and nacelle tilt scheduling was used to limit the deceleration to a level acceptable in terms of possible commercial operations. Using these techniques, a reduction of the peak approach sound pressure

level of 8 dBA was achieved on a hemisphere surrounding the aircraft, as compared to the baseline approach.

The sub-conclusions of this work are presented below:

Performance/Acoustic Tiltrotor Model

- The longitudinal performance model was shown to accurately predict the steady-state fuselage pitch angle when compared to flight test data. Although the model neglects unsteady aerodynamic effects, it was able to capture the trends associated with slow maneuvers. The performance model was developed to be flexible so that it can study the non-uniqueness of the tiltrotor's performance solutions by either prescribing or solving for the various unknown performance parameters.
- The design and training of the acoustic neural network resulted in the network's ability to predict measured noise levels and directivity within approximately ± 1.2 dBA. By carefully selecting the inputs into the model, it was able to capture both the level and the directivity trends associated with impulsive noise sources such as BVI and HSI noise. The training methodology ensured that the network was capable of generalizing. This was illustrated by the network's ability to accurately predict data that was not included in the training set. The final neural network was comprised of 64 neurons in the first hidden layer and 16 neurons in the second hidden layer.

Tiltrotor Noise Understanding

From studying the measured noise data (modeled through the acoustic neural network), the following conclusions were obtained:

- It was shown that thickness noise and HSI noise were mainly secondary to BVI noise during an approach procedure. However, HSI noise can dominate at airspeeds higher than 100 knots in level flight and possibly propagate strongly to the ground because of the low nacelle tilt. Therefore, it is favorable to perform most of the deceleration to 100 knots in the airplane mode of flight, and then to start the transition to helicopter mode. This avoids high advancing tip Mach numbers and therefore limits the level of thickness noise. Larger wing flap deflections can be used to fly at low airspeeds in airplane mode.
- In addition to being a strong function of the flight path angle, BVI noise is also a function of the nacelle tilt and the airspeed. For a given flight path angle BVI noise was shown to be stronger at higher nacelle tilts, when the aircraft is near helicopter mode, and at higher airspeeds.
- The BVI directivity patterns associated with changes in flight path angle and airspeed agree well with basic phasing arguments. As the aircraft increases its descent angle, the BVI hotspots tend to shift from the front of the aircraft toward the rotors' advancing side and move downward, away from the plane of the rotor. From an analysis similar to the research in Ref. 118, it was revealed that the most prevalent types of interactions for this particular aircraft, with its high disk loading and three-bladed rotor, are oblique interactions of Type α and Type β.

- A probable explanation to the presence of strong BVI noise at fairly high inflow conditions was presented through BVI geometry arguments. These arguments illustrated that relatively small miss-distances could occur for younger BVIs, even for high inflow conditions. It was also shown that for a three-bladed rotor, the radiation efficiency of the younger BVIs could increase because of acoustic wave phasing effects.

A study was conducted to assess the effects of various flight trajectory and aircraft configuration parameters on the rotor's average inflow, which is an indication of the BVI miss-distance trends. The following findings were a result of this trend-based analysis:

- It was shown that steep descent angles and large decelerations tend to reduce the average inflow value, which leads to smaller miss-distances and to an increase in the likelihood of strong BVI noise. Because of the high rotor disk loading, the flight path angle and deceleration needed to push the wake *above* the rotor are thought to be excessive and outside the limits of safe operations. The nacelle tilt also has a large effect on the average inflow that leads to smaller average inflow magnitudes at nacelle tilts closer to helicopter mode.
- The baseline approach consisted of a 6° descent starting at 100 knots, with a 60°-to-90° nacelle tilt conversion accomplished at a constant 1.5 deg./sec. nacelle tilt-rate. The fuselage pitch and flap deflection were fixed. For the baseline approach, the average inflow value was small during a large portion of the approach, and the maximum deceleration caused by the nacelle tilting upward was -0.10 g's, which is high and exceeds typical commercial operations limit.

- Flattening the flight path angle was effective in constraining the average inflow while a gradual reduction in the nacelle tilt-rate as the aircraft neared helicopter mode was successful in constraining the deceleration.
- Average inflow constraints corresponding to a particular level of measured BVI noise were developed and used to design constrained approaches. It was found that constraining the BVI noise level on a hemisphere below 105 dBA and 107 dBA was possible by adjusting the flight path angle and nacelle tilt-rate. However, constraining the BVI noise level on a hemisphere below the level of other non-impulsive noise was impractical, because it required the aircraft to climb for most of the simulation.

Low BVI Noise Approaches

- Enforcing a constant average inflow constraint of $\bar{\lambda}_{limit} = -0.035$ and a deceleration constraint of $\dot{V}_{limit} = -0.050$ required modifying the flight path angle, flying level for a very short time, and reducing the nacelle tilt-rate to 0.4 deg./sec. when the nacelle tilt reached approximately 76°. The noise reduction obtained from this approach profile was fairly limited (approximately 2 dBA reduction in average SEL on the hemisphere), since the constraints were not based on measured noise data. However, the approach still provided substantial noise reductions on the ground for the case where it was initiated at the same altitude and range as the baseline approach. For the more realistic case of achieving the same final altitude and range as the baseline approach, the main effect of this approach was to elongate the ground noise contours. This yielded an 11 dBA peak SPL reduction at a ground observer 1,500 feet to the side of the aircraft's flight path.

- Enforcing an inflow constraint on the hemisphere that corresponds to a maximum BVI noise of 107 dBA required the flight path angle to be reduced to approximately -1.5° for 30 seconds. Then, the flight path angle was gradually allowed back toward the original -6°. This constrained approach provided better noise reduction results than the approach that used a constant average inflow constraint. The average sound exposure level on the hemisphere was reduced by approximately 3 dBA from the baseline approach. The peak SPL at the source (hemisphere) during this approach was approximately 6 dBA lower than for the baseline approach. The ground area covered by high noise levels was also substantially reduced, especially in the sideline direction.
- The third constrained approach profile provided the best noise reduction results. Its design enforced an inflow constraint that corresponded to a maximum of 105 dBA on a hemisphere. To achieve this constraint, a 30 second segment of a very shallow descent angle and a short climb were necessary. This approach provided for the largest reduction of the average sound exposure level at the source (approximately 5 dBA). The peak SPL on the hemisphere during this approach was reduced by 8 dBA when compared to the baseline approach. The ground noise contours were much narrower than for the baseline approach. This approach provided a peak sound pressure level reduction over the baseline approach of 11 dBA at a centerline point and 10 dBA at a sideline observer location when both approaches were initiated at the same range and altitude. These drastic noise reduction benefits were mitigated when both approaches were flown so as to achieve the same final altitude and range, since the low-noise approaches were designed to reduce noise at the source and not on the ground. Still, a 2 dBA peak SPL reduction at observer A and a 14 dBA peak SPL at observer B were obtained.

6.2.1 General Noise Abatement Guidelines for the XV-15

By condensing the above-mentioned conclusions, a simple set of general approach guidelines can be proposed to reduce the level of impulsive noise emitted by the XV-15. Note that the following guidelines are specific to the XV-15 since they are a function of the aircraft's weight, rotor design, and tip speed, along with various other aircraft design parameters.

- Decelerate to less than 100 knots in airplane mode in order to avoid HSI noise or strong thickness noise.
- Use a slow nacelle tilt-rate between $i_N = 60°$ and $i_N = 90°$ to avoid large decelerations and small inflow values.
- Flatten descent angle during the decelerating conversion to helicopter mode until the airspeed falls below approximately 50 knots.

6.3 Recommendations for Future Work

The results presented in this Dissertation are very promising, however, the study of tiltrotor noise and noise reduction is still a subject of active research. In terms of this research's focus, the following points are important to gain even more insight into the tiltrotor approach noise problem.

Performance Modeling

- The proprotor system of a tiltrotor consists of highly twisted blades that often operate at high angles-of-attack. In this Dissertation, it is assumed that the inflow angle is small

and that the blade does not experience stall or reverse flow on the retreating side. Incorporating a high inflow capability into the performance model would improve the results at lower nacelle tilts and allow the model to be used throughout the range of possible configurations, from airplane mode to helicopter mode.

- The effects of rotor/wing interactions were neglected because a previous study (Ref. 91) showed that those effects were negligible in the restricted flight regimes considered. However, a more extensive study into the effects of those interactions could yield important results, especially if experimental results are obtained. Indeed, during approaches at relatively high airspeeds, the airframe can carry a significant amount of lift and produce fairly high induced velocities at the rotor disk, which could alter the inflow through the rotor and, consequently, alter the BVI noise levels.
- A quasi-static assumption was used that neglects the effects of unsteady airframe aerodynamics, unsteady rotor aerodynamics, and rotor inflow dynamics. This assumption limits the applicability of the performance/acoustics model to small accelerations or decelerations. The limiting cases for which this assumption is valid need to be validated through experiments. At the time of this writing, the quasi-static assumption used for acoustic representations is being investigated at the University of Maryland through a flight test program involving a conventional helicopter (Ref. 119).

Acoustic Flight Test Data

- No acoustic time history or frequency information was available for this research. In order to better study the acoustic results from the flight test data, acoustic waveform information should be analyzed. Examining the waveforms allows for a clearer

identification of the type of noise prevalent at a particular microphone location. The frequency spectrum of a signal also plays a major role in the atmospheric propagation of noise, a factor neglected in this analysis.

- The hemisphere acoustic data was tied to the performance data by first re-propagating the noise on a hemisphere to the ground and then by calculating the emission time of a particular noise level. It would be much simpler and lead to less possible sources of error to directly use time histories of the ground microphone measurements.
- The rotor's tip-path-plane angle plays a very important part in a rotorcraft's noise characteristics. Therefore, the rotor gimbal angle should be measured in future flight tests in order to more clearly identify performance/acoustics relationships and also to provide a better assessment of the performance model's predictive capabilities.

Acoustic Neural Network

- This research demonstrated that a neural network was a useful tool in modeling the acoustic characteristics of a tiltrotor aircraft. However, the potential of neural computing was not exploited to its fullest in this application and a more efficient neural network could be designed to fit the acoustic dataset.

Low Noise Approaches

- The low-noise approaches were designed to reduce BVI noise at the source. It was shown that avoiding BVI noise requires flattening the flight path angle, which necessitates flying closer to the ground and can mitigate the noise reduction benefits of

the candidate approaches. Therefore, approach profiles that aim to minimize the noise on the ground should be developed, with the BVI noise reduction guidelines developed in this research as a foundation.

- In this Dissertation, low BVI noise approaches were constructed by applying constraints on the average inflow and on the deceleration. The inflow constraint was satisfied by modifying the flight path angle and the deceleration constraint was enforced by modifying the nacelle tilt-rate. An improvement in this procedure would be to implement an optimization scheme that uses any combination of available flight trajectory and configuration parameters to reduce noise and to minimize deviations in the intended flight trajectory. Instead of using the average inflow value as a measure of BVI noise, the measured acoustic data, interpolated through the neural network, should be used directly by the optimizer.
- The effects of vehicle drag should be investigated to determine if any simple aircraft modification could lead to better noise abatement procedures. For example, it is possible that deployable drag devices or larger wing flaps could be used at low airspeeds to produce an X-force that would alter the tiltrotor's tip-path-plane angle and lead to a more favorable rotor operating condition.

In addition to the suggestions mentioned above, more research is required in the field of tiltrotor wake modeling. In particular, more experimental studies regarding the effects of the twin vortex system on BVI noise would be valuable. Also, it would be worthwhile to study the effects of such a highly twisted blade on the level and directivity of thickness noise.

Implementation Issues

Although the low BVI noise approaches designed in this research are though to be feasible, some issues will arise when the time comes to actually fly those approaches. The following issues should therefore be studied further:

- Because of high pilot workload, it is not likely that tiltrotors will be equipped with variable nacelle tilt-rate capabilities in the near future. A study of the noise resulting from approximating the required smooth nacelle tilt time history with a more strict nacelle tilt scheduling is required.
- An assessment of the suggested low BVI noise profiles through piloted simulations would be invaluable. Such an assessment would provide important answers to some of the implementation issues and provide an evaluation of the approaches from a more practical standpoint. Issues relating to safety of flight should also be investigated.
- Finally, it is believed that fully automated approaches would be the best way to implement the approach profiles designed in this research. In Ref. 37, a flight director was used to provide the pilot with nacelle tilt, flight path angle, and airspeed cues but this resulted in high pilot workload for approach profiles that required a combination of those parameters to be adjusted in a short amount of time. Therefore, it was also suggested in Ref. 37 that fully automated approaches be tested.

References

[1] – Bell Boeing Joint Service Program, Brochure 3646-01S, 2001.

[2] – Zuk, J., Statement before the Subcommittee on Space and Aeronautics, House of Representatives, Hearing entitled: "A Review of Vertical Takeoff and Landing Technology in the National Airspace System," retrieved February 17, 2004 from http://www.house.gov/science/space/may09/zuk, May 9, 2001.

[3] – Schmitz, F.H., Stepniewski, W.Z., Gibs, J., Hinterkeuser, E., "A Comparison of Optimal and Noise-Abatement Trajectories of a Tilt-Rotor Aircraft," NASA CR-2034, January 1972.

[4] – Brieger, J.T., Maisel, M.D., Gerdes, R., "External Noise Evaluation of the XV-15 Tiltrotor Aircraft," American Helicopter Society National Specialists' Meeting on Aerodynamics and Aeroacoustics, Arlington, TX, Feb. 25-27, 1987.

[5] – George, A.R., Smith, C.A., Maisel, M.D., Brieger, J.T., "Tilt Rotor Aircraft Aeroacoustics," American Helicopter Society 45th Annual Forum, Boston, MA, May 22-24, 1989.

[6] – Edwards, B. D., "XV-15 Tiltrotor Low Noise Characteristics," American Helicopter Society 46th Annual Forum, Washington, DC, May 21-23, 1990.

[7] – Hirschberg, M., "V/STOL: The First Half-Century," American Helicopter Society, Vertiflite, March/April 1997.

[8] – Maisel, M.D., Giulianetti, D.J., Dugan, D.C., "The History of the XV-15 Tilt Rotor Research Aircraft from Concept to Flight," NASA/SP-2000-4517, 2000.

[9] – National Air and Space Museum (2004), retrieved February 17, 2004 from http://www.nasm.si.edu/museum/udvarhazy.htm.

[10] – Bell Helicopter (2004), retrieved February 17, 2004 from http://www.bellhelicopter.com/aircraft/military/bell_eagle_eye.html.

[11] – Bell Helicopter (2004), retrieved February 17, 2004 from http://www.bellagusta.com/html/theAircraft/ba_609/images/609firstFlight02-1000.jpg.

[12] – Schmitz, F.H., Stepniewski, "The Reduction of VTOL Operational Noise Through Flight Trajectory Management," AIAA Paper 71-991, 8th Annual Meeting and Technical Display, Washington, DC, October 25-28, 1971.

[13] – Stepniewski, W.Z., Schmitz, F.H., "Possibilities and Problems of Achieving Community Noise Acceptance of VTOL," *The Aeronautical Journal*, Vol. 77, No. 750, Royal Aeronautical Society, June 1973, pp. 311-326.

[14] – Gibs, J., Stepniewski, W., Spencer, R., Kohler, G., "Noise Reduction of a Tilt Rotor Aircraft Including Effects on Weight and Performance," NASA CR-114638, June 1973.

[15] – Maisel, M.D., "XV-15 Tilt Rotor Research Aircraft Familiarization Document," NASA TM X-62407, January 1975.

[16] – Maisel, M.D., Weiberg, J.A., Brown, J.H., "A Review of the Design and Acoustics Considerations for the Tilt Rotor Aircraft," NASA Quiet, Powered-Lift Propulsion Conference, Lewis Research Center, November 1978.

[17] – Huston, R.J., Golub, R.A., "Noise Considerations for Tiltrotor," AIAA Paper 89-2359, AIAA/ASME/SAE/ASEE 25th Joint Propulsion Conference, Monterey, CA, July 10-12, 1989.

[18] – Maisel, M.D., "XV-15 Tilt Rotor Flight Acoustics Test Experience – Including the Advanced Technology Blades," Tilt Rotor Aircraft Noise Workshop, Georgia Institute of Technology, GA, March 28-29, 1991.

[19] – Cox, C., “Tilrotor Aircraft Operational Effects on Noise,” Presented at the NATO CCMS Symposium on Noise Aspects of Rotary Wing Aircraft, CA, August 1-2, 1991.

[20] – Ahuja, K.K., “Tiltrotor Aircraft Noise: A Summary of the Presentations and Discussions at the 1991 FAA/Georgia Tech Workshop,” Systems Control Technology, Inc., Arlington, VA. Jan 1992.

[21] – Sternfeld, H., “Evaluation of the Impact of Noise Metrics on Tiltrotor Aircraft Design,” NASA CR-198240, 1995.

[22] – Marcolini, M.A., Burley, C., Conner, D.A., Acree, C.W., “Overview of Noise Reduction Technology in the NASA Short Haul (Civil Tilt Rotor) Program,” SAE International Powered Lift Conference, Jupiter, FL, November 18-20, 1996.

[23] – Shank, S., “Tiltrotor Interior Noise Characteristics,” AHS and Royal Aeronautical Society Technical Specialists’ Meeting on Rotorcraft Acoustics/Fluid Dynamics, Philadelphia, PA, October 15-17, 1991.

[24] – Lyle, K.H., Burley, C.L., Prichard, D.S., “A Comparison of Measured and Predicted XV-15 Tiltrotor Surface Acoustic Pressures,” AHS Technical Specialists’ Meeting for Rotorcraft Acoustics and Aerodynamics, Williamsburg, VA, October 28-30, 1997.

[25] – Lyle, K.H., “XV-15 Structural-Acoustic Data,” NASA TM-112855, 1997.

[26] – Maisel, M.D, Harris, D.J., “Hover Tests of the XV-15 Tiltrotor Research Aircraft,” AIAA Paper 81-2501, AIAA/SETP/SFTE/SAE/ITEA/IEEE 1st Flight Testing Conference, Las Vegas, NV, November 11-13, 1981.

[27] – Edwards, B. D., “External Noise of the XV-15 Tiltrotor Aircraft,” NASA CR-187463, May 1991.

[28] – Golub, R.A., Becker, L.E., Rutledge, C.K., Smith, R.A., Conner, D.A., “Some Far-Field Acoustics Characteristics of the XV-15 Tiltrotor Aircraft,” AIAA Paper 90-3971, AIAA 13th Aeroacoustics Conference, Tallahassee, FL, October 22-24, 1990.

[29] – Conner, D. A., Wellman, B., “Far-Field Hover Acoustic Characteristics of the XV-15 Tiltrotor Aircraft with Advanced Technology Blades,” AHS/RAeS Technical Specialists Meeting on Rotorcraft Acoustics and Fluid Dynamics, Philadelphia, PA, October 15-16, 1991.

[30] – Hoad, D.R., Conner, D.A., Rutledge, C.K., “Acoustic Flight Experience with the XV-15 Tilt Rotor Aircraft with the Advanced Technology Blades,” Proceedings of the 14th DGLR/AIAA Aeroacoustics Conference, Aachen, Germany, May 11-14, 1992.

[31] – Conner, D. A., Wellman, B., "Hover Acoustic Characteristics of the XV-15 Tiltrotor Aircraft with Advanced Technology Blades," NASA TM-111578, 1993.

[32] – Santa Maria, O.L., Wellman, J.B., Conner, D.A., Rutledge, C.K., "Tiltrotor Acoustic Flight Test: Terminal Area Operation," American Helicopter Society 48th Annual Forum, Washington, DC, June 3-5, 1992 (alternate paper, not in proceedings).

[33] – Edwards, B. D., "XV-15 Tiltrotor Low Noise Terminal Area Operations Testing," NASA CR-1998-206946, February 1998.

[34] – Conner, D.A., Marcolini, M.A., Edwards, B.D., and Brieger, J.T., "XV-15 Tiltrotor Low Noise Terminal Area Operations," American Helicopter Society 53rd Annual Forum, Virginia Beach, VA, April 29-May 1, 1997.

[35] – Edwards, B.D., Conner, D.A., "XV-15 Tiltrotor Aircraft: 1997 Acoustic Testing," NASA TM-2003-212151, April 2003.

[36] – Conner, D.A., Marcolini, M.A., Decker, W.A., Cline, J.H., Edwards, B.D., Nicks, C.O., and Klein, P.D., "XV-15 Tiltrotor Low Noise Approach Operations," American Helicopter Society 55th Annual Forum, Montreal, Quebec, Canada, May 25-27, 1999.

[37] – Edwards, B.D., Conner, D.A., "XV-15 Tiltrotor Aircraft: 1999 Acoustic Testing - Test Report," NASA TM-2003-212152, April 2003.

[38] – Conner, D.A., Edwards, B.D., Decker, W.A., Marcolini, M.A., and Klein, P.D., "NASA/Army/Bell XV-15 Tiltrotor Low Noise Terminal Area Operations Flight Research Program," AIAA/CEAS 6th Aeroacoustics Conference, Lahaina, Hawaii, June 2000.

[39] – Conner, D.A., Page, J.A., "A Tool for Low Noise Procedures Design and Community Noise Impact Assessment: The Rotorcraft Noise Model (RNM)," Heli-Japan 2002, Tochigi, Japan, November 11-13, 2002.

[40] – Decker, W., "Handling Qualities Evaluations of XV-15 Noise Abatement Landing Approaches Using a Flight Simulator," American Helicopter Society 57th Annual Forum, Washington, D.C., May 9-11, 2001.

[41] – McCluer, M.S., Dearing, M., "Measuring Blade-Vortex Interaction Noise Using the YO-3A Acoustics Research Aircraft," 22nd European Rotorcraft Forum, Brighton, UK, September 17-19 1996.

[42] – Kitaplioglu, C., McCluer, M., and Acree, Jr., C.W., "Comparison of XV-15 Full-Scale Wind Tunnel and In-Flight Blade-Vortex Interaction Noise," American Helicopter Society 53rd Annual Forum, Virginia Beach, VA, April 1997.

[43] – Lee, A., Mosher, M. “An Acoustical Study of the XV-15 Tilt Rotor Research Aircraft,” AIAA Paper 79-0612, 1979.

[44] – Marcolini, M.A., Conner, D.A., Brieger, J.T., Becker, L.E., Smith, C.D., “Noise Characteristics of a Model Tiltrotor,” American Helicopter Society 51st Annual Forum, Fort Worth, TX, May 9-11, 1995.

[45] – Light, J.S., Kitaplioglu, C., Acree, C.W., “XV-15 Aeroacoustic Testing at NASA Ames,” 23rd European Rotorcraft Forum, Dresden, Germany, Sept. 16-18, 1997.

[46] – Kitaplioglu, C., Acree, C.W., Light, J.S., “XV-15 Aeroacoustic Testing at NASA Ames Research Center,” *Journal of the American Helicopter Society*, Vol. 45, No. 3, July 2000, pp. 191-198.

[47] – Kitaplioglu, C., “Blade-Vortex Interaction Noise of a Full-Scale XV-15 Rotor Tested in the NASA Ames 80-by 120-Foot Wind Tunnel,” NASA TM 208789, July 1999.

[48] – Kitaplioglu, C., Betzina, M., Johnson, W., “Blade-Vortex Interaction Noise of an Isolated Full-Scale XV-15 Tilt-Rotor,” American Helicopter Society 56th Annual Forum, Virginia Beach, Virginia, May 2-4, 2000.

[49] – Nguyen, K., Betzina, M., and Kitaplioglu, C., "Full-Scale Demonstration of Higher Harmonic Control for Noise and Vibration Reduction on the XV-15 Rotor," American Helicopter Society 56th Annual Forum, Virginia Beach, VA, May 2000.

[50] – Kitaplioglu, C., Johnson, W., "Comparison of Full-Scale XV-15 Blade-Vortex Interaction Noise Calculations with Wind Tunnel Data," American Helicopter Society International Technical Specialist Meeting On Aerodynamics, Acoustics, and Test and Evaluation, San Francisco, CA, January 23-25, 2002.

[51] – Young, L.A., "Tilt Rotor Aeroacoustic Model (TRAM): A New Rotorcraft Research Facility," Heli Japan 98: AHS International Meeting on Advanced Rotorcraft Technology and Disaster Relief, Gifu, Japan, April 1998.

[52] – Young, L.A.; Booth, E.R., Jr.; Yamauchi, G.K.; Botha,G.; and Dawson, S., "Overview of the Testing of a Small-Scale Proprotor," American Helicopter Society 55th Annual Forum Proceedings, Montreal, Canada, May 1999.

[53] – Johnson, J.L., Young, L.A., "Tilt Rotor Aeroacoustic Model Project," Confederation of European Aerospace Societies (CEAS), Forum on Aeroacoustics of Rotorcraft and Propellers, Rome, Italy, June 1999.

[54] – Booth, E.R., McCluer, M., Tadghighi, H., "Acoustic Characteristics of a Model Isolated Tiltrotor in DNW," American Helicopter Society 55th Annual Forum, Montreal, Quebec, Canada, May 25-27, 1999.

[55] – Burley, C.L., Brooks, T.F., Charles, B.D., McCluer, M., "Tiltrotor Aero-acoustic Code (TRAC) Prediction Assessment and Initial Comparisons with TRAM Test Data," 25th European Rotorcraft Forum, Rome, Italy, Sept. 14-16, 1999.

[56] – Yamauchi, G., Burley, C., Mercker, E., Pengel, K., and JanakiRam, R., "Flow Measurements of an Isolated Model Tilt Rotor," American Helicopter Society 55th Annual Forum, Montreal, Canada, May 1999.

[57] – Swanson, S.M., Swanson, A.A., McCluer, M.S., Yamauchi, G.K., "Airloads measurements from a 1/4-scale tiltrotor wind tunnel test," 25th European Rotorcraft Forum, Rome, Italy, Sept. 14-16, 1999.

[58] – Johnson, W., "Calculation of the Aerodynamic Behavior of the Tilt Rotor Aeroacoustic Model (TRAM) in the DNW," American Helicopter Society 57th Annual Forum Proceedings, Washington, D.C., May 2001.

[59] – Johnson, W., "Influence of Wake Models on Calculated Tiltrotor Aerodynamics" American Helicopter Society International Technical Specialists Meeting On

Aerodynamics, Acoustics, and Test and Evaluation, San Francisco, California, January 2002.

[60] – McCluer, M.S. and Johnson, J.L., "Full-Span Tiltrotor Aeroacoustic Model (FS TRAM) Overview and Initial Testing," American Helicopter Society Aerodynamics, Acoustics, and Test and Evaluation Specialist Meeting, San Francisco, CA, January 23-25, 2002.

[61] – Young, L.A., et al., "Insights into Airframe and Rotor-on-Wing Interactions from a 0.25-Scale Tiltrotor Wind Tunnel Model," American Helicopter Society International Technical Specialists Meeting On Aerodynamics, Acoustics, and Test and Evaluation, San Francisco, California, January 2002.

[62] – Charles, B.D., JanakiRam, R.D., Hassan, A.A., Quackenbush, T.R., "An Assessment of Current Methodology for Predicting Tiltrotor Blade-Vortex Interaction Aerodynamics," American Helicopter Society 51st Annual Forum, Fort Worth, TX, May 9-11, 1995.

[63] – Tadghighi, H., Rajagopalan, G., Burley, C., "Simulation of Tiltrotor Fountain Flow Field Effects Using a Finite Volume Technique - An Aero/Acoustic Study," American Helicopter Society 51st Annual Forum, Fort Worth, TX, May 9-11, 1995.

[64] – Liu, S.R., Brieger, J., Peryea, M., "Model Tiltrotor Flow Field/Turbulence Ingestion Noise Experiment and Prediction," American Helicopter Society 54th Annual Forum, Washington, DC, May 20-22, 1998.

[65] – George, A.R., Coffen, C.D., Ringler, T.D., "Advances in Tilt Rotor Noise Prediction," 14th Aeroacoustics Meeting, Aachen, Germany, May 11-14 1992.

[66] – Jumper, S.J., Prichard, D., Golub, R.A., "Tiltrotor Ground Noise Reduction from Rotor Parametric Changes as Predicted by ROTONET," AHS and Royal Aeronautical Society Technical Specialists' Meeting on Rotorcraft Acoustics/Fluid Dynamics, Philadelphia, PA, October 15-17, 1991.

[67] – Rutledge, C.K., George, A.R., "A Comparative Analysis of the XV-15 Tiltrotor Hover Test Data and WOPWOP Predictions Incorporating the Fountain Effect," NASA CR-189455, 1991.

[68] – Coffen, D.D, George, A.R., "Analysis and Prediction of XV-15 Tilt Rotor Discrete Frequency Aeroacoustic Noise with WOPWOP," NASA CR-187684, 1990.

[69] – Coffen, D.D, Charles, D., George, A.R., "Analysis and Prediction of XV-15 Tilt Rotor Hover Noise," American Helicopter Society 46th Annual Forum, Washington, DC, May 21-23, 1990.

[70] – Coffen, D.D, "Tilt Rotor Hover Aeroacoustics," NASA CR-177598, 1992.

[71] – Polak, D.R., George, A.R., "Experimental Aerodynamic and Aeroacoustics Investigation of a Scaled Tilt Rotor in Hover," American Helicopter Society 50th Annual Forum, Washington, DC, May 11-13, 1994.

[72] – George, A.R., "Tilt Rotor Aircraft Aeroacoustics," NASA CR-203040, 1996.

[73] – Riley, R.G. Jr., "Civil Tiltrotor Noise Impact Prediction Methodology," American Helicopter Society 48th Annual Forum, Washington, DC, June 3-5, 1992.

[74] – Boyd, Jr., D.D., "Challenges in Rotorcraft Acoustic Flight Prediction and Validation," 41st AIAA Aerospace Sciences Meeting, Reno, NV, January 6-9, 2003.

[75] – Burley, C.L., Marcolini, M.A., Brooks, T.F., Brand, A.G., Conner, D.A., "Tiltrotor Aeroacoustic Code (TRAC) Predictions and Comparison with Measurements," American Helicopter Society 52nd Annual Forum, Washington, DC 1996.

[76] – Burley, C.L., Brooks, T.L., Marcolini, M., Brand, A.G., Conner, D.A., "Tilt-rotor Aeroacoustic Code (TRAC) Predictions and Comparisons with Measurements," *Journal of the American Helicopter Society*, Volume 45, No. 2, April 2000, pp. 80-89.

[77] – Brentner, K.S., "Prediction of Helicopter Rotor Discrete Frequency Noise—A Computer Program Incorporating Realistic Motions and Advanced Acoustic Formulation," NASA TM 87721, Oct., 1986.

[78] – Jones, H.E, Burley, C.L., "A Study of the Effects of Blade Shape on Rotor Noise," American Helicopter Society Technical Specialists Meeting for Rotorcraft Acoustics and Aerodynamics, Williamsburg, Virginia, October 1997.

[79] – Lyle, K.H., Burley, C.L., Prichard, D.S., "A Comparison of Measured and Predicted XV-15 Tiltrotor Surface Acoustic Pressures," AHS Technical Specialists' Meeting for Rotorcraft Acoustics and Aerodynamics, Williamsburg, VA, October 28-30, 1997.

[80] – Prichard, D.S., "Initial Tiltrotor Aeroacoustic Code (TRAC) Predictions for the XV-15 Flight Vehicle and Comparison with Flight Measurements," American Helicopter Society 56th Annual Forum, Virginia Beach, VA, May 2-4, 2000.

[81] – Boyd, Jr., D.D., Burley, C.L., "Analysis of Measured and Predicted Acoustics from an XV-15 Flight Test," American Helicopter Society 57th Annual Forum, Washington, DC, May 2001.

[82] – Hawles, D. R., "Flight Operations to Minimize Noise," Presented at the American Helicopter Society-AIAA-University of Texas at Arlington Joint Symposium on

Environmental Effects of VTOL Designs, Arlington, Texas, Nov 16-18, 1970, and Vertiflite, Feb 1971.

[83] – Helicopter Association International, Fly Neighborly Committee, "*Fly Neighborly Guide*," HAI, 1971.

[84] – Chen, R.T.F., Hindson, W.S., and Mueller, A.W., "Acoustic Flight Tests of Rotorcraft Noise-Abatement Approaches Using Local Differential GPS Guidance," presented at the AHS Specialists Conference on Rotorcraft Aeromechanical Technologies, Fairfield County, CN, Oct 11-13, 1995.

[85] – Lappos, N., Arnold, J., Erway, P., and McConkey, E.," The Development of a Decelerating Helicopter Instrument Landing system Using Differential GPS", American Helicopter Society 56th Annual National Forum, Virginia Beach, VA, May 2-4, 2000.

[86] – Janikaram, R.D. and Khan, H., "Prediction and Validation of Helicopter Descent Flyover Noise," American Helicopter Society 56th Annual Forum, Virginia Beach, VA, May 2-4, 2000.

[87] – Schmitz, F.H. "Reduction of Blade-Vortex Interaction (BVI) Noise through X-Force Control", *Journal of the American Helicopter Society*, Vol. 43, Number 1, January 1998, pp. 14-24.

[88] – Schmitz, F.H., Gopalan, G., and Sim, B.W., "Flight Path Management and Control Methodology to Reduce Helicopter Blade-Vortex Interaction (BVI) Noise," *Journal of Aircraft*, Vol. 39, No. 2, March-April 2002, pp.193-205.

[89] – Abello, J.C., George, A.R., "Rotorcraft BVI Noise Reduction by Attitude Modification," AIAA/CEAS 5th Aeroacoustics Conference and Exhibit, Bellevue, WA, May 10-12, 1999.

[90] – Abello, J.C., George, A.R., "Wake Displacement Study of Attitude and Flight Parameter Modifications to Reduce Rotorcraft Blade-Vortex Interaction (BVI) Noise," AIAA/CEAS 9th Aeroacoustics Conference and Exhibit, Hilton Head, SC, May 2003.

[91] – Gervais, M. "Tiltrotor Blade-Vortex Interaction (BVI) Noise Control Through Non-Unique Longitudinal Force Trim," Tiltrotor/Runway Independent Aircraft Technology and Applications Specialists' Meeting of the American Helicopter Society, Arlington, Texas, March 2001.

[92] – Gervais, M., Schmitz, F.H., "Tiltrotor BVI Noise Reduction Through Flight Trajectory Management and Configuration Control," AIAA/CEAS 8th Aeroacoustics Conference, Breckenridge, CO, June 17-19, 2002.

[93] – Gervais, M., Schmitz, F.H., “Tiltrotor BVI Noise Abatement Using Flight Trajectory Management and Aircraft Configuration Control,” presented at the AIAA Guidance, Navigation and Control Conference, Austin, TX, August 2003.

[94] – Gessow, A., Crim, A.D., “An Extension of Lifting Rotor Theory to Cover Operation at Large Angles of Attack and High Inflow Conditions,” NACA TN-2665, April 1952.

[95] – Castles, W., New, N.C., “A Blade-Element Analysis for Lifting Rotors That is Applicable for Large Inflow and Blade Angles and Any Reasonable Blade Geometry,” NACA TN 2656, July 1952.

[96] – Johnson, W., “Analytical Model for Tilting Proprotor Aircraft Dynamics, Including Blade Torsion and Coupled Bending Modes, and Conversion Mode Operation,” NASA-TM-X-62369, 1974.

[97] – Johnson, W., “Analytical Modeling Requirements For Tilting Proprotor Aircraft Dynamics,” NASA-TN-D-8013, 1975.

[98] – Johnson, W., “An Assessment of the Capability to Calculate Tilting Prop-Rotor Aircraft Performance, Loads and Stability,” NASA-TP-2291, 1984.

[99] – Harendra, P.B., Joglekar, M.J., Gaffey, T.M., Marr, R.L., "V/STOL Tilt Rotor Study. Volume 5: A Mathematical Model for Real Time Flight Simulation of the Bell Model 301 Tilt Rotor Research Aircraft," NASA-CR-114614, 1973.

[100] – Ferguson, S.W., Hanson, G.D., Churchill, G.B., "Simulation Validation of the XV-15 Tilt-Rotor Research Aircraft," American Helicopter Society 40th Annual Forum, Arlington, VA, May 16-18, 1984.

[101] – Ferguson, S.W., "A Mathematical Model for Real Time Flight Simulation of a Generic Tilt-Rotor Aircraft," NASA CR-166536, Rev. A, September 1988.

[102] – Ferguson, S.W., "Development and Validation of the Generic Tilt-Rotor Simulation (GTRSIM) Program," NASA CR-166537, March 1988.

[103] – Prouty, R.W., "*Helicopter Performance, Stability and Control*," Krieger Publishing Company, Malabar, FL, 1995.

[104] – Weiberg, J.A., and Maisel, M.D., "Wind-Tunnel Tests of the XV-15 Tilt Rotor Aircraft," NASA TM-81177, April 1980.

[105] – Hoak, D. E. et al., "USAF Stability and Control DATCOM," Air Force Flight Dynamics Laboratory, Wright-Patterson Air Force Base, Ohio, Revised 1978.

[106] – Lesching, A., Wagner, S., "Theoretical Model to Calculate Aerodynamic Interference Effects Between Rotor and Wing of Tiltrotors," 16th European Rotorcraft Forum, Glasgow, September 1990.

[107] – Liu, J., McVeigh, M.A., Mayer, R.J., and Snider, R.W., "Model and Full-Scale Tiltrotor Hover Download Tests," 55th Annual Forum of the American Helicopter Society, Montreal, Quebec, Canada, May 25-27, 1999.

[108] – Felker, F.F., Light, J.S., "Rotor/Wing Aerodynamic Interactions in Hover" American Helicopter Society 42nd Annual Forum, Washington, DC, June 2-4, 1986.

[109] – Celi, R., "*ENAE 635 – Helicopter Stability and Control*," Class notes, September 2000.

[110] – Beddoes, T.S., "A Wake Model for High Resolution Airloads," 2nd International Conference on Basic Rotorcraft Research, Triangle Park, NC, 1985.

[111] – Leishman, J.G., "*Principles of Helicopter Aerodynamics*," Cambridge University Press, New York, 2000.

[112] – Lambert, M., "Flying the XV-15 and V-22 Tilt-Rotors," *Interavia*, Vol. 43, December 1988, pp. 1282-1286.

[113] – Page, J., Plotkin, K., "Acoustic Repropagation Technique, Version 2," Wyle Research Report, WR 01-04, January 2001.

[114] – Gopalan, G., Schmitz, F.H., Sim, B.W., "Flight Path Management and Control Methodology to Reduce Helicopter Blade-Vortex Interaction (BVI) Noise," American Helicopter Society Vertical Lift Design Conference, San Francisco, CA, January 19-21, 2000.

[115] – Demuth, H., Beale, M., "*Neural Network Toolbox User's Guide*," The MathWorks Inc., 7th Printing, June 2002.

[116] – Mehrotra, K., Chilukuri, M.K., Ranka, S., "*Elements of Artificial Neural Networks*," Second Printing, The MIT Press, MA, 2000.

[117] – Kottapalli, S., Kitaplioglu, C., "Neural Network Representation of External Tilt-Rotor Noise," *Journal of the American Helicopter Society*, Vol. 47, Number 2, April 2002, pp. 109-114.

[118] – Schmitz, F.H. and Sim, B.W., "Radiation and Directionality Characteristics of Helicopter Blade-Vortex Interaction Noise," *Journal of the American Helicopter Society*, Vol. 48, Number 4, October 2003, pp. 253-269.

[119] – Schmitz, F.H., Sim, B.W., Beasman, T., “Validation of Quasi-Static Acoustic Mapping (Q-SAM) Approach for Maneuvering Rotorcraft Blade-Vortex Interaction Noise Prediction,” American Helicopter Society 60th Annual Forum, Baltimore, MD, June 7-10, 2004.